Analysis of Acto-myosin Network Remodelling - Towards a Comprehensive Understanding of Tissue Closure Events

Dissertation

zur

Erlangung der naturwissenschaftlichen Doktorwürde

(Dr. sc. nat.)

vorgelegt der

Mathematisch-naturwissenschaftlichen Fakultät

der

Universität Zürich

von

Laurynas Pasakarnis

aus

Litauen

Promotionskomitee

Prof. Dr. Damian Brunner (Leitung der Dissertation)

Prof. Dr. Konrad Basler

Prof. Dr. Markus Affolter

Prof. Dr. Christof Aegerter

Zürich 2016

Table of Contents

Selected abbreviations

AM acto-myosin

AMC actin/MyoII cable

ANB actin nucleation burst

AS amnioserosa

AS-epidermis-SqhKO embryos with MyoII depletion in the amnioserosa and epidermis cells

AS-SqhKO embryos with MyoII depletion in the amnioserosa cells

AS-yolk-SqhKO embryos with MyoII depletion in the amnioserosa and the yolk cell

DC dorsal closure

deGradFP degrade green fluorescent protein (nanobody-mediated protein degradation method)

DPP/BMP decapentaplegic/bone-morphogenetic factor

ECM extracellular matrix

EE enhancer element

ES-SqhKO embryos with MyoII depletion in the epidermis cells

GBE germ-band extension

GBR germ-band retraction

GJ gap junction

GOI gene of interest

JNK Jun-N-terminal kinase

LatB Latrunculin B

LE leading edge

LOF loss-of-function

Mbs.N300 constitutively active MyoII phosphatase

MC midgut closure

MGC mechanically-gated ion channels

MPCs midgut progenitor cells

MyoII non-muscle myosin II

NLS nuclear localization signal

ORF open reading frame

PM plasma membrane

recAS-SqhKO embryos with amnioserosa cells recovering from MyoII depletion

ROI region of interest

ROS reactive oxygen species

TIPI TEV-induced protein inactivation

YC yolk cell

Summary

Morphogenetic events during which tissue gaps close are common in metazoan embryogenesis. In the fruit fly *Drosophila melanogaster* several such tissue closures occur at the dorsal side of the developing embryo. The first, dorsal closure (DC), starts after the retracting germ-band reveals an extra-embryonic tissue, the amnioserosa (AS). During DC the AS tissue shrinks and the surrounding epidermis fronts come together for the final sealing. DC provides a versatile model system for *in vivo* studies of cell behaviour and tissue biomechanics. In the first part of my work, I studied the force producing capacities of the epidermis and AS tissue. Previously, two models were proposed to explain how these produce the contractile forces driving DC. The additive force model suggested that both tissues produce sufficient force to drive DC on their own. While the AS tissue does so by constriction of the apical cell surfaces, the cells at the epidermis front together form a supra-cellular actin-myosin cable (AMC) that was proposed to act similar to a purse string. Contradicting the additive force model, the tissue ratchet model suggested that AS cells and epidermis must act together, ratchet-like, and close the dorsal discontinuity in a step-wise manner. To address the discrepancies between the two models, I used the deGradFP system to eliminate the function of the main force producing protein - non-muscle myosin II (MyoII) - in a tissue-specific and acute manner. I demonstrated that DC cannot proceed without AS cell contractility and that the AMC cannot drive the closure on its own. Vice versa, if the AMC is removed, AS tissue contractility alone is sufficient to complete DC. The results refute both previous models, and reveal that the force produced by apical AS cell constriction is necessary and sufficient for DC.

In the second part of my work, I investigated the mechanism of apical AS cell surface constriction. Early during DC, AS cells undergo repeated cycles of cell surface contractions and expansions that over time evolve into a gradual apical cell constriction. I revealed that cell-autonomous, transient actin nucleation bursts (ANBs) are at the basis of such "pulsed" contractions. Surprisingly, I found that these actin bursts occur independent of MyoII. This challenges the previously proposed role of mechanically-gated ion channels (MGCs) and calcium ions (Ca^{2+}) in triggering ANBs. To find other factors that could induce ANBs, I performed a drug-based screen, however, the results were inconclusive.

Besides being recruited to the transient apical actin bursts, MyoII also progressively accumulates at the AS cell-cell adherens junctions. Data from other model systems supports the hypothesis that MyoII at the junctions acts as an intracellular clutch stabilizing the contraction produced by the apical MyoII. My experiments with embryos recovering from MyoII inactivation suggested that the junctional MyoII can drive apical constriction of the AS cells without the need of the apical MyoII population.

Finally, I discovered a spatio-temporal gradient of morphogen Dpp signalling in the AS tissue and clarified that Dpp does not instruct apical constriction of AS cells.

In the third part, I describe a so far neglected, second closure event - midgut closure (MC). MC occurs just below the AS tissue and involves endoderm displacement over the large yolk cell (YC) lying in the centre of the embryo. I reveal a so far unknown contractile activity at the YC surface that is mediated by travelling cortical MyoII waves. These waves produce mechanical forces that are transmitted to the overlying AS and epidermis tissues. I also reveal other contractile structures and processes in the YC concluding that MC bears a striking resemblance to the epiboly process observed in higher organisms. Finally, I show that simultaneous inactivation of MyoII in the YC and the AS tissue prevents all closure events at the dorsal surface of the embryo. My results unveil the YC as an active contributor to tissue morphogenesis rather than only being a passive storage entity as was previously thought. In the end, I stress the importance of taking a holistic view of embryogenesis as a series of intertwined processes rather than focussing on single model systems in isolation from their environment.

In the final part, I summarize a number of experimental strategies and methods that I helped to develop and improve in several collaborations.

Zusammenfassung

Morphogenetische Ereignisse, bei denen Gewebelücken geschlossen werden, sind häufige Vorgänge während der Embryonalentwicklung von Metazoa. Mehrere solcher Gewebeschliessungen treten an der dorsalen Seite eines sich entwickelnden *Drosophila melanogaster* Fruchtfliegenembryos auf. Die erste, die dorsale Schliessung (DC), beginnt nach dem Rückzug des Keimbandes, welches extraembryonales Gewebe, die Amnioserosa-Zellen (AS), freilegt. Während der dorsalen Schliessung schrumpft das Amnioserosa-Gewebe. Dieser Vorgang bringt die Epidermiszellen, welche die AS umgeben, zusammen, um das Gewebe zu verbinden. DC stellt ein vielseitiges Modellsystem dar, um Zellverhalten *in vivo* sowie die Biomechanik von Geweben zu erforschen.

Im ersten Teil meiner Arbeit untersuchte ich die Fähigkeit der Epidermis und des AS-Gewebes, Kräfte für die dorsale Schliessung zu erzeugen. Bisher wurden zwei Modelle postuliert, die die nötige Erzeugung der kontraktilen Kräfte für die dorsale Schliessung durch Epidermis und AS beschreiben. Das ergänzende, additive Kräftemodell schlägt vor, dass beide Gewebe in der Lage sind, die dorsale Schliessung selbstständig zu veranlassen. Das AS-Gewebe schafft dies durch die Konstriktion, der Verkleinerung, der apikalen Zelloberfläche. Dahingegen formen die Epidermiszellen an der Zellfront ein gemeinsames, zellübergreifendes Aktin-Myosin Kabel (AMC), welches ähnlich einer Schnur agiert. Im Gegensatz zum additiven Kräftemodell, benötigt das Ratschenmodell die Zusammenarbeit von epidermalen und AS-Gewebe, um die dorsale Öffnung schrittweise, wie bei einer Ratsche, zu verschliessen. Um die gegensätzlichen Vorhersagen beider Modelle zu untersuchen, benutzte ich das deGradFP-System. Damit eliminierte ich die Funktion des Proteins, welches für den Grossteil der Kräfteproduktion verantwortlich ist, nicht-muskuläres Myosin II (MyoII), gewebespezifsch und akut. Ich zeige auf, dass die dorsale Schliessung nicht ohne die Kontraktion des AS-Gewebes stattfinden kann. Entgegen bisheriger Vorhersagen bewirkt das Aktin-Myosin Kabel ohne Mithilfe des AS-Gewebes die dorsale Schliessung nicht. Im Gegensatz dazu vermag das AS-Gewebe, trotz Entfernung des Aktin-Myosin Kabels, die dorsale Öffnung zu verschliessen. Diese Ergebnisse widerlegen beide bisher publizierte Modelle und zeigen auf, dass die Kräfte, welche durch die Kontraktion der apikalen AS-Zelloberfläche erzeugt werden, sowohl notwendig als auch ausreichend für die dorsale Schliessung sind.

Im zweiten Teil meiner Doktorarbeit untersuchte ich den Mechanismus der Konstriktion der apikalen Amnioserosa-Zelloberfläche. Früh während des Vorgangs der dorsalen Schliessung durchlaufen AS-Zellen wiederholte Zyklen von Zelloberflächenverkleinerung und Vergrösserung, welche sich im Laufe des Prozesses zu graduellen apikalen Konstriktionen entwickeln. Ich fand heraus, dass zellautonome, vorübergehende Erhöhungen der Aktinnukleation (ANBs) die Grundlage für solche “pulsierende” Zelloberflächenverkleinerungen sind. Ich konnte ausserdem aufzeigen, dass

diese Anhäufungen von Aktin überraschender-weise unabhängig von MyoII auftreten. Diese Beobachtungen stehen im Gegensatz zu bisher publizierten Ergebnissen, die eine Rolle mechanisch gesteuerter Ionenkanäle (MGCs) und Kalziumionen (Ca^{2+}) zum Auslösen der Aktinanhäufungen vorsehen. Um andere Signalwege für die Aktivierung der ANBs zu finden, führte ich einen Medikamenten-basierten Screen durch. Jedoch waren die Ergebnisse nicht beweiskräftig.

MyoII wird zum einen zu den vorübergehenden ANBs rekrutiert, häuft sich aber auch zunehmend an den Adherens Junctions; den Zellverbindungen zwischen den AS-Zellen, an. Ergebnisse von anderen Modellsystemen unterstüzten die Hypothese, dass MyoII als Kuppler zwischen Zellen an Junction fungiert, um die Kontraktion, welche vom apikalen MyoII hervorgerufen wird, zu stabilisieren. Eigene Experimente mit Embryonen, welche sich von einer MyoII-Inaktivierung regenerieren, weisen darauf hin, dass MyoII an den Junctions selbstständig die apikale Konstriktion der AS-Zellen antreiben kann, ohne die Mithilfe der apikalen MyoII-Population.

Ausserdem entdeckte ich einen räumlich-zeitlich geregelten Gradienten des Morphogens Dpp innerhalb des AS-Gewebes und stelle klar, dass Dpp nicht Auslöser für die apikalen Konstriktionen der AS-Zellen ist.

Im dritten Teil meiner Arbeit beschreibe ich ein bisher vernachlässigtes Verschluss-Ereignis – die Schliessung des Mitteldarms (MC). MC läuft direkt unterhalb des AS-Gewebes ab und beinhaltet die Verschiebung des Endoderms über die grosse Dotterzelle (YC), welche zentral im Embryo gelegen ist. Ich zeige eine bisher unbeschriebene kontraktile Aktivität in der Dotterzelloberfläche auf, welche durch sich wellenförmig fortbewegendes MyoII charakterisiert ist. Diese Wellen erzeugen mechanische Kräfte, welche auf die darüberliegenden AS- und Epidermisschichten übertragen wird. Ich dokumentiere ebenfalls andere kontraktile Strukturen und Vorgänge innerhalb des Dotters, welche mich zur Schlussfolgerung bringen, dass die Schliessung des Mitteldarms eine verblüffende Ähnlichkeit zur Epibolie aufweist, welche in höheren Organismen stattfindet. Zuletzt präsentiere ich das gleichzeitige Ausschalten von MyoII innerhalb der Dotterzelle und des AS-Gewebes. Dies verhindert alle Schliessungsprozesse an der dorsalen Seite des Embryos. Meine Ergebnisse enthüllen, dass die Dotterzelle einen aktiven Beitrag zur Gewebe-Morphogenese leistet und nicht nur eine, wie bisher vermutet, passive Speichereinheit darstellt. Zu guter Letzt hebe ich die Notwendigkeit hervor, die Embryonalentwicklung ganzheitlich zu betrachten, als eine Abfolge von vernetzten Ereignissen, und nicht nur einzelne Modelsystem isoliert von ihrer Umgebung zu untersuchen.

Im letzten Teil meiner Arbeit fasse ich eine Reihe von experimentellen Strategien und Methoden zusammen, welche ich in mehreren Kollaborationen entwickelt und verbessert habe.

Chapter 1. General Introduction

How an organism is created from a single cell is a challenging question. As complex as organisms are, their development is extremely reproducible and robust process. Yet it also displays a considerable cellular heterogeneity within an individual tissue or an organ arising due to the stochastic nature of molecular interactions. Over the last decades, tremendous input to understanding development came from genetics, molecular biology, biophysics and computational modelling. However, developmental processes cannot be looked at via the prism of only a single scientific discipline. Different methodologies used in various fields lead to conclusions that are not always compatible with each other. For example, computational modelling can accurately predict cellular responses within a certain parameter space, but classical genetics approaches fail to be in agreement with the proposed model. The novel and non-invasive molecular tools that are used to probe the principles of development can overcome such discrepancies. Everything considered, an immense effort is still needed from the scientific community to completely understand embryonic development.

Embryogenesis is a multi-layered phenomenon primarily driven by a complex network of genes, morphogens and signalling pathways. Downstream of the cellular identity and at the basis of cellular behaviour are the proteins that execute the essential functions like cell growth, cell shape change or cell motility. In this work I show that tissue re-modelling during morphogenesis relies on a self-organized acto-myosin (AM) networks. These networks are essential on both short- and long time scales and act over a range of magnitudes from nanometers to hundreds of micrometers. Nevertheless, common organization principles still apply at all of these scales. The primary aim of this thesis is to understand how AM networks drive the morphogenesis. A secondary aim is to demonstrate the importance of looking at development not as a single process isolated in space and time, but as a complex and intertwined phenomenon. A third aim is to facilitate application of novel molecular tools that would permit addressing protein functions and overcome the limitations of classical genetics.

1.1. The basis of acto-myosin networks

Actin is one of the most abundant proteins in eukaryotic cell. Mainly present in the cell cytoplasm, actin exists in two forms – monomeric G-actin and filamentous F-actin. Being an ATPase, actin hydrolyses ATP after the monomers are incorporated into the growing filament. However, the latter is kept stable due to slow dissociation of cleaved phosphate[1]. While *in vitro* such polymerization happens simply in the presence of ATP, in cells hundreds of actin-binding

proteins regulate the dynamics of polymerization in a strict spatio-temporal manner[1,2]. Extensive studies revealed proteins that nucleate, stabilize, cross-link, cap, break and displace actin filaments (Fig. 1A)[2–4]. Combined with the intrinsic nature of actin polymerization, this allows complete re-organization of actin networks in timescales from nanoseconds to minutes and hours. The importance of actin and its regulators in building the cell cytoskeleton is undeniable[4]. From building a cell cortex to facilitating vesicle transport, actin structures have diverse functions (Fig. 1B). In this work, we mainly focus on the cellular force-producing ability of actin.

Polymerization of actin networks alone is sufficient to locally produce mechanical forces[1,2]. However, when combined with the motor activity of myosin proteins, the extent of such forces increases tremendously. The myosin superfamily is comprised of up to 17 classes of motor proteins, yet it is non-muscle myosin II (MyoII) that drives morphogenesis[5–7] (also see Appendix 4). MyoII is a multi-protein complex that consists of three subunit pairs: two heavy chains (HCs), two regulatory light chains (RLCs), and two essential light chains (ELCs)[5]. While HCs provide the actual motor activity in an ATP-dependent manner, ELCs stabilize the structure of HCs. A critical feature of MyoII is to form anti-parallel mini-filaments that crosslink F-actin and slide the individual actin filaments against each other[4,5,8]. MyoII cross-linking and contractile functions are regulated mainly by reversible RLC phosphorylation on Ser19[4,5]. This greatly increases ATPase activity of MyoII in the presence of actin, but has little or no effect on MyoII affinity for actin[5].

In vitro experiments demonstrated that acto-myosin (AM) contractility could be reconstituted in simple systems consisting of only purified actin, myosin and ATP[9,10]. In contrast, a single cell contractome is tremendously complicated (Fig. 2A)[11]. Most importantly, key proteins controlling AM network behaviour affect both the actin polymerization dynamics and MyoII contractility (Fig. 2B)[11]. Over the decades, evidence implicated Rho family GTP-ases as the central regulators of AM networks[11–13]. RhoA, Rac and Cdc42 are both activating and repressing various AM components including actin nucleators such N-WASP and motors like MyoII[11]. Generally, a developmental gene program lies upstream of small GTP-ases that triggers spatio-temporal expression or re-localization of these proteins[14,15].

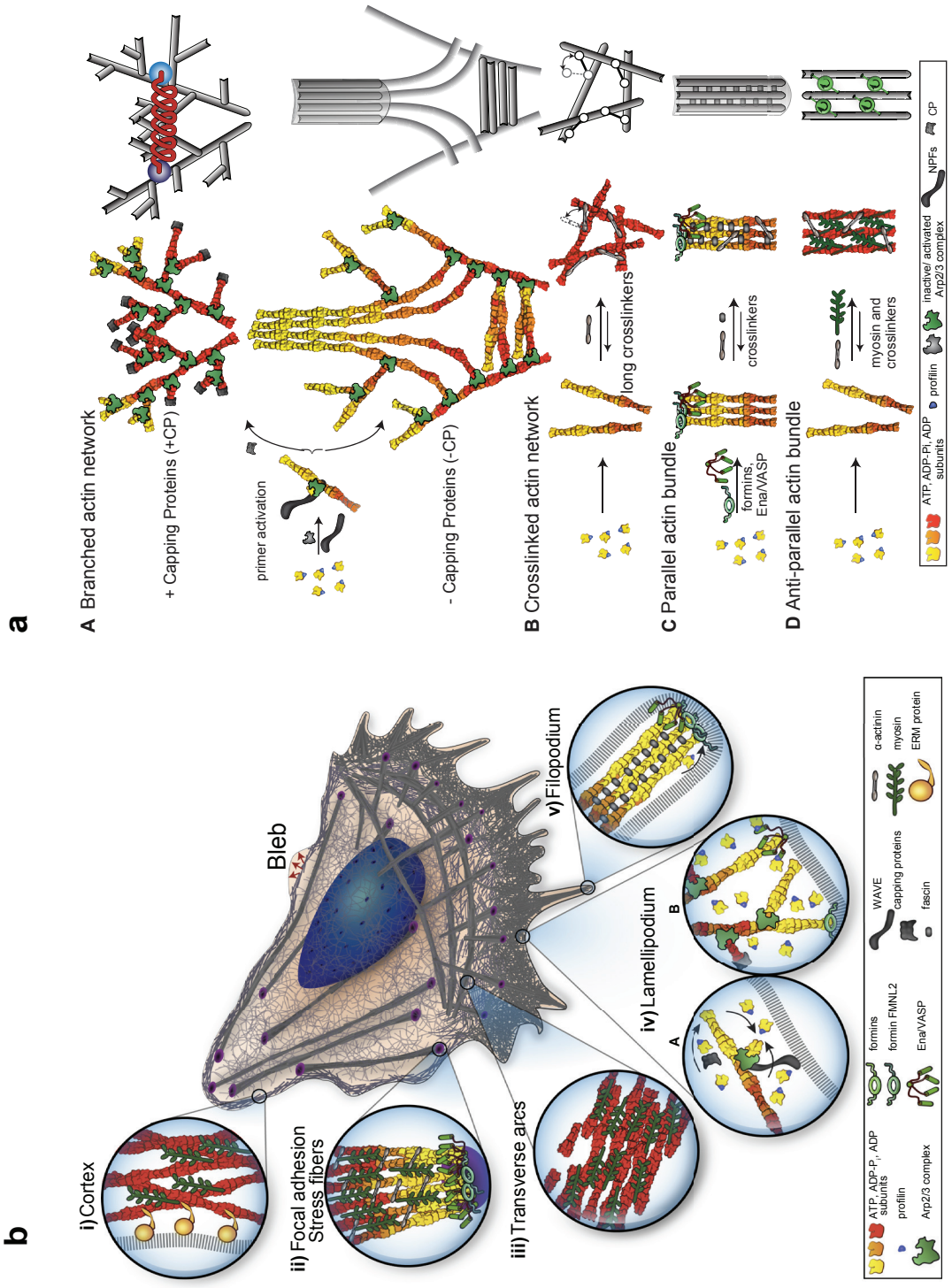

Figure 1. Most common actin organizations found *in vivo*. (a) Actin network structures and their mechanical description. A: a branched actin network. In the absence of capping proteins (-CP), actin filaments grow longer and can bend or coalesce into a parallel bundle. B: long cross-linkers organize actin filaments into networks. C: short cross-linkers tightly pack unbranched filaments into a stiff and straight bundles. D: molecular motors, such as myosins, are dynamic links that cross-link antiparallel filaments into a contractile unit, which acts as an active spring. **(b)** Example of migrating cell that contains distinct actin structures in different subcellular locations. All these structures are specialized for precise function: i) The actin cortex maintains cell shape; ii) Contractile bundles span the cell body and withstand large mechanical forces; iii) Transverse arcs of antiparallel actin filaments are contracting to provide traction and pulling forces; iv) Localized polymerization of branched actin networks pushes the plasma membrane forward creating the lamellipodia; v) Parallel actin bundles elongate to form sensory organelles filopodia. Images adapted from Blanchoin, Boujemaa-Paterski, Sykes and Plastino 2014.

a

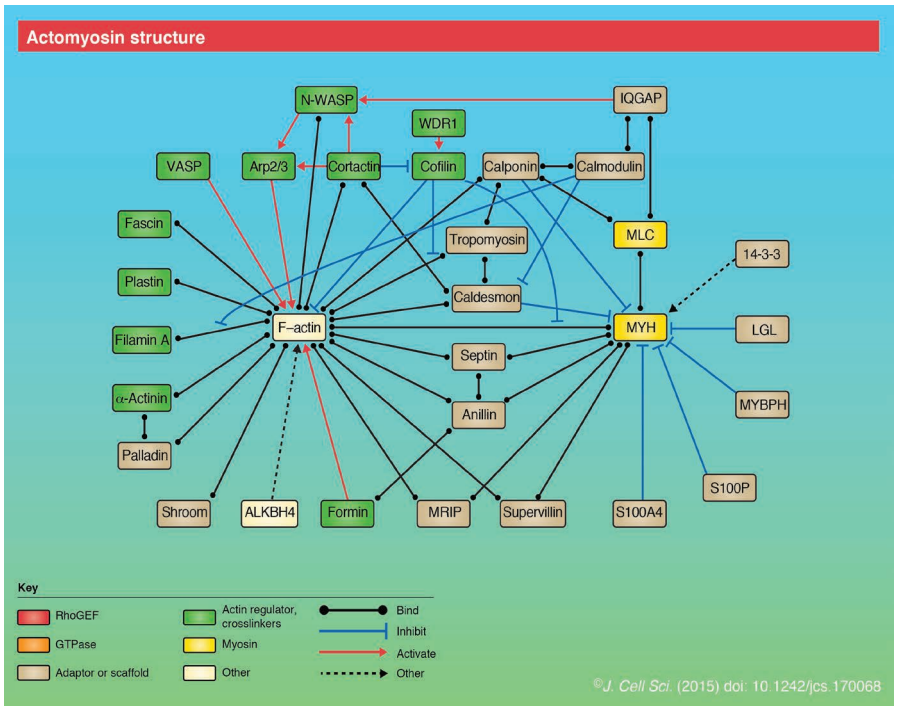

b

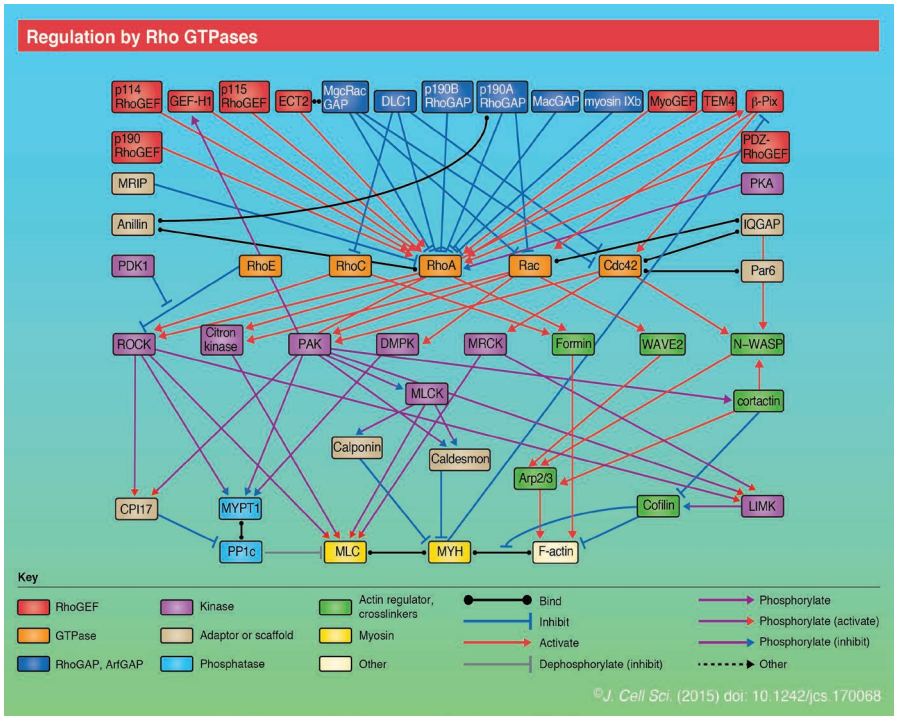

Figure 2. A systems view of non-muscle cell contractome. (a) Structure of principal actomyosin (AM) network components. The basic architecture of actin network is either linear (formin-mediated) or branched (Arp2/3-N-WASP-mediated) and this affect its ability to interact with Myosin II (yellow, MLC-MHC). Other actin or Myosin II regulators, adaptors or scaffold proteins adapt the network behavior according to the needed function. **(b)** AM regulatory network by Rho-family GTPases. Rho-family GTPases are activated downstream of external signals and regulate AM contractility through the activation of target proteins. RhoA is most commonly associated with AM contractility, but RhoC, Cdc42 and Rac1 are also positive regulators affecting several AM components. Images adapted from Zaidel-Bar, Zhenhuan and Luxenburg 2015.

1.2. Acto-myosin-driven mechanical forces during development

The classical example of AM-mediated contractility is the force produced by muscle cells. However, AM of non-contractile cells is the major force-producer during embryogenesis[6–8,16,17] (also see Appendix 4). At the very core of development, i.e. increasing cell number from a single fertilized cell, is the AM-driven cytokinesis. After the multiple cell divisions, embryos reach typical "ball-of-cells" blastoderm stage when morphogenetic movements start forming germ layers and setting up the body plan of the organism. Most if not all morphogenetic processes depend on AM contractility. Almost any type of active cell movement – whether single or collective – depends on interaction between the intracellular AM network and the extracellular matrix[8,16,18,19]. Finally, once the organism is formed the fine-tuning and maintenance of cell shape and tissue integrity depends on AM networks.

Generation of diverse tissue shapes and movements requires diverse means by which AM contractility can be modulated. Every developmental process operates a different spatio-temporal control over AM networks, yet several common themes of AM organization emerge. Depending on the composition of cross-linking proteins, F-actin can form either thick bundles or a thin meshwork[6–8,16]. As a result, MyoII motor activity will cause diverse outcomes when applied to such networks. For example, MyoII would result in isotropic contraction of actin meshwork as all actin filaments are oriented at different angles relative to each other. In contrast, anti-parallel actin bundles would be displaced anisotropically following their orientation. As a consequence the mechanical properties of AM networks depend on such actin filament organization[4,6,19]. Generally, loose networks are easily deformed, allowing the forces to be pulsed or polarized. In contrast, dense and stiff networks can resist compression and external stresses. In any case, the forces produced by such contracting AM networks will not lead to any productive outcome such as cell shape change or cell movement unless they are anchored to either a plasma membrane, cellular junctions or an extracellular matrix (ECM). If anchored, contracting a loose AM meshwork will induce isotropic deformation, whereas bundled AM networks will generate tensioned cables. During embryonic development, the entire range of AM behaviours are observed, from loose polarized anisotropic flows to supra-cellular purse-strings[6,7,16] (also see Appendix 4).

In developmental biology an emphasis is put on classical examples of morphogenetic processes, such as gastrulation, neurulation or convergent extension. Nonetheless, mechanical

aspects and the role of AM contractility is recognized in a growing number of other developmental systems such as tissue involution, folding, tube formation or vascularization[6,7]. On a large scale, AM networks drive the formation of the whole organism as demonstrated by the gradient of AM contractility in *C. elegans* zygote polarization and retrograde AM flow during zebrafish epiboly[20,21]. On a smaller scale, AM networks orchestrate intracellular forces to coordinate single cell shape changes and cell movements. In the end, the coordination of mechanical forces on local and global tissue scales is essential for integrating short-term changes with the overall morphogenesis during the span of several hours[6,16,22].

1.3. Dorsal closure in *Drosophila melanogaster*

Dorsal closure (DC) in embryos of the fruit fly *Drosophila melanogaster* provides a powerful model system to study tissue closure events *in vivo*. During the mid-embryogenesis, a retracting germ-band exposes an extra-embryonic amnioserosa (AS) tissue, which is flanked laterally by the two sheets of epidermis cells[23,24] (Fig. 3A). These converge over a period of several hours, until they first meet at the anterior and posterior canthi from where they gradually connect along the dorsal midline in a process called zipping. During the epidermis convergence, AS cells gradually constrict their apical surface and eventually fold up to close into a tube just below the sealed epidermis[25,26]. Shortly after the tube closure, they are disposed of through apoptosis[27,28].

Early studies identified the JNK and Dpp signalling pathways as instructive signals that trigger the changes in cell behaviour needed for the closing force production. Zygotic mutants of genes encoding members of these signalling pathways result in "dorsal-open" phenotypes causing a large hole in the larval cuticle[29–31]. Proteins regulating cytoskeleton dynamics and remodelling such as small GTP-ases Rho1, Rac and Cdc42 were found to be key downstream effectors of JNK and Dpp signalling[32,33]. Despite a plethora of cell biological, genetic and biophysical analysis, as well as diverse computational modelling attempts, the exact contribution of the various forces to DC remains unclear (Fig. 3B). Genetic analysis showed that non-muscle myosin II (MyoII) is at the center of force-production in both the AS tissue and the epidermis[34,35]. Thereby, each of the cells forming the leading edge (LE) of the closing epidermis generates a contractile actin/MyoII cable (AMC). This cable spans the dorsal, apical cell edge, which connects the epidermis with the neighbouring AS tissue (Fig. 3B). Specialized adhesion sites protruding into the neighbouring epidermis cells interconnect the ends of

individual actin cables such that altogether they form a supra-cellular cable surrounding the opening[25]. Apical constriction of the AS cells requires MyoII activity, not in a continuous manner, but such that it produces repeated cycles of cell surface contraction and expansion[36,37] (Fig. 3B). Such "pulsing" of AS cell surfaces is constitutive and governed by transient actin and MyoII foci[38–40]. These foci evolve into a continuous AM meshwork at the late stages of DC, when AS cells accelerate the apical constriction[38,39]. In addition, MyoII accumulates at the adherens junctions to form a belt that may contribute to apical cell constriction[38,39,41]. Recently, the apoptotic program was shown to trigger an initial volume loss, which contributes to the overall AS tissue surface reduction and also precedes the apical constriction[42] (Fig. 3B).

Interfering with tissue tension via laser-induced tissue ablations showed that AS tissue is under tension and, therefore, must provide a pulling force on the surrounding epidermis sheets[43]. Laser ablations of AMC formed by the LE cells suggested that the cable produces a force reminiscent of a purse-string[43,44]. Based on these data, an additive force model was proposed, which states that one tissue could compensate for the loss of force-producing capacity of the other and vice versa. Thus, DC is conceptually understood as an equilibrium of mechanical forces with a net force vector directed dorsal-ward[45]. Either tissue (AS or epidermis) harbors an excessive force-producing capacity needed for the opening to close[45,46]. In addition, this particular model is supported by genetic rescue experiments with embryos carrying a loss-of-function mutation in *zipper* (*zip*), which encodes the MyoII heavy chain. Over-expression of GFP-tagged Zip in the AS tissue or in epidermis cells, was sufficient to rescue the dorsal open phenotype[35]. Additional laser wounding and mechanical jump experiments provided further evidence for the additive force model, showing that if the integrity of either one of the tissues is compromised, the other up-regulates force-production to complete DC[46,47]. Despite all this evidence, doubts remain as all such laser experiments not only disrupt force production, but also affect tissue integrity and, in addition, cause wound healing responses, such as secondary actin/MyoII purse-strings[44].

The later discovery that the rapid AS cell surface oscillations produce the force pulling on the surrounding epidermis brought up an alternative model[36]. The model posits a tissue-wide ratchet, where local force pulses of the AS cells drive dorsal-ward movement of the neighbouring epidermis front. This results in a moderate shortening of the AMC in the affected LE cells. Assuming that the cells maintain the shortened cable, this provides a clutch preventing the ventral-ward retraction of the LE. Supporting this model is the fact that in embryos carrying mutations in the JNK encoding gene *basket*, DC is hampered according to the degree of the AMC defect, which is highly variable in these mutants due to maternal protein contribution[29,36].

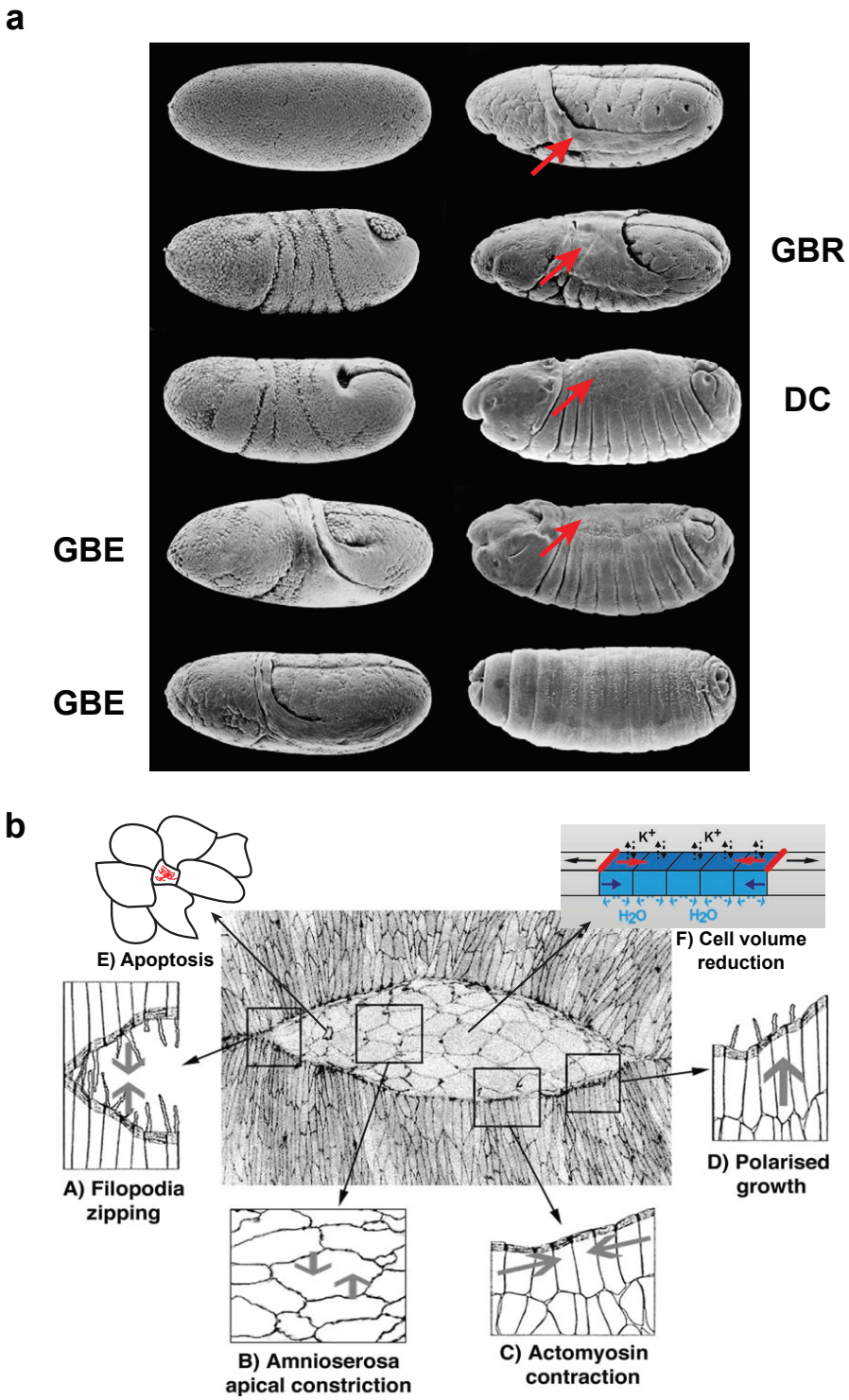

Figure 3. Dorsal closure (DC) during *D. melanogaster* embryogenesis. (a) Scanning electron microscope images of developing *D. melanogaster* embryo. After the germ-band extension (GBE) embryo adopts a stereotypical tissue arrangement with amnioserosa (AS, red arrow) being folded by the germ-band. During the subsequent germ-band retraction (GBR), AS cells are gradually unfolded and exposed to the dorsal surface of the embryo (red arrows). Once GBR finishes, DC takes place and seals the dorsal opening. Adapted from FlyBase. (**b)** Current view of DC as a complex biomechanical process. Zipping process (A) seals the two epidermis sheets together. The convergence of epidermis is driven by AS cell apical constriction (B) with a contribution from acto-myosin contraction in the leading edge of epidermis (C). In addition, epidermis cells undergo polarized growth (D) directed towards the dorsal midline. AS cell apoptosis (E) and AS cell volume reduction (F) contributes DC at various stages. Adapted from Jacinto et al. 2003[48] and Saias et al. 2015[42].

In principle, the two models are not mutually exclusive. It is possible that the tissue ratchet acts in early phases of DC, when the opening is large and the actin/MyoII purse-string is still weak and incomplete. Later in the process, where most effects of mutants and laser-induced ablations were monitored, both forces are sufficient to drive the closure. The ideal experiment to rule out one or the other model is to selectively remove MyoII activity in the AS tissue and in a separate experiment also in the epidermis. Previous attempts to do so have not been sufficiently tissue-specific to produce unambiguous results[35,43,47,49]. Similarly, over-expression of dominant-negative forms of various regulators of actin dynamics[50,51] or negative regulators of signalling pathways[26] were not strong enough to produce complete loss-of-function phenotypes. In addition, most of these perturbations interfered with the upstream components of the final force production and affected proteins with multiple targets in the cell, e.g. actin, Rho1[52–54], or their expression was not tightly controlled[35]. Unfortunately, the short time window during which DC happens also limits the usage of traditional gene knock-down techniques like RNA interference (RNAi). Accordingly, RNAi-based screens in already differentiated epidermal or AS cells revealed very few factors interfering with DC[55].

1.4. Molecular tools for depleting protein function

Developmental biology relies on traditional reverse or forward genetics. Therefore, perturbation of gene function whether on gene, mRNA or protein level is essential. Classical mutagenesis screens provided vast numbers of genes, the functions of which were elucidated using various techniques. However, it was molecular cloning and whole genome sequencing that allowed unprecedented analysis of gene functions. Parallel to genome sequencing, RNAi was discovered whereby small single-stranded and genetically encoded RNA molecules were shown to deplete their target mRNAs[56]. This led to rapid diversification of RNAi tools, ranging from synthetic RNAi probes or morpholinos to genetically encoded libraries of RNAi for most known genes.

As more and more studies were done using RNAi or classical mutagenesis, there was a growing number of cases where these methods were not adequate anymore and were contaminated with secondary or off-target effects. The concern with the former arose from the fact that protein stability was much higher than previously assumed, and removing a gene or its mRNA did not affect the protein function. Additionally, using transcriptome analysis it was revealed that a great number of genes are transcribed at very low levels leading to 1-2 mRNA

transcript molecule per cell[57]. Thus, while RNAi effect could be measured and detected on highly abundant transcripts, to target a single mRNA in the cell became a challenge. Because of these reasons, functional depletion at gene or mRNA level is relatively slow and very often is only observable after several/dozen cell divisions or an extended period of time. Thus, these methods can be rarely used for acute functional depletion.

Over the last decade a number of methods were developed aiming for targeted and acute protein inactivation[58]. In addition, protein systems were engineered to be mis-localized, aggregated or post-translationally modified rather than just depleted. The commonly applicable methods for interfering with protein function are summarized in Table 1. The underlying mechanism of these molecular tools differs greatly, but the main themes focus on depleting proteins by 1) abrupt damage by reactive-oxygen-species (ROS) (e.g. KillerRed, miniSOG, CALI/FALI), 2) utilizing degradation machinery of the cell (e.g. TIPI, deGradFP, DARPins, TEV-protease mediated cleavage, auxin-inducible degron, phospho-degron) or 3) exploiting temperature or light switches (e.g. temp-sensitive proteins, heat- or light-inducible degrons, CRY2/CIB, LOV2). Most of these protein inactivation tools can be easily engineered by adding a specific protein tag to the gene-of-interest (GOI). Most importantly, all of these allow incredibly fast inactivation of desired proteins when compared to the classical genetics or RNAi. A few of them even permit precise protein inactivation in a subcellular region, such as all light/laser-induced degradation tools (KillerRed, miniSOG, CALI/FALI, heat- or light-inducible degron, CRY2/CIB, LOV2). Others allow achieving tight spatio-temporal genetic control over the protein degradation if combined with tissue or cell-specific expression systems (e.g. TIPI, deGradFP, DARPins, TEV-protease mediated cleavage, phospho-degron). Contrary to RNAi and especially gene removal methods, several of these inactivation methods are completely reversible and within several minutes to hours restore protein function *de novo* (e.g. KillerRed, miniSOG, CRY2/CIB, LOV2).

The continuously increasing number of such new molecular tools is offset by the fact that not one of them is universal and absolutely perfect in every respect. Obviously, external damage by ROS besides the protein of interest also depletes nearby proteins. Degradation-based methods can be overwhelmed by highly expressed and translated proteins as the gene expression is normally not affected and constantly produces new proteins that again need to be targeted. Some methods demand specialized equipment (e.g. KillerRed, miniSOG, CRY2/CIB, LOV2), specific-substances (e.g. CALI/FALI, auxin-inducible degron) or certain conditions (e.g. constitutive darkness for CRY2/CIB, LOV2 in the "non-degraded" state). Finally, most if not all methods require generation of transgenic animals or cell lines, where GOI is replaced

or engineered with the appropriate tag. It is also critical that the extra protein tag does not interfere with normal protein function. Earlier endogenous protein tagging or plasmid making required laborious molecular cloning approaches, but upon the advent of CRISPR/Cas9 system, a quick gene modification at the endogenous locus became a reality. Even though the efficiency of genome engineering is constantly improving, a vast choice of protein depletion methods combined with the power of CRISPR/Cas9 opens unprecedented possibilities to probe gene functions throughout all model organisms.

Method	Induction	Prerequisites	Drawbacks	Reference
CALI/FALI	light (depends on the fluorophore)	External dye; transgenics; dark state	ROS damage nearby off-target proteins	[59]Jay et al., 1988; [60]Surrey, et al., 1998;
miniSOG (CALI)	blue light	miniSOG protein tag; transgenics; dark state	ROS damage nearby off-target proteins	[61]Shu et al., 2001
KillerRed (CALI)	green light	KillerRed protein tag; transgenics; dark state	ROS damage nearby off-target proteins; intrinsic dimerization prevents fusion with protein of interest	[62]Bulina et al., 2006
KillerRed - SuperNova version (CALI)	green light	KillerRed/SuperNova protein tag; transgenics; dark state	ROS damage nearby off-target proteins	[63]Takemoto et al., 2013
CRY2/CIB	blue light	Large CRY2 protein tag; transgenics; dark state	Unwanted minimal activity in the dark state	[64]Kennedy et al., 2010
CRY2 photobodies	blue light	Large CRY2 protein tag; transgenics; dark state	Aggregation might sequester off-target proteins	[65]Yu et al., 2009; [66]Taslimi et al. 2014
LOV2	blue light	transgenics; dark state	Unwanted minimal activity in the dark state	[67]Renicke et al., 2013
deGradFP	over-expression	GFP protein tag; transgenics; over-expression system	Not every GFP-tagged protein can be degradable; takes considerable amount of time to reverse the effects	[68]Caussinus et al., 2011
DARPins	over-expression	DARPin protein tag; transgenics; over-expression system	For specific targets DARPin needs to be made, but for GFP/mCherry they were already generated	[69]Brauchle et al., 2014
GFP-nanotrap	over-expression	GBP protein tag; transgenics;	Target protein is only mis-localized and not de-	[70]Rothbauer et al. (2008);

		additional TEV over-expression system	degraded; limited application beyond plant cells	[71]Schornack et al. (2009)
TEV-mediated cleavage	TEV over-expression	DARPin protein tag; transgenics; additional TEV over-expression system	Splitting the target protein might not inactivate it	[72]Harder et al., 2008
TIPI	TEV over-expression	TIPI protein tag; transgenics; additional TEV over-expression system	Stable version of protein is always needed as a control	[73]Taxis et al., 2009
Auxin-induced degron (AID)	External auxin addition	AID protein tag; transgenics	Less spatio-temporal control over protein inactivation	[74]Nishimura et al., 2009
C-terminal/bi-directional degron	TEV over-expression	Large bi-directional degron tag; transgenics	Unwanted minimal inactivation activity without exposing the degron	[75]Jungbluth et al., 2010
Heat-inducible degron	Heat	Protein fusion with large Arg-DHFR enzyme; transgenics	Model system must work in 23-37°C; lack of subcellular resolution	[76]Dohmen et al., 1994
Temperature-sensitive mutations	Heat	transgenics	Lack of subcellular resolution; maybe irreversible	Expanded by [77]Tan et al., 2009 introducing inteins
Small molecule inhibitors	Chemical compound application	Different external chemical compound for every target	Affects mostly enzymes and is unspecific most of the times; can be expensive	-
GFP-nanotrap	Over-expression	GBP protein tag; transgenics	Target protein is only mis-localized and not de-degraded; limited application beyond plant cells	[70]Rothbauer et al. (2007); [71]Schornack et al. (2009)

Table 1. Commonly used methods for depleting protein functions.

1.5. Goals and structure of this thesis

AM networks give rise to fascinating emerging behaviours at both cell and tissue levels. The ability to be rapidly re-modelled makes the network a highly adaptable system that can adjust to external and internal forces without the need of complex genetic circuitry. Therefore, to understand the role of AM networks, it is necessary to study and perturb them at the most downstream component actin/MyoII. The more upstream from AM networks the interference, the more processes are affected (Fig. 2B) eventually changing the developmental context

altogether. This thesis is aimed at studying AM networks *in vivo* using tissue closure events as model systems. In addition, using novel tools to achieve unprecedented acute and tissue-specific protein inactivation, I try to answer the key questions and solve discrepancies between the models of dorsal closure (DC) in the fruit fly *Drosophila melanogaster*.

In Chapter 2, I present compelling evidence of how force components are orchestrating tissue closure events – one of the key developmental hallmarks of morphogenesis. Using DC as a model system, I apply acute protein depletion to interfere with tissue force production in otherwise wild-type developing embryos. The results dismiss the current models of DC and suggest that it is a single tissue-driven closure event.

In Chapters 3 and 4, I focus on amnioserosa cells (AS) – the main force provider during DC – and demonstrate that its apical cell surface contractions are mechanistically different than current views based on other model systems. I also suggest a possible connection between the short scale AM networks and the global cell sheet morphogenesis via the apical cell constriction. Finally, I address several misconceptions about the role of upstream developmental signal Dpp during the AS cell apical constriction.

In Chapter 5, I describe in great detail so far neglected tissue closure event during *D. melanogaster* embryogenesis powered by a single yolk cell. I demonstrate the role of AM network in the yolk cell and reveal its effects on the surrounding tissues. I also propose tissue closing mechanism, which is not too dissimilar from the epiboly in higher animals. With this example, I also stress the importance of looking at the morphogenesis as an interconnected process rather than focusing on a single model system ignoring concomitant processes around it.

In Chapter 6, I describe materials and experimental procedures used in this study.

In Appendix 1, I describe the strategies that I used to improve and develop non-invasive tools for studying mechanical forces during the embryogenesis. I reveal the importance of such methods in helping to overcome genetic limitations posed by the nature of *D. melanogaster* embryonic development.

In Appendix 2, I show additional data relevant to Chapter 2 and the study published in Eltsov et al. 2015[25].

In Appendix 3, I show data and stand-alone observations during the various processes in *Drosophila* embryogenesis.

In Appendix 4, I include the publications published during the course of this PhD.

Chapter 2. Tissue-specific, acute MyosinII activity depletion dismisses current models of tissue force orchestration in dorsal closure

This chapter is a manuscript currently re-submitted and under revision in Nature Cell Biology.

Pasakarnis, L., Frei, E., Caussinus, E., Affolter, M. and Brunner, D. Tissue-specific, acute MyosinII activity depletion dismisses current models of tissue force orchestration in dorsal closure.

LP and DB conceived and planned the experiments; LP performed the experiments; LP and EF generated fly strains used in the study; EC and MA provided unpublished fly strains; LP and DB analysed the data and wrote the manuscript.

2.1. Introduction

Morphogenetic events during which tissue gaps close are common to metazoan embryogenesis. The generation of the relevant forces requires precise spatial and temporal control of changes in gene expression and cell architecture. Defective closure results in arrested or abnormal embryogenesis. In vertebrate development such defects can result in cleft lips or palates or in spina bifida[78,79]. Dorsal closure (DC) in embryos of the fruit fly *Drosophila melanogaster* provides a versatile model system for *in vivo* studies of tissue closure. During mid-embryogenesis, germ band retraction expands the amnioserosa (AS) tissue, which ends up flanked laterally by two sheets of epidermis cells[23]. These sheets converge over a period of several hours, during which they first meet at the anterior and posterior canthi of the AS tissue. From there, the epidermis fronts fuse along the dorsal midline in a process called zipping.

The F-actin associated motor MyosinII (MyoII) produces two main forces that were suggested to drive the convergence of the epidermis fronts[34,35]. The AS tissue produces a first force, which pulls the surrounding epidermis dorsally[43]. AS cells thereby gradually constrict their apical surfaces[43]. The epidermis cells forming the leading edge (LE) of the closing epidermis add a second force by placing a contractile actin/MyoII cable (AMC) parallel to the LE at their dorsal apical side[34,35,43]. The cables of individual cells connect via specialized adhesion sites to form a contractile super-cellular cable that surrounds the entire opening[25,43]. Despite a plethora of cell biological, genetic, and biophysical analyses, as well as diverse computational modelling attempts, the exact contribution of these forces to DC remained unclear. Several experiments suggested that each force alone is in excess of what is needed to drive closure, suggesting independent, additive functions[45,46]. More recently, rapid AS cell surface oscillations were described[36]. Such pulsing of AS cell surfaces is constitutive and governed by repetitively appearing actin and MyoII foci[36,38–40]. AS cell surface contractions

lead to transient dorsal-ward displacements of the neighbouring LE. Since the LE starts moving dorsally in a stepwise manner with the appearance of the AMC, an alternative model in which the two forces combine to form a ratchet mechanism was proposed[36]. Thereby, AS cell-driven transient LE displacements locally shorten the AMC, which functions as a clutch preventing ventral-ward LE retraction while AS cells relax. The two models are not mutually exclusive as the tissue ratchet was suggested to act early in DC, when the opening is large and the gradually maturing AMC is still weak, while later the AMC becomes sufficiently strong to act independently[36].

Selective removal of MyoII-mediated force activity in the AS or epidermis tissue is the ideal experiment for testing both models. Previous attempts to do so did not produce unambiguous results since maternally deposited mRNA and protein produced pleiotropic and non-penetrant mutant phenotypes and tissue-specificity of ectopically expressed rescuing or inhibitory factors remained questionable[26,35,49,50]. Similarly, laser-mediated ablation of subsets of cells cannot be extrapolated to global tissue behaviour, since injured tissues rapidly react by forming ectopic AMCs surrounding the wound[43,44,46,47].

To overcome previous experimental limitations, we selectively applied a protein knock-down approach for acute MyoII depletion in the AS or epidermis tissue[68]. Our results exclude the additive force model since alone, the AMC cannot drive DC alone. The AS tissue, in turn, can autonomously drive DC, excluding the necessity of a global tissue ratchet, which merely appears to promote DC onset. Zipping occurs without epidermal MyoII in support of recent electron microscopy data suggesting a MT-mediated mechanism[25]. Our results suggest a structural role for the AMC, which is important for correct cell-cell matching during zipping. Finally, laser-mediated AS tissue incisions reveal a MyoII-dependent, isotropic tissue tension component that adds to a MyoII-independent, directional component.

2.2. Results

2.2.1. The AMC cannot drive DC

The additive force model proposes that epidermis and AS tissue each harbour an excessive force-producing capacity needed to close the opening[45,46]. To test this possibility, we selectively removed MyoII activity in each tissue, prior to DC onset, by targeting GFP-tagged

Sqh (Sqh-GFP), the MyoII light chain, to the protein degradation machinery using deGradFP[68,80]. In our experiments, maternal and zygotic Sqh were depleted (Methods, section 6.1.3). In this way, we followed DC in wild type embryos lacking one or the other tissue-specific force.

We first investigated the contribution of the epidermal AMC by depleting Sqh-GFP in the AS tissue (AS-SqhKO). To drive UAS-mediated deGradFP, we expressed Gal4 via the 332.2 enhancer element (332.3-Gal4)[81]. Unlike the commonly used c381-Gal4 enhancer element, 332.2-Gal4 is strictly AS tissue-specific throughout DC (Fig. 9A)[81,82]. Consistently, Sqh-GFP arranged into the typical pearl string-like arrangement in LE cells of all AS-SqhKO embryos (n=23) suggesting an intact AMC (Fig. 4A-4B). In AS cells, Sqh-GFP started forming multiple, non-motile particles at the extended germ band stage (Fig. 4C). These particles were attributed to protein degradation but could also be depleting protein activity by aggregation[68]. As previously indicated by a proof of principle experiment for deGradFP-mediated protein depletion, DC failed in AS-SqhKO embryos and the AS tissue eventually ruptured (Fig. 4C)[68]. This phenotype is fully penetrant and protein-specific as expression of mCherry-tagged Sqh in AS tissue rescued AS-SqhKO embryos (Methods, section 6.1.3; Fig. 50). AS-specific Sqh depletion did not affect Jnk signaling (Fig. 9B)[83]. To evaluate the efficiency of deGradFP-mediated MyoII depletion in AS-SqhKO embryos, we compared them to embryos overexpressing the previously used, MyoII-inhibiting, constitutively active MyosinII phosphatase (UAS-Mbs.N300) in AS tissue[42,84,85]. In UAS-Mbs.N300 embryos, DC proceeded and finally completed (Fig. 9C-9D). This suggests that deGradFP-mediated MyoII depletion is much more efficient than MbsN300-mediated inactivation. To exclude that AS tissue-specific MyoII depletion indirectly affects AMC force production we compared AMC tension in wild type and AS-SqhKO embryos with laser-mediated tissue incisions (Fig. 9E)[42,43,45,46,54]. We could not detect a significant difference between control and AS-SqhKO embryos (Fig. 4D). We conclude that the AMC cannot produce sufficient force to drive DC.

AS-SqhKO embryos showed clear changes in the initial morphogenesis of the AS tissue. In most cases, the anterior and posterior ends of the two lateral epidermis fronts, and thus the AMCs did not fuse. In the wild type this occurs prior to DC onset and AMC formation (Fig. 4B). This suggests that prior to DC the AS tissue drives morphogenesis of the anterior and posterior epidermis tissue. Since AS-SqhKO embryos showed some AS tissue surface reduction, we quantitatively compared mutant and wild type DC dynamics. We first measured the AS tissue surface area over time (Fig. 4E). Setting the end of germ-band retraction as time-point zero (Methods, section 6.2.4), control embryos completed DC in 270±60min. DC onset,

depicted by the beginning of net dorsal-ward movement of the LEs, occurred after 80±30min. AS tissue area change was measured relative to the area at the end of germ band retraction. The area decrease was sigmoidal in wild type embryos (Fig. 4F). AS-SqhKO embryos initiated an area decrease similar to the wild type, but subsequently this slowed down and arrested within 90±30min (Fig. 4F, Fig. 9F). This shows that AS tissue-specific loss of MyoII activity arrests DC at an early stage.

We next quantified dorsal-ward LE displacement by measuring gap width (Fig. 4E; Methods, section 6.2.4). In control embryos gap width initially increased for 60±30min (Fig. 4G). Notably, the total AS tissue area simultaneously decreased revealing a change in overall tissue shape (Fig. 4E, Fig. 9F). AS-SqhKO embryos started with a larger gap width than the wild type. Gap width immediately started decreasing until eventually arresting with roughly the starting width of control embryos (Fig. 4G, Fig. 9G).

Previous studies investigated the contribution of zipping to DC by describing gap length shortening parallel to the embryonic AP axis, starting with zipping onset (137±15min in our movies)[37,46,47,86]. We now included the analysis of the time period starting with the end of germ band retraction up to the onset of zipping, which covers more than two hours and found that gap length already started decreasing at time-point zero with an initial acceleration (Fig. 9H; Methods, section 6.2.4). A second acceleration point occurred as expected at around the time when zipping initiated. In AS-SqhKO embryos no zipping occurred and gap length did not change much suggesting that the initial gap shortening is mediated by the AS tissue (Fig. 9H).

2.2.2. The AS tissue autonomously drives DC

So far our results exclude the additive force model, but not the tissue ratchet model, which predicts that neither tissue can autonomously drive DC[36]. We therefore selectively depleted Sqh-GFP in the epidermis. The *pannier* (*pnr*) enhancer element has been used to express Gal4 in the dorsal-most 8-10 rows of epidermis cells before and during DC[87]. *Pnr*-mediated deGradFP expression caused DC arrest (Fig. 10A). However, we noticed deGradFP expression leaking into a variable number of AS cells (Fig. 10B). These expanded their apical surfaces while in unaffected cells it gradually decreased, indicating that mutant cells counteracted wild type cell contraction. We found similar leakiness with several other reportedly epidermis-specific enhancer elements (Table 6 in Appendix 2)[35,88–91]. To overcome this problem, we generated a P-element insertion to express the Gal4 inhibitor Gal80 in AS cells, which

completely suppressed *pnrGal4*-mediated deGradFP leakiness in the AS tissue (Fig. 10C-10D; Methods, section 6.2.1)[92]. Embryos with such epidermis-specific Sqh-GFP depletion (ES-SqhKO) completely lacked the typical, pearl string-like Sqh-GFP arrangement at the LE (Fig. 5A-5B). Also, they lacked an actin cable, suggesting efficient MyoII inactivation and confirming that actin cable formation requires MyoII as previously shown (Fig. 5B-5C)[50]. All ES-SqhKO embryos completed DC, although 92% ended up with various degrees of puckering and 41% eventually ruptured the epidermis anteriorly (Fig. 11A-11B). Laser-mediated cutting of the epidermis tissue parallel to the LE in the region of the cells affected in ES-SqhKO embryos showed that the recoil velocity of the wound edges did not change in ES-SqhKO embryos suggesting that epidermis tissue tension was not affected (Fig. 11D). Also, Jnk signaling was not affected in ES-SqhKO embryos (Fig. 11E)[83]. Altogether, this shows that the AS tissue can autonomously drive DC and that AMC loss primarily affects zipping and tissue integrity.

To evaluate the efficiency of MyoII depletion in ES-SqhKO embryos, we monitored the presence of an AMC in embryos selectively overexpressing UAS-Mbs.N300 in the epidermis (Methods, section 6.2.5). We detected short actin cable fragments all along the LE suggesting that the loss of MyoII function is much more severe in ES-SqhKO embryos than in embryos overexpressing UAS-Mbs.N300 (Fig. 5C, Fig. 11E). Furthermore, laser-mediated incisions of the LE showed that compared to control embryos, the line tension along the LE was significantly reduced in ES-SqhKO embryos confirming that AMC function is severely reduced (Fig. 5D, Fig. 11C).

DC completion without AMC does not exclude AMC contribution to closing force production. Since such a contribution would alter closure dynamics in ES-SqhKO embryos, we quantified DC dynamics as before. AS tissue area changes in ES-SqhKO embryos revealed a 60-90min delay in DC completion (Fig. 5E). Gap width measurements showed that this was caused by delayed onset of DC while subsequent epidermis convergence was similar to the wild type, except for a moderate reduction of maximal closure speeds (Fig. 5F, Fig. 11F-G). This suggests a role for the AMC in promoting DC onset.

To test whether this early force contribution of the AMC is additive to AS tissue activity, we simultaneously expressed deGradFP in AS tissue and dorsal epidermis tissue by combining *pnr*-and 332.3-mediated Gal4 expression. Embryos lacking an AMC and MyoII activity in AS cells, showed initial closure dynamics similar to AS-SqhKO embryos (Fig. 4F). This suggests that the early contribution of the AMC does not simply add to AS tissue activity.

In addition, this result shows that the initial AS tissue area decrease in AS-SqhKO embryos, is AMC independent.

2.2.3. The AMC provides zipping integrity

The finding that ES-SqhKO embryos complete DC with nearly wild type dynamics implies that force generation during zipping is MyoII independent. Yet, puckering phenotypes as seen in ES-Sqh-GFP embryos most certainly reflect zipping defects suggesting some AMC function in zipping[93]. Consistently, gap length decreased much slower and with more variable speeds in ES-SqhKO embryos than in the wild type (Fig. 6A). Furthermore, the initially wavy epidermis fronts, which gradually straighten up with the appearance of the AMC in the wild type, remained wavy throughout DC in ES-SqhKO embryos (Fig. 5B, Fig. 6B). As in the wild type, LE cells started extending dynamic lamellae and filopodia that explored the space above the adjacent AS tissue. However, these extensions were clearly longer and wider in ES-SqhKO embryos than in the wild type (Fig. 6B). With these alterations, the zipping fronts frequently arrested for short time periods and jumped over a couple of cells (Fig. 6C). We further investigated this phenotype, by depleting MyoII function in defined stripes of epidermal cells using the *engrailed* (en) enhancer element[88,94]. In such *en*ES-SqhKO embryos, LE cell protrusions were elongated in en-expressing stripes of LE cells (en-stripes) revealing a cell autonomous effect (Fig. 6D). Unlike in the wild type, protrusions of cells from neighbouring en-stripes frequently made transient contacts (at least once per stripe) (Fig. 6D). At the zipping fronts, additional contacts were made between non-matching, opposing en-stripes (Fig. 6D). Only the anterior-most one or two matching en-stripe pairs (1.63±1.41 of 10 pairs per embryo, n=160), managed to zip without ectopic contacts. At the time when tissue sealing was completed, ectopic connections between neighboring en-stripe pairs often remained (7.31±1.58 of 10 pairs per embryo, n=160 pairs). This considerable mismatching is prone to affect zipping continuity and provides a likely explanation for the puckering defects in ES-SqhKO embryos (Fig. 11A).

2.2.4. Apical constriction is strictly MyoII-specific

Since we found that the AS tissue alone drives DC, apical constriction of AS cells is likely to be the key force generating process. In DC, gradual apical actin/MyoII compaction, as well

as a belt-like enrichment of actin and MyoII at adherens junctions, was reported[38,39,41]. The exact role of these two MyoII pools is not clear. Since with the ES-SqhKO embryos we have an experimental setup in which dorsal closure is driven solely by the AS tissue, we wondered whether the mutants would show changes in any of the two MyoII pools, possibly giving a hint at its role in autonomous, apical AS cell constriction. For this, we compared Sqh-GFP dynamics in AS cells of wild type and mutant embryos (Methods, section 6.2.3). In wild type cells, periodic Sqh-GFP foci first appeared towards the end of germ band retraction (Fig. 7A). As DC progressed, Sqh-GFP foci increasingly compacted and eventually transformed into a continuous meshwork as previously described[38,39]. In parallel, Sqh-GFP signal gradually increased at the adherens junctions starting 40-60min into DC (Fig. 7A-7B). In agreement with the previously reported graded arrest of cell surface oscillations, apical and junctional Sqh-GFP signals increased earlier in AS cells closer to the LE than in more centrally located ones (Fig. 7B)[36,39,95]. Sqh-GFP dynamics were not affected in ES-SqhKO embryos suggesting that the behaviour of both MyoII pools is fully tissue autonomous and not modulated by forces added by the AMC in the surrounding tissue (Fig. 7C). In AS-SqhKO embryos all Sqh-GFP was trapped in largely immotile, fluorescently stable particles located all over the cell surface and at adherens junctions (Fig. 4D). The relative Sqh-GFP fluorescence intensity merely showed background fluorescence fluctuations providing further support for complete MyoII inactivation in this tissue (Fig. 12A; Methods, section 6.2.3).

It was previously noted that motors other than MyoII could provide redundant motor activity[34,35]. Since we achieve unprecedented depletion of MyoII function, we could test for such redundancy, which should become evident in AS-SqhKO embryos. Since AS cell surface areas of AS-SqhKO were larger and more variable as compared to the wild type, we normalized area amplitudes for quantification (Fig. 12B-12C; Methods, section 6.2.3). With each contraction, wild type cells changed their apical surface area by 40-60% (Fig. 8A). AS-SqhKO embryos showed only marginal cell surface fluctuations indicating that MyoII is the main motor activity in AS cells (Fig. 8A, Fig. 12C).

MyoII is a multi-protein complex, in which the Myosin heavy chain Zipper is the force producing motor activity[34]. To exclude that Zipper still functions in the absence of Sqh, we analysed Zipper localization in AS-SqhKO embryos. In wild type AS cells, mCherry-tagged Zipper (mCherry-Zipper; Methods, section 6.2.1) localized to apical MyoII foci and to adherens junctions similar to Sqh-GFP (Fig. 8B). In AS-SqhKO embryos mCherry-Zipper, but not actin, co-localized with Sqh-GFP in the aggregates, suggesting that Zipper function is co-depleted (Fig. 8C, Fig. 12D).

2.2.5. MyoII does not contribute to directional AS tissue tension

Previous results had suggested that AS cell surface oscillations depend on tissue tension and that tension is isotropic[36,45,86,96]. We investigated the contribution of MyoII to tissue tension, by measuring recoil distances of vertices around laser-mediated cuts of adherens junctions, in wild type and AS-SqhKO embryos (Fig. 8D; Methods, section 6.2.6). Compared to the wild type, vertex recoil was greatly reduced in AS-SqhKO embryos showing that MyoII produces considerable tension in the apical tissue section (Fig. 12E). Values were highly variable, raising the possibility that tissue tension has an additional, directional component that affects vertex recoil depending on the position relative to the incision. To further investigate this we correlated vertex recoil distance with the angle between a line along the cut junction and a line connecting a vertex and the incision point (Fig. 12F; Methods, section 6.2.6). Vertices recoiling within a +/-15° range had much higher recoil values than the rest in wild type and AS-SqhKO embryos (Fig. 12E-12F). These results show that besides a MyoII-dependent isotropic component, AS tissue tension has a MyoII-independent directional component. Previously, AS tissue tension estimation must have been including some additional mechanical effects. Since those experiments involved cutting clean holes through the entire depth of the epithelium, it is likely that these effects are linked to cutting the thin basal lamina and/or the yolk cell, which tightly align with the basal AS tissue surface[86,97]. To compare our results, which describe cuts that leave the basal tissue intact, with the published clean cuts, we extracted the maximum recoil values of vertices delimiting a cut junction and the angle between the junction and the embryonic AP axis (Methods, section 6.2.6). In contrast to the published values for wild type AS tissue, we found little correlation with our more selective cuts in the wild type (Fig. 8G-8H). Similarly, we observed little correlation in AS-SqhKO embryos (Fig. 8G-8H). Furthermore, our wild type values were up to 5 times lower than the published[86]. This indicates that the basal lamina and/or the yolk cell, directly or indirectly transmit a directional tissue tension component that does not align with the embryonic AP-axis.

2.3. Discussion

Here we present data excluding two previously proposed models describing force orchestration during DC. Using tissue-specific, acute MyoII depletion, we demonstrate that

forces produced by the epidermis and AS tissue are neither additive nor do they need to work together in a ratchet system. Instead, apical constriction of the AS tissue autonomously drives DC, while the epidermal AMC provides zipping integrity.

The ratchet model was based on the description of pulsed apical AS cell surface contractions, which transiently pull on the neighbouring epidermis[36]. The forming AMC was then proposed to provide a clutch that locally prevents ventral-ward retraction of the epidermis after such displacement. Our data refute this as a main mechanism, as DC proceeds with nearly wild type kinetics without an AMC. Yet, such embryos initiate DC with a delay. Since at this stage the AMC in wild type embryos still is fragmented, a role in which it locally serves as clutch seems plausible even though this ratchet mechanism is non-essential.

A second model had proposed an additive role of the two forces where each force alone was sufficient to autonomously drive DC. Our results with AS tissue-specific MyoII depletion show that the AMC cannot drive the process on its own as DC arrests at the very early stages. It is highly unlikely that this is due to stiffening of the AS tissue in such embryos, as stiffening was shown to correlate with an increase in MyoII activity while MyoII reduction leads to tissue softening, also evident when the tissue ruptures in such mutants[84,98]. These results thus refute the additive force model too. The initial, short phase of closing activity in such embryos occurs when the forming epidermal AMC would still be non-continuous and not yet able to produce much additive force. Consistently, elimination of the AMC in AS-SqhKO embryos did not change the initial closure dynamics. Most likely, this phase thus reveals the contribution of the volume reduction of AS cells, which a previous study showed to be triggered by an apoptotic signal at the onset of DC[42]. Importantly also, this study had excluded a force contribution of apoptotic cell delamination at such early stages.

Our results are based on an experimental approach that differs from previous studies in several critical aspects. Above all, we achieved unprecedented protein depletion efficiency, right from the beginning of DC and simultaneously in all the cells. Previous studies used tissue-specific rescue of hypomorphic *myoII* mutants that did not affect maternally contributed *myoII* mRNA and protein pools[42,51,99]. This allowed proceeding through early embryogenesis, and mutant phenotypes emerged at various stages of DC, when a critical number of cells had slowly run out of maternally contributed material. Such chronic phenotypes were highly pleiotropic and difficult to interpret since the risk of secondary cellular adaptations is much higher than in our acute depletion approach. The global nature of mutants may in addition have added indirect effects on the observed phenotypes, thus further obscuring their unambiguous interpretation. This extrapolates to experiments in which such phenotypes were rescued selectively in one or

the other tissue. For this reason, some studies included tissue-specific overexpression of dominant negative MyoII or of constitutively active MyoII phosphatase[42,51,84]. In contrast to those experiments, we observed DC arrest with AS-specific MyoII depletion suggesting that such approaches lacked sufficient depletion efficiency and possibly tissue specificity. Emphasizing the importance of tissue specificity the loss of MyoII activity in just a few AS cells hampers the capacity of the tissue to drive DC without AMC. Obviously, controlling the leakiness of the driver elements used for tissue-specific interference is critical.

High tissue specificity was given when manipulating tissue forces via laser-mediated tissue incisions, and results supported the additive force model[43,45,46]. Most likely, the discrepancy with our results is based on ectopic AMCs that rapidly form at the boundary of tissue incisions and provide additional closing forces[44,46]. Therefore, wounding does not seem to be the optimal tool to study tissue dynamics for longer periods. Nevertheless, it is clear that tissue recoil immediately following a laser cut provides a good description of a given tissue tension. Our respective experiments suggest that MyoII provides isotropic AS tissue tension, while the basal lamina and/or the yolk cell, which closely underlie the basolateral side of AS cells, directly or indirectly contributes a MyoII-independent, directional force component[97]. Since most epithelia are tightly linked to extracellular matrix, this highlights the necessity of considering apical and basal systems for the proper understanding of tissue mechanics.

Identifying the AS tissue as sole force generator, revives the question about how AS cells coordinate fast, pulsed cell surface oscillations with much slower, gradual, apical constriction. Based on the additive force model and mathematical modelling it was hypothesized that AS cells possess a subcellular ratchet mechanism as described in other *Drosophila* tissues[37,100]. There, two mechanisms were suggested: During gastrulation, periodic apical actin/MyoII contractions may cause an incremental compacting of the apical actin meshwork[39,101]. During germ band extension, contracting apical actin/MyoII foci flow towards the junctions of intercalating cells where they locally shorten the actin/MyoII belt at the adherens junctions[102]. We find evidence that the very large AS cells use both mechanisms, as we found apical actin/MyoII meshwork density and junctional MyoII to increase. Thereby, AS cells at the tissue periphery remodel faster than cells in the middle, which is congruent with the previously reported unequal apical constriction pattern and the sequential arrest of surface oscillations[36,37,95].

Despite not providing the previously proposed purse string activity, the AMC clearly provides line tension that straightens the epidermis fronts. Its absence does not affect overall LE cell distribution, which may be maintained by the adherens junctions connecting LE and

AS cells[25,103,104]. Also, we find no clear evidence for a role of the AMC in integrating or balancing forces produced by the simultaneously occurring, morphogenetic processes of adjacent tissues. The only obvious role for the AMC is to restrict the protrusive activity of LE cells, as in its absence protrusions are significantly enlarged. A consequence is the formation of ectopic bridging connections between neighbouring segments, which interferes with smooth zipping and most likely is responsible for the frequently observed, final puckering defect. It remains to be shown why MyoII activity loss leads to longer LE cell protrusions. The most likely scenario is that the concomitant loss of the AMC increases the free actin pool. This will promote F-actin formation in the cell protrusions and extend their elongation phase. Similarly, the dis-equilibration of F-actin nucleators or other actin organizing proteins, could promote F-actin formation in cell protrusions. Alternatively, the AMC or MyoII directly delimits cell protrusion length in an unknown fashion and its removal relieves inhibition.

Notably, zipping still occurs in the absence of MyoII activity, which supports recent findings suggesting that in this process the sealing forces are microtubule-mediated[25,94]. Also, these reports showed that the AS tissue folds up into a tube below the zipping fronts, reminiscent of neurulation, which drives closure of the dorsal epidermis in chordates. Our data reveal autonomy of AS tissue remodelling suggesting that mechanistically, the two processes may be more related than previously thought.

2.4. Future directions

Using acute and tissue-specific MyoII inactivation we demonstrated that AS tissue autonomously drives DC via the pulsed apical constriction. Thus, we aim to decipher the mechanism of pulsed AS cell surface contractions that are short-term (investigated in Chapter 3) and connect them with the long-term AS cell apical constriction (investigated in Chapter 4). For the latter part, it is necessary to find whether the apical constriction is an autonomous property of AS cells or such behaviour is instructed by the signals emanating from the epidermis. We are addressing the role of one such instructive signal – morphogen Dpp – in Chapter 4.

Various mechanisms of apical constriction exist during development. Therefore, another key step is to disentangle how such process happens in the AS tissue. Currently, several models exist implicating two MyoII populations in the AS cells[37,98,100]. Yet they all rely on classical genetics or protein over-expression that does not efficiently and specifically inhibit

MyoII (e.g. Mbs.N300, dominant negative form of Rho1)[40,42,50,84]. We further explore AS cell apical constriction and role of different MyoII populations in Chapter 4. So far our results are limited due to a heterogeneous nature of genetic set-up that we use. Thus, a novel, more acute and precise protein inactivation tools are necessary. We attempted to develop such tools and describe them in Appendix 1.

Since we exclude AMC from producing the closing force, the obvious next step is to address the function of AMC during DC. By analysing ES-SqhKO phenotypes during and after epidermis zipping, we hypothesized that the role of AMC is to evenly space out the epidermis cells. In addition, the tensioned cable could transmit the strain along the cable length generated by the zipping. Hence the AMC could make the zipping process more robust. Since the expression of deGradFP can be genetically controlled, it would be interesting to use enhancer elements that are expressed later during DC (e.g. LEGal4) to inactive MyoII. We have established such assay already (see Appendix 2, Fig. 53B) allowing to analyse how zipping is compromised by the acute loss of MyoII contractility after the process has already started.

We also have shown that tissue tension directionality observed by cutting through AS cell monolayer does not depend on the apical tension generated by MyoII (Fig. 8E-8H). Thus, it is necessary to explore is generating such tension anisotropy in the system. One possibility could be the basal lamina (BL) underlying the AS tissue. To test this, mutants for BL components can be analysed. However, it was shown that such zygotic mutants show variable penetrance and phenotypes and, thus, cannot be interpreted unambiguously[97,105,106]. Alternatively, the underlying yolk cell could contribute to tension anisotropy. This is a likely possibility as we observe dynamic MyoII behaviour on the surface of the yolk cell. In chapter 5, we describe the acto-myosin dynamics and demonstrate that MyoII contractility in the yolk cell dramatically affects AS cells and epidermis.

2.7. Summary of the key findings/hypotheses of Chapter 2

- Acute and tissue-specific MyoII inactivation overcomes previous experimental limitations and dismisses the two main models of DC
- AS cells can autonomously drive DC, whereas epidermal AMC cannot
- MyoII does not produce zipping force *per se*, but loss of MyoII activity in the epidermis affects zipping integrity
- Apical constriction of AS cells is not affected by the loss of AMC line tension in the LE

- MyoII contributes to isotropic, but not directional, tissue tension in the AS tissue
- Underlying basal lamina or the yolk cell could account for the tension directionality when cutting through the AS tissue layer

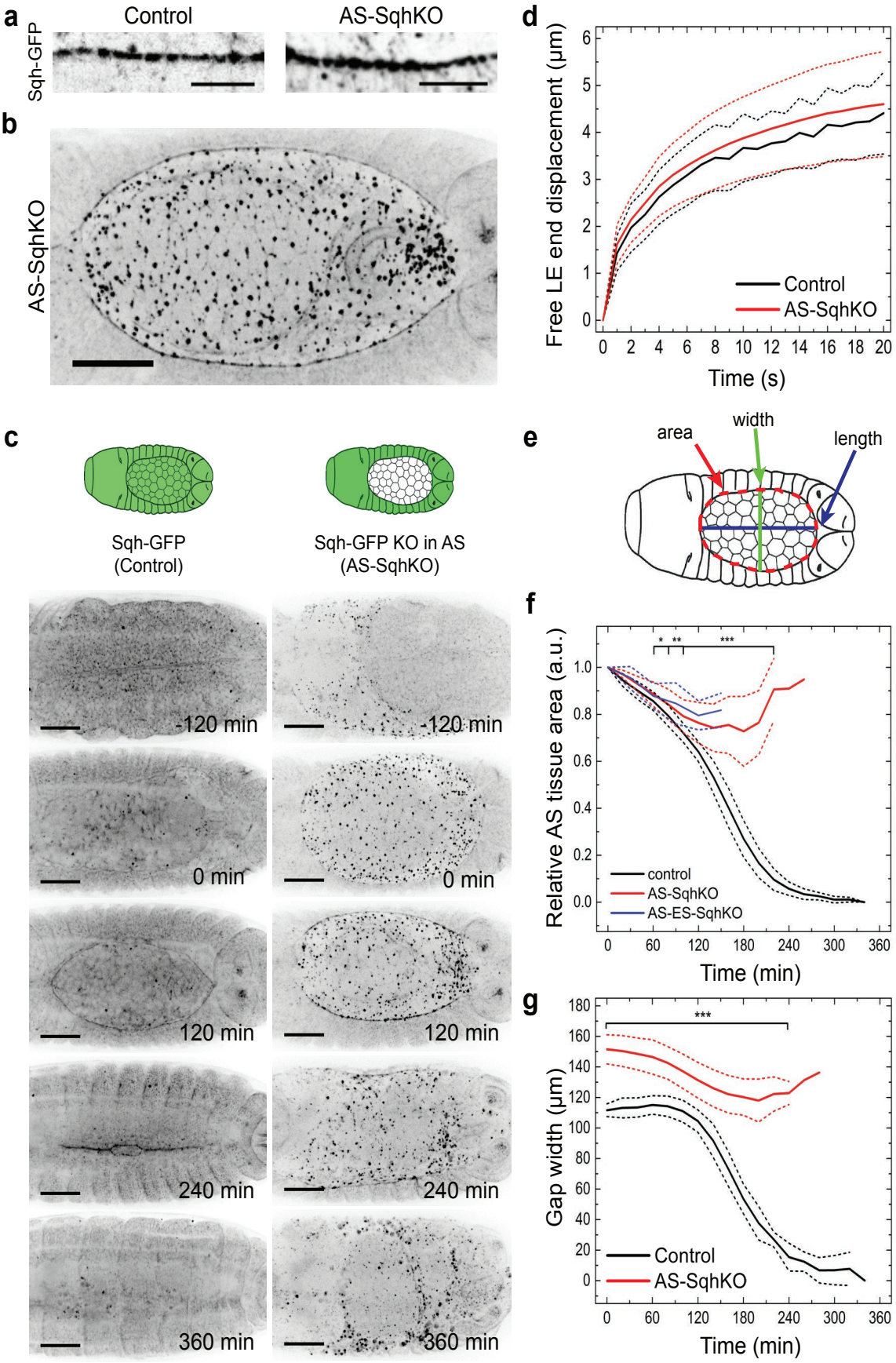
a
Control
AS-SqhKO
Sqh-GFP
b
AS-SqhKO
c
Sqh-GFP
(Control)
Sqh-GFP KO in AS
(AS-SqhKO)
-120 min
-120 min
0 min
0 min
120 min
120 min
240 min
240 min
360 min
360 min
d
Free LE end displacement (µm)
Time (s)
Control
AS-SqhKO
e
area
width
length
f
Relative AS tissue area (a.u.)
Time (min)
control
AS-SqhKO
AS-ES-SqhKO
g
Gap width (µm)
Time (min)
Control
AS-SqhKO

Figure 4. The AMC cannot drive DC. (a) Typical "Pearl-string" arrangement of Sqh-GFP at the LE in control and AS-SqhKO embryos at ~90min. Scale bar: 5μm. **(b)** Sqh-GFP in an AS-SqhKO embryo showing the intact AMC along the entire LEs, which were unable to meet anteriorly and posteriorly as in the wild type due to the inactive AS tissue. Scale bar: 50μm. **(c)** Selected movie frames showing germ band retraction and DC in control and AS-SqhKO embryos. 0 min depicts the end of germ band retraction. Cartoons: In green, tissues with functional Sqh-GFP. Scale bar: 50μm. See methods section for epidermis/AS tissue boundary specification. **(d)** Average displacement of LE borders generated by a laser-mediated incision in control (n=53; 29 embryos) and AS-SqhKO embryos (n=44; 22 embryos). Dashed lines: Standard deviation. **(e)** Cartoon showing the measured AS tissue area (red dashed line), tissue length (blue line) and tissue width (green line). **(f)** Relative area occupied by the AS tissue in control- (n=19), AS-SqhKO (n=23) and AS-ES-SqhKO embryos (n=7). Dashed lines: Standard deviation. *$p<0.05$, **$p<0.01$, ***$p<0.001$. **(g)** Gap width of the dorsal opening in control (n=19) and AS-SqhKO embryos (n=23). Dashed lines: Standard deviation. ***$p<0.001$.

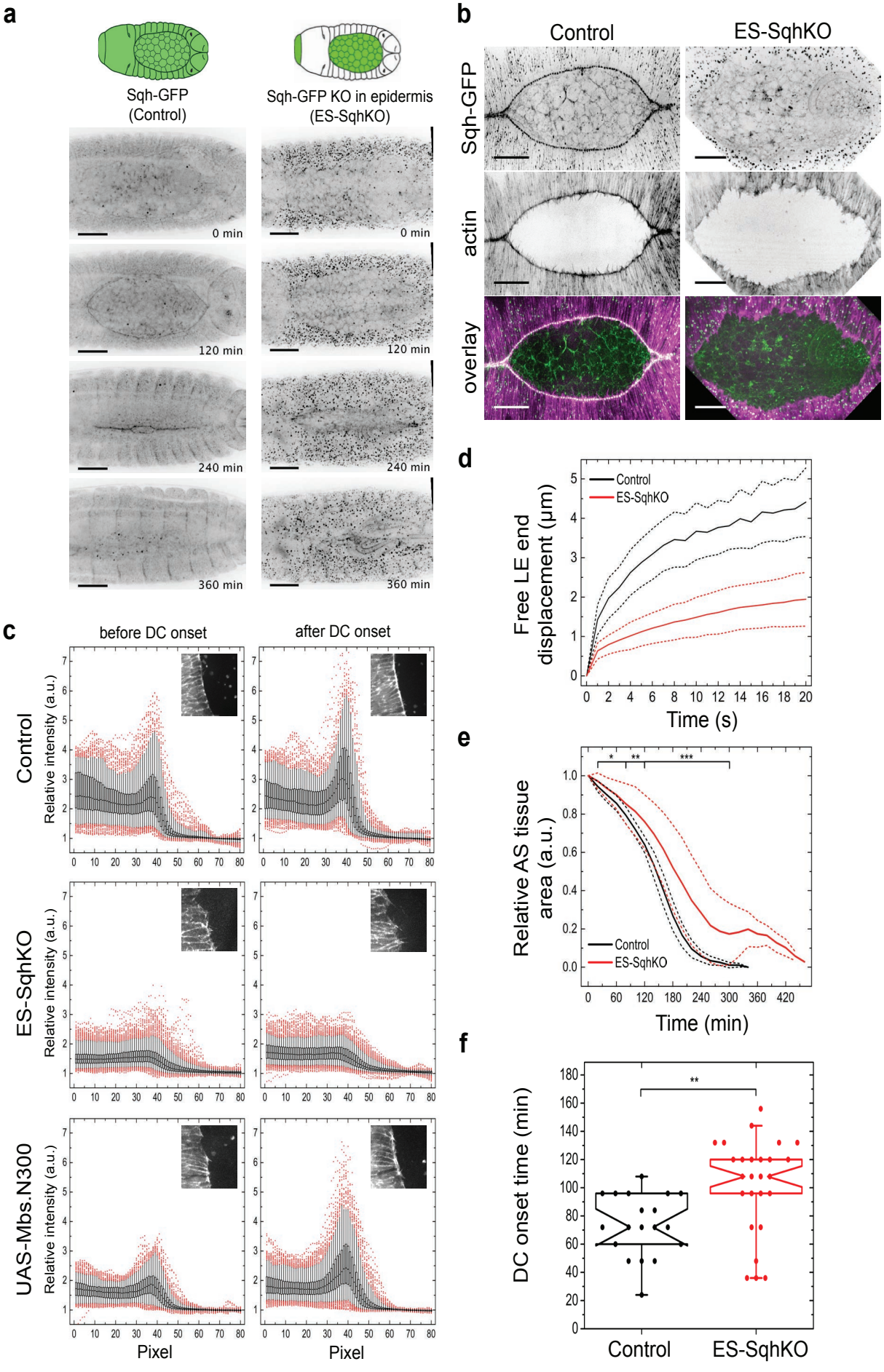
a
Sqh-GFP
(Control)
Sqh-GFP KO in epidermis
(ES-SqhKO)
0 min
120 min
240 min
360 min
b
Control
ES-SqhKO
Sqh-GFP
actin
overlay
c
before DC onset
after DC onset
Control
ES-SqhKO
UAS-Mbs.N300
Relative intensity (a.u.)
Pixel
d
Free LE end displacement (μm)
Control
ES-SqhKO
Time (s)
e
Relative AS tissue area (a.u.)
Control
ES-SqhKO
Time (min)
f
DC onset time (min)
Control
ES-SqhKO

Figure 5. AS tissue drives DC. (a) Selected movie frames showing DC progression in control and ES-SqhKO embryos. The dashed red line represents the LE. Cartoons: In green, tissues with functional Sqh-GFP. Scale bar: 50μm. **(b)** Comparison of Sqh-GFP and mCherry-moesin-labelled F-actin localization in control- and ES-SqhKO embryos. Scale bar: 50μm. **(c)** Actin cable intensity measurements of 2 movie frames, 1hour apart, one selected before and one after DC onset. Each panel shows standard box plots of 80 pixel-wide intensity profiles measured along the LEs of 7 control (n=364), 11 ES-SqhKO (n=743) and 9 MyoII-phosphatase-overexpressing embryos (n=454) (see also Supplementary Fig. 4g and Methods). Inlets illustrate sections of measured LEs. Grey lines: 5-95 percentiles, red dots: 5% outliers. **(d)** Average displacement of LE borders generated by a laser-mediated incision in control embryos (n=53; 29 embryos) and ES-SqhKO (n=19; 10 embryos). Dashed lines: Standard deviation. **(e)** Relative area occupied by the AS tissue in control (n=19) and ES-SqhKO embryos (n=26) embryos. Dashed lines: Standard deviation. *$p<0.05$, **$p<0.01$, *** $p<0.001$. **(f)** Standard notched box plots depicting times of DC start in control (n=19) and ES-SqhKO (n=26) embryos. Whiskers show 5-95 percentiles. ** $p<0.01$.

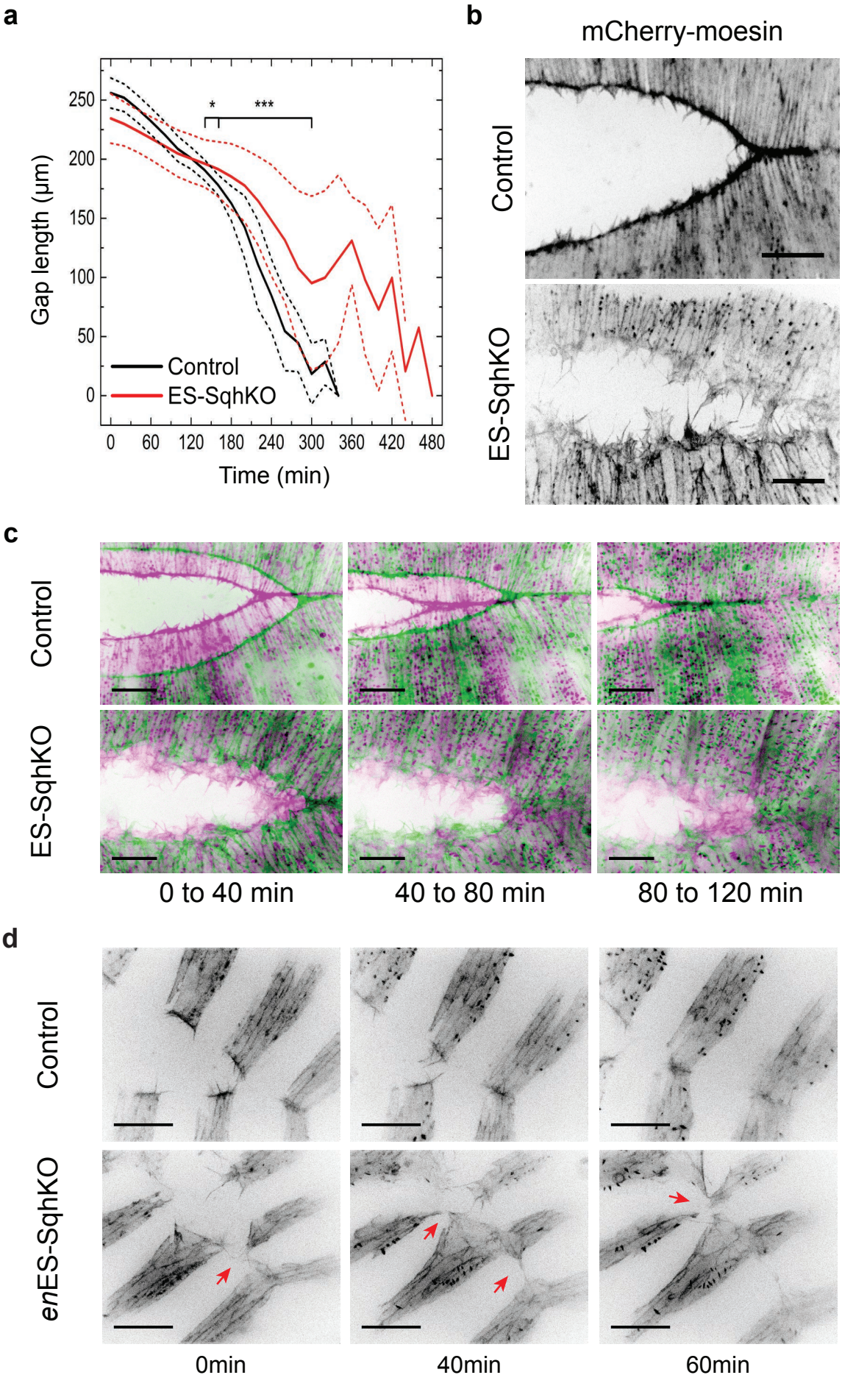
a
Gap length (μm)
250
200
150
100
50
0
*
***
Control
ES-SqhKO
0
60
120
180
240
300
360
420
480
Time (min)
b
mCherry-moesin
Control
ES-SqhKO
c
Control
ES-SqhKO
0 to 40 min
40 to 80 min
80 to 120 min
d
Control
enES-SqhKO
0min
40min
60min

Figure 6. Altered zipping in ES-SqhKO embryos. (a) Length change of the dorsal opening in control (n=19) and ES-SqhKO embryos (n=26). Dashed lines: Standard deviation. *p<0.05, ***p<0.001. **(b)** F-Actin in the LE of control and ES-SqhKO embryos. Scale bar: 10μm. **(c)** Selected movie frames comparing advancing zipping fronts in discrete time windows (green=beginning; magenta=endpoint) in control and ES-SqhKO embryos. Scale bar: 10μm. **(d)** mCherry-Moesin-labelled F-actin in zipping en-stripes of epidermis cells in control and *en*ES-SqhKO embryos. Red arrows depict ectopic connections linking the majority of neighbouring, Sqh-GFP-depleted cell stripes in *en*ES-SqhKO embryos. Scale bar: 20μm.

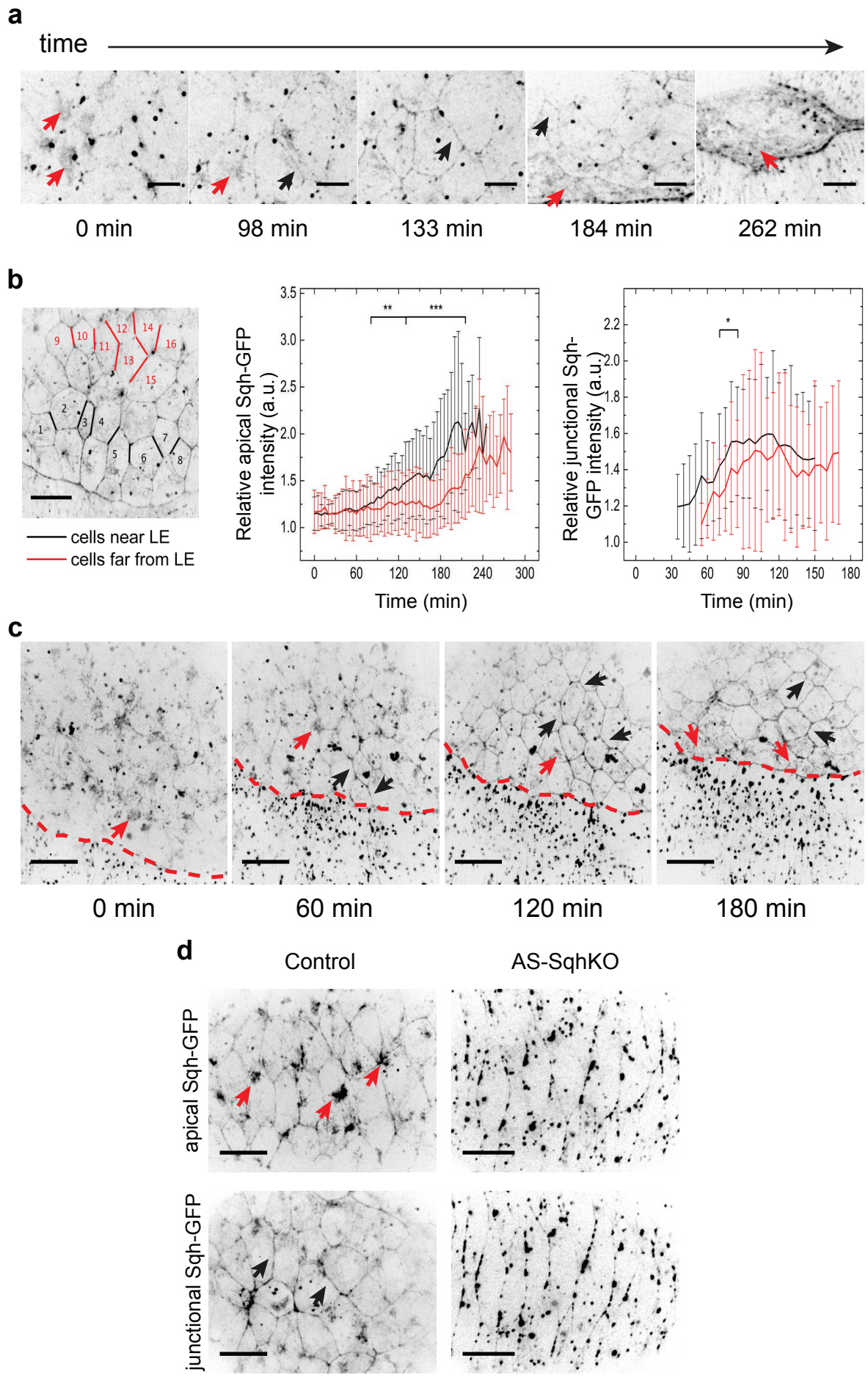
a
time
0 min
98 min
133 min
184 min
262 min
b
cells near LE
cells far from LE
Relative apical Sqh-GFP intensity (a.u.)
Time (min)
Relative junctional Sqh-GFP intensity (a.u.)
Time (min)
c
0 min
60 min
120 min
180 min
d
Control
AS-SqhKO
apical Sqh-GFP
junctional Sqh-GFP

Figure 7. AS tissue-autonomous MyoII dynamics in ES-SqhKO embryos. (a) Evolution of pulsatile Sqh-GFP networks into accumulated apical and junctional Sqh-GFP pools. Scale bar: 10μm. **(b)** Intensity profiles of Sqh-GFP pools during DC, averaging cells from 5 embryos. Middle panel: Apical Sqh-GFP intensities of AS cells situated near the LE (black; cells 1-8 in left panel; n=56) or situated far from the LE (red; cells 9-16 in left panel; n=54). Right panel: Junctional Sqh-GFP intensities near the LE (black; black junctions in left panel) and far from the LE (red; red junctions in left panel). Error bars: Standard deviation. *p<0.05, **p<0.01, ***p<0.001. **(c)** Evolution of pulsatile Sqh-GFP networks into accumulated apical and junctional Sqh-GFP pools in ES-SqhKO embryos. Black and red arrows indicate progressive junctional and apical Sqh-GFP accumulation respectively, first in cells near the LE and later in cells further away. Red dashed line depicts the LE. Scale bar: 20μm. **(d)** Sqh-GFP localization in AS cells of control and AS-SqhKO embryos. Red arrows indicate selected oscillating Sqh-GFP foci (top panels) and black arrows (bottom panels) indicate junctional Sqh-GFP pools. Scale bar: 10μm.

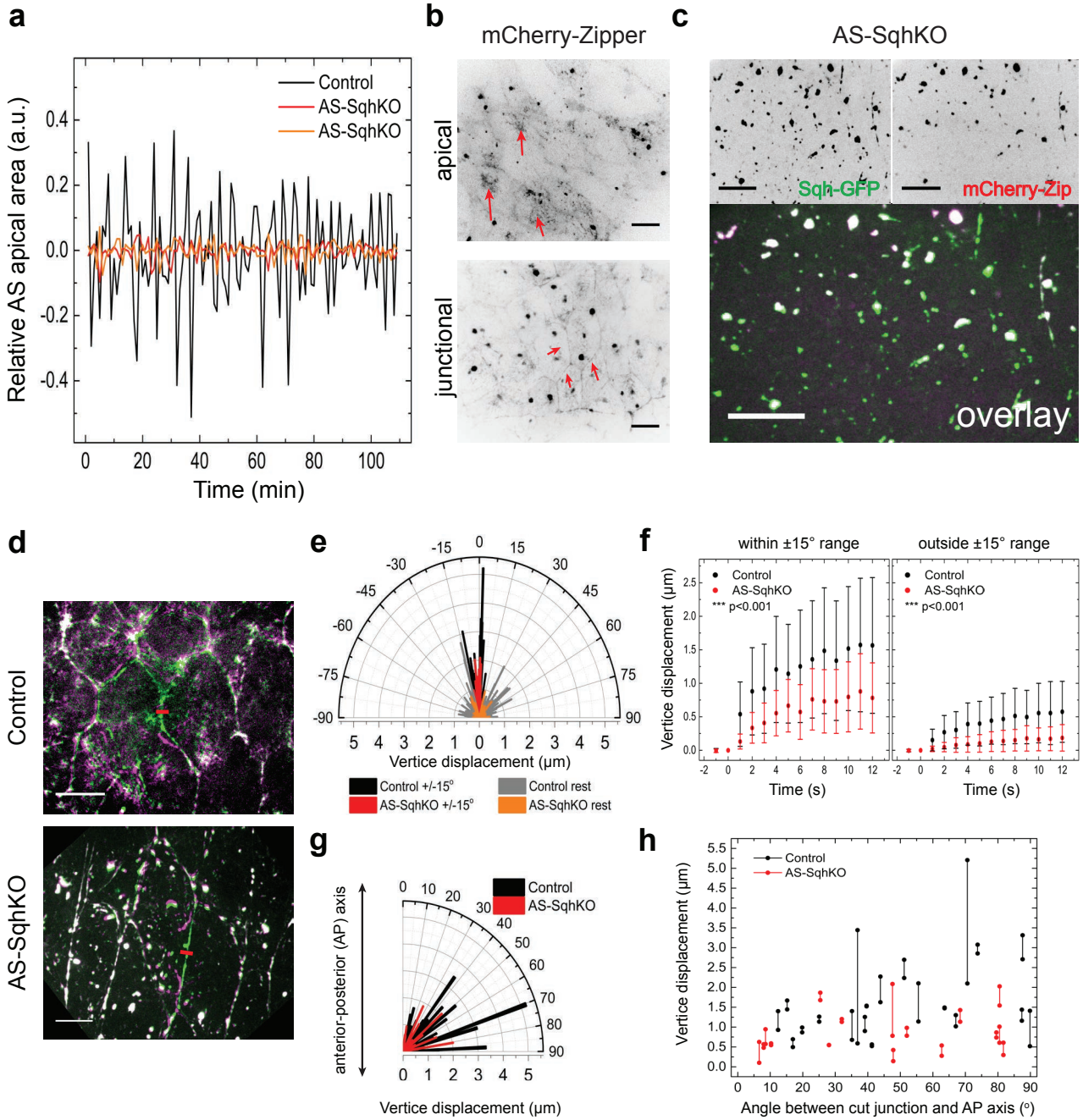
a
Relative AS apical area (a.u.)
Time (min)
Control
AS-SqhKO
AS-SqhKO
b
mCherry-Zipper
apical
junctional
c
AS-SqhKO
Sqh-GFP
mCherry-Zip
overlay
d
Control
AS-SqhKO
e
Vertice displacement (µm)
Control +/-15°
AS-SqhKO +/-15°
Control rest
AS-SqhKO rest
f
within ±15° range
outside ±15° range
Vertice displacement (µm)
Control
AS-SqhKO
*** p<0.001
Time (s)
g
anterior-posterior (AP) axis
Control
AS-SqhKO
Vertice displacement (µm)
h
Vertice displacement (µm)
Control
AS-SqhKO
Angle between cut junction and AP axis (°)

Figure 8. MyoII, a stand-alone motor mediating isotropic AS tissue tension. (a) Representative curves of normalized apical area dynamics in AS cells of control (black line) and AS-SqhKO embryos (red/orange lines). Control: 1 cell shown of 16 analysed cells from 2 embryos; AS-SqhKO: 2 cells shown of 29 analysed cells from 4 embryos. **(b)** mCherry-Zipper localization in AS cells. Red arrows indicate oscillating apical (top) and junctional (bottom) MyoII pools. Scale bar: 10μm. **(c)** mCherry-Zipper and Sqh-GFP co-localization in AS cells of AS-SqhKO embryos. Scale bar: 10μm. **(d)** AS vertex recoil following laser incision (red line) comparing control and AS-SqhKO embryos. Green: Frame imaged before cutting. Magenta: Frame imaged 12s later. Scale bar: 10μm. **(e)** Correlation of vertex displacement 12s after laser incision and angles between displacement direction and orientation of the cut junction, comparing AS cells of control (black, 157 vertices in 22 embryos) and AS-SqhKO embryos (red, 104 vertices in 17 embryos). Black/grey columns represent vertices of control embryos that are within/outside the ±15º range of the cut junction respectively. Red/orange columns represent vertices of AS-SqhKO embryos that are within/outside the ±15º range of the cut junction respectively. **(f)** Alternative representation of e), showing vertex recoils over 12sec and pooling vertices recoiling within and outside the range of ±15º angles. Error bars: Standard deviation. ***$p<0.001$. **(g)** Correlation of maximum displacement of the two vertices delimiting a cut junction and the angle between the junction and the embryonic AP-axis comparing control (black, 38 vertices in 19 embryos) and AS-SqhKO embryos (red, 34 vertices in 17 embryos). **(h)** Alternative representation of g).

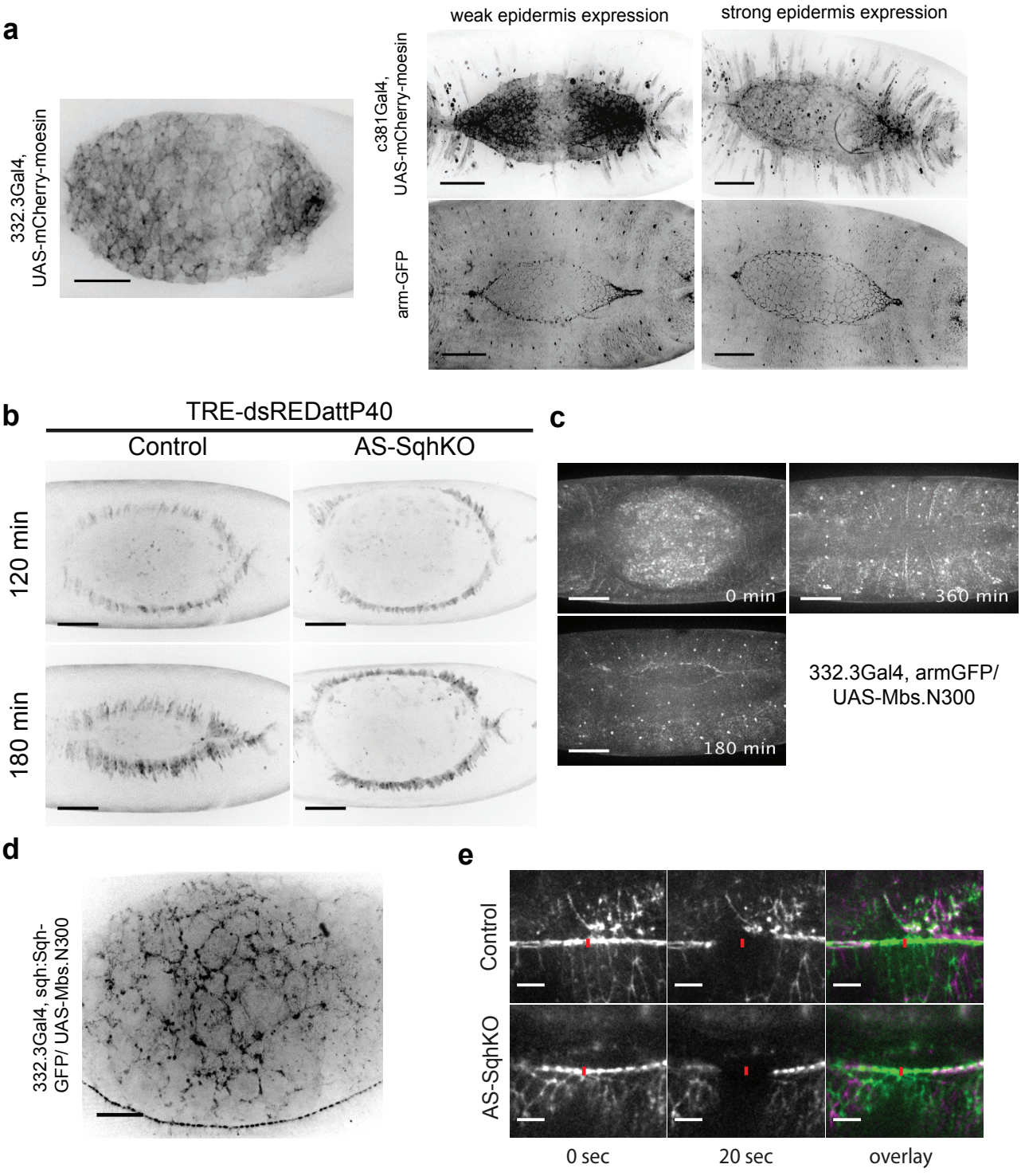
a
weak epidermis expression
strong epidermis expression
332.3Gal4, UAS-mCherry-moesin
c381Gal4, UAS-mCherry-moesin
arm-GFP
b
TRE-dsREDattP40
Control
AS-SqhKO
120 min
180 min
c
0 min
360 min
180 min
332.3Gal4, armGFP/ UAS-Mbs.N300
d
332.3Gal4, sqh:Sqh-GFP/ UAS-Mbs.N300
e
Control
AS-SqhKO
0 sec
20 sec
overlay
f
Relative area change (%/min)
Time (min)
g
LE convergence speed (µm/min)
Time (min)
h
Gap length (µm)
Time (min)

Figure 9. (a) UAS-mCherry-moesin expression pattern of the most commonly used AS-specific Gal4 enhancer elements 332.3Gal4 and c381Gal4. Arm-GFP outlines the AS tissue in the embryos with leaky c381Gal4 expression. Scale bar: 50μm. **(b)** Selected movie frames showing DC in control and AS-SqhKO embryos expressing the Jnk signalling reporter TRE-dsREDattP40. Scale bar: 50μm. **(c)** Selected movie frames showing DC progression in embryos, over-expressing constitutively active MyoII phosphatase (UAS-Mbs.N300) in the AS tissue. Scale bar: 50μm. **(d)** Sqh-GFP-expressing embryos, selectively expressing UAS-Mbs.N300 in the AS tissue. Scale bar: 20μm. **(e)** LE recoil 20 seconds after laser-mediated AMC incision (red line) in control and AS-SqhKO embryos at ~90min. The AMC is depicted by the pearl-string-like Sqh-GFP signal. 0s (green in the overlay) depicts the frame taken immediately before the incision. Scale bar: 10μm. **(f)** Relative gap area change (%/min) in control (black, n=19) and AS-SqhKO embryos (red, n=23). *p<0.05, ***p<0.001. Dashed lines: Standard deviation. **(g)** Convergence speeds of the two lateral LEs in control (black, n=19) and AS-SqhKO embryos (red, n=23). Dashed lines: Standard deviation. **(h)** Gap length changes of in control (black, n=19) and AS-SqhKO embryos (red, n=23). Dashed lines: Standard deviation. *p<0.05, ***p<0.001.

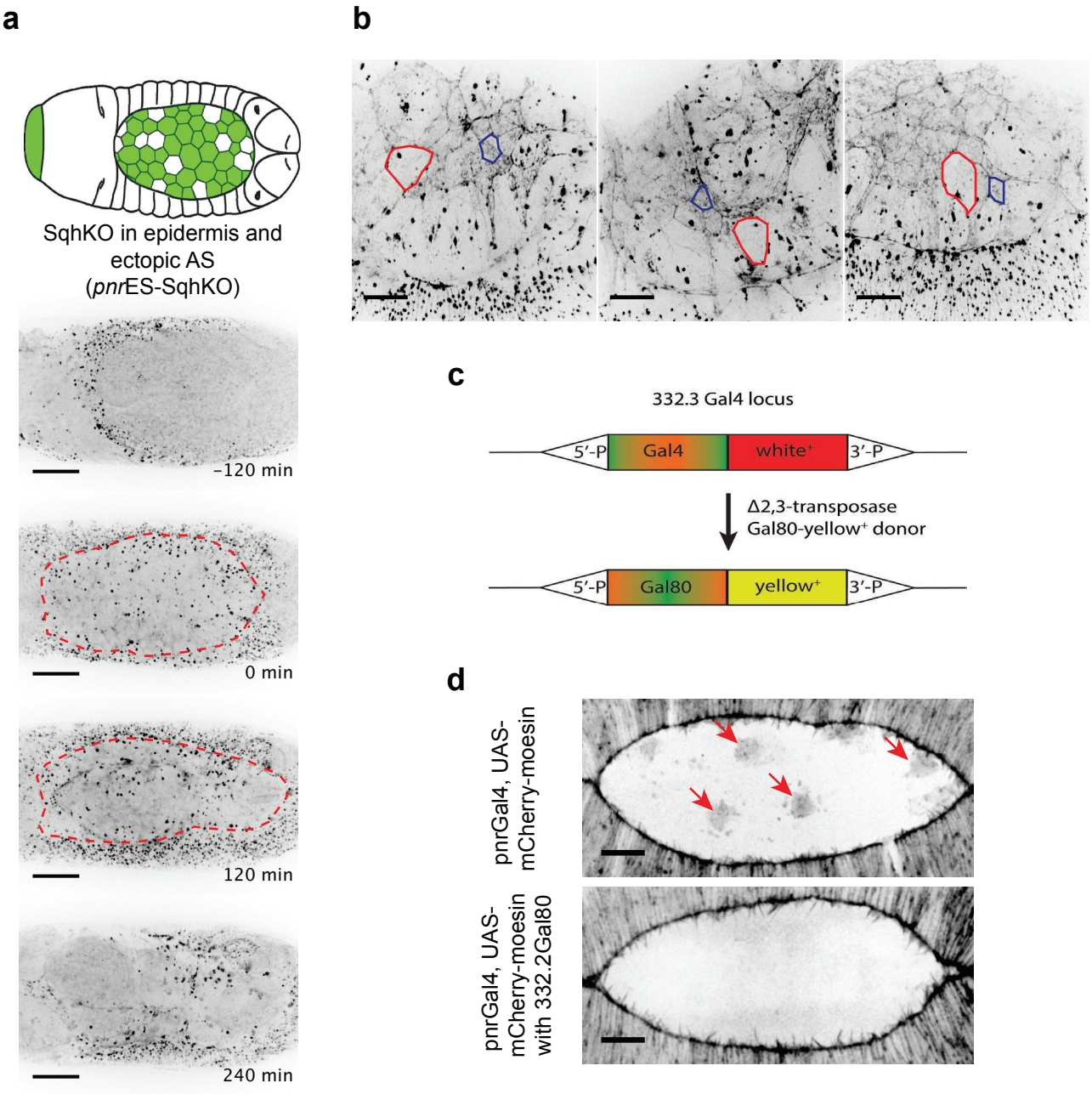
a
SqhKO in epidermis and ectopic AS (pnrES-SqhKO)
−120 min
0 min
120 min
240 min
b
c
332.3 Gal4 locus
5′-P
Gal4
white+
3′-P
Δ2,3-transposase
Gal80-yellow+ donor
5′-P
Gal80
yellow+
3′-P
d
pnrGal4, UAS-mCherry-moesin
pnrGal4, UAS-mCherry-moesin with 332.2Gal80
e
332.3Gal80/UAS-Mbs.N300; pnrGal4, UAS-mCherry-moesin

Figure 10. (a) Selected movie frames showing germ band retraction and DC failure in *pnr*ES-SqhKO embryos, with the leaky *pnr* enhancer element. The dashed red line represents the LE. Cartoon: In green are cells with functional Sqh-GFP. Scale bar: 50μm. **(b)** 3 examples of embryos expressing deGradFP with the leaky *pnr* enhancer element. One example each of an affected, expanding AS cell and an unaffected, constricting AS cell is outlined in red and blue respectively. Scale bar: 20μm. **(c)** Strategy for *Gal4* swapping with *Gal80* in the *332.3* locus. **(d)** Embryos in which the leaky *pnr* enhancer element was used to drive expression of the actin-marking mCherry-moesin without (top) and in combination with 332.3Gal80 (bottom). Red arrows indicate AS cells with ectopic mCherry-moesin expression by *pnr*. Scale bar: 10μm. **(e)** F-actin in an embryo selectively expressing UAS-Mbs.N300 in the epidermis using *pnr*Gal4 and 332.3Gal80 to suppress leaking into the AS tissue. Scale bar: 50μm.

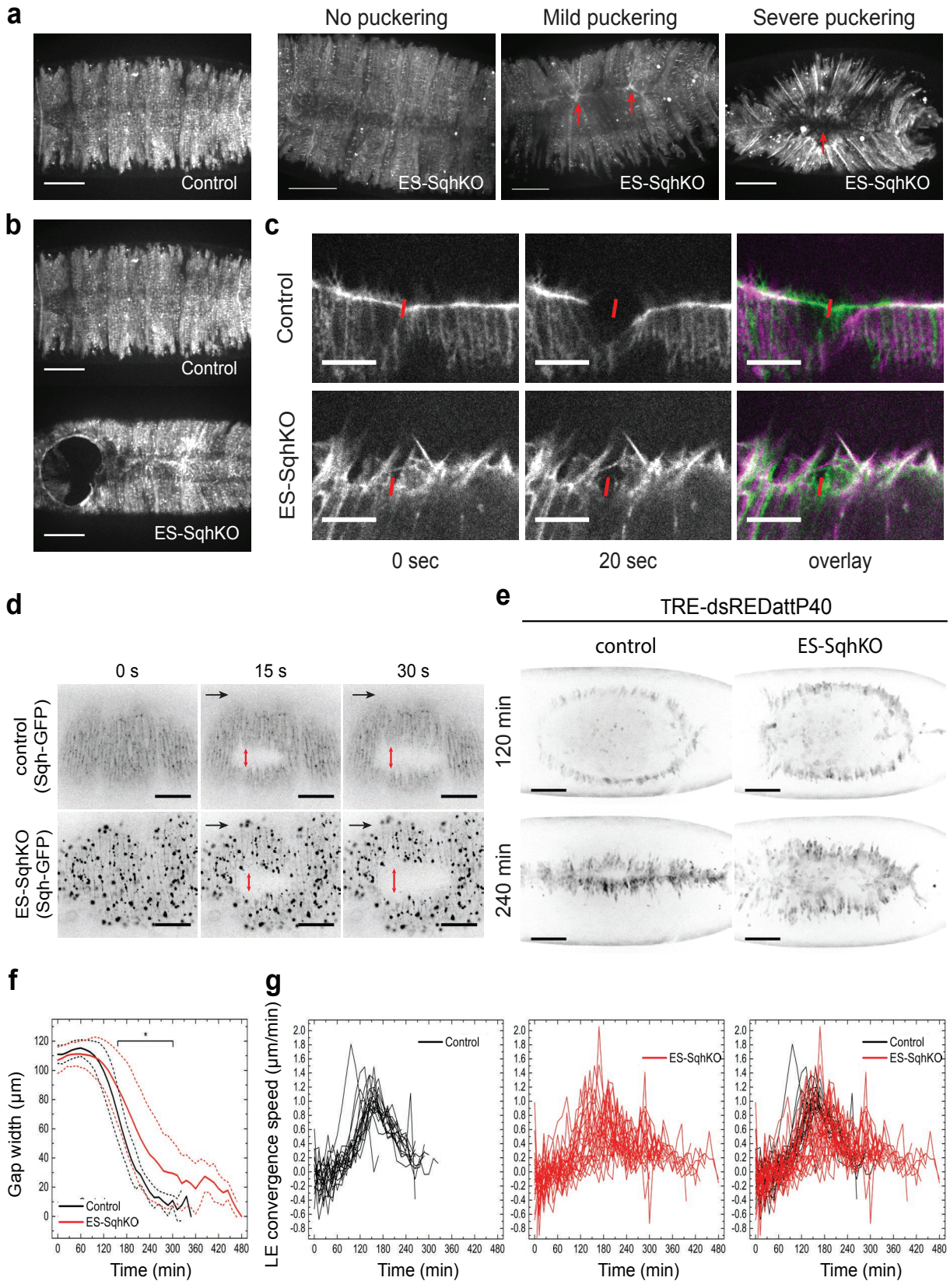
a
No puckering
Mild puckering
Severe puckering
Control
ES-SqhKO
ES-SqhKO
ES-SqhKO
b
Control
ES-SqhKO
c
Control
ES-SqhKO
0 sec
20 sec
overlay
d
0 s
15 s
30 s
control (Sqh-GFP)
ES-SqhKO (Sqh-GFP)
e
TRE-dsREDattP40
control
ES-SqhKO
120 min
240 min
f
Gap width (μm)
Control
ES-SqhKO
Time (min)
g
LE convergence speed (μm/min)
Control
ES-SqhKO
Time (min)

Figure 11. (a) mCherry-moesin (labels F-actin) expressing control and ES-SqhKO embryos at the end of DC. 8% of the embryos show no puckering defects (n=89), 65% show mild puckering defects (red arrows) and 27% show a severe puckering defect. Scale bar: 50μm. **(b)** mCherry-moesin (labels F-actin) expressing control and ES-SqhKO embryos at the end of DC. In 41% of the embryos (n=95) the anterior epidermis ruptures. Scale bar: 50μm. **(c)** LE recoil 20 seconds after laser-mediated LE incision (red line) in control and ES-SqhKO embryos (magenta in the overlay). 0s depicts the frame taken immediately before the incision (green in the overlay). The fluorescence shows F-actin labelled by mCherry-moesin. Scale bar: 10μm. **(d)** Recoil of epidermis (Sqh-GFP labelled) after laser incision in control and ES-SqhKO embryos. Red arrows indicate the extent of tissue recoil, black arrows show the direction of the laser cut. Scale bar: 20μm. **(e)** Selected movie frames showing DC in control and ES-SqhKO embryos expressing the Jnk signalling reporter TRE-dsREDattP40. Scale bar: 50μm. **(f)** Gap width change in control (n=19) and ES-SqhKO embryos (n=26). Dashed lines: Standard deviation. (g) Convergence speeds of the two lateral LEs in control (black, n=19) and ES-SqhKO embryos (red, n=26). The right panel is an overlay of the first two panels.

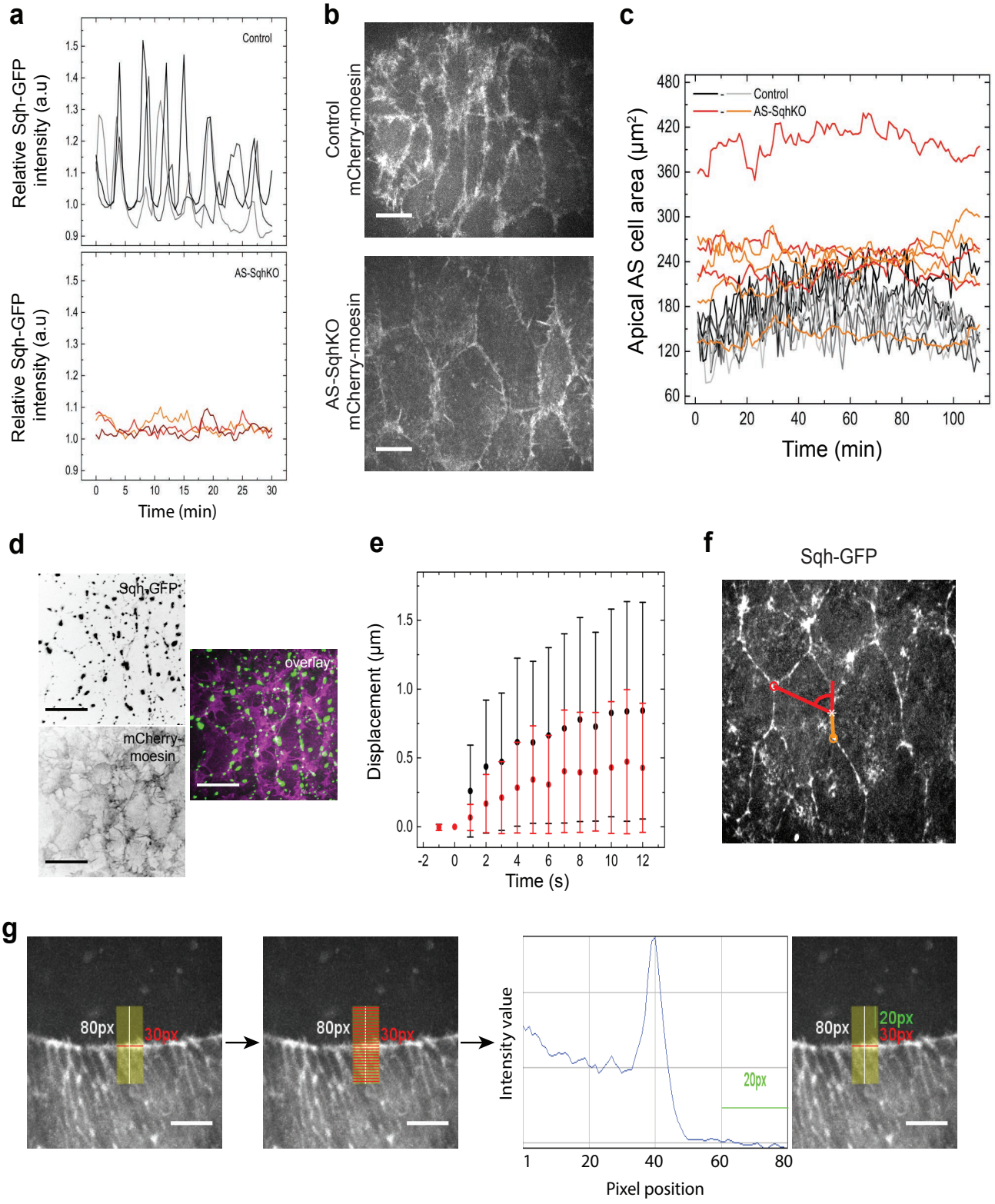
a
Relative Sqh-GFP intensity (a.u)
Control
AS-SqhKO
Time (min)
b
Control mCherry-moesin
AS-SqhKO mCherry-moesin
c
Apical AS cell area (µm²)
Control
AS-SqhKO
Time (min)
d
Sqh-GFP
mCherry-moesin
overlay
e
Displacement (µm)
Time (s)
f
Sqh-GFP
g
80px
30px
Intensity value
20px
Pixel position

Figure 12. (a) Comparison of Sqh-GFP intensity oscillations over time in AS cells of control and AS-SqhKO embryos. For the control 3 of 12 cells analysed in 2 embryos are shown. For AS-SqhKO 3 of 24 cells analysed in 5 embryos are shown. **(b)** Comparison of F-actin in AS cells of control and AS-SqhKO embryos. Scale bar: 10μm. **(c)** Comparison of the apical AS cell surface area dynamics in control (black/grey) and AS-SqhKO (red/orange) embryos. For the control 8 of 16 analysed cells in 2 embryos are shown. For AS-SqhKO 8 of 29 cells analysed in 4 embryos are shown. **(d)** Sqh-GFP degradation aggregates and F-actin localization (mCherry-moesin labelled) in AS-SqhKO embryos. Scale bar: 20μm. **(e)** Vertex recoil in the first 12s following a laser incision of a junction connecting 2 AS cells in control (black, 157 vertices in 22 embryos) and AS-SqhKO embryos (red, 104 vertices in 17 embryos). Displacement values of all tracked cell vertices were pooled for each time point. Error bars: Standard deviation. **(f)** Illustration of the method to set the angle between a tracked cell vertex and the ablated junction. The two vertices delimiting an ablated junction have an angle of 0º (orange line). All other vertices are at a certain angle from the ablated junction (red line, max. ±90º). The star indicates the incision point. **(g)** Procedure for LE intensity measurements (Methods). The yellow rectangle indicates the 80 30-pixel lines (red) and the way they were placed on the LE. The 3rd frame shows an example of one set of 80 average intensity values obtained from measurements in one yellow rectangle. All measurements for each of the 80 values were assembled into box plots in Fig. 2c. In green: Position of the 20 30-pixel lines the average of which was used to normalise the intensity profile. Scale bar: 10μm.

Chapter 3. Mechanism of pulsed AS cell surface contractions

This chapter is a manuscript in preparation.

Pasakarnis, L., Frei, E., Dreher, D., Brunner, D.

LP and DB conceived and planned the experiments; LP performed the experiments; LP and EF generated fly strains used in the study; DD provided histograms in Fig. 14B; LP and DB analysed the data and wrote the manuscript.

3.1. Introduction

3.1.1. Actin network dynamics in epithelia

Live imaging of developing epithelia revealed that these tissues are not just static barriers, but show extremely dynamic behaviour. Numerous tissues undergoing morphogenesis in *C. elegans*, *Drosophila*, *Xenopus* and zebrafish display tightly orchestrated acto-myosin (AM) network behaviour[6,7,17,107] (also see Appendix 4). Relatively slow developmental processes such as apical constriction of AS cells were described decades ago using standard immunofluorescence techniques. However, live imaging using fluorescently tagged proteins revealed that AS cells undergo apical constriction every 4-5min[36,39]. An obvious candidate governing such contractile activity was the AM network. Live AM reporters revealed dramatic fluorescence intensity changes over time revealing that AM coalesces into defined foci that dissolve within seconds to minutes. With further advances in imaging techniques, such pulsatile activities were found in numerous other tissues that undergo morphogenetic changes[6,16,107]. Surprisingly, such spontaneous pulsed contractions are conserved across the species and are also found in the less complex organisms such as algae *Volvox* or a slime-mold *Dictyostelium*.

In all described examples of transient AM foci, the phenomenon occurs on a pre-existing actin cell cortex[16,107–109]. Nonetheless, the coalescence starts from a diffuse network that becomes more concentrated and intense over time. The increase in AM fluorescence normally precedes the cell contraction. In contrast, the dissolution of the foci leads to cell relaxation. Thus, the cyclic appearance of AM foci correlates with the cyclic changes in cell shapes. Though the increase in MyoII fluorescence slightly lags the increase in F-actin fluorescence, such difference was found to be not significant[38,39]. Intriguingly, the frequencies of AM foci across the species and tissues are very similar and range between 1-5min[17]. In addition, they also correlate with a cell size, as, for example, smaller *Drosophila* mesoderm

cells are contracting more frequently than larger AS cells[17]. Very often AM foci frequencies change over time, like in the case of AS cells, where initially long AM coalescence cycles gradually become more frequent[38,41]. It is generally assumed that longer cycles of AM foci correlate with no productive tissue contraction, whereas an increase in AM foci frequency is associated with increasing tissue contractility[17,109].

In addition to being localized at a single focus, AM network can generate flows or waves across the cell cortex before dispersing[22,102,110–112]. The intrinsic property of actin to form filaments already accounts for such wave behaviour. Upon ATP binding, actin monomer is incorporated in to a growing filament. ATP is then hydrolysed, but a lag in releasing the actin monomer allows the filament to still grow[1,2]. When the addition of new monomers equalizes with the rate of their removal, actin undergo treadmilling activity that allows the filament to move forward by polymerization alone. When treadmilling actin filaments are combined into a network, the latter can exert a pushing force against the encountered object. Such force production is extensively studied during the protrusive migration of single cells[4,113]. At the cell front edge, actin network polymerization pushes the plasma membrane forward thus building a lamellipodia that adheres to the substrate, on which the cell is moving. To create such Brownian-ratchet-like behaviour actin network must contain a repertoire of modifying proteins, such as actin nucleators N-WASP and Arp2/3 complex that branch the network[1,2]. To maintain a steady-state treadmilling, actin filaments need to be severed at the de-polymerizing end to release free G-actin monomers. This is achieved by cofilin/ADF family of proteins that destabilize actin filaments and eventually lead to their fracture[4,9]. At the same time, the actin bundling proteins like formins or fascin must be excluded from such network.

In principle, the actin treadmilling is one-directional, but it can be dramatically altered by the cross-linking and motor activity of MyoII. Actin polymerization flows can be enhanced by contractility gradients as seen in *C. elegans* zygote polarization or become oriented as described during *Drosophila* germ-band cell intercalation[21,102]. Evidence suggests that actin treadmilling and thus AM foci can become pulsatile, due to MyoII breaking F-actin by contracting the network. Recent computational modelling suggests that travelling AM waves can spontaneously arise in AS cells from the elastic contractile materials provided some turnover exists in the system[110]. That such MyoII turnover exists was demonstrated using FRAP experiments in AS cells, where the bleached region of AM foci recovered before the foci disassembled[38]. Thus, AM network is thought to depend on MyoII and act as a single contractile unit that governs cell deformations in AS cells.

3.1.2. Models of AS cell surface contractions and role of Ca^{2+}

In Chapter 2, we demonstrated that MyoII activity and AS cell apical constriction is the main driving force of DC. However, AS cells exhibits periodic oscillations of their apical area prior to the net apical constriction[36,39]. Several models propose how such cell pulsing works and is coordinated across the tissue. The initial cross-correlation analysis revealed that neighbouring AS cells tend to oscillate either in-phase or anti-phase with a clear preference for the latter[36]. This suggested that cell contraction is triggered by the pulling forces of neighbouring cells. Laser incision at the boundary between the two AS cells produces pulsing arrest of the two ablated cells and their immediate neighbours. Such tension-based model is further supported by *in silico* simulations, whereby changes in tissue tension and intracellular force parameters can shift cell behaviour from pulsed to non-pulsed and vice versa. All this evidence indicates a high degree of mechanical coupling between the neighbouring AS cells.

Utilizing holographic laser incisions and single AS cell isolation from its neighbours, an alternative model was proposed[96]. Authors observed that a single AS cell after the mechanical isolation continues to expand for several seconds if it was expanding before. In contrast, a cell constricts if it was constricting before. Thus, the model proposes that AS cells are mechanically independent from their neighbours. Interestingly, the experimental results were fitted to the same tension-based model applied earlier[36] - just by reducing spring-like strains along the cell-cell boundaries[96]. It was further suggested that the mechanical autonomy of AS cells relies on basal displacement of viscous cytoplasm after the apical contraction. Once the apical AM focus is dissolved, the bulk of cytoplasm flows back to the apical side, thus passively expanding the apical cell surface.

While the two models are not mutually exclusive, a more detailed quantitative analysis revealed higher level of co-ordination that could not be achieved merely by apico-basal coupling via the viscous cytoplasm[37]. It was shown that regions and strings of AS cells oscillate in-phase in one direction and anti-phase in the perpendicular direction. In addition, AS cells can reverse their oscillation phase within seconds and several neighbouring cells can become synchronous or asynchronous for short periods. As a result, tissue behaviour during such pulsing stage is very chaotic and cells appear to be more fluid-like deforming relatively easily. Only when the net apical constriction is initiated AS cells start to become solid-like and behave more as a uniform cell sheet[98].

One way of coordinating apical cell area oscillations was proposed by Hunter et al. 2014 and also relied on a tension-based model[114]. The authors observed that uncaging Ca^{2+} in AS cells induces their apical contraction. Using pharmacological inhibitors and RNAi against the mechanically-gated ion channels (MGCs), authors observed defects in DC and AS cell morphology[114]. They also suggested a model, whereby contracting AS cells would stretch their neighbours thus opening MGCs in them. This would cause Ca^{2+} influx from extracellular space into the neighbours and induces AM contraction. However, genetic evidence for the role of MGCs is weak since RNAi knock-down of only 2 out of 15 MCGs (*ripped pocket* and *dtrpA1*) caused phenotypes, which surprisingly were not present in the homozygous mutants[114]. In addition, all the phenotypes shown were systemic rather than AS-specific with severe defects in the epidermis, germ-band and involuting head. Nonetheless, chelating Ca^{2+} ions either intracellularly or extracellularly impeded closure progression suggesting a possible Ca^{2+} role during DC[114].

Over the years, the importance of Ca^{2+} ions for AM contractility has become undisputable. The classical example – muscle contraction induced by Ca^{2+} release from the sarcoplasmic reticulum into the cytoplasm due to a neuronal stimulation. In nearly all muscle cells Ca^{2+} acts via calmodulin and myosin light-chain kinase (MLCK) that leads to Ser19 phosphorylation of myosin II light chain[11]. This allows bringing the actin bundles to myosin mini-filaments. While this is the most common pathway in smooth muscles, in striated muscles Ca^{2+} mainly acts via binding to troponin that alleviates myosin II steric inhibition. It was also demonstrated that non-contractile cells, e.g. immune mast cells, also exhibit intracellular Ca^{2+} spikes after the exposure to antigen[115]. Interestingly, Ca^{2+} spikes were correlating with the re-arrangement of actin cytoskeleton and oscillations of actin nucleators. Similarly, in the growth cones and dendrites of neurons transient Ca^{2+} spikes lead to increased protrusive activity of filo- and lamellipodia[116]. Recently, stochastic Ca^{2+} spikes were documented in early *Drosophila* embryos in non-excitable cells like germ-band epithelia, but their role remains elusive[117].

Advance in endogenous Ca^{2+} imaging revealed another striking phenomena in epithelial cells. Upon external mechanical injury or focused laser damage, intracellular Ca^{2+} increase is observed in wounded cells, but also in the cells surrounding the wound[118–120]. Such intracellular Ca^{2+} spread is dependent on gap junctions – protein channels between the two cells allowing their electrochemical coupling. These transient Ca^{2+} waves are associated with the initial steps in tissue repair process and usually leads to actin cytoskeleton remodelling[118,119]. Jacinto and colleagues demonstrated that in *Drosophila* notum such Ca^{2+} wave is translated

into a supracellular contractile wave of AM towards the wound edge[118]. The wound size positively correlates with the distance where such AM wave starts, eventually leading to the formation of actin protrusions and the purse-strings at the wound edge. The authors found that Ca^{2+}-binding protein Gelsolin that severs actin filaments is required for coupling Ca^{2+} wave to the AM wave[118]. Other molecules like reactive oxygen species (ROS), purines (e.g. ATP) or nitric oxide (NO) are also released into the extracellular space upon wounding and mediate transcription independent wound healing responses[121,122]. ATP and H_2O_2 release is closely linked to the recruitment of immune cells like astroglia or macrophages that eliminate damaged cells[119,122]. By contrary, in the small wounds such damaged cells are extruded from the tissue either by their neighbours or via cell-autonomous apical constriction[28,123].

Using acute MyoII inactivation we reveal that apical actin oscillations in AS are independent of both MyoII and tissue tension. This is contrary to the generally assumed but never confirmed idea that AM acts a single entity in AS cells. Our results challenge tension-based model for generation of actin nucleation burst (ANB) in AS cell. We also demonstrate that AS cells are able to contract without the Ca^{2+} influx. In addition, using endogenous Ca^{2+} imaging, we suggest the explanation for cell pulsing arrest observed after laser ablating cell-cell boundaries. We propose that cell-autonomous oscillator triggers ANBs in AS cells, yet the trigger remains elusive. Finally, we also explore possible mechano-chemical AS cell coupling that could be dependent on conductance through the intracellular gap junctions.

3.2. Results

3.2.1. Actin nucleation burst generation in AS cells is cell-autonomous and neither tension nor MyoII-dependent

Using deGradFP we have achieved strong depletion of Sqh-GFP and hence MyoII function, in both AS and epidermis cells (see Chapter 2). We have also demonstrated that MyoII accumulates in degradation aggregates as a complex, where both the light chain (Sqh) and the heavy chain (Zip) is present (Chapter 2, Fig. 8C). Since MyoII appears on the apical AS membrane in a pulsed manner together with actin[38,39], it is generally assumed that the contractile acto-myosin network acts as a single entity in the AS cells. Hence, we also predicted that the actin nucleation bursts (ANBs) should be absent in AS cells of AS-SqhKO embryos. Surprisingly, when labelling actin with mCherry-moesin in AS-SqhKO embryos, we could

detect clear intensity oscillations of mCherry-moesin signal similar to the wild-type (Fig. 13A-13B). We hypothesized that these ANBs might appear in AS tissue either in a cell-autonomous fashion or they could be triggered by the contractile activity in the yolk cell below (such activity is described in detail in Chapter 5). When Sqh-GFP was depleted simultaneously in AS tissue and the yolk cell (hereafter, AS-yolk-SqhKO), we still detected ANBs in AS cells supporting the former hypothesis (Fig. 13A).

In a previous study it was stated that such ANBs were absent in zygotic *zipper* mutants (*zip*^{1}/*zip*^{1}), although the relevant data was not shown[38]. Therefore, to confirm that ANBs are not an artefact of deGradFP over-expression or MyoII aggregation, we checked if such oscillations are also present in embryos, where MyoII was perturbed by other means. In summary, we detected ANBs in every tested genotype: 1) AS-yolk-SqhKO (Fig. 13A), 2) AS-specific over-expression of constitutively active MyoII phosphatase (AS-Mbs.N300, Fig. 13B), 3) zygotic *zipper* mutant (*zip*^{1}/*zip*^{1}) and 4) complete *zipper* knock-out, in which the *zipper* ORF was replaced with an attB-dsRED cassette using CRISPR/Cas9 (Fig. 13B, Fürst and Brunner, unpublished). All these perturbations suggest that pulsed ANBs in AS appear cell-autonomously and independent of MyoII activity. In addition to ANBs, all of the other actin-dependent structures like actin cortex, filopodia and lamellipodia were present and were dynamic in Sqh-GFP-depleted cells (Fig. 13C).

Even though F-actin was observed to create waves and flows both independently[112,124] and with the need of MyoII[102,125], in classic examples of apical constriction (i.e. gastrulation) it is assumed that the appearance of actin/MyoII (AM) foci depends on both components[101]. In addition, apical cell pulsing and contractile wave progression through the cell is often modelled by taking AM as a single contractile unit[41,110]. We thus wondered if ANB dynamics are affected when MyoII activity is lost in AS cells. To quantify wave parameters, we measured the fluorescence intensity of the mCherry-moesin signal in AS cells in movies of control, AS-SqhKO and AS-yolk-SqhKO embryos (Methods, section 6.3.3). We then auto-correlated the signal intensities over 900s windows for every measured cell and extracted the average periods from obtained auto-correlation functions (together with David Dreher; Methods, section 6.3.3). We then plotted period distributions according to their relative frequency (Fig. 14A). While ANB frequencies were peaking at similar intervals that were reported previously, the increase in longer periods in both AS-SqhKO and AS-yolk-SqhKO was evident (Fig. 14A). It was shown that apical area oscillations are correlating between neighbouring cells with some tissue regions being in anti-phase and some being in-phase[36,37]. Thus, we performed cross-correlation analysis of the actin bursts in all possible neighbour combinations for all three genotypes (Fig.

14B-14C; Methods, section 6.3.3). While ANBs correlated in ~50% of the control embryos, correlation dropped to ~40% in both AS-SqhKO and AS-yolk-SqhKO (Fig. 14B-14C). In addition, those that still correlated in Sqh-GFP-depleted cells appeared to be more in-phase than anti-phase (21-15% in AS-SqhKO, 23-19% in AS-yolk-SqhKO compared to 24-25% in the control). It is worth to note here, that oscillation patterns differ slightly in individual cells and between the embryos due to the limited number of cells that can be analysed in a single field of view. Nevertheless, the general trend in reduced correlation in cells lacking MyoII indicate that in the wild-type ANBs are modulated by MyoII.

It was previously proposed that generation of actin pulses is dependent on tissue tension[36,40,100,114], whereby a contracting cell expands its neighbour and thus trigger its contraction. By locally releasing tissue tension with laser-mediated incision, it was shown that the apical surface areas of nearby AS cells stop oscillating, while those of distant AS cells do not[36,40]. Thus, we hypothesized, that the relevant actin waves are tension-dependent too, and should cease to appear immediately following tissue tension release by laser incision. Interestingly, we observed that after cutting a single adherens junction connecting the two cells, ANBs continued to appear in all AS cells, but a few immediate neighbours (Fig. 15A-15B). We observed the same result in control and AS-SqhKO AS cells, which substantiates the idea that the generation of ANBs is tension-independent. In the few AS cells that neighbour the two ablated ones, ANB intensity was reduced or they ceased briefly consistent with previously reported similar behaviour of MyoII[40]. These cells also started to extend lamellipodia that covered the damaged cells and sealed the opened hole in the tissue. Such behaviour is typically associated with the wound healing response, which we also detected with independent experiment and will describe later in Chapter 3 Section 3.2.2. Similarly, we also observed AS cells extending lamellipodia when AS was about to rupture and gaps in tissue appeared in AS-SqhKO or AS-yolk-SqhKO embryos (Fig. 13C).

An alternative way of releasing tissue tension was proposed by Jayasinghe et al. 2013 who used CO_2 or Argon gas to anesthetize embryos[96]. While the authors showed that apical cell area oscillations cease in AS tissue upon CO_2 application, so do all the other processes since embryos are depleted of oxygen and consequently energy production. Nevertheless, anaesthesia should mimic loss-of-tension state of the tissue. We anesthetized embryos by applying CO_2 or Argon gas (Fig. 16A-16B) using a custom-built setup on a spinning-disk confocal microscope and imaged the process. We observed that ANBs did not cease immediately after CO_2/Argon application, but gradually slowed down and were completely gone in less than 45-60min (Fig. 16A-16C). The same happened for the ANBs in AS-SqhKO

embryos (Fig. 16D). Once the CO_2 flow was stopped and replaced with a standard air, ANBs re-appeared in control and AS-SqhKO embryos (Fig. 16A, 16C-16D). They did so all at the same time and were in-phase for 1-2 periods until becoming asynchronous again (Fig. 16C). Interestingly, such re-establishment of ANBs is different from their initial *de novo* formation at the final stages of germ-band retraction. There, they appear in a more heterogeneous salt-and-pepper manner[38]. After such a CO_2/Argon-induced "reset" of ANBs, control embryos continued DC, whereas AS-SqhKO still failed.

3.2.2. AS cells can autonomously contract in both Ca2+-dependent and –independent manner

We next wanted to know if ANBs comprise F-actin or could be produced by the G-actin alone. For this we injected pharmacological compounds into the yolk cell underlying the AS tissue (Methods, section 6.3.1). Within minutes after the injection of latrunculin B that prevents actin polymerization ANBs in AS cells disappeared together with the other actin-dependent structures like filopodia and cortical actin network (Fig. 17A). Similar effects were observed after cytochalasin D injection that disrupts actin filaments, but also prevents actin polymerization (data not shown). We next injected a standard MyoII inhibitor blebbistatin to confirm that the ANBs occur independent of MyoII. Unfortunately, we did not observe MyoII signal depletion in AS cells even though the blebbistatin is considered to be a membrane-permeable compound (data not shown). During blebbistatin injections we also noticed that within 2-5min after the injection, part of the AS tissue briefly contracted and then relaxed again. Since blebbistatin was dissolved in DMSO, we performed control injections of DMSO only into the embryo. Indeed, we could detect local contractions of AS tissue areas that were variable in size, most likely reflecting local DMSO concentrations (Fig. 17B). After such a transient contraction, AS cells continued pulsing and constricting normally. No such effects were detected in water-injected embryos or placebo embryos, where the injection needle was only pierced into the yolk cell, but nothing was released (data not shown). In addition, we find that the DMSO effect is concentration-dependent since injecting a 1:10 dilution in H_2O resulted in smaller contracting AS tissue areas and injecting a 1:100 dilution did not cause any contraction at all (data not shown). We conclude that on a short time scale, DMSO causes local AS tissue contraction.

Based on experiments with reconstituted liposomes and tissue culture cells it was suggested that DMSO application changes membrane bilayer properties leading to higher

permeability for H_2O, ions (e.g. Ca^{2+}) and small molecules[126,127]. We thus hypothesized that Ca^{2+} influx could be responsible for such a transient contraction of AS cells as Ca^{2+} was shown to trigger a signalling cascade that eventually lead to MyoII activation via calmodulin and myosin light chain kinase (MLCK)[128]. Therefore, we injected DMSO into embryos expressing a GCaMP V calcium biosensor, which is myristoylated and thus bound to the plasma membrane (PM)[129]. Surprisingly, we did not see any Ca^{2+} influx in the contracting region making this an unlikely cause of DMSO-mediated cell contraction (Fig. 17B). An alternative possibility is that DMSO induces actin polymerization rather than Ca^{2+}-dependent MyoII activation. To test this, we injected DMSO into AS-SqhKO embryos, expressing mCherry-moesin in the AS cells. Indeed, we observed a transient actin polymerization in AS cells (Fig. 17C), but since these cells lacked functional MyoII, such polymerization did not lead to contraction. These results indicate that DMSO triggers AS cell contractions without the need of Ca^{2+}-dependent activation of MyoII.

Recently, it was proposed that by stretching neighbouring cells a contracting AS cell opens up mechanically-gated ion channels in the former. The resulting Ca^{2+} influx would then cause their contraction[114]. A key finding was that chelating Ca^{2+} by injecting caged NG-EGTA and then uncaging the drug in individual AS cells with UV light causes their contraction. However, this experiment did not allow discriminating between Ca^{2+}-mediated activation of MyoII via calmodulin-MLCK and Ca^{2+}-induced actin polymerization. We therefore repeated this experiment in wild-type embryos and in AS-SqhKO embryos lacking MyoII activity. For unknown reasons, we were not able to reproduce the original experiment using the published NG-EGTA Ca^{2+} chelator. As an alternative, we used ionomycin that was shown to open K^+-gated Ca^{2+} channels that lead to intracellular Ca^{2+} influx[130]. Since the drug required dissolving in DMSO, we subsequently diluted DMSO-dissolved ionomycin 1:100 in H_2O to achieve unproblematic solvent concentrations. Upon injection of 100µM ionomycin into GCaMP V-expressing control embryos, we detected a transient Ca^{2+} influx and local AS cell contractions (Fig. 17D). To test whether such contraction was via calmodulin-MLCK MyoII activation or actin polymerization, we injected ionomycin into embryos where MyoII was depleted in AS cells and actin was labelled with mCherry-moesin. To exclude any effects from the contractile activity of the underlying yolk cell we chose to observe AS-yolk-SqhKO embryos. After injecting 100 µM ionomycin we observed that actin polymerized in MyoII-depleted AS cells (Fig. 17E) suggesting that Ca^{2+} influx directly triggers actin polymerization.

It is important to stress that the cytotoxic effect of ionomycin that was reportedly described in different assays in cell culture and *in vivo*[131,132]. We could also detect similar

cytotoxic effects in embryos after we injected higher ionomycin concentrations (1mM or 10mM). At these high concentrations actin immediately polymerized into thick filaments and such polymerization was permanent with all the cells failing to recover and dying within minutes (Fig. 17F). Therefore, while the results suggest that Ca^{2+} influx triggers polymerization of actin network independent of MyoII, this conclusion needs to be taken with care.

3.2.3. AS cell coupling via gap junctions depends on cortical cell tension

We showed that ANBs correlate less between neighbours in MyoII-depleted cells than in wild-type cells (Fig. 14B, 14C). This suggests that MyoII-mediated contractions somehow coordinate ANBs. Since we did not find evidence for a role of Ca^{2+} influx through mechanically gated ion channels as primary trigger of ANBs, we speculated that it could depend on solute transport via the gap junctions (GJs)[133,134]. Therefore, we injected carbenoxolone – a commonly used GJ inhibitor – into control and AS-SqhKO embryos[135–138]. In both, ANBs disappeared, within minutes of injecting 1M carbenoxolone. After another 10-15 minutes, ANBs gradually re-appeared mostly starting from the outer regions of the AS tissue (Fig. 18A). Surprisingly, we also detected that in some AS cells, two ANBs re-appeared simultaneously in the same cell (Fig. 18B), which was previously not observed in wild-type AS cells[38,39,41]. These results suggest that ANBs of neighbouring cells are coupled via GJs. The injection of high Cbx concentrations (10mM) induced cytotoxic effects leading to complete loss of actin structures and embryos dying within minutes (data not shown).

Next, we analysed the flux through GJs of neighbouring AS cells. One way is to monitor Ca^{2+} diffusion from one cell to the other using the GCaMP biosensor, which becomes fluorescent upon Ca^{2+} binding. Using GCaMPs it was shown in different epithelia that laser-mediated cell wounding causes a sharp rise of intracellular Ca^{2+}. The Ca^{2+} then flows into the neighbouring epithelial cells via the GJs[119,139]. To monitor Ca^{2+} in AS cells, we chose to use a myristoylated version of GCaMP (myr-GCaMP), which is one of the most sensitive Ca^{2+} biosensors to date[129]. Following laser-mediated wounding of a single AS cell, we detected a significant myr-GCaMP intensity flash in the wounded cell. After 1-2 seconds, a varying number of direct neighbouring cells showed a similar flash (Fig. 19A). On average a single AS cell is in direct contact with 5-7 neighbours (i.e. first neighbors). However, the Ca^{2+} spread to these was not even (Fig. 19A-19B). Moreover, in some cases we detected a transient myr-GCaMP flash even in "second" neighbours that were not in direct contact with the wounded cell (Fig. 19A-19B). Following the initial flash, the myr-GCaMP persisted for 4-5min in the

wounded cell, but disappeared much more rapidly, with variable kinetics, in the neighbouring cells (Fig. 19A-19B). Interestingly, additional laser cuts in an already wounded cell did not cause additional myr-GCaMP flashes in the neighbours (Fig. 19C). This indicates that immediately after the first Ca^{2+}-induced flash, transmission through the GJs shuts down. Such gap junction shut-off was previously associated with the first steps in tissue wound healing [121,139]. To test whether the Ca^{2+}-induced myr-GCaMP flashes in cells neighbouring a wounded cell indeed reflected Ca^{2+} flux between the two cells rather than a signalling dependent release from the cells internal Ca^{2+} stores in the ER, we wounded AS cells in embryos, in which we had injected the membrane-impermeable Ca^{2+} chelator EDTA into the perivitelline space. The logics were that the EDTA blocks extracellular Ca^{2+} thus preventing the influx of free Ca^{2+} into the wounded cell. Consistently, we could no longer detect myr-GCaMP flashes in wounded cells. Also the neighbouring cells showed no obvious myr-GCaMP signal changes showing that they indeed are caused by Ca^{2+} influx from the wounded neighbor (Fig. 19D). Altogether, these results strongly support the possibility that AS cells trigger ANBs in their neighbours via GJs and that such a signal can propagate beyond the direct neighbours. They also show that after wounding the cells GJs become gated.

Earlier we showed that following laser ablation of cell-cell junctions, most neighbours still generated ANBs and only a few of the surrounding cells were devoid of ANBs (Fig. 15A-15B). When performing the same experiments in the presence of myr-GCaMP, the decay of the induced myr-GCaMP signal in some first neighbours was very slow or did not occur at all. It is conceivable that these cells correspond to the ones no longer able to form ANBs (Fig. 19E). Interestingly, when wounding cells with such high myr-GCaMP signal intensity, their respective neighbours did not show myr-GCaMP flashes (Fig. 19E). This suggests that the cells had already shut down their GJs following the first influx of signal from the cells wounded by the initial cell-cell junction ablation.

While the adhesion between epidermis and AS cells is studied in great detail, the presence of gap junctions between the two tissues is not well defined. A first hint that the two tissues are not linked comes from laser-mediated wounding of the lateral epidermis[119]. In these experiments the induced Ca^{2+} wave was never observed to spread into the AS tissue. However, these data were not fully conclusive as the wounds were placed at a considerable distance to the AS tissue and we have seen that with increasing distance from a wound the intracellular Ca^{2+} concentration drops below levels that GCaMP sensors can detect. Therefore, we cut AS-, or epidermis cells close to the AS/epidermis tissue boundary. While in these experiments GCaMP flashes spread to the neighbouring cells of the same tissue, we could never observe

any GCaMP signal being induced in neighbouring cells of the other (Fig. 19F-19G). This suggests that GJs are either absent or closed between the two tissues.

The apical surface area oscillations of AS cells generate transient pulling forces acting on the neighbouring cells. It is evident that this will enlarge the surface of the latter if these happen to be in a relaxed state[36]. In previous publications it was proposed that GJ conductance depends on membrane tension or the shearing/stretching state of the actin cortex, in which GJ channels are embedded[140–142]. Thereby, mechanical stress is thought to open the GJs via a rotational shape change, while relaxation would send them back into a closed state. If that holds true for AS cells, we would expect that reducing AS tissue tension or interfering with ANBs and thus the ability of cells to produce transient pulling forces should also impede GJ conductance. To test this idea, we wounded AS cells of embryos injected with latrunculinB to depolymerize all actin structures, including the actin cortex. Within 5min following injection, the actin cortex was no longer detectable. Laser-mediated single-cell wounding produced a GCaMP flash in the wounded cell, but we could not detect the clear GCaMP flashes spreading into the surrounding cells as in the wild type, (Fig. 20A). Only in few of the direct neighbours we could detect some GCaMP signal in the very near vicinity of the damaged cell (Fig. 20B). This suggests that AS tissue relaxation causes GJ closure, which is in line with what was previously suggested. To see whether this holds true also for other tissues we repeated the experiment in the same, latrunculinB-treated embryos, this time wounding individual cells of the surrounding epidermis. Surprisingly, in this case we observed GCaMP flashes spreading into the surrounding cells similar to the wild type (Fig. 20C). LatrunculinB-mediated actin depolymerization removes all F-actin, including the filamentous actin required for vesicular transport. Hence, it is possible that in the large AS cells we might affect GJ conductance by inhibiting the delivery of GJ components to the plasma membrane, which may be less critical in the much smaller epidermis cells[143,144]. To address this possibility, we injected embryos with CK-666, a drug that inhibits Arp2/3 and thus selectively blocks the nucleation of branched F-actin networks, such as the actin cortex[145]. Laser-mediated wounding of AS cells in CK-666-injected embryos revealed similar results as with latrunculin B. GJ conductance amongst AS cells was abolished (Fig. 20D), while in the epidermis tissue it was not affected (data not shown). In conclusion, actin/myosinII-mediated mechano-sensitivity and tissue tension-dependency of GJ conductance appears to be dependent on the nature of the tissue and thus not a universal feature of epithelia.

We showed earlier, that the DMSO solvent on its own has a concentration-dependent effect on AS cell contractility (Fig. 17B). In some cases, sub-regions of AS cells contract via

Ca^{2+}-independent induction of actin polymerization and in other cases they do not. Thus, we distinguished between the two events when laser-wounding the cells expressing myr-GCaMP. In the cases where no local AS contraction occurred, laser wounding of single AS cell produced the same response as in the non-injected embryos where Ca^{2+}-induced flash spread into the immediate neighbours (Fig. 20E). By contrary, if local AS tissue contraction occurred after DMSO injection, GJ conductance was abolished in such contracting AS cells (Fig. 20F). Overall, this suggest that extreme shear stress applied to or removed from the actin cortex is influencing the GJ conductance in AS cells.

An alternative way of reducing tissue and cell cortical tension is using CO_2/Argon anesthesia[96]. When these gases are applied, AS cells completely lose their actin dynamics (Fig. 16). Thus, we performed laser incisions on such "CO_2-anesthesized" embryos, but could not observe any prominent Ca^{2+}-induced myr-GCaMP intensity flash (Fig. 21). Only after over-exposing images, a weak intensity change could be seen (not shown). After replacing the anesthetizing gas with fresh air was applied and embryos were recovering, laser incisions evoked Ca^{2+}-induced flashes that also spread into the neighbours (Fig. 21). While these results support the idea that actin cortex is required for proper GJ conductance, the failure to evoke Ca^{2+}-induced flash in the wounded cell might reveal additional AS cell properties.

We also tested for a role of the other cytoskeleton element, the microtubules, in the regulation of GJ conductance. Conductance was not affected when depleting embryos from microtubules by injecting the microtubule de-polymerizing drug colcemide[94]. In these embryos, the spreading of Ca^{2+}-induced GCaMP flashes from wounded AS cells to their neighbours was similar to the wild type showing that in the AS tissue, microtubules are not involved in GJ conductance (data not shown).

3.2.4. Gap junction dynamics and importance during DC

To date, there is only a single study by Guiliani et al. 2013 on the role of GJs during DC implicating a role for Innexin-3 (Inx3), but not other innexins, in the process[146]. The work relied solely on genetics and fluorescence imaging of immunofluorescently labelled, fixed embryos, which does not provide any temporal resolution. It is therefore difficult to extract the exact involvement of GJs in the rapid apical surface area oscillations of AS cells. Therefore, we started investigating the spatiotemporal dynamics of GJs with live imaging of wild type and mutant embryos. Unfortunately, endogenous gene trap lines for any of the three main innexins (Inx1-3) were not available. We therefore used an over-expression construct, where UAS

promoter sequences were driving the expression of a genetic construct encoding GFP-tagged Inx3 (Inx3-GFP)[147,148]. Consistent with the reported immunolabelling data, in AS cells Inx3-GFP localized to distinct punctae or small patches at the plasma membrane (Fig. 22A)[146]. Some Inx3-GFP punctae were also visible in the cytoplasm probably revealing the protein population that is being trafficked to or from the plasma membrane (data not shown). As expected, almost all of these puncta localized below the adherens junctions in AS cells (Fig. 22A). Along with an apical surface contraction, the GJ puncta distributed along a shortening cell-cell junction compacted accordingly (Fig. 22B). More importantly, these movements mostly followed the movement of the more apical positioned adherens junctions with a short time delay (Fig. 22B). This suggests a drag exerted by the basolateral membrane or cortex on the moving adherens junctions[96]. Yet, the exact delay in movement was not always obvious consistent with the notion that AS cells are not the "typical" epithelial columns, but rather have dynamic basolateral surfaces that can behave independent of the cell apex[42] (Oliveira and Brunner, unpublished). Consistently, when apical surface oscillations of AS cells were affected, such as in zygotic zip^{1}/zip^{1} mutants, these puncta still localized to the cell edges and merely showed reduced dynamicity (Fig. 22C). Overall, this suggests that GJ channels experience mechanical stress when cells contract their apical cell surface, which potentially can affect their activity state.

In their study, Giuliani et al. based their argumentation on the role of Inx3 mainly on genetic interference involving large deficiencies (Df(3R)BSC789 and Df(3R)BSC806) that span a major region around *inx3* and most likely affect multiple gen products[146]. To be more conclusive, one would ideally want to use a more specific mutant of *inx3*. As to date such a specific loss-of-function mutant does not exist, we decided to generate one using the CRISPR/Cas9 recombination system[149]. Two CRISPR recognition sites flanking the *inx3* ORF were identified for targeting (Fig. 23A). Since *inx3* lies in the intronic region of another gene, *sponge* (*spg*), we made sure to avoid *spg* exons. Together with guideRNAs targeting the two CRISPR recognition sites, we injected a donor plasmid containing two 1kb sequences homologous to the regions outside the *inx3* gene (HR1 and HR2 in Fig. 23A) and flanking a sequence encoding the dsRED fluorescent protein and attP and loxP sites. In this way, we replaced the endogenous *inx3* sequence with an attP-loxP-dsRED-loxP cassette (Methods, section 6.3.4). We obtained 3 independent events and named all of them $\Delta inx3^{dsRED}$ as they are genetically identical. The $\Delta inx3^{dsRED}$ alleles were lethal in trans to the major deficiency Df(3R)BSC789 used by Giuliani et al[146]. The loxP-dsRED-loxP sequence was later removed using Cre recombinase leaving only the attP site ($\Delta inx3^{attP}$) and maintaining the lethality over

the deficiency Df(3R)BSC789. When we imaged homozygous *Δinx3*^{dsRED} embryos using moesin-GFP-labelled actin as a reporter, we did not observe any of the defects reported by Giuliani et al. (e.g. severe kinks in the epidermis or incomplete closure)[146] (Fig. 23B). We neither detected any apparent defects in apical surface area oscillations of AS cells. We conclude that the phenotypes reported for mutants homozygous for deficiencies covering the *inx3* locus are not specifically due the absence of zygotic Inx3, but rather arising from the loss of another nearby gene, from the combinatorial effects of a multi-gene loss, or from second site modifiers that had accumulated on the balanced chromosomes.

Despite the absence of a phenotype in our specific *inx3* deletion mutants, we could not exclude a role for this protein as one of the other innexins might well provide redundant rescuing activity, since these proteins can form homotypic and heterotypic GJ channels[134,148]. To test this possibility, we generated embryos that were homozygous mutant for *Δinx3*^{dsRED} and *inx2* (*inx2*^{G0118}). In such double mutants, we observed variable DC defects, ranging from mild puckering to zipping failure and tissue rupturing resulting in complete DC failure (Fig. 23C). The variability of the mutant phenotypes most likely is due to the maternally contributed gene products. The phenotypes were enhanced when *Δinx3*^{dsRED} was combined with a homozygous small deletion Df(1)BSC867, which encompasses the *inx1* and *inx2* genes (Fig. 23D). Besides *inx1* and *inx2*, the deficiency Df(1)BSC867 also includes *boudin* – a gene needed to build proper septate junctions[146]. Loss of this gene could explain the increased phenotypic penetrance however since AS cells do not form septate junctions, all cell-autonomous effects in AS cells should be due to a loss of all 3 innexins[150]. Our preliminary observations indicate that in some mutant embryos the shapes of AS cells are distorted (Fig. 23E), but for a clear conclusion further quantitative analysis of cell shapes is needed.

3.2.5. Cell-autonomous oscillator in AS cells

Using acute and by far the most effective MyoII activity depletion ever, we demonstrate that ANBs in AS cells appear independently from MyoII. The results argue in favour of a biochemical oscillator system that is independent of MyoII and of cell-deformation. Nevertheless, previous reports suggested that cell surface area deformations are to some degree coordinated between the cells[36,37]. Recently, the model of a self-organized, contractile AM system was proposed, that is sufficient to elicit spontaneous cell contraction cycles[110]. The model includes a lag phase to recycle or reload its components and MyoII as a critical component. We demonstrate that such cycling occurs without the motor activity of MyoII

suggesting that actin merely exhibits treadmilling activity rather than being concentrated by MyoII cross-linking and filament sliding as proposed in the contractile model[110]. F-actin in our system thus behaves similar to what was reported in the leading edges of motile cells[4,113]. Actin treadmilling would also imply that the activity at least one critical component needed to polymerize actin should also cycle. We could not detect any obvious oscillations in protein levels of either the Arp2/3 complex (Fig. 24A) that nucleates branched F-actin networks or of WASpRBD-GFP, a biosensor for the activity of the cdc42 GTP-ase, which is a classical switch controlling F-actin nucleation via N-WASP[151] (data not shown). This argues in favour of protein activation/inactivation, for example by phosphorylation/de-phosphorylation cycles, to play a role, should these components be involved. Yet we cannot exclude that due to the rather weak fluorescence signal present in such experiments, we are just unable to detect the critical fluctuations.

In this context, we also investigated the Rho1 GTP-ase, which has been promoted as key regulator of many AM activities and cell shape changes in developing epithelia[52,152]. RhoI is responsible for direct activation of the F-actin nucleating formin Dia and also, via the kinase Rok, of MyoII[52,152]. Recently, it was shown that Rho1 cycles with MyoII controlling its phosphorylation/de-phosphorylation cycles during germ-band extension[125].In AS cells, a GFP tagged version of Rho1 (GFP-Rho1) localized mainly to the plasma membrane, with occasional density increases at the cell apexes that could potentially reflect pools of local protein activity (Fig. 24B). Due to the very intense Sqh-GFP aggregates in AS-SqhKO embryos it was not possible to visualize GFP-Rho1 and RBD-GFP for comparison, in the absence of MyoII. To try discriminating between the active and inactive Rho1pools, we imaged RBD-GFP, a biosensor for Rho1 GTP-ase activity[151]. We could not observe any oscillatory behaviour of RBD-GFP (Fig. 24B). .

We next went about to interfere with actin treadmilling in AS cells by modulating the activity of Twinstar (Tsr), the Drosophila cofilin. Cofilins sever actin filaments thereby facilitating their de-polymerization and increasing the ratio of G-actin/F-actin[9]. In motile cells, RNAi of cofillin was shown to decrease lamellipodia formation due to the resulting, reduced G-actin pool, which prevented new F-actin polymerization at the leading edge[4,153]. Ectopic expression of a dominant-negative Tsr variant (DN-Tsr) in AS cells, did not cause any significant difference in the ANB dynamics (Fig. 24C). Similarly, ectopic expression of a constitutively-active cofillin form (CA-Tsr) did not cause any major defects and only marginally shortened the average ANB periods (Fig. 24D). Even though period distributions were statistically different between the control and CA-tsr (at p=0.05, Mann-Whitney test), the

median value was reduced only by 30s (Fig. 24D). This suggests that the expression of DN-Tsr and CA-Tsr does not interfere enough with F-actin treadmilling, either because levels are too low or because F-actin nucleation bursts are much faster than the severing activity of cofilin.

All in all, we find no evidence that much of the factors known to regulate and control F-actin network dynamics, including actin monomer concentration, the Arp2/3 complex and the Rho family of small GTPases are rate limiting for ANBs. This argues for an independent molecule or entity (factorX) that could trigger ANBs and that cycles in the cells either by becoming more/less abundant or more or less active. Based on our findings supporting cell-cell coupling of ANBs via GJs, factorX should obviously be able to pass through the GJs in order to influence the neighbours. Since GJs are "size-sieves", this narrows the candidates down to ions, secondary messengers (e.g. cyclic nucleotides or inositol phosphate (IP_3)), aminoacids, or small metabolites. Our data with the myr-GCaMP biosensor do not support a role for Ca^{2+} even though these ions were proposed to coordinate ANBs amongst AS cells (Fig. 24E)[114]. Together with further evidence, which we will discuss below in section 3.3.3, we therefore rule out Ca^{2+} as factorX.

In a first attempt to screen for factorX, we injected embryos with various chemical compounds and looked for effects in DC. Two of them, cyclic-GMP (cGMP) and sildenafil, an inhibitor of cGMP-phosphodiesterase type 5, did not show any phenotype different from the control. When injecting purified cyclic-AMP (cAMP), we detected a transient re-arrangement of the plasma membrane and actin in what appeared to look like cell blebbing (Fig. 24F). Thereafter, the apical AS cell surface returned to its normal, oscillating behaviour. To test for a role of inositol phosphate (IP_3), we injected the PI3-kinase inhibitor wortmannin, which was shown to cause a rapid loss of multi-phosphorylated phosphoinositides[154]. Following the injection, we could still detect ANBs (Fig. 24G). Since in these embryos, DC tissues ruptured and embryonic development failed within 4-6 hours, we are confident that the drug was effective (data not shown). Finally, we ectopically expressed a kinase-dead PI3-kinase construct (DN-PI3K), which acts as a dominant negative in the AS cells. Also this did not lead to a major change in ANB frequency (data not shown) further excluding a possible role of PI3-kinase and IP_3 signalling in apical AS cell surface area oscillations. Thus, the preliminary screen for factorX did not reveal any convincing candidates and the trigger for ANBs remains elusive.

3.3. Discussion

3.3.1. Actin and MyoII are two separate entities in AS

Acto-myosin (AM) contractility is one of the most common mechanisms generating mechanical force at both tissue and single cell levels[6,7,16,107]. Numerous experimental evidence and *in silico* modelling revealed a plethora of ways in how AM can assemble/disassemble[110,112,124,125], move as travelling or standing waves[110,115,124] or act as molecular clutches and purse-strings[7,107,155]. All this diversity clearly cannot be easily generalized to a single model of AM dynamics that can be applied to all cell types and morphogenetic processes. Using acute, specific and so far the strongest MyoII function depletion in AS cells, we reveal that underlying AM behaviour in AS cells is different from what is generally assumed based on previous results and results from other experimental model systems.

We demonstrate that pulsed AS cell contraction is tissue tension- and MyoII-independent, but the latter contributes to the observed transient coordination of cell deformations between neighbouring cells[36,37,156]. So far the AM network in AS cells is considered as a simplified two-component contractile system, where AM acts a single unit[41,110]. We demonstrate that the two main components – actin and MyoII – are separate entities with their own dynamics. Recently, it was shown that during germ-band extension MyoII activity is controlled by a complex, self-organized biochemical network that eventually enables contractility of the underlying actin cortex[125]. It is likely that such a network also exists for controlling MyoII activity in AS cells, yet it must act downstream of a pace making system.

We analysed the so far most efficient, most confined and most controlled MyoII depletion in AS cells. Yet, we cannot fully exclude that some functional MyoII remains that is beyond the fluorescence detection limit. However, it is very unlikely that such a massively reduced functional MyoII pool could be sufficient to maintain normal oscillatory AM dynamics. Additional support for ANB independence of tissue tension and MyoII comes from our recovery experiments after CO_2/Argon anaesthesia. Even if one assumes a stochastic nature of Sqh-GFP degradation efficiency or that different AS cells could have different amounts of functional MyoII left, ANBs are almost simultaneously upon recovery (Fig. 16). At least two anaesthesia-recovery cycles in the same embryo does not affect such behaviour (data not shown). As expected, all the less effective perturbations of MyoII activity used before did not

behave differently in such experiments (Fig. 13B). Nevertheless, combining two perturbation methods (e.g. deGradFP and Mbs.N300 over-expression) in a single embryo would further strengthen our arguments even more.

3.3.2. Tension-based AS apical area contractions or mechanical AS cell autonomy?

While most current models argue for tension-based coordination of ANBs[36,40,100], some recent evidence exists that AS cells are mechanically independent as we propose here[96]. The support for the generally accepted model comes from classical genetics, numerous computational models and from laser incision experiments, whereby local release of tension was postulated to cause arrest of apical AS area oscillations[36,40]. In this work we suggest that this arrest is a consequence of a non cell-autonomous wound healing response elicited by Ca^{2+} influx via GJs from the damaged cells (Fig. 19E). Alternatively, laser incisions might damage the basolateral parts of the cells neighbouring the injured cell thus inducing cell-autonomous wound healing response. It was shown that cells upon wounding re-arrange their cytoskeleton[118,157], which would account for the observed arrest of apical surface area oscillations. Co-wounding of neighbouring cells is possible as AS cells have very dynamic basolateral surfaces whereby cells extend massive basal protrusions that frequently extend below first, second and even third neighbours[42] (Oliveira and Brunner, unpublished). Yet, in this scenario it is not easy to explain the requirement for GJs.

Even though we show that ANB generation is tension-independent, the hypothesis proposed earlier by Hutson and colleagues[96] that AS cells are completely mechanically autonomous is incompatible with the fact that AS cells can be stretched by more than 40% from the average area as observed in this and previous studies (Chapter 2, Fig. 8A)[17,36,39,40]. Mechanical independence hypothesis was supported by observation that apical and basal surfaces of some AS cells oscillate in an anti-phase manner. While viscous cytoplasm could explain the passive return of apical cell areas back to the resting state after a contraction, only the external force provided[96] by the contracting neighbour could lead to area deformation beyond the resting state. Thus while AS cells are mechanically autonomous in initiating the apical contraction, the pulling forces of the neighbours affect the final apical area deformation.

Building on a tension-based model, it was suggested that a contracting cell would open mechanically-gated ion channels (MGCs) in the neighbouring cell by stretching its apical cortex[114]. As a result, ion influx (particularly Ca^{2+}) would lead to a contraction of the stretched neighbour. The authors of this study had found a weak correlation between local PKC2-Ca^{2+}

biosensor intensity increase at the plasma membrane and the change of the apical cell perimeter that occurred in ~30% of cells[158]. We used a much more sensitive Ca^{2+} biosensor that was bound to the PM and thus did not have the extremely noisy, naturally fluctuating signal of PKC2-Ca^{2+} and we could not detect any intensity oscillations indicative of transient Ca^{2+} influxes during the cell pulsing (Fig. 24E). Even though PM-bound Ca^{2+}-biosensors are the most sensitive ones available to date[129], this does not exclude that endogenous Ca^{2+} fluctuations are so minuscule that they are simply beyond the detection limit of light microscopy. However, we would argue the same to be true for the previously used PKC2-Ca^{2+}sensor and that the noisy signal of this biosensor by chance would pretend co-occurrence of signal increase and cell contraction.

While Hunter et al. focused exclusively on Ca^{2+}, using microinjection of pharmacological compounds we demonstrate that AS cells can contract in a Ca^{2+}-dependent and a Ca^{2+}-independent manner. Ca^{2+}-dependent contraction is consistent with NG-EDTA-chelated Ca^{2+} uncaging[114]. Even though we were unable to reproduce these results from Hunter et al., using ionomycin we show that alleviating intracellular Ca^{2+} induces an AS cell contraction (Fig. 17D). While the compound induces actin polymerization independent of MyoII, this could be an indirect effect of the previously reported cytotoxicity of the drug[131,132] (Fig. 17E-17F). Furthermore, we reveal that AS cells can contract in the absence of Ca^{2+} influx. Such contraction occurs via actin polymerization and argues strongly against the proposed role of MGCs. If the stretch-induced MGC ion influx model would be correct AS cells initially contracting without Ca^{2+}-influx (Fig. 17B) would dramatically stretch the non-contracting cells and thus lead to Ca^{2+} influx via MGCs in these stretched cells. However, there is no Ca^{2+} influx into any of the AS cells during such contraction strongly arguing against not only MGCs, but also against Ca^{2+} itself being the trigger of ANBs.

The independent nature of ANBs needs an explanation. How does MyoII fit in? While every ANB is generated independently of MyoII, in the wild-type MyoII rapidly accumulates on such F-actin structures, contracts them and in this way causes cell deformation. Clearly these deformations affect the apical cell surface area, but they in addition are likely to generate shear forces acing on the basolateral membrane. It was shown that apical and basal surface deformations of AS cells can be anti-correlated indicating that the lateral membrane is stretched away from the vertical position[96]. Consistently, we observed that following an apical contraction as monitored by the contraction of the adherens junction belt outlining the AS cells, the more basolaterally positioned GJs contracted too, but were lagging behind the adherens junctions (Fig. 22B). Currently, this cannot be generalized to all AS cells and further analysis

of cell shapes in 3D with higher Z resolution is needed to confirm this. Even if basolateral membrane drag were not applicable to all contracting AS cells, this could still provide a link to couple the basic oscillatory behaviour of ANBs with the coordinating role of MyoII-mediated tension changes. Such MyoII-dependent mechanical coupling is supported by the finding that many neighbouring cells are pulsing perfectly in-phase or anti-phase for extended periods of time[36,37] (Dreher and Brunner, unpublished). An intriguing possibility is that basolateral GJs could be part of the proposed mechanical coupling between AS cells. In support of this, we show that GJ conductance in the AS tissue depends on cortical cell tension. Interestingly, it is reduced in "relaxed" cells with a depleted actin cortex as well as in extremely contracting cells (Fig. 20E-20F). This argues for the need of tightly balancing the forces applied on the actin cortex. Alternatively, the channels of GJs could be open by default, as generally assumed, and just allow diffusion of intracellular factors as a function of concentration gradients. However, surprising differences between GJ conductance in epidermis and AS tissue, would suggest that GJ permeability is controlled in AS cells. In addition, our laser surgery experiments show that under certain conditions GJs do shut down.

So far, only one study provided some evidence for a requirement of the GJ subunit Innexin-3 in DC. This emphasizes the difficulties posed by traditional genetics to address protein functions during embryogenesis[146]. With this idea in mind, we engineered *innexin-3* locus using CRISPR/Cas9 such that we can now easily generate various tagged versions of the protein in the endogenous locus. This will allow tissue-specific and acute protein KO using either deGradFP, TIPI or CRY2[64,73] methods and will overcome the limitations of classical genetics. Even though these methods provide the by far best way to specifically address protein function, the redundancy between the innexins already seen with zygotic alleles might remain a critical problem. Therefore, it is desirable that in addition alternative methods probing the role of GJs during DC more directly will be designed.

3.3.3. The proposed model of AS cell surface contractions is still missing an important puzzle-piece

Taking into account AS cell autonomy that our data revealed together with the observed mechanical coupling, we proposed the following AS apical area contraction model (Fig. 25). An oscillating factorX gradually accumulates in AS cells and upon reaching a critical concentration triggers an ANB (Fig. 25, i-ii). Upon actin polymerization free MyoII docks onto the F-actin. When the actin network has reached sufficient density, MyoII crosslinks the filaments and via motor activity drives network contraction, which translates into deformation

of the cell apex and compression of the adherens junctions (Fig. 25, iii). This cell deformation adds strain to the GJs below the adherens junctions and changes their conductance such that a fraction of factorX can move into the neighbouring cell (Fig. 25, iii). This shortens the time for this cell in reaching a critical concentration of factorX or even leads to immediate triggering of an ANB should the cell already be near the critical concentration (Fig. 25, iv). An ANB depletes factorX which starts to build up again (Fig. 25, iii-iv). Sufficient time, or neighbouring cell area deformation induced by MyoII docking on the ANB then completes the cycle (Fig. 25, v). Since oscillator cycles naturally are stochastic in every cell, but can be influenced by the neighbours, such mechanism could lead to a number of contraction phases observed between the neighbours[37,156] (Dreher and Brunner, unpublished.). In the absence of MyoII contractility the oscillator would still cycle although with some delay since the input from the neighbours would be reduced. This is supported by increased period length of AS-SqhKO and AS-yolk-SqhKO cells (Fig. 14A).

Even though we cannot completely exclude Ca^{2+} as being ANB generator, our data argues strongly against that. First, we show that AS cells can contract in Ca^{2+}-independent way (Fig. 17B). Second, intracellular Ca^{2+} concentration is very low in cells and does not fluctuate in high dynamic range. Any spontaneous increase above the threshold level would immediately lead to Ca^{2+}-induced Ca^{2+} release from the endoplasmic reticulum stores. This would eventually lead to prominent spikes in Ca^{2+} biosensor intensity, which would be clearly detectable. In fact, we can detect such instances with the sensitive myr-GCaMP in the epidermis shortly after DC (Appendix 2, Fig. 63). However, we do not see any of these intensity spikes in AS cells (Fig. 24E). Even though, in the study by Hunter et al., MGCs were pharmacologically affected, the focus was put exclusively on Ca^{2+} excluding any other ions that might trigger the contraction[114,158]. Our preliminary screen also excludes IP_3 signalling via Ca^{2+} since neither pharmacological inhibition, nor dominant-negative expression of PI3-kinase affected the ANBs. The observation that extreme local AS tissue contraction induced in Ca^{2+}-independent manner does not lead to Ca^{2+} influx in any of the stretched AS cells strongly argues against the role of MCGs in the process (Fig. 17B). In addition, in MyoII-depleted cells both tissue tension and cell area deformations are absent (Chapter 2, Fig. 8A) arguing that MCGs would not be opened to cause any Ca^{2+} influx. Yet ANBs are still generated in such a case. From all the evidence, we conclude that Ca^{2+} and MCGs are not the main cause for ANBs and tension-mediated coupling of apical AS cell areas.

3.4. Future directions

To support our working model of apical AS cell surface contractions, it is necessary to find the factorX that can trigger ANBs in the cell. Obviously, only a subset of small molecules that are candidates for triggering ANBs were screened in this study and a role of few of them (e.g. cAMP) was not yet tested genetically. Thus, either a random or candidate-based genetic screen is an option. However, due to strong maternal effects classical EMS mutagenesis screen might miss the candidates as it relies on zygotic recessive loss-of-function. In addition, recent RNAi screen revealed mostly well-known genes involved in DC and only a few novel ones[55]. Therefore, a screen for direct protein inactivation is a necessity.

To fully exclude Ca^{2+} as factorX, additional genetic analysis is necessary. Recently, a number of genetically encoded proteins sequestering cyclic-nucleotides and ions like Ca^{2+} were designed allowing to overcome potentially cytotoxic effects of the commonly used pharmacological inhibitors[159,160]. In particular, vertebrate parvalbumin over-expression in Drosophila neurons was used to sequester intracellular Ca^{2+} upon action potential induced Ca^{2+} influx[161]. Such a tool would allow addressing the role of Ca^{2+} during pulsed AS cell contractions. In addition, it could also circumvent wound-healing responses allowing more unambiguous interpretation of the effects caused by tissue tension release.

To further support ANB independence from MyoII, removal of myosin function with two or more perturbations would be beneficial. While genetically such an approach is not trivial, we are attempting to create deGradFP-mediated Sqh-GFP KO in an otherwise *zip* null mutant background. Alternatively, we are trying to improve the acuteness of MyoII inactivation by using CRY2-mediated protein sequestering or by engineering endogenous *zipper* alleles to create a temperature-sensitive form of Zipper (Fürst and Brunner, unpublished). Even though we show good evidence that ANB generation is tension-independent, addressing this further with the current standard approaches like laser-incisions might not be the perfect way as they involve a wound healing response. To clearly discriminate between the effects of tension release and wound healing, novel optogenetic tools will be necessary to induce tension release without triggering the wound healing responses. This idea is one of the driving forces for creating light-or-temperature inducible MyoII inactivation and is discussed further in Appendix 1.

Recent work by DeRenzis and colleagues revealed that the actin cortex of gastrulating *Drosophila* epidermis cells can be disassembled in a light-inducible manner using CRY2-CIB-

mediated de-phosphorylation of phosphoinositides[162]. Such a genetic approach would complement our data on GJ conductance changes in cells where the actin cortex was affected pharmacologically by latrunculinB and CK-666 injection. While genetically, the role of GJ is still not conclusively addressed, KO allele of *inx3* containing the attP landing site provides an invaluable tool for further modification of this GJ component. Simple tagging with fluorophores and expressed at endogenous levels, might already reveal critical information on the dynamics of these channels that were previously obscured by protein over-expression. Yet the key goal is to acutely remove GJ function in the AS tissue. While deGradFP does not appear to work well with transmembrane proteins, as shown for E-cadherin[68], different approaches like TIPI or nanobody-mediated mis-localization can be used to perturb GJ dynamics[73].

3.5. Summary of the key findings/hypotheses of Chapter 3

- Actin nucleation bursts (ANBs) in AS cells are generated independently from MyoII and tissue tension
- Previous cellular effects attributed to loss-of-tissue tension after laser ablation are most likely caused by early steps of wound healing induced by elicited Ca^{2+} influx and previous data interpretation is likely to be misleading.
- AS cells can contract and polymerize actin in a Ca^{2+}-dependent and a Ca^{2+}-independent manner
- Ca^{2+} and mechanically-gated ion channels (MCGs) can be excluded as the basic underlying mechanism of ANB generation
- Gap junctions (GJs) are possible candidates for coupling oscillating AS cells as GJ conductance depends on cortical actin tension in the AS tissue
- The generated knock-out (KO) alleles of *innexin-3*, containing an attP site, provide a new tool for the analysis of GJs

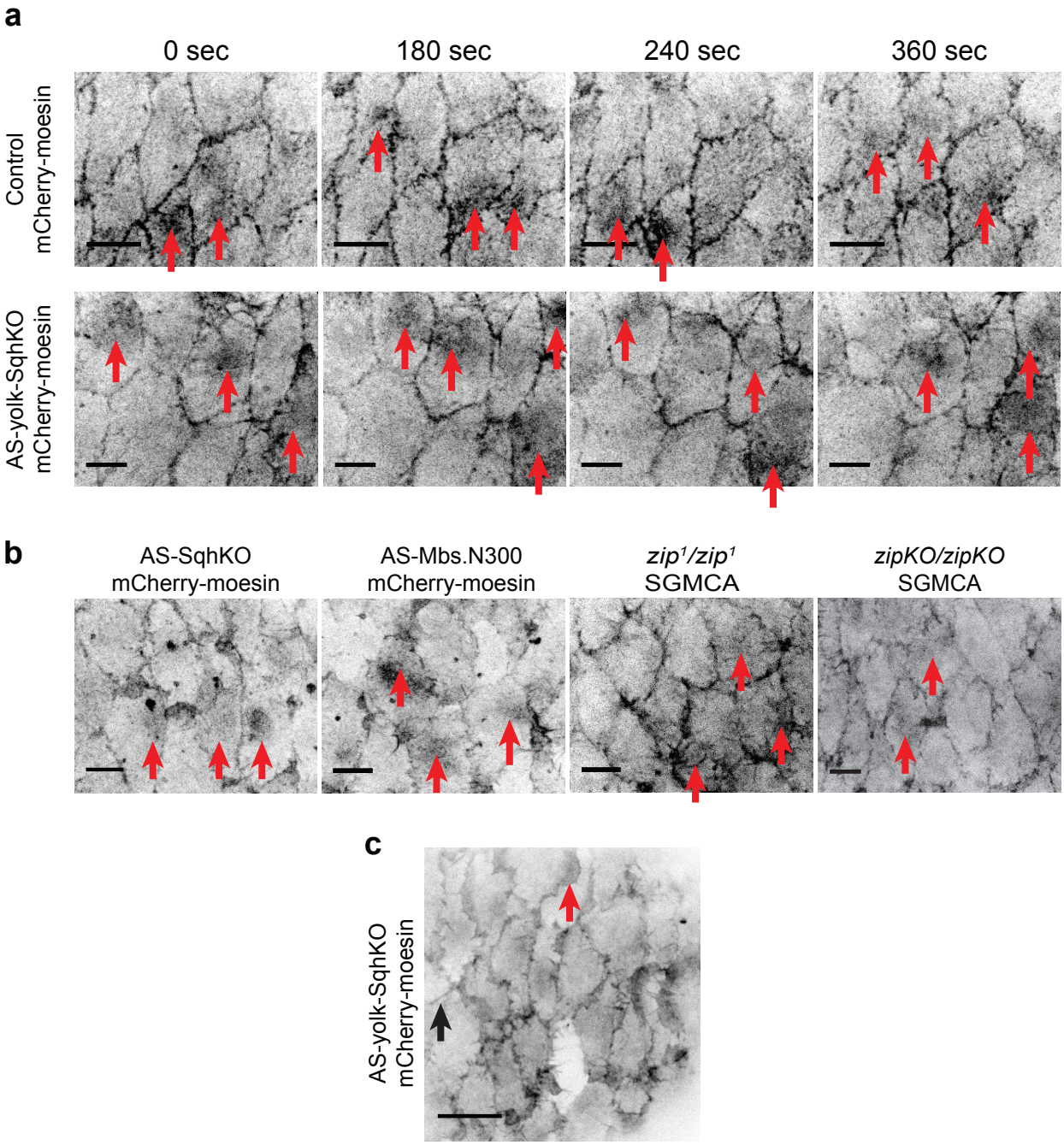

Figure 13. Actin nucleation bursts (ANBs) are present in AS cells after MyoII inactivation. (a) Selected movie frames showing ANBs (red arrows) in AS cells of control and AS-yolk-SqhKO embryos. mCherry-moesin labels F-actin. Scale bar: 10µm. **(b)** ANBs (red arrows) in AS cells where MyoII activity was perturbed by different means. From left to right: AS-SqhKO – deGradFP over-expression; AS-Mbs.N300 – over-expression of constitutively active MyoII phosphatase; zip^{1}/zip^{1} – embryos homozygous for the amorphic mutant allele of MyoII heavy chain Zip; zip^{KO}/zip^{KO} - embryos homozygous for the complete knock-out allele of Zip. mCherry-moesin or SGMCA (GFP-moesin) labels F-actin. Scale bar: 10µm. **(c)** F-actin structures such as filopodia (black arrow) and lamellipodia (red arrow) in AS cells of AS-yolk-SqhKO embryos. Scale bar: 20µm.

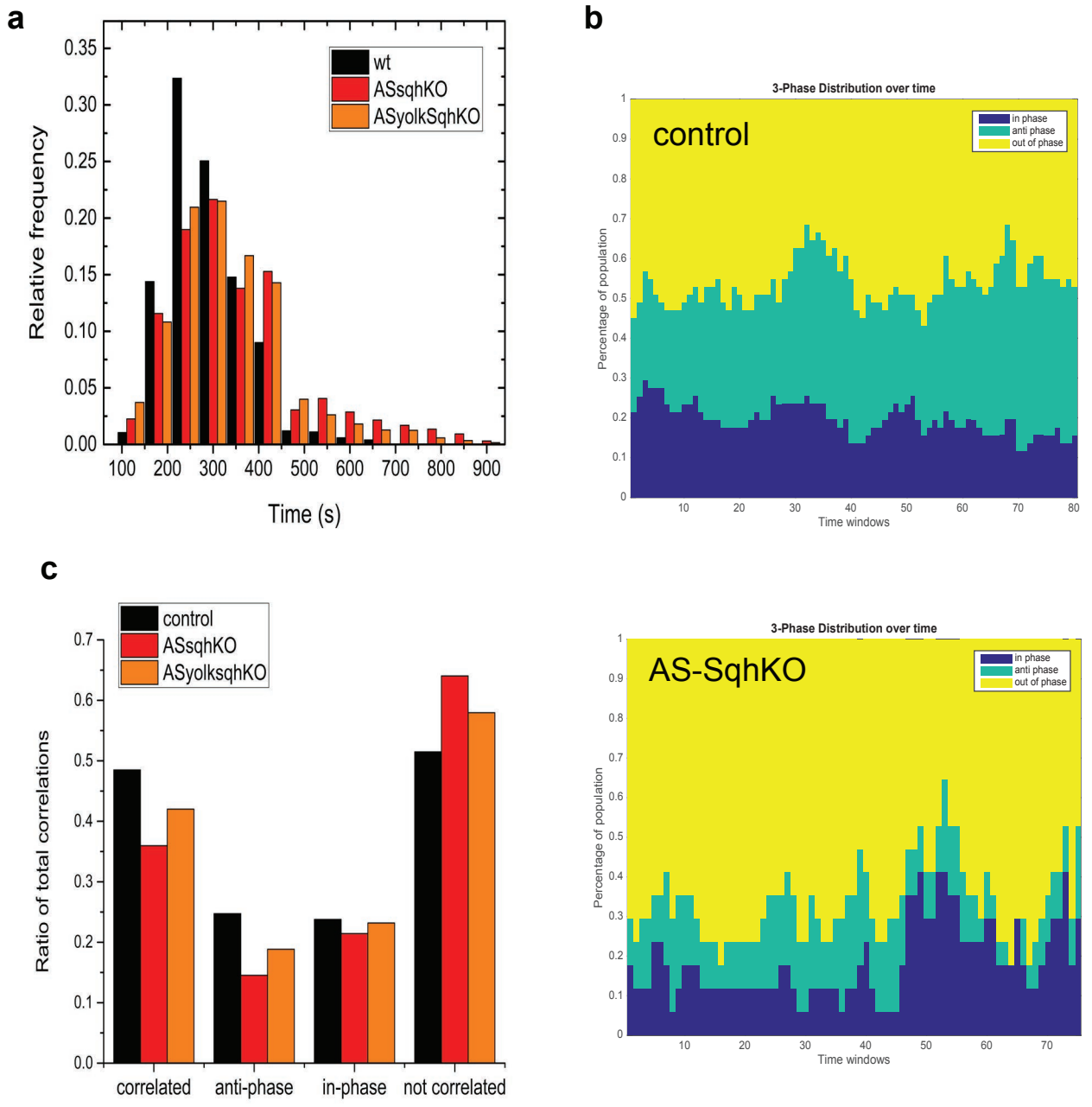

Figure 14. ANB behaviour is affected in MyoII-depleted AS cells. (a) Relative frequency histogram of ANB periods in control (black bars), AS-SqhKO (red bars) and AS-yolk-SqhKO (orange bars) embryos. Control: n=6389 periods in 72 cells from 3 embryos; AS-SqhKO: n=11386 periods in 106 cells from 5 embryos; AS-yolk-SqhKO: n=5709 periods in 90 cells from 4 embryos. **(b)** Examples of stacked histogram of cross-correlation functions (CCFs) between the ANBs in neighbouring AS cells in control (top) and AS-SqhKO (bottom) embryos. Bars show the percentage of neighbouring AS cells where ANBs are generated in-phase (dark blue), anti-phase (light blue) or out-of-phase (yellow). Control: n= 3723 CCFs from 53 unique neighbouring cell pairs from 1 embryo; AS-SqhKO: n=1156 CCFs from 17 unique neighbouring cell pairs from 1 embryo. Histograms provided by D. Dreher. **(c)** Histograms of average phase distribution of ANBs in the neighbouring AS cells in control (black bars), AS-SqhKO (red bars) and AS-yolk-SqhKO embryos. Correlated ANBs are the sum of anti-phase and in-phase correlations, not correlated ANBs are the remaining out-of-phase correlations. Control: n=13508 CCFs from 155 unique neighbouring cell pairs from 3 embryos; AS-SqhKO: n=22712 CCFs from 205 unique neighbouring cell pairs from 5 embryos; AS-yolk-SqhKO: n=11738 CCFs from 177 unique neighbouring cell pairs from 4 embryos.

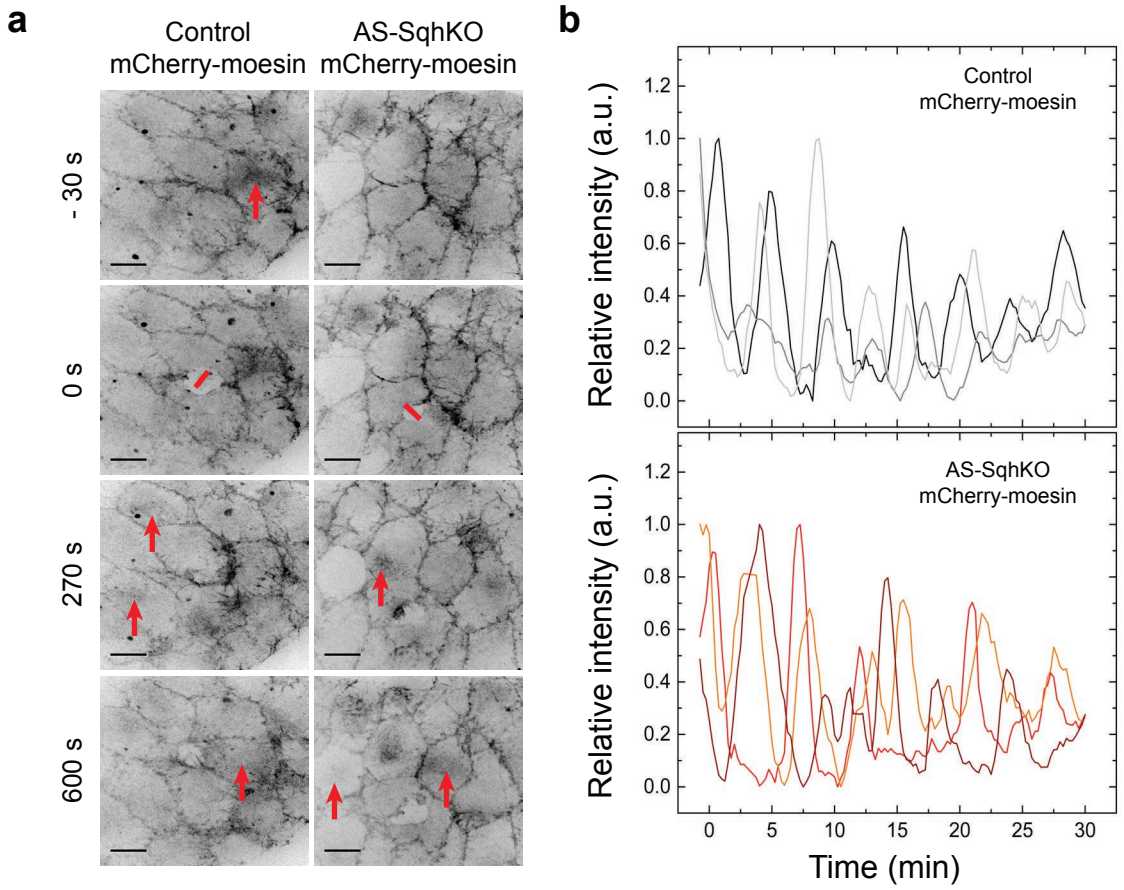

Figure 15. Generation of ANBs in AS cells is independent of tissue-tension. **(a)** Selected movie frames showing ANBs (red arrows) in AS cells after the laser incision (red line) in control and AS-SqhKO embryos. mCherry-moesin labels F-actin. 0s depicts first frame after the laser incision. Scale bar: 10µm. **(b)** Representative curves of normalized mCherry-moesin fluorescence intensities from (a) in the AS cells neighboring those where laser incision was performed. Control: 3 cells shown of 35 from 5 embryos; AS-SqhKO: 3 cells shown of 31 from 5 embryos.

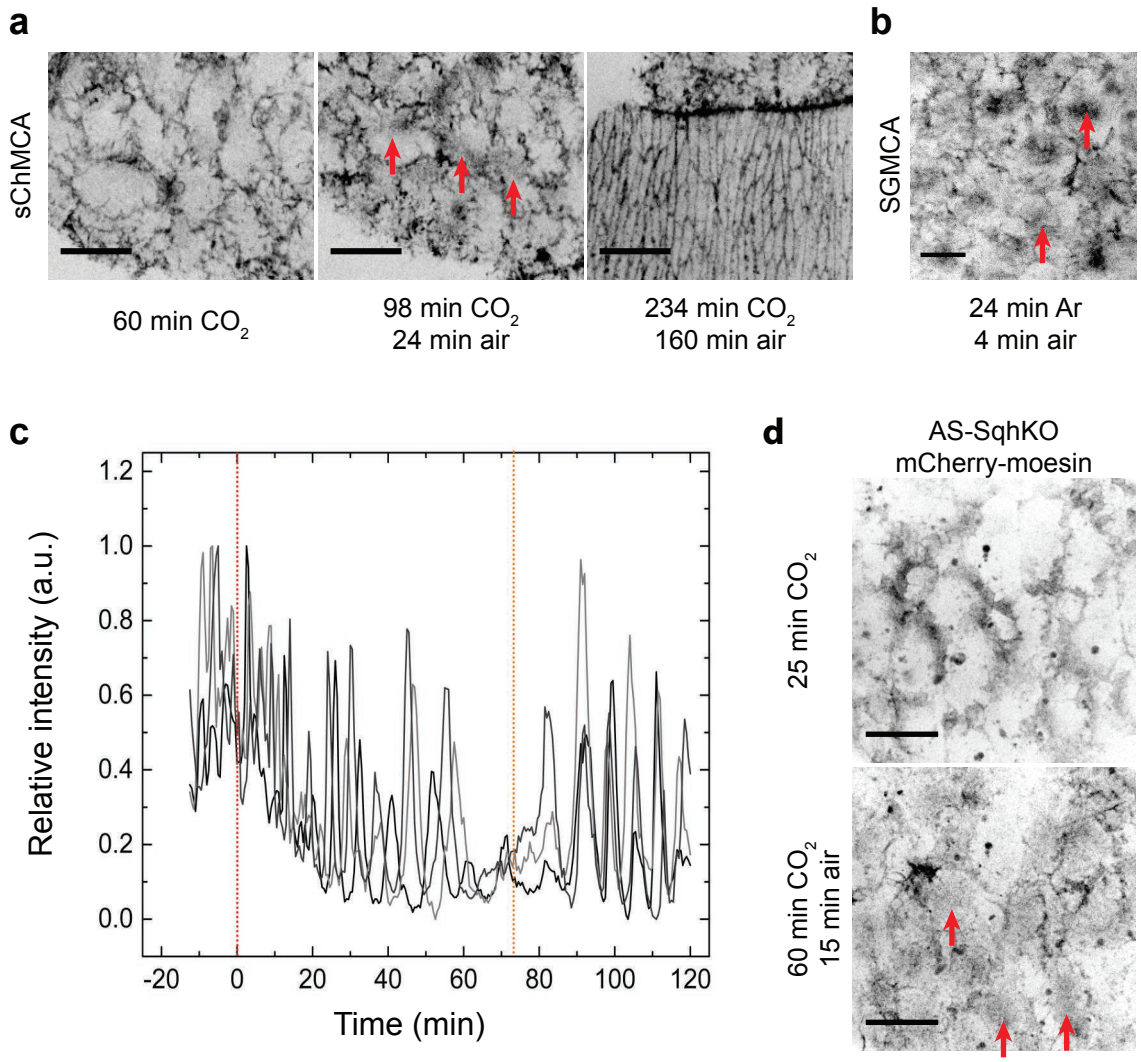

Figure 16. Anaesthesia of embryos eliminates ANBs in AS cells. (a) Selected movie frames showing AS cells during and after CO_2 anaesthesia. ANBs (red arrows) are absent in CO_2-anesthetized embryos, but re-appear after CO_2 is replaced with the normal air. Left frame - 60min after CO_2 was applied; middle frame - 24min after CO_2 was replaced with the normal air; right frame - 160min after CO_2 was replaced with the normal air. sChMCA (moesin-mCherry) labels F-actin. Scale bar: 20µm. **(b)** ANBs (red arrows) re-appear in the AS cells that recover from Argon anaesthesia. Frame depicts AS cells 4min after Argon was replaced with the normal air. SGMCA (GFP-moesin) labels F-actin. Scale bar: 10µm. **(c)** Representative curves of normalized fluorescence intensities from 3 AS cells (black to light grey) from (a). Red dashed line corresponds to CO_2 application, orange dashed line corresponds to CO_2 replacement with the normal air. 3 cells shown of 6 from 1 embryo. **(d)** Selected movie frames showing AS cells during and after CO_2 anesthesia in AS-SqhKO embryos. mCherry-moesin labels F-actin. ANBs (red arrows) are absent in CO_2-anesthetized embryos (top), but re-appear after CO_2 is replaced with the normal air (bottom).

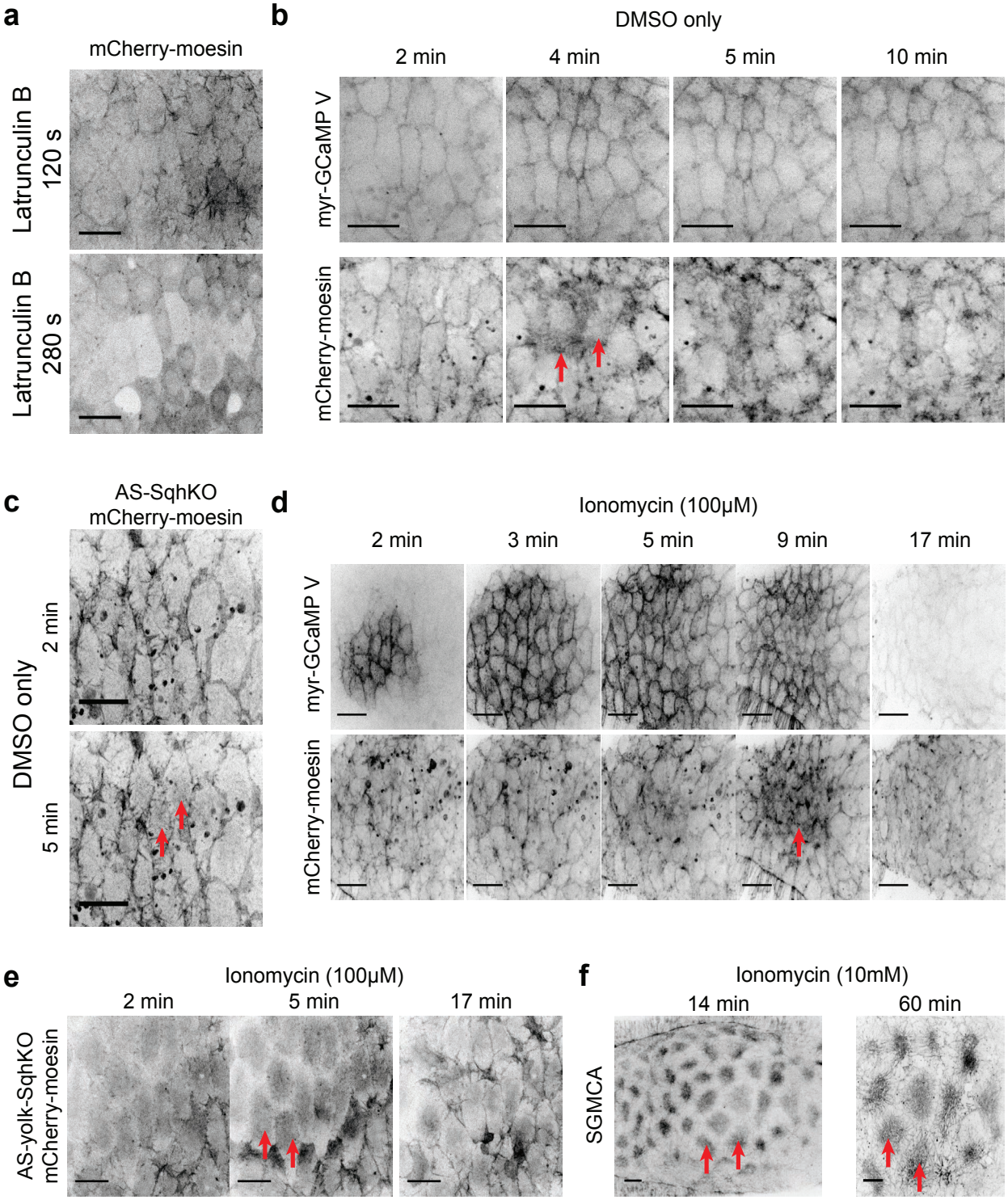
a
mCherry-moesin
Latrunculin B 120 s
Latrunculin B 280 s
b
DMSO only
2 min
4 min
5 min
10 min
myr-GCaMP V
mCherry-moesin
c
AS-SqhKO mCherry-moesin
DMSO only
2 min
5 min
d
Ionomycin (100μM)
2 min
3 min
5 min
9 min
17 min
myr-GCaMP V
mCherry-moesin
e
Ionomycin (100μM)
2 min
5 min
17 min
AS-yolk-SqhKO mCherry-moesin
f
Ionomycin (10mM)
14 min
60 min
SGMCA

Figure 17. AS cells can contract in Ca^{2+}-dependent and Ca^{2+}-independent manner. (a) Selected movie frames showing AS cells after latrunculin B (LatB) injection below them. Actin structures disappear after LatB treatment. Scale bar: 20μm. **(b)** Selected movie frames showing AS cells after DMSO injection below them. AS cells transiently contract (red arrows), but do so without any intracellular Ca^{2+} influx. Scale bar: 20μm. **(c)** Selected movie frames showing AS cells after DMSO injection below them in AS-SqhKO embryos. Actin transiently polymerizes in AS cells (red arrows). Scale bar: 20μm. **(d)** Selected movie frames showing AS cells after ionomycin injection below them. AS cells transiently contract (red arrows) after an intracellular Ca^{2+} influx. Scale bar: 20μm. **(e)** Selected movie frames showing AS cells after ionomycin (100μM) injection in AS-yolk-SqhKO embryos. Actin transiently polymerizes (red arrows) in AS cells. Scale bar: 20μm. **(f)** Selected movie frames showing AS cells after injection of high (10mM) ionomycin concentration. Actin polymerizes into thick bundles that do not dissolve. Scale bar: 10μm. F-actin is labelled with mCherry-moesin in **a-e** and with SGMCA (GFP-moesin) in **f**. Ca^{2+} is monitored by membrane-tethered myr-GCaMPV biosensor in **b** and **d**.

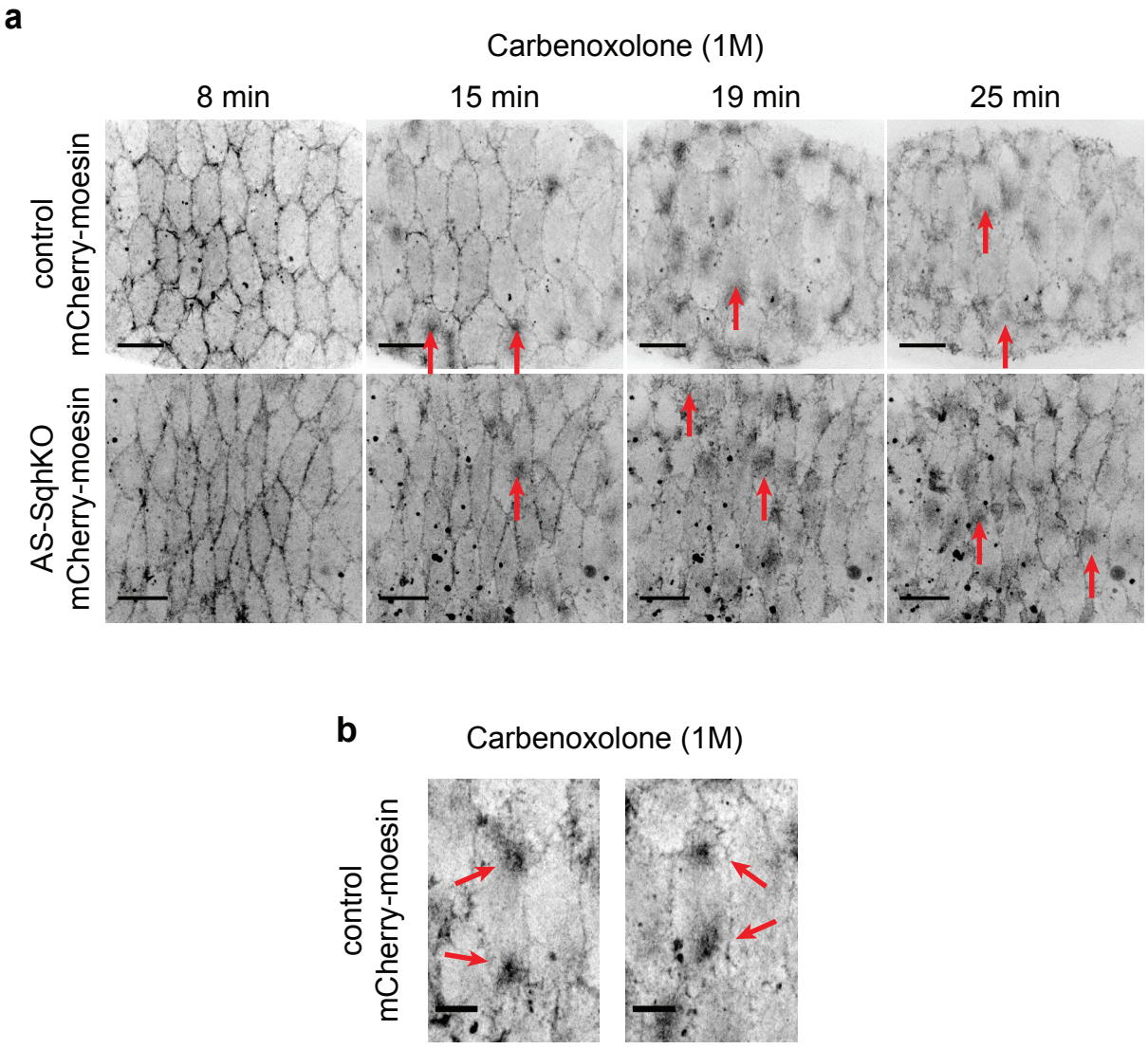

Figure 18. Gap junction inhibitor carbenoxolone transiently eliminates ANBs in AS cells. (a) Selected movie frames showing AS cells after carbenoxolone (Cbx) injection in control and AS-SqhKO embryos. ANBs (red arrows) disappear after the injection, but re-appear shortly after. Scale bar: 20 μm. **(b)** Magnified regions of single AS cells in control embryos where ANBs recover after Cbx injection. Two independent ANBs (red arrows) appear simultaneously in a single cell. Scale bar: 10μm. mCherry-moesin labels F-actin in a-b.

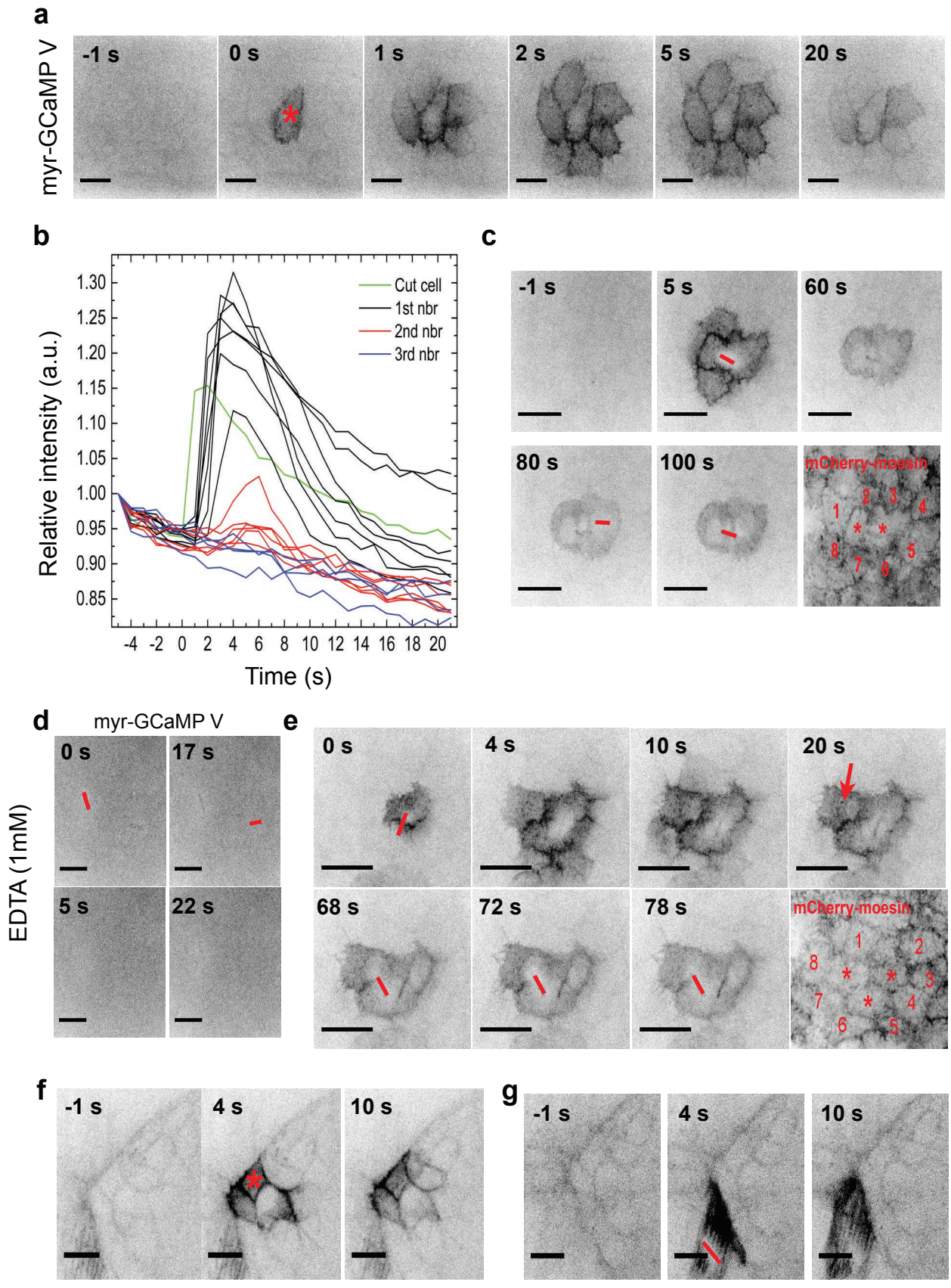
a
myr-GCaMP V
-1 s
0 s
1 s
2 s
5 s
20 s
b
Relative intensity (a.u.)
Time (s)
Cut cell
1st nbr
2nd nbr
3rd nbr
c
-1 s
5 s
60 s
80 s
100 s
mCherry-moesin
d
myr-GCaMP V
EDTA (1mM)
0 s
17 s
5 s
22 s
e
0 s
4 s
10 s
20 s
68 s
72 s
78 s
mCherry-moesin
f
-1 s
4 s
10 s
g
-1 s
4 s
10 s

Figure 19. Laser incision induces intracellular Ca^{2+} wave that spreads into the neighbouring AS cells. (a) Selected movie frames showing appearance and dissolution of intracellular Ca^{2+} wave that originates from single AS cell where laser incision (red star) was performed. Scale bar: 10µm. **(b)** Representative curves of normalized fluorescence intensities of myr-GCaMPV biosensor from AS tissue region, where laser incision was performed. Green shows the cell, where laser incision was performed; black shows AS cells that are 1^{st}, or immediate neighbours; red show AS cells that are 2^{nd} neighbours; blue shows AS cells that are 3^{rd}, or distant neighbours. **(c)** Selected movie frames showing that repeated laser incisions (red line) in the same AS cells (red stars) do not elicit Ca^{2+} wave in the neighbours (cells 1-8). mCherry-moesin labels F-actin. Scale bar: 10µm. **(d)** Selected movie frames showing that laser incisions (red lines) do not elicit Ca^{2+} wave in the embryos, where EDTA was injected into the perivitelline space. Scale bar: 10µm. **(e)** Selected movie frames showing that laser incision (red line, 0s) between two AS cells can cause neighbouring cell to sustain high intracellular Ca^{2+} levels (red arrow, 20s). Subsequent laser incision (red line, 68s) of such neighbouring cell fails to elicit Ca^{2+} wave. mCherry-moesin labels F-actin to show laser ablated cells (red stars) and the neighbouring AS cells (cells 1-8). Scale bar: 10µm. **(f)** Selected movie frames showing that Ca^{2+} wave elicited after laser incision in the AS cell next to the epidermis do not spread into the epidermis. Scale bar: 10µm. **(g)** Selected movie frames showing that Ca^{2+} wave elicited after laser incision in the epidermis cells close to the AS tissue do not spread into the AS cells. Scale bar: 10µm. Ca^{2+} is monitored by membrane-tethered myr-GCaMPV biosensor in **a-g**.

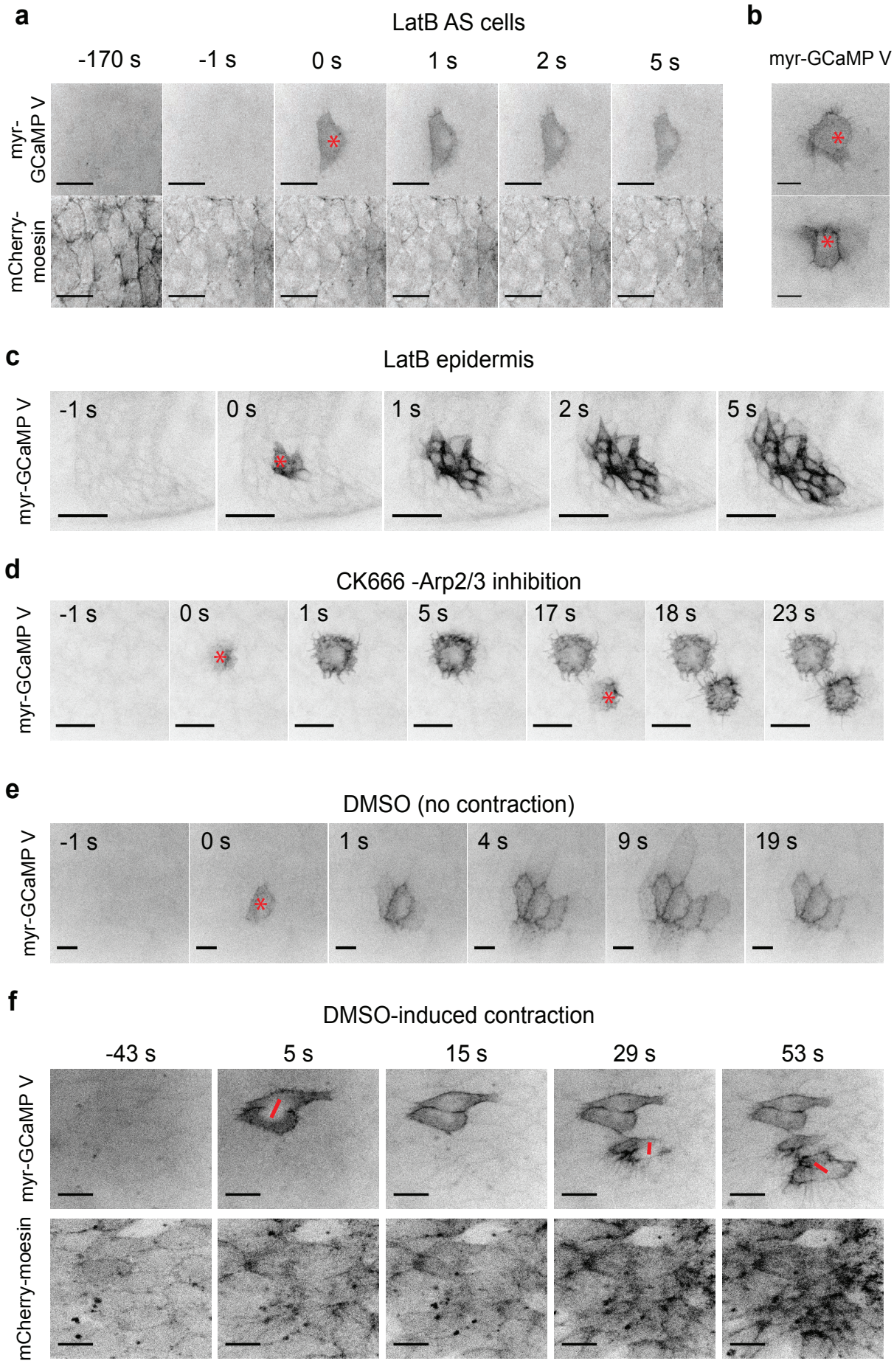
a
LatB AS cells
-170 s
-1 s
0 s
1 s
2 s
5 s
myr-GCaMP V
mCherry-moesin
b
myr-GCaMP V
c
LatB epidermis
myr-GCaMP V
-1 s
0 s
1 s
2 s
5 s
d
CK666 -Arp2/3 inhibition
myr-GCaMP V
-1 s
0 s
1 s
5 s
17 s
18 s
23 s
e
DMSO (no contraction)
myr-GCaMP V
-1 s
0 s
1 s
4 s
9 s
19 s
f
DMSO-induced contraction
-43 s
5 s
15 s
29 s
53 s
myr-GCaMP V
mCherry-moesin

Figure 20. Perturbation of mechanical AS cell properties affects permeability of gap junctions. (a) Selected movie frames showing Ca^{2+} flash after the laser incision (red star) in LatB-treated AS cells. The elicited Ca^{2+} flash is limited to the incised cell. 0s depicts the time-point of laser incision. Scale bar: 10µm. **(b)** Selected examples showing that Ca^{2+} wave spreads marginally into the neighbours after the laser incision (red star) in LatB-treated AS cells. Scale bar: 10µm. **(c)** Selected movie frames showing Ca^{2+} wave in LatB-treated epidermis cells. 0s depicts the time-point of laser incision. Scale bar: 20µm. **(d)** Selected movie frames showing the laser incision (red star) in the AS cell that does not contract upon DMSO injection. The elicited Ca^{2+} wave spreads to the neighbouring cells. 0s depicts the time-point of laser incision. Scale bar: 10µm. **(e)** Selected movie frames showing laser incisions (red lines) in AS cells that contract as a result of DMSO injection. The elicited Ca^{2+} flashes are limited to the incised cells. 0s is the reference of the first laser incision. Scale bar: 10µm. Ca^{2+} is monitored by membrane-tethered myr-GCaMPV biosensor in **a-f**, mCherry-moesin labels F-actin in **a, e** and **f**.

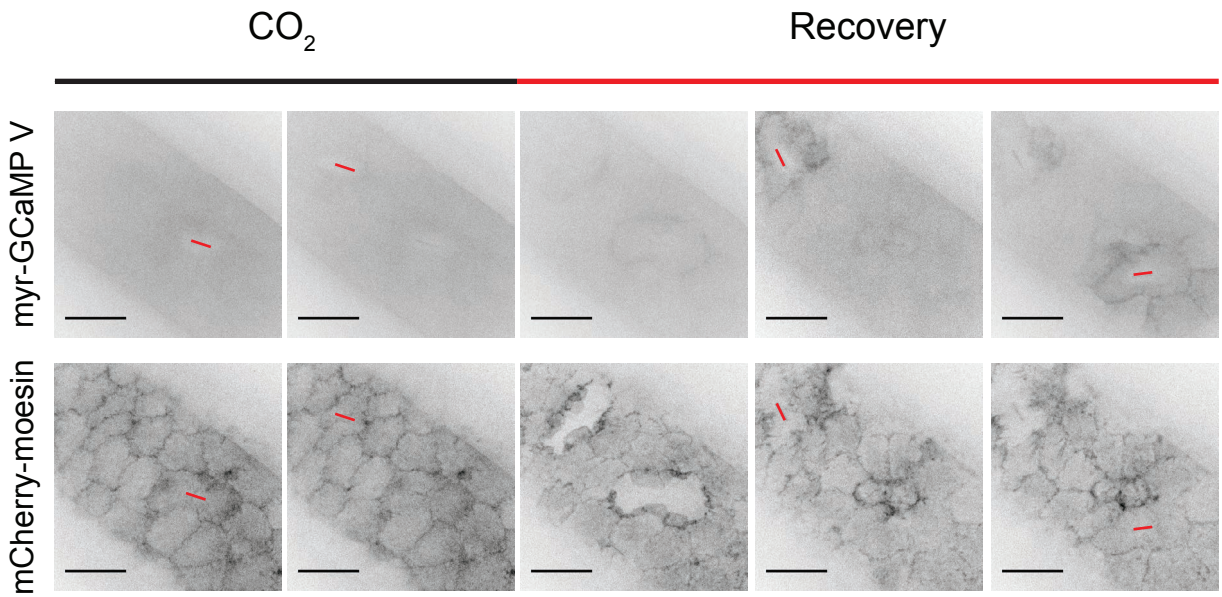

Figure 21. Intracellular Ca^{2+} waves are inhibited in CO2-anesthetized embryos. Selected movie frames showing the laser incisions (red lines) in the AS cells from embryos anesthetized and recovering from CO_2 anaesthesia. In anesthetized embryos Ca^{2+} flashes do not appear, whereas in recovering embryos they appear and spread into the neighbours. Ca^{2+} is monitored with membrane tethered myr-GCaMP V biosensor, mCherry-moesin labels F-actin. Scale bar: 20µm.

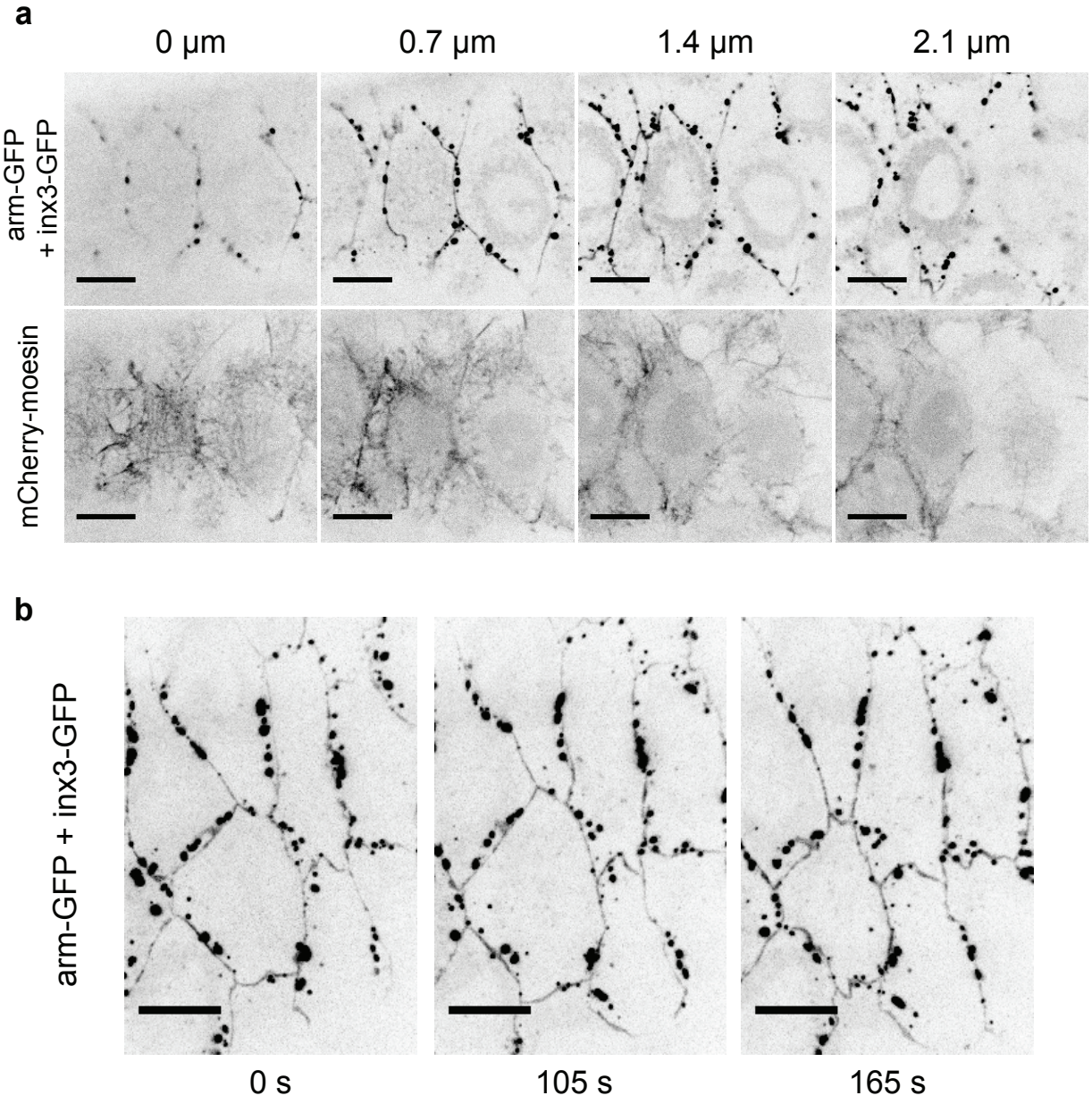

Figure 22. Gap junctions are displaced during the apical AS cell surface contractions. (a) Selected single planes of a Z stack showing the position of gap junctions (GJs) relative to the adherens junctions (AJs). Inx3-GFP labels GJs that localize to punctae below the apical AS cell surface. Arm-GFP labels AJs, mCherry-moesin labels F-actin. Scale bar: 10µm. **(b)** Selected movie frames showing movement of GJs with respect to the AJs during the apical AS cell surface contractions. Inx3-GFP labels GJs, arm-GFP labels AJs. Scale bar: 10µm. **(c)** Localization of GJs is not affected in homozygous *zip*^{1}/*zip*^{1} MyoII mutant embryos. Inx3-GFP labels GJs. Scale bar: 10µm.

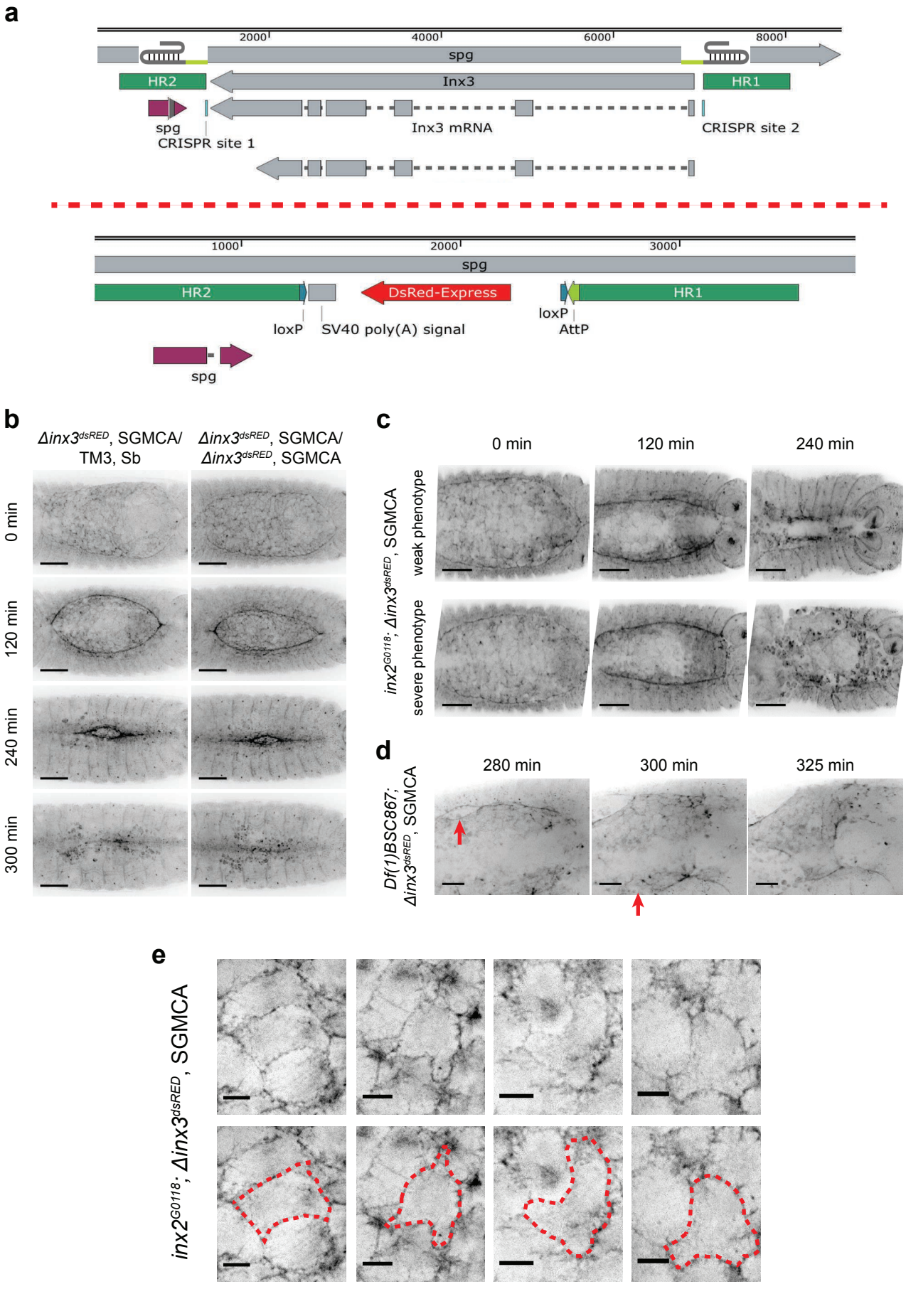
a
2000
4000
6000
8000
spg
HR2
Inx3
HR1
spg
CRISPR site 1
Inx3 mRNA
CRISPR site 2
1000
2000
3000
spg
HR2
DsRed-Express
HR1
loxP
SV40 poly(A) signal
loxP
AttP
spg
b
Δinx3dsRED, SGMCA/ TM3, Sb
Δinx3dsRED, SGMCA/ Δinx3dsRED, SGMCA
0 min
120 min
240 min
300 min
c
0 min
120 min
240 min
inx2G0118; Δinx3dsRED, SGMCA
weak phenotype
severe phenotype
d
280 min
300 min
325 min
Df(1)BSC867; Δinx3dsRED, SGMCA
e
inx2G0118; Δinx3dsRED, SGMCA

Figure 23. Loss of gap junctions leads to pleiotropic phenotypes during DC. (a) Schematic illustration of CRISPR/Cas9-mediated generation of *innexin-3* (*inx3*) knock-out (KO) allele. Top: genomic region of *inx3*. Bottom: engineered $inx3^{dsRED}$ KO allele. CRISPR sites 1 and 2 outside the *inx3* ORF were used to guide Cas9 nuclease. Donor plasmid containing homology regions HR1 and HR2 as well as attP-loxP-dsRED-loxP cassette were provided to guide DNA repair machinery resulting in $inx3^{dsRED}$ allele. **(b)** Selected movie frames showing DC in $inx3^{dsRED}$ heterozygous and $inx3^{dsRED}$/ $inx3^{dsRED}$ homozygous embryos. SGMCA is labels F-actin. 0 min depicts the end of germ-band retraction. Scale bar: 50µm. **(c)** Selected movie frames showing DC in double $inx2^{G0118}/inx2^{G0118}$, $inx3^{dsRED}/inx3^{dsRED}$ homozygous embryos. Embryos with weakly penetrant phenotypes (top panels) complete DC with minor defects. Embryos with severely penetrant phenotypes (bottom panels) fail to seal the epidermis and rupture. SGMCA labels F-actin. 0 min depicts the end of germ-band retraction. Scale bar: 50µm. **(d)** Selected movie frames showing DC in double *Df(1)BSC867/ Df(1)BSC867*, $inx3^{dsRED}/inx3^{dsRED}$ homozygous embryos. *Df(1)BSC867* deletion covers genomic region containing *inx1*, *inx2* and *boudin (bou).* DC fails in such embryos due to multiple ruptures between the AS tissue and epidermis (red arrows). SGMCA labels F-actin. 280min depicts the time after the end of germ-band retraction. Scale bar: 20µm. **(e)** Examples of severely deformed AS cells (red dashed lines) in double $inx2^{G0118}/inx2^{G0118}$, $inx3^{dsRED}/inx3^{dsRED}$ mutant embryos. Scale bar: 10µm.

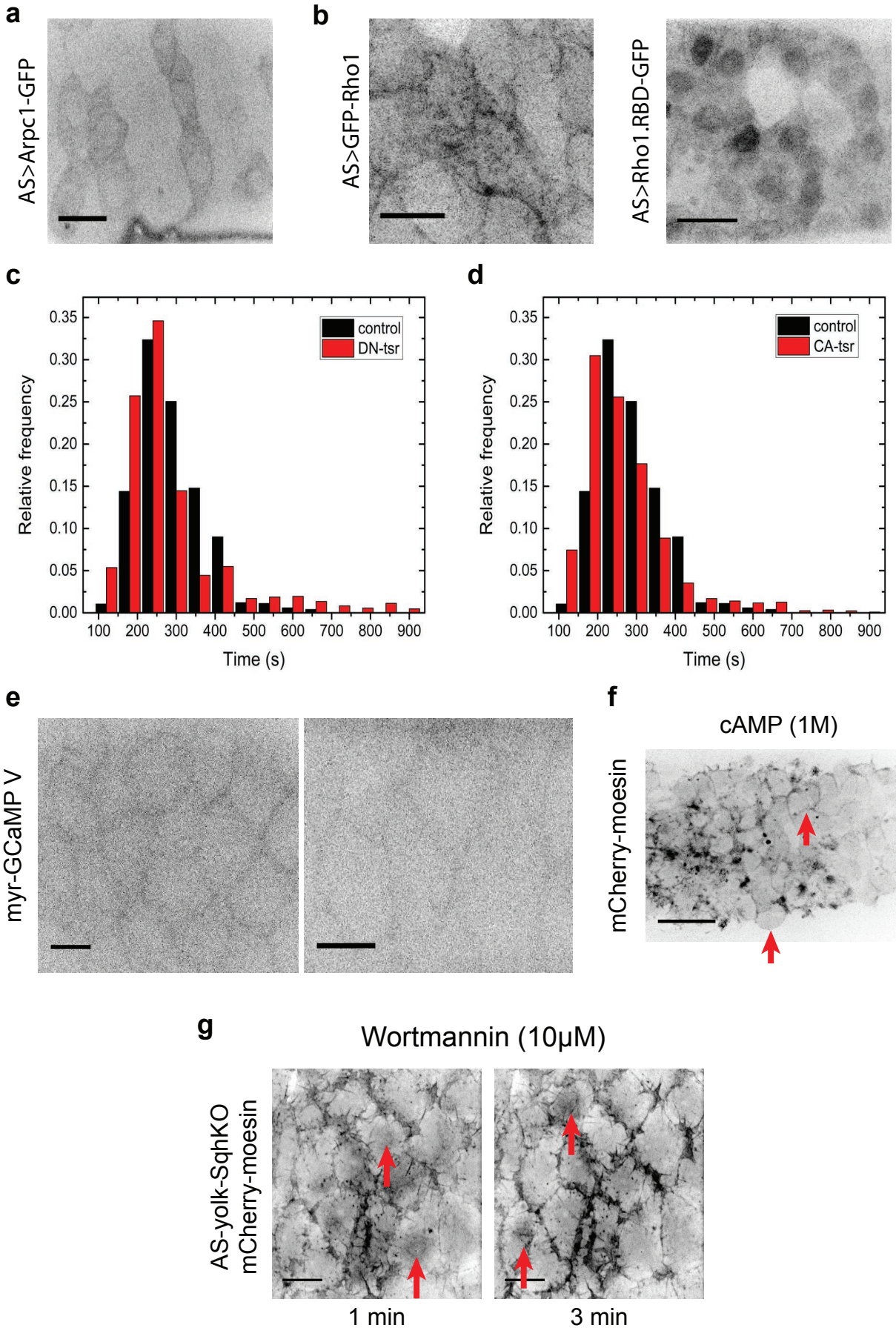
a
AS>Arpc1-GFP
b
AS>GFP-Rho1
AS>Rho1.RBD-GFP
c
Relative frequency
0.35
0.30
0.25
0.20
0.15
0.10
0.05
0.00
100 200 300 400 500 600 700 800 900
Time (s)
control
DN-tsr
d
Relative frequency
0.35
0.30
0.25
0.20
0.15
0.10
0.05
0.00
100 200 300 400 500 600 700 800 900
Time (s)
control
CA-tsr
e
myr-GCaMP V
f
cAMP (1M)
mCherry-moesin
g
Wortmannin (10μM)
AS-yolk-SqhKO
mCherry-moesin
1 min
3 min

Figure 24. Preliminary candidate screening for potential ANB trigger in AS cells. (a) Region of AS cells expressing GTP-tagged subunit of Arp2/3 (Arpc1 in *Drosophila*). Scale bar: 10µm. **(b)** Left: region of AS cells expressing GFP-tagged Rho1 small GTPase. Increased signal intensity (red arrow) is detected in some AS cells. Scale bar: 10µm. Right: region of AS cells expressing GFP-tagged biosensor (Rho1.RBD) for Rho1 small GTPase activity. Besides high nuclear fluorescence intensity, no obvious increased signal intensity is detected. Scale bar: 20µm. **(c)** Relative frequency histogram of ANB periods in control embryos (black bars) and embryos, expressing dominant-negative form of F-actin-severing protein cofillin (DN-tsr in *Drosophila*). Control: n=6389 periods in 72 cells from 3 embryos; DN-tsr: n=5549 periods in 65 cells from 4 embryos. **(d)** Relative frequency histogram of ANB periods in control embryos (black bars) and embryos, expressing constitutively active form of cofillin (CA-tsr). Control: n=6389 periods in 72 cells from 3 embryos; CA-tsr: n=2294 periods in 25 cells from 2 embryos. **(e)** Two examples of AS tissue regions expressing membrane-tethered Ca^{2+} biosensor myr-GCaMPV. No obvious differences in fluorescence intensity are detected in AS cells. Scale bar: 10µm. **(f)** Region of AS cells 4min after cAMP injection into the embryo. Membrane bleb-like structures (red arrows) appear in the cells. mCherry-moesin labels F-actin. Scale bar: 20µm. **(g)** Region of AS cells in AS-yolk-SqhKO embryos 1 and 3 min after the injection PI3-kinase inhibitor wortmannin (1mM) into the embryos. ANBs still appear in the AS cells (red arrows). mCherry-moesin labels F-actin. Scale bar: 20µm.

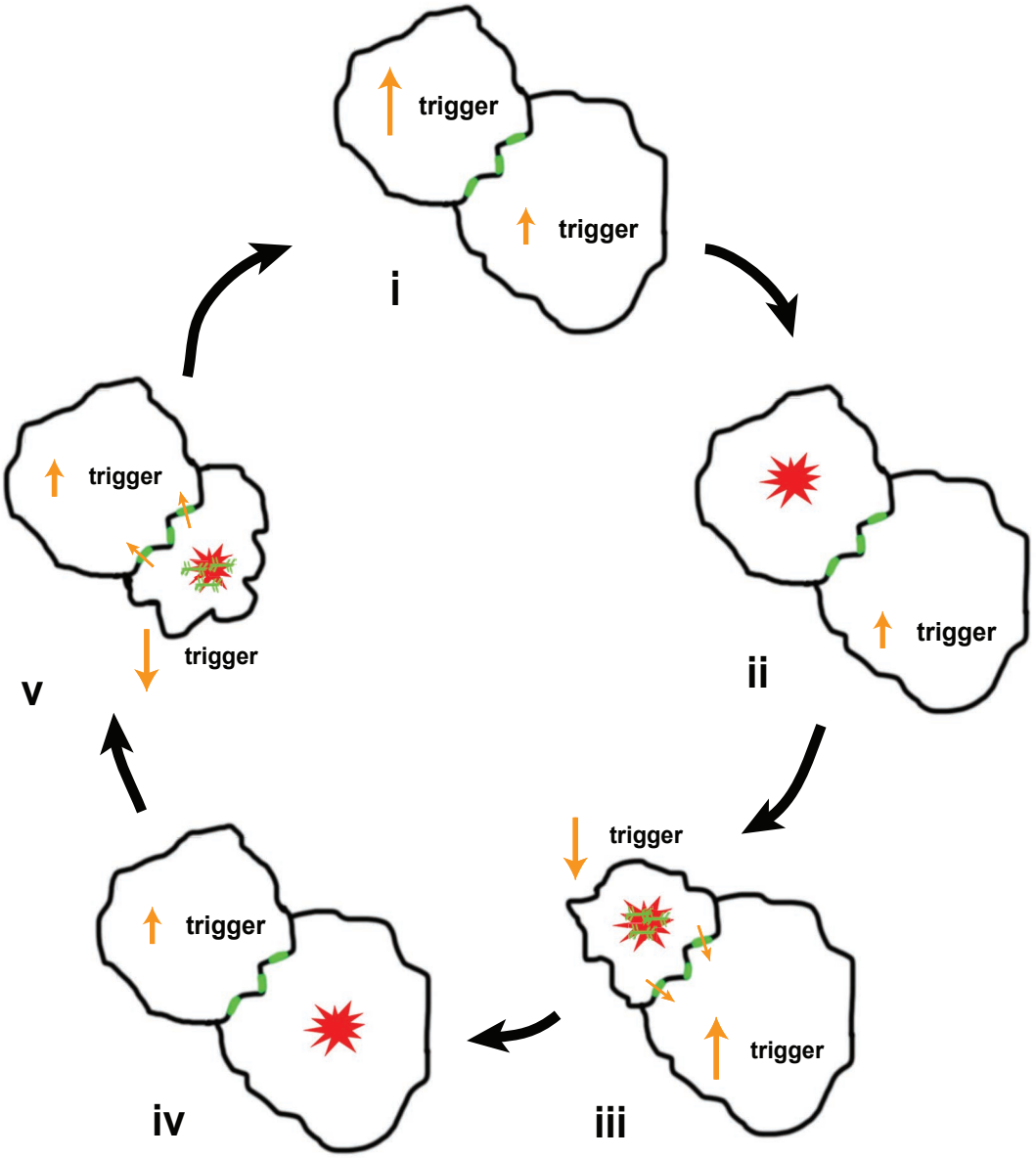

Figure 25. Proposed working model of apical cell surface contractions in the two AS cells. (i) Cell autonomous oscillating ANB trigger increases at differing rates in the two cells (yellow arrows). **(ii)** Once critical trigger concentration is reached, ANB is formed in the cell (red star). **(iii)** MyoII (green filaments) then docks onto the ANB and leads to apical area contraction. As a result ANB trigger is actively pushed or passively diffuses via the gap junctions (green lines) to the neighbouring cell; **(iv)** Transport via gap junctions speeds up ANB trigger accumulation in the neighbouring cell and leads to ANB formation; **(v)** MyoII then docks on the ANB in the neighbouring cell, contracts its apical cell area and the cycle continues.

Chapter 4. Role of decapentaplegic (Dpp) in controlling apical and junctional MyoII pools in AS cells

This chapter consists of two major sections each suitable for a part of the manuscript.

Pasakarnis, L., Atzeni, F., Frei, E., Aegerter, C., Brunner, D.

LP and DB conceived and planned the experiments; LP performed the experiments; LP and EF generated fly strains used in the study; FA and CA created *in silico* computational model; LP and DB analysed the data and wrote the manuscript.

4.1. Introduction

4.1.1. Emerging themes of cell apical constriction

Tissue morphogenesis is driven by collective cell shape changes. Cell deformations that occur within an epithelium monolayer can lead to a variety of shapes, forms and folds. Apical cell constriction is one such fundamental cell shape change that is exploited numerous times and across species during the embryogenesis. In chapter 2, we showed that previously described apical constriction of AS cells is the only force that is sufficient to complete DC on its own. Live imaging of AS tissue revealed that cells do not reduce their apical surface continuously, but do so in a pulsed manner[36,39] (also see Chapter 3). Similarly, pulsed apical constriction also drives other invagination events in *Drosophila* mesoderm and *C. elegans* ventral endoderm[101,163].

In different model systems and species, apical constriction can have differing characteristics, but common themes are emerging[107,155]. First, the mechanical force is produced via acto-myosin (AM) contractility, which can be pulsatile, continuous or can flow through the cell surface. Second, the direction of AM forces can be isotropic or anisotropic to allow constriction according to the body plan. Third, for AM contractility to result in cell shape changes, it needs to be coupled to adhesion complexes at the cell surface. Fourth and most importantly, such coupling between cells allows force transmission throughout the tissue, making apical constriction a collective process. Finally, due to a transient nature of pulsatile AM activity, any cell deformation needs to be stabilized in order to result in the net change over time.

During *D. melanogaster* gastrulation, coordinated apical constriction of mesodermal cells drives the invagination of the tissue[101]. Similar to other model systems, observed cell shape changes are triggered by coalescing AM foci at the apical surface[101,164]. Such AM foci are dynamic and with every cycle move toward the center of cell apical surface. This results in

central-ward directed AM force, which translates into apical constriction due to the inward movement of the apical adherens junctions. The transient apical pulses are stabilized by maintaining higher levels of MyoII at the apical cell surface after every contraction[101]. AM coupling to adherens junctions also allow apical MyoII organization into a supra-cellular system that connects every cell in the tissue along the anterior-posterior axis of the embryo[101,165]. Similarly, endoderm ingression during *C. elegans* gastrulation is triggered by isotropic and central-ward directed AM flows at the cell apex[163]. However, these pulsatile AM flows do not produce significant cell deformation initially, suggesting a lack of coupling of AM network to the cell junctions. Only after several cycles the force exerted by AM is sufficient to induce a stepwise reduction of the apical cell area[163].

Studies of neural tube formation in vertebrates suggested that, in contrast to *Drosophila* gastrulation, force is produced by the contraction of circumferential AM bundles underlying the adherens junctions[166–168]. A recent *in vivo* study in several other epithelial tissues confirmed that circumferential AM bundles organize into sarcomere-like structures similarly to muscle cells[169]. MyoII activity in such bundles reduces the distance between the sarcomeric repeats by pulling antiparallel F-actin together. This is analogous to driving a purse-string-like contraction, but at a single junction level. The coordination across the whole tissue is achieved by a repeated pattern of sarcomere-like structures that are aligned across the cell boundary[169]. Importantly, studies in cell culture revealed that even AM bundles without a clear sarcomere arrangement also generate tension around the apical circumference and thus can drive apical constriction[170–172]. Therefore, two different AM structures alone – linear bundles or apical networks – can generate sufficient force for apical cell constriction.

In AS tissue, both of these AM populations (apico-medial and junctional) are observed and, therefore, can potentially work together to contribute for DC. While the apical AM foci appears during the retracting germ-band stage, junctional MyoII accumulates only throughout the DC. Such appearance correlates with the straightening of adherens junctions that are initially wiggly[39]. Hence, it is proposed that junctional MyoII population could act as a clutch that stabilizes the contraction generated by the apico-medial AM network. Mechanistically, this would be very similar to the germ-band cell intercalation, where pulsatile apical AM foci shorten vertical D/V junctions and junctional AM stabilizes such transient shortening. Over time AS cells also accumulate apico-medial AM to form a continuous meshwork[38,39,41]. Such accumulation leads to increased stiffness of the tissue[98]. Similar to *Drosophila* gastrulation, an increase in apical AM and tissue stiffness would not require a junctional ratchet. Instead, a transition from relatively loose to a supra-cellular AM network throughout the cells would be

enough to power induce collective apical constriction. Superficial tissue strain analysis supported a transition to such a supra-cellular AM network during the last phases of DC[37,98].

Different biochemical signalling modules are being discovered which govern transitions from pulsatile to sustained apical constriction. Even though most of them have a variety of upstream signals, eventually these lead to MyoII activation via Rho/Rok-induced phosphorylation of MyoII regulatory light chain (RLC)[11]. During *Drosophila* gastrulation transcription factors Twist and Snail play a crucial role in instructing AM accumulation at the apical cell cortex. In the absence of Twist, AM no longer persists at the cell apex and supra-cellular meshwork formation is disrupted[164]. Recently, it was demonstrated that a G-protein-coupled receptor (GPCR), Smog, acting downstream of Twist, modulates Rho recruitment at the apical cell surface[173]. Lack of either Smog of G-protein complexes disrupts both apical constriction and cell intercalation. Similarly, Rho and Rho-activating proteins play important roles during DC, but their effects have not been disentangled due to lack of tissue specificity and chronic effects of zygotic mutants. In contrast to GPCRs, it was suggested that, in AS cells, the apical protein complexes aPKC/baz/Par-6 regulate apical MyoII accumulation[38,41]. While baz promotes AM foci assembly, aPKC antagonizes it, thus modifying the duration and time intervals between the assemblies. Apical accumulation of MyoII over time correlates with aPKC/baz apical accumulation. However, the evidence is weak since zygotic mutants fail to produce noticeable defects and the effects caused by over-expressing aPKC or baz are marginal. During vertebrate neurulation and *Drosophila* germ-band extension (GBE) another set of cues, planar cell polarity (PCP) components, play an instructive role confining the apical constriction or directed junctional shrinkage, respectively[174]. Therefore, throughout the embryonic development, several different ways of apically constricting cells exist and a single unifying way cannot be applied to all model systems.

Using a genetic framework based on recovery from deGradFP MyoII inactivation, we aim to delineate the different MyoII populations and their role in AS apical constriction during DC. We show that AS cells can apically constrict without the need of forces provided by the apico-medial MyoII pool. However, such constriction is not efficient to complete DC as cell-cell junctions attain different AM contractility rates. As a consequence stronger cell-cell junctions rip the weaker ones open. We further support these observations by using computational modelling and suggest that the pulsing apico-medial MyoII pool is necessary to equilibrate cellular noise in junction strengths.

4.1.2. Role of Decapentaplegic signalling during DC

Mechanical cues act at various levels to drive cellular processes throughout embryogenesis. Yet at the very top of embryonic development lie complex gene regulatory networks and signalling pathways. For example, the aforementioned Twist and Snail transcription factors instruct proper *Drosophila* gastrulation[164]. JAK/STAT signalling has been shown to inhibit apical MyoII accumulation during intercalating cells in the germ-band, so that AM flows could be directed towards the shrinking vertical junctions[102]. During vertebrate neural tube formation, Wnt signalling pathway is predominant in controlling apical constriction[175,176]. In summary, all these regulatory gene networks lead to downstream control of AM components or network contractility. DC is another good example of close interplay between the genetic and mechanical control of morphogenetic process.

DC is controlled by two evolutionary conserved signalling pathways: the stress-induced c-Jun N-terminal kinase (JNK) and morphogen Decapentaplegic (Dpp) pathways. Classical embryonic mutants for either JNK or Dpp pathway components DC fail to seal dorsally leading to a dorsal-open phenotype[29,30,33]. Early DC studies showed that Dpp is an effector of JNK signalling in the epidermis[30,31,177]. Consistently, the ectopic expression of a constitutively active form of the Dpp receptor thick-veins (Tkv) rescues the lack of JNK signalling[30]. In the epidermis, the downstream targets of Dpp were shown to be the small GTP-ases Cdc42 and Rho[33], thus leading to the formation of AMC and filopodia in the LE. Recently, it was proposed that Dpp and JNK are intertwined in a feed-forward loop that controls differentiation of LE cells[178]. The authors argued that during DC, JNK provides positional information of the LE and Dpp ensures that the cells interpret such information robustly. Thus, instead of conferring positional information itself, Dpp signalling acts as a filter for unwanted JNK activity[178]. Additional evidence for a role of Dpp in DC robustness was given by another study where authors suggest that DPP signalling protects epidermis cells from JNK-induced apoptosis[179].

DPP is a secreted morphogen and *Drosophila* homologue of bone morphogenetic factor (BMP) family of proteins in higher organisms including mammals[180]. Dpp/BMP signalling pathway is mostly studied in the context of morphogen gradients that provide positional information for the cells within a tissue. Two classical examples of Dpp-mediated tissue patterning are the imaginal discs of Drosophila and the neural tube of vertebrates. In the former case, cells along the anterior-posterior (AP) boundary of wing imaginal dick secrete Dpp, which is received by the cell across the wing pouch[181]. Besides patterning the wing imaginal

disc, Dpp also stimulates cell proliferation[182]. Similarly, in the neural tube, BMPs are secreted from the roof plate and induce *Hox* gene transcription in the receiving cells[183,184]. Additionally, BMPs confer apico-basal cell polarity for the neuronal precursor cells[183,184]. Together with another morphogen, Sonic Hedgehog (Shh), emanating from the floor plate, BMPs create incredibly precise layers of different cell identities along the cross-section of neural tube[183].

Dpp signalling network is very intricate and far from being completely disentangled. Nevertheless, it can be summarized as follows[182]. In the "off" state of Dpp signalling, levels of transcriptional repressor Brinker (*brk*) are high in the cells. This suppresses most of Dpp target genes. When the morphogen Dpp reaches a cell, it binds and cross-links two surface receptors - type I receptor Ykv and type II receptor Punt (Pnt). These receptors are tyrosine kinases and are homologues of mammalian TGBF-β membrane receptors. In such ligand-receptor bound confirmation, constitutively active Pnt phosphorylates Tkv, which consecutively phosphorylates intracellular protein Mothers against dpp (Mad, SMAD in vertebrates). Phospho-Mad (pMad) then interacts with the mediator Medea and this complex translocates into the nucleus. There, pMad–Medea complex binds the silencer elements of *brk* locus and also recruits Schnurri (Shn) – another transcriptional repressor. Eventually, transcription of *brk* stops. The silencing of *brk* leads to de-repression of several genes, e.g. *optomotor-blind* (*omb*). For other genes, e.g. *spalt major* (*salm*) both removal of brk repression and activation by pMad–Medea are necessary. Finally, several genes were shown not to be repressed by *brk* in the absence of Dpp, but still become activated upon signalling induction.

As a result Dpp signalling can induce long and short range effects, whereby weak silencing of *brk* would de-repress one class of genes, and strong *brk* repression together with concomitant activation would induce different class of genes[182]. Eventually, the whole signalling cascade is turned-off due to activation of inhibitory Smad proteins (e.g. *daughters-against-dpp, dad*) that act as negative feedback inhibitors at several levels of the cascade. Alternatively, the cells move away from Dpp source and thus pathway switches itself off due to the loss of agonist[182]. However, there is an intense debate on how Dpp reaches the target cells in the first place. Classical morphogen models implied that Dpp is freely diffusing in the extracellular space to reach its targets. Alternatively, Dpp binding to cell surface proteo-glypicans *dally* and *dally-like* suggested a restricted diffusion model[185]. Several other models like epithelial transcytosis or increased Dpp-internalization further away from the source were proposed. However, role of long epithelial protrusions – cytonemes – is quickly gaining ground in numerous model systems including the *Drosophila* imaginal discs. The model proposes that cells away from the Dpp source extend actin-based protrusions reaching the Dpp source. Since

cytonemes were shown to contain Tkv and Pnt receptors, it is likely that they play a role in the establishment of Dpp signalling gradient[186].

Dpp influences DC on several levels. First, the identity of both AS and epidermis cells are conferred in the blastoderm dorsal nuclei where Dpp patterns dorso-ventral (DV) axis of the embryo[187]. Second, the LE starts to secrete Dpp during the GBE stage[188,189]. Third, at the onset of DC, JNK-dependent wave of Dpp expression is triggered in the LE[188,189]. Even though Dpp, which is over-expressed in the LE, diffuses over the epidermis and AS cells[189], the exact mechanism of how the endogenous morphogen spreads during DC is not known. Deciphering what these Dpp expression waves lead to is genetically very challenging. LOF *dpp* alleles result in ventralised embryos[190] preventing their analysis during DC. Zygotic mutant alleles of *tkv* develop normally and show developmental defects only during germ-band retraction (GBR) and DC[191,192]. A similar situation is described with *pnt* and *saxophone* - a third Dpp receptor - mutants. However, pleotropic effects of these phenotypes hinders clear interpretation. For example, a common *tkv* mutant phenotype is the loss of adhesion between the AS tissue and the epidermis, which is also observed in JNK pathway mutants or mutants for integrin components (e.g. αPS3)[106,191,193]. These results only suggest that both AS tissue and epidermis mediate Dpp-dependent connection forming a coherent epithelial layer, without discriminating which tissue contributes more to such adhesion. Nevertheless, the evidence for the role of Dpp in epidermis is extensive and supported by a number of studies[26,30,178,188,193,194]. Dpp involvement in apical AS constriction is highly debatable. A study by Jacinto and Martinez-Arias reports that in *tkv* zygotic mutant AS cells undergo pulsed surface contractions, but fail to apically constrict over time[188]. By contrast, work by Martinez-Arias and Gorfinkiel demonstrated that AS cells undergo apical constriction in the same *tkv* zygotic mutants[17]. As illustrated here, zygotic mutant analysis does not allow for an accurate dissection of the tissue-specific role of Dpp during DC.

It is clear that both genetics and mechanics work together to generate, stabilize and coordinate cellular activities. It is not clear, however, how this results in robust tissue behaviour. At the moment, it is assumed that signalling pathways have a primary role in the establishment of initial conditions that will later could be self-sustained due to biomechanical control. In this chapter, we address the discrepancies of the role of Dpp during DC, emphasizing apical constriction of AS cells. Using a live Dpp signalling read-out, we show a spatio-temporal gradient in the AS cells that is established prior to DC. This gradient does not change significantly within the course of DC and seems not to influence MyoII dynamics in the AS. Finally, we show that tissue-specific perturbation of such gradient does not affect DC.

4.2. Results

4.2.1. Junctional MyoII is sufficient for apical constriction of AS cells

To decipher the roles of apical and junctional MyoII during AS cell apical constriction, ideally, it is necessary to remove one MyoII population without perturbing the other. We have successfully inactivated both MyoII populations simultaneously by ectopic deGradFP expression using a strong AS-specific enhancer element (EE) *332.3*Gal4 (see Chapter 2). Next, we hypothesized that less strong expression of deGradFP would partially inactivate Sqh-GFP and thus could affect the dynamics of the two MyoII populations differently. Screening AS- or epidermis-specific expression patterns revealed an interesting set of EEs, including a tandem of EEs (*dpp*[4B] and *dpp*[8B])[91] contributing to the expression of the morphogen *dpp*. Dpp is expressed in AS cells during their specification and is down-regulated during the extended germ-band stage prior to DC[187]. When we used this tandem of EEs to inactivate Sqh-GFP prior to DC, we noticed that later on, when dpp is down-regulated and dorsal closure had started, the AS tissue in such embryos (hereafter termed recAS-SqhKO) was heterogeneous. Some cells contained Sqh-GFP aggregates, while others did not (Fig. 26A). These Sqh-GFP aggregates are likely to be caused by left-overs of Gal4 and deGradFP from the preceding expression phase. Thus, we hypothesized that the MyoII pool is recovering in an uneven fashion from earlier deGradFP inhibition, generating a mosaic tissue with some cells having recovered while others had not yet done so.

To further investigate this heterogeneity we first counted how many cells were not affected by deGradFP in recAS-SqhKO embryos. We defined the unaffected cells as those with no Sqh-GFP degradation aggregates and with a cytoplasmic Sqh-GFP signal that is higher than the background (Fig. 26A, Methods, section 6.4.1). In addition, these cells showed periodic apical Sqh-GFP foci (Fig. 26A). In contrast, all other cells lacked the typical Sqh-GFP foci and instead contained Sqh-GFP aggregates (Fig. 26A). To estimate the number of both cell types, we picked multiple AS tissue regions irrespective of their relative position and counted the number of cells with 63X or 100X objectives (Methods, section 6.4.1). We found that all the regions contained a varying number of unaffected cells (Fig. 26A). Therefore, we could not draw any conclusions on whether there is an emerging pattern explaining a certain ratio of affected vs unaffected cells. On average, ~21±15% of AS cells in recAS-SqhKO embryos can be classified as unaffected at any given time-point (Fig. 26A). Particularly interesting to us,

were cases where single unaffected AS cells were completely surrounded by affected cells. Such unaffected cells still showed clear, periodically appearing apical Sqh-GFP foci (Fig. 26B). This observation strongly supports our previous findings that generation of actin nucleation bursts (ANBs) is cell-autonomous and pulling forces from the neighboring cells are not needed to generate these bursts (see Chapter 3).

Next, we imaged DC in recAS-SqhKO embryos and noticed that all AS cells over time reduced their apical cell surface areas regardless of whether they were affected or not. This confirmed that MyoII activity is recovering in the affected cells. We then looked at the apical *z* planes of the recovering cells, but surprisingly in most of them we did not detect any obvious apical MyoII foci (Fig. 26C). Instead, we observed an obvious increase in junctional MyoII signal suggesting that the recovery from MyoII depletion occurs differently in individual AS cells, with some first recovering their junctional pool and others in addition recovering the apical pool that forms periodic foci (Fig. 26C). To investigate the recovery further, we measured the changes of Sqh-GFP signal intensities of the affected cells over time, distinguishing junctional- and apical cell surface signals (Methods, section 6.4.1.). To keep track of the apical AS cell surface areas, we measured the area outlined by the recovering junctional MyoII. Sqh-GFP signal intensities in unaffected AS cells were used as a reference to compare the intensities in all the recovering cells (Fig. 26B). In only ~26% of AS cells we detected re-appearing apical Sqh-GFP foci (Fig. 27A-B). In most of the cases, this occurred towards the end of the measurement period, and in general, such recovering foci were not as intense as in unaffected cells (Fig. 27A). In contrast, junctional Sqh-GFP recovered in all of the affected cells (~84.5% of total AS cells) starting much earlier than the apical Sqh-GFP foci recovery. The remaining 15.5% were the aforementioned, unaffected AS cells that showed periodic apical Sqh-GFP oscillations right form the beginning. These cells also increased their junctional Sqh-GFP over time (Fig. 27A-B). Most of the cells, both unaffected and affected, recovering, reduced their apical cell surface areas to some extent. This however, varied considerably from cell to cell. (Figs. 27A, 27C). The area reduction correlated positively with the apical cell perimeter indicating that cells undergo apical constriction (Fig. 27C). Since this mostly occurred in cells lacking apical MyoII foci, this contradicts the current view that these foci drive apical constriction and leads to the conclusion that junctional MyoII alone can drive apical AS cell constriction. However, it was shown recently using light-sheet microscopy that AS volume reduction contributes to DC[42]. When the AMC starts forming in the epidermis, the average height of AS cell stays constant, whereas the cell volume decreases by ~30%[42]. We reasoned that as a consequence, such reduction of bulk cell volume inevitably would lead to a

reduction of the apical cell surface areas. Therefore, we wanted to discriminate if the apical cell surface area changes in recovering AS cells are due to the volume loss or due to junctional MyoII activity. For this, we compared the relative cell surface area decrease with shape change reflected by the cell surface elongation factor, describing how ellipsoid or circular the surface area is. We assumed that if the apical area reduces due to volume loss only, the cell shape or the elongation factor should not change much. In contrast, any contractile MyoII activity would tend to change cell shape anisotropically. When we compared all cells in recovering embryos, the majority of them reduced their apical areas by more than 30% already giving an indication that cell volume decrease alone is not sufficient (Fig. 27D, right half). In addition, most of the cells, including the cells reducing their surface area by less than 30%, showed a reduction of the elongation factor by more than 50% (Fig. 27D, top left quarter). This suggests that the cells are re-shaping to become rounder. The average surface area decrease (Fig. 27E) and the elongation factor reduction (Fig. 27F) were similar between unaffected and affected, recovering cells. We also did not observe any obvious differences between the two types of recovering cells, suggesting that re-appearance of apical MyoII does not make a difference (Fig. 27C-27F). Overall, we conclude that the majority of AS cells in recAS-SqhKO embryos that are recovering from MyoII depletion, undergo active apical constriction, and that this is largely driven by constricting junctional MyoII.

The fact that cells without apical MyoII foci are able to constrict, suggests that cell-cell junctions can shorten autonomously, which questions previous findings suggesting that junctional shortening is driven by apical MyoII foci[39,100]. Indeed, in recAS-SqhKO embryos, we detected single cell-cell junctions that individually shortened independent of the presence of apical foci and of whether neighboring junctions did so too (Fig. 28A). Surprisingly, even very long (~25µm) cell-cell junctions shortened in such a way (Fig. 28B). In support of autonomous junctional contractility, we also detected cases where junctions shortened against the pulling forces of neighboring, unaffected cells (data not shown). Previously, it was demonstrated that during cell-intercalation in *Drosophila* germ-band, MyoII flows shorten the vertical cell-cell junctions[102]. To quantitatively exclude that apical MyoII foci contribute or even drive junctional shortening in recovering AS cells, we measured the intensities of apical Sqh-GFP next to such junctions in both cells sharing the junction (Methods, section 6.4.1). We detected only marginal Sqh-GFP signal fluctuations next to the shortening junctions (Fig. 28C). We confirmed that such intensity fluctuations are minor compared to the Sqh-GFP oscillations in unaffected cells in the same embryos (Fig. 28D). Therefore, we conclude that cell-cell junctions in AS cells shorten autonomously and independently of the apico-medial MyoII pool.

By visualizing cell area decrease, it became apparent that while most cells were reducing their apical surface, some cells did not constrict much or even expanded (Fig. 27C-27F, lower left quarter). In addition, recAS-SqhKO embryos failed DC suggesting that closure by junctional apical constriction alone is not sufficient (Fig. 29A). Thus, we wanted to understand why closure is ineffective in such embryos. We showed earlier that ectopic *pnr*Gal4 expression of deGradFP in AS cells, which also results in a mosaic of affected and unaffected cells, leads to affected cells being expanded by their unaffected neighbors (Chapter 2, Fig. 10A-B). We hypothesized that if individual junctions can shorten on their own they must also exert pulling forces on the junctions to which they are directly linked via the cell vertices. Such pulling should become best visible in cases where two shortening junctions act on the two vertices shared with a third junction. Indeed, we found such cases in recAS-SqhKO embryos and observed that a constricting junctions expanded the others (Fig. 29B). Junctional expansion was not limited to the junctions that had not yet recovered sufficient Sqh-GFP to drive contraction, as we also observed cases of expanding junctions that before had shortened (Fig. 29C). This suggests a tug-of-war situation, in which contracting junctions exert pulling forces on surrounding junctions, which can lead to the expansion of the latter if these cannot produce sufficient resistance forces. Thus, it seems that while junctional shortening can autonomously drive apical constriction it results in a rather inefficient process, in which stronger cell junctions prevent the shortening of the weaker, sometimes even expanding them. This explains the DC failure of such mosaic embryos and suggests that an equilibrating process is in place in the wild type.

To further explore this, we hypothesized that the MyoII-driven, pulsed AS apical cell surface contractions provide such an equilibrating mechanism. Thereby, we propose that the strong periodic contractions would accelerate and support the shortening of all junctions, including the weaker. To explore this possibility we used a mathematical "*in silico*" model of apical AS cell surface oscillation (Atzeni, Aegerter and Brunner, unpublished). Simulating periodic, apical AS cell contractility with reaction-diffusion kinetics, recapitulated *in vivo* dynamics. When adding active cell-cell junctions by introducing contractile cell-cell boundaries of oscillating AS cells, sustained apical constriction resulted. Importantly but not surprisingly, such contractile boundaries could drive apical constriction and closure of the opening even in the absence of the apical cell surface oscillations. We next introduced some cell-to-cell variation to the contractile junctions such that every junction was different in strength. In the presence of the apical AS cell surface oscillation closure turned out to be very robust against such variation. However, in the case where this apical MyoII pool was absent,

such variable tensioned rings could no longer drive even closure and the overall cell behavior readily reproduced what we had observed *in vivo* in recAS-SqhKO embryos. Similar cell-shape patterns were emerging in the simulations with some cells getting extremely small and others expanding being pulled by their neighbors. In agreement with *in vivo* data, in these simulations individual junctions were in a similar tug-of-war state. Thus, by using computational modelling and *in vivo* observations we propose that the role of pulsed apical contractions generally is to equilibrate natural cell-to-cell variability that produces different junctional strengths, allowing for even apical constriction driven tissue contraction in morphogenesis.

4.2.2. Morphogen Decapentaplegic (Dpp) does not control AS cell apical constriction

We demonstrated that AS cells are capable of apically constricting solely by MyoII-dependent junctional shortening without the need of apico-medial MyoII pool. While apical foci of MyoII become evident in AS during the retracting germ-band (GBR) stage, junctional MyoII is not present until ~40-60 min after GBR[38,39] (this work - Chapter 2, Fig. 7B). Moreover, junctional MyoII accumulates slightly earlier in AS cells closer to epidermal LE (Chapter 2, Fig. 7B). Such accumulation correlates with AS pulsing arrest and induced apical constriction[38,39]. So far the trigger for such sequential event is not found, yet LE-secreted morphogen Dpp is a potential candidate for encoding a positional information in AS tissue. To estimate the status of Dpp signalling in AS cells, we used a live reporter, where promoter sequences of a Dpp target gene *dad* drive the expression of GFP fused to nuclear localization signal (NLS, hereafter *dad*>GFP^{NLS}). Strikingly, the intensities of *dad*>GFP^{NLS} in AS cells were graded depending on their distance from the LE (Fig. 30A). The first row of AS cells showed the highest nuclear intensity, whereas nuclei intensities in the middle of the opening were barely detectable (Fig. 30A). Consistently, cell nuclei in between displayed intermediate intensities, yet still following a graded pattern. This suggests that Dpp signalling status is higher in the cells next to the LE, than in those farther away from the LE.

Earlier it was shown that the first row of AS cells is specialized and mediates Dpp-dependent adhesion to epidermal cells[26]. Immunolabelling of endogenous Dad and other Dpp target proteins (e.g. U-shaped and Hindsight) confirmed that in the first row of AS cells, these genes are up-regulated[26]. However, all immunolabelling-based studies did not reveal the graded Dpp response in AS cells farther away from the LE. Therefore, we wanted to reveal whether

the graded *dad*>GFP^{NLS} signal in AS cells could be an imaging artefact. 3D reconstruction of *dad*>GFP^{NLS} embryos from *z* stacks obtained with spinning-disk confocal microscope confirmed that the nuclear intensities are graded from the LE towards the middle AS cells (Fig. 30B). The same embryos expressing ubiquitously-driven RFP tagged with NLS (*ubi*>RFP^{NLS}) did not show such graded intensities neither in maximum intensity z projections (MIP) nor in 3D reconstruction (Fig. 30B). The same was observed for the embryos where nuclei were marked by Histone-mRFP (data not shown). Since emission wavelengths differ between GFP and RFP, we also looked at the embryos, where GFP^{NLS} was driven by *ubi* promoter – *ubi*>GFP^{NLS}. 3D reconstruction revealed no obvious graded signal distribution in the nuclei (Fig. 30B). On the contrary, MIPs of *ubi*>GFP^{NLS} embryos showed higher nuclear intensities in the middle AS cells (Fig. 30C). In addition, *ubi*>GFP^{NLS} MIPs revealed nuclei from the yolk cell, which obscured AS cell nuclei in such images (Fig. 30C). Higher nuclear *ubi*>GFP^{NLS} intensities in the middle region of AS were no longer present upon background illumination subtraction using Gaussian filtering (data not shown; Methods, section 6.4.2). We conclude that graded *dad*>GFP ^{NLS} nuclear intensities in AS are not an imaging artefact and represent differences in Dpp signalling status.

Next, we wanted know when such *dad*>GFP^{NLS} signal gradient is established in AS cells. Several waves of Dpp expression are reported in the early embryo, one of them even defining the AS cell identity during blastoderm cellularization[187,188]. Surprisingly, nuclear *dad*>GFP^{NLS} signal started to increase in the AS tissue only after GBE at ~280-360 min before the start of DC (Fig. 31A). During the extended germ-band phase, *dad*>GFP^{NLS} signal also increased in the lateral epidermis consistent with observations that during this stage epidermal LE starts to express Dpp[188]. Interestingly, when the AS tissue is folded inside the embryo by the extended germ-band, *dad*>GFP^{NLS} signal in AS cells increased, but the gradient was not clearly visible (Fig. 31A, -160min). It only started to emerge during the GBR (Fig. 31A, -60min) and was clearly visible at the end of GBR (Fig. 31A, 0min). This suggests that *dad*>GFP^{NLS} gradient seen in AS cells reflects not only the spatial information provided by Dpp, but also the temporal information, i.e. how far the cell is from a Dpp source and how long the cell was receiving Dpp.

It is possible that such acute dad gradient formation could occur due to a burst of Dpp expression in the LE during a short window before GBR starts and ends (~90±30min). Alternatively, AS cells that are folded inside the embryo during GBE are being just suddenly exposed due to a considerable morphogenetic movement so that the gradient becomes visible. Arguing against the former is that only two main waves of Dpp expression were reported so

far – one shortly after GBE and the second during the onset of DC, but no brief Dpp pulse during GBR was detected[187–189]. We further noticed that in varying number of AS cells above the boundary between the underlying hindgut and the yolk cell, *dad*>GFP^{NLS} signal was very weak or was completely absent (Fig. 31B). Tracing back these cells to extended germ-band stage revealed that they are folded on top of the germ-band epidermis (Fig. 31C). This part of epidermis will eventually end-up being ventral after GBR. AS cells folded on top of epidermis were placed away from LE-secreted Dpp and thus showed no *dad*>GFP^{NLS} signal (Fig. 31C). During GBR these cells showed no increase in *dad*>GFP^{NLS} and finally were placed above the aforementioned boundary between the hindgut and the yolk cell (Fig. 31B). Therefore, we conclude that Dpp signalling gradient observed during DC is established in the folded AS cells prior to DC and is revealed by the morphogenetic movement of the retracting germ-band.

We then asked if such *dad*>GFP^{NLS} signal gradient is dynamic and changes over time or it is just a static representation of Dpp signalling that AS cells experienced while being folded inside the embryo. To address this question, we measured nuclear *dad*>GFP^{NLS} signal intensities over the 2hour course starting 30±5min prior to the net dorsal-ward movement of the two LEs (Methods, section 6.4.2). We could only accurately measure the intensities for 2 hours as past this time-point peripheral AS cell nuclei were displaced underneath the epidermis while the central AS nuclei were pushed deeper into the embryo due to cells elongating apico-basally. In both cases, this prevented us from tracking the nuclei unambiguously. For every nucleus we obtained a fluorescence profile over time and normalized it to the starting intensity value (Methods, section 6.4.2). To allow comparison of fluorescence intensity changes between different nuclei and different embryos we fitted a linear regression model to every intensity profile and obtained a first order regression coefficient (Fig. 32A). Thus, the nuclei with increasing relative fluorescence will have a positive coefficient, whereas the nuclei with little or no changes in relative fluorescence will have a regression coefficient close to zero (Fig. 32A-32B). We then plotted regression coefficients of every nucleus against its distance from the LE at the beginning of measurements. Surprisingly, the increase in *dad*>GFP^{NLS} fluorescence intensity is only evident for the first two rows of AS cells with distal cell nuclei not increasing their intensities (Fig. 32C). In contrast, nuclear intensities in ubiquitously expressed *ubi*>GFP^{NLS} did not show such a pattern. Most of the nuclei in *ubi*>GFP^{NLS} increased in fluorescence intensity over time, but this was independent from the distance from LE (Fig. 32C). This shows that AS cells are able to sense Dpp during DC, but the gradient of signalling status does not change over time (Fig. 32B-32C). Thus, we conclude that previously described

second wave of Dpp expression at DC onset only affects the first two rows of AS cells during the course of DC.

Our data indicates that after *dad*>GFP^{NLS} gradient is established during the extended germ-band stage, it does not change much over the course of DC. We cannot exclude that at the very last DC stages even the middle AS cells would show *dad*>GFP^{NLS} signal increase. However, such a time-point would mark the final stages of apical constriction for most AS cells. We further reasoned that if the second wave of Dpp is not responsible for sequential MyoII accumulation at the cell junctions then, the history of Dpp signalling could induce such a sequential event. To address this hypothesis, we compared nuclear *dad*>GFP^{NLS} signal intensities with junctional MyoII, where heavy chain Zipper was tagged with mCherry. Since there is no way to distinguish to which cell MyoII belongs in the common shared junction, we utilized the rare single AS cells that do not express Gal4 from *332.3* enhancer element (Fig. 33A). For such non-expressing cells, we measured signal intensities of nuclear *dad*>GFP^{NLS} and junctional Zip-mCherry in all their neighbouring cells (Methods, section 6.4.3). Correlation of the two intensities revealed only a medium correlation when all embryos/cells were pooled (Fig. 33B, Pearson's correlation coefficient $r = 0.475$). However, 2 out of 4 embryos (8 cells in total) showed weak or no correlation ($r < 0.3$). We, therefore, conclude that Dpp signalling history alone cannot account for the sequential junctional MyoII appearance.

To validate our correlation analysis, we also looked at zygotic mutants of main Dpp cell surface receptor *tkv*, which also expressed Zipper-GFP. We detected junctional MyoII in most tkv^{8}/tkv^{8} or tkv^{8}/tkv^{7} embryos, even though in some parts of AS tissue MyoII was less evident at the junctions (Fig. 33C). We next looked at *dad*>GFP^{NLS} in these zygotic *tkv* mutants. In agreement with previous reports, we detected strong reduction of *dad*>GFP^{NLS} signal (Fig. 33D). However, we still detected considerable nuclear signal in the AS even though the gradient was not so evident. In comparison, in tkv^{8}/tkv^{8} embryos *dad*>GFP^{NLS} signal in the epidermis was barely detectable in agreement with the previous immunolabelling studies (Fig. 33D)[188]. Due to inconsistent data of *tkv* LOF effect on AS cell apical constriction[37,188], we imaged at least 16 embryos of both tkv^{8}/tkv^{8} and tkv^{8}/tkv^{7} genotypes together with moesin-GFP-labelled actin. Not surprisingly, we detected varying phenotypic penetrance where some embryos almost completed DC and some were tearing apart without much of DC happening (Fig. 34). In agreement with previous data, we still detected actin bursts in the AS indicative of pulsed apical cell surface contractions[188] (data not shown). In mild cases AS cells fully apically constricted almost completing DC and in severe cases AS cells apically constricted to some extent before the tissues ruptured (Fig. 34). Hence, we conclude that *tkv* zygotic mutants

show differentially penetrant effects on apical AS cell constriction, yet MyoII still accumulates junctionally in these embryos.

We then reasoned that if Dpp instructs junctional MyoII accumulation and, thus, AS cell apical constriction, we expect that increase in Dpp signalling would lead to a faster apical constriction and DC rates. Additionally, we expect that over-activation of Dpp pathway in AS cells would abolish *dad*>GFP^{NLS} signal gradient since all the cells should experience high signalling levels. To test our hypothesis, we over-expressed Dpp specifically in the AS cells. Surprisingly, *dad*>GFP^{NLS} signal gradient was still present at the end of GBR (Fig. 35A). However, as DC progressed all AS cell nuclei increased in fluorescence intensity supporting our previous data that AS cells are able to sense Dpp during DC stage (Fig. 35A). We next over-expressed constitutively-active version of tkv (tkv^{Act}) that was shown to up-regulate Dpp signalling independently of Dpp binding[188]. In such a case, *dad*>GFP^{NLS} signal also increased while DC progressed. Nevertheless, over-expressing either Dpp or tkv^{Act} in AS did not lead to a significant difference in total DC time (Fig. 35B). We conclude that increase in Dpp signalling and, thus, target gene activation specifically in AS cells, does not affect DC.

Since in some zygotic *tkv* mutant embryos AS cells apically constrict and, in others, they constrict less, we wanted to avoid such unambiguity and remove Dpp signalling in a tissue-specific manner. We first over-expressed dominant-negative version of tkv (DN-tkv) in the AS tissue, but this did not interfere with DC (data not shown). We next over-expressed Dpp signalling inhibitor Dad in AS cells and, in addition, visualized *dad*>GFP^{NLS} signalling reporter. Initially, we tried *7K*Gal4 enhancer element, which was shown to be expressed exclusively in the first row of AS and lead to DC failure with UAS-Dad over-expression[26]. However, we could only detect a minor reduction in *dad*>GFP ^{NLS} intensity in several first row cells (Fig. 36). Contrary to what was shown in Wada, et al., DC completed normally (Fig. 36). We were puzzled by such outcome and thus used other AS-specific enhancers to over-express Dad. Most of them eliminated *dad*>GFP^{NLS} signal gradient in AS very clearly (Fig. 36). Using 3 enhancer elements (*P0172*Gal4, *krüppel*Gal4 and tandem *dpp[4B]-dpp[8B]*Gal4) we could eliminate *dad*>GFP^{NLS} signal efficiently in the majority of AS nuclei (Fig. 36). Surprisingly, in all cases DC completed on time and without obvious defects. We confirmed that Dad over-expression works since *7K*Gal4/UAS-Dad, *Krüppel*Gal4/UAS-Dad and *dpp[4B]-dpp[8B]*Gal4/UAS-Dad adult flies were not viable. Our data demonstrates that suppression of Dpp signalling specifically in AS cells does not interfere with DC progression contrary to what was deduced from *tkv* mutant analysis.

4.3 Discussion

4.3.1. Re-visiting apical constriction models of AS cells

Apical constriction is widely utilized throughout the development to change tissue shapes, folding and overall morphology[107]. Earlier, we demonstrated that DC is driven solely by the apical constriction of AS cells that eventually form a tube underneath the epidermis (Chapter 2)[25]. In all known examples of apical constriction, as gastrulation or neurulation, the process mostly depends on acto-myosin contractility[6,7,16,107]. While different mechanisms were proposed for specific developmental process, a common theme emerges, whereby apico-medial and junctional pools of MyoII coordinate force production to deform apical cell areas. In this chapter, we addressed the contribution of these two MyoII pools during the apical constriction of AS cells.

So far all known methods to remove MyoII function, cannot target either apico-medial or junctional MyoII pools exclusively, but rather disturbs the whole MyoII population. Even though we used the most specific MyoII inactivation by deGradFP, we also removed both MyoII populations (Chapter 2, Fig. 7D). Yet by controlling the levels of deGradFP activity and thus Sqh-GFP inactivation, we could restore MyoII function in AS due constitutive expression of Sqh-GFP. Our results upon such MyoII recovery suggest that apical constriction of AS cells can be driven by junctional MyoII alone. These conclusions do not completely dismiss the role of apico-medial MyoII in AS cells since, at the very final steps of DC, AS cells need to change their shape to form a tube[25]. Only apical accumulation of MyoII could explain dramatic changes from convex to concave surface areas next to the zipping canthus observed by electron-tomography[25]. However, we propose that prior to these last stages, while cells are still pulsatile, reduction in the net apical area occur primarily via junctional shortening of AS. In agreement with our genetic data, a study on mechanical properties of AS cells done by laser-hole drilling revealed that tension on the cell-cell junctions is higher during the earlier phases of apical constriction[25]. Consistently, in the very last stages of DC, AS tissue becomes more solid-like with the mechanical stress increasing primarily in the cell center indicating the accumulation of apico-medial MyoII.

Intriguingly, as we propose that DC is more similar to neurulation than it was previously thought (Chapter 2)[25], neurulation in *Xenopus* and chicken is driven primarily by circumferential contractile network at the cell adherens junctions[166–168]. Such mechanism is

different from the apical constriction during the gastrulating mesoderm of *Drosophila*, where step-wise increase in apico-medial rather than junctional MyoII exhibits molecular ratchet behaviour[101]. However, we cannot fully exclude junctional MyoII acting as a clutch in the hypothetical internal AS cell ratchet proposed by *in silico* modelling[100]. Assuming the internal ratchet is the only way that AS can apically constrict, then apico-medial MyoII pulse would be the obvious force-generator, whereas junctional MyoII would be a clutch stabilizing cell deformation after the pulse. However, in addition to whole apical area reduction, we also observe AS junctions shortening actively without the apical force-generator arguing that contractile force is intrinsic to the junctions. Such force produced by a junction could be enhanced by an apical burst. However, the clutch function is clearly not essential to reduce the apical area of AS cells. We also rule out the possibility of cell apical areas shrinking merely by cell volume loss, as was proposed by Saias et al. In both wild-type cells and cells with only junctional MyoII, we observe initially elongated AS cells rounding up over time indicating anisotropic contraction (Fig. 27D)[38].

An alternative ratcheting mechanism was proposed by Lecuit and colleagues during GBE whereby only the vertical junctions shorten in intercalating cells[102]. This is achieved via planar polarized MyoII flow towards the shrinking junction. Rather than vertical junctions shrinking on their own, local junction shortening produced by MyoII flow is fixed by gradual accumulation of junctional MyoII[102]. In such case stabilization, rather than active constriction of the junction, achieves the desired result. Two arguments make this model incompatible with AS cell apical constriction. Firstly, the average junction length in AS prior to net apical constriction is ~10 µm, with some junctions being longer than 20 µm, mainly along the medio-lateral embryonic axis[39]. By contrast, the average vertical junction length in germ-band epithelium is only ~3-4 µm[102,195] Therefore, such junctional stabilization might work only in the relatively short distances. Meanwhile, we observe AS cell junctions that are ~25 µm and shrinking actively to at least ~40% of the initial length (Fig. 28B). Secondly, during germ-band cell intercalation, the flows of MyoII are strictly perpendicularly polarized with respect to the shrinking junction. Meanwhile, many of the apical MyoII bursts are isotropic and those that create flows/waves are mostly oriented parallel to the longest cell junctions that shorten the most[38,39]. Thus, junctional stabilization mechanism would be highly inefficient in AS cells due to lack of planar polarity cues and the sheer size of the cells.

Even though we see actively shrinking junctions in AS cells, such DC is very inefficient and eventually fails (Fig. 29A). In such embryos, we immediately noticed a tug-of-war situation that junctions undergo, with some of them being ripped open, while others over-

constricting. However, the effect is less pronounced than in the cells either completely lacking or having MyoII as seen with "leaky" *pnr* enhancer driving deGradFP in AS cells. In this case, the former cells are torn-up by their wild-type neighbours (Chapter 2, 10B). Thus, instead of all-or-nothing response (i.e. contracting or expanding), the area changes in recovering AS cells are more subtle. We cannot exclude that the remaining unaffected cells in recovering embryos perturb force balance to such a degree that it alters DC progression. However, this is unlikely since we observe that junctions can shrink against the pulling forces of such unaffected cells. Alternatively, shortening junctions could be explained by increased E-cadherin endocytosis, however, it would not be consistent with the tug-of-war situation. It is highly unlikely that E-cadherin endocytosis rates would differ so dramatically in different regions of a single cell and between the individual cells to cause one junction shortening faster than the others.

The inherent contractile properties of every junction prompted us to investigate junctional noise hypothesis, whereby we propose that apico-medial MyoII pool or foci are needed to equalize differences in AS junction strengths. Such differences might arise stochastically by unequal recruitment of MyoII to the junctions. In such a way, apical MyoII foci in the neighbouring cells would stretch the stronger junction. This would prevent its over-constriction and ripping-open the weaker junctions. In agreement with this, our *in silico* model only leads to the same tug-of-war situation when the junctional noise is implemented and apico-medial MyoII contractility is removed. Importantly, such a model would allow explaining why and how short-term AS cell apical surface pulses are combined with the long-term slower process of gradual apical AS cell constriction.

4.3.2. Dpp signalling gradient in AS tissue is not essential for DC

MyoII plays a critical role during DC. We demonstrated that MyoII-dependent apical constriction of AS cells is the sole force-producing process that is essential for DC (Chapter 2). We also proposed that junctional MyoII is capable of driving such apical AS constriction independently from apico-medial MyoII pool (this Chapter, section 4.2.1). Yet initially AS cells lack junctional MyoII whereas apico-medial pool oscillates within period of minutes leading to no net cell apical constriction. How such transition from pulsatile phase to apical cell constriction is triggered is not yet known. Secreted morphogen Dpp was proposed to mediate this transition, however, ambiguous interpretations of Dpp-receptor mutant *tkv*

phenotypes did not allow to draw clear conclusions. Our data presented here helps to clarify the role of Dpp during AS cell apical constriction.

Our approach relied on live Dpp signalling reporter *dad*>GFP^{NLS} as opposed to previous studies that used immunolabelling or GFP-tagged Dpp pathway components[188,189]. Thus, we could efficiently detect spatio-temporal gradient of Dpp signalling activity in AS cells that previous studies failed to observe. Even though AS cells start receiving Dpp from the epidermis at the extended germ-band stage (~5-6 hours prior to the DC), the gradient only becomes visible after a morphogenetic movement of the germ-band that exposes AS tissue (Fig. 31A). Consistent with the two proposed waves of Dpp expression in the LE, we detect that Dpp signalling gradient is established during the first wave at the extended germ-band. This occurs when AS tissue is folded inside the embryo. It was shown that this first wave of Dpp expression facilitates *zipper* transcription in both AS cells and epidermis in ACK-dependent manner[189]. However, only the transcription of *zipper* could not account for the rapid effects of MyoII localization to adherens junctions seen during DC. Therefore, we reasoned that either the cellular "memory" of Dpp signalling status or the second wave of Dpp expression in the LE could induce MyoII re-localization. Weak correlation between *dad*>GFP^{NLS} nuclear signal and Zip-mCherry amount at the junctions argue against the cellular "memory". We also do not see far reaching effects of the second wave of Dpp expression. Only the first two rows of AS cells show increase in *dad*>GFP^{NLS} nuclear intensity within the critical time of junctional MyoII accumulation. Even if diffusion of Dpp could be somehow restricted in the AS tissue, an alternative model could still work whereby moving the LE (Dpp source) will physically appear closer and closer to the middle AS cells and hence could lead to MyoII accumulation. Yet we also rule out this possibility as *dad*>GFP^{NLS} gradient is not actively changing as cells appear closer to the LE. In addition, MyoII accumulates much faster in the middle AS cells than could be expected due actual LE movement.

Puzzled by inconsistent results of *tkv* LOF effects on AS cell ability to apically constrict, we re-analysed both tkv^{8}/tkv^{8} homozygous and tkv^{7}/tkv^{8} trans-heterozygous zygotic mutants. Not surprisingly, we found that due to different maternal contribution in some embryos, AS cells apically constricted, whereas in others they did not (Fig. 34). To overcome such ambiguity, we chose an alternative approach by switching off Dpp signalling using Dad over-expression specifically in the AS tissue. Using enhancer elements that drive Gal4 and thus Dad, at very early time-points in AS cell specification (e.g. *krüppel* and *dpp*), we could effectively eliminate *dad*>GFP^{NLS} gradient in AS tissue without any effect on DC. An important point to stress here is that *dad*>GFP^{NLS} signalling reporter only shows the

transcriptional output of Dpp pathway. Dpp is known to induce two groups of target gene transcription, both of which are repressed by *brk*[182]. Surprisingly, transcriptional activation by Dpp signalling is not needed for timely DC as *tkv* mutant phenotypes are completely rescued in double *tkv, brk* mutant and DC completes without a significant delay[178]. This suggests that merely de-repression of *brk* is enough to elicit all the responses required for DC. We then went one step further and demonstrated that target gene activation and *brk* de-repression is not needed in the AS to drive DC (Fig. 36). Thus, we conclude that DC phenotypes of *tkv* LOF can be attributed only to the defects in the epidermis, but not the AS. Supporting this, recent evidence suggests that JNK-induced activation of pro-apoptotic *reaper* in the epidermis is prevented by Dpp signalling via Shnurri co-repressor[179]. Thus it is likely that *tvk* mutant epidermis become more susceptible to both JNK-induced stress responses and loss of integrin-dependent adhesion as shown earlier[26]. Consistent with this idea, only the constitutively-active, but not the wild-type form of receptor tkv expressed in AS cells can restore adhesion between the two tissues and rescue dorsal cuticle phenotypes of *tkv* mutants[188].

Using transcriptional Dpp signalling read-out, we rule out Dpp as an instructive signal for MyoII transition from pulsatile behaviour to directed apical constriction. Obviously, transcriptional output is delayed from the original Dpp binding due to intermediate steps needed to produce and translocate GFP^{NLS} to the nucleus. Therefore, we cannot fully exclude that at some step in the signalling cascade, an alternative and direct way could lead to MyoII re-localization. Intriguingly, such case was shown to exist in *Drosophila* wing imaginal disc, where epithelial cells undergo Dpp-dependent cuboidal-to-columnar transition by re-localizing Rho1 – an upstream activator of MyoII[196]. Nevertheless, such transition happens over the course of a few days and still depends on target gene activation/de-repression via Mad and Brk respectively[196]. Alternatively, it was shown that aPKC/Par-3 complex build-ups gradually at the apical AS surface and promotes MyoII accumulation[38,41]. Yet the activating signal upstream of aPKC/Par-3 is still necessary and no transcription-independent link was found between Dpp and aPKC/Par-3 polarity complex so far.

Overall, we conclude that spatio-temporal Dpp signalling gradient and sequential MyoII accumulation in AS cells are not linked, but rather coincide with the graded pattern from the LE. Even though such Dpp signalling gradient would provide an elegant way of instructing relatively chaotic cells like AS to perform and behave in a more organized way. Importantly, we show that AS cells are sensing Dpp secreted from the LE, but why such a gradient exists and if it is necessary at all is still to be shown. One potential reason could be the prevention of premature apoptosis. During the inter-digitation of vertebrate limbs, cell farther away from

Dpp source in the forming digits undergo apoptosis[197]. Preliminary correlation of *dad*>GFP^{NLS} signal and apoptosis rate in AS cells revealed weak relationship between the two since AS cells with both higher and lower *dad*>GFP^{NLS} nuclear intensities were de-laminating first during DC. Alternatively, such a gradient could be just an unutilized remnant of the Dpp signalling that the cell has experienced before.

4.4. Future directions

Using conditional MyoII recovery form deGradFP inactivation, we demonstrated that AS are able to apically constrict by junctional MyoII alone. However, inactivation aggregates of Sqh-GFP obscure the quantitative measurements of recovering junctional and apico-medial MyoII populations effectively. Therefore, a more clear-cut way to acutely disrupt one pool of MyoII, but not the other, is highly needed. One such alternative could be fusing nanobodies or DARPins to a protein that would target MyoII to the adherens junctions at the same time also depleting apico-medial MyoII pool. Few obvious candidates for such fusion would be armadillo, a-catenin, E-Cadherin, crumbs that were shown to localize or build-up cell adherens belt. However, a major drawback in such a case could be the inability to control such re-localization. Thus, a more acute and reversible re-localization is necessary. Light-inducible association of proteins perhaps would be the perfect way in this case. It was recently shown that light-inducible CRY2-CIB interaction could be exploited in *Drosophila* embryos[162]. Thus, tagging arm, a-catenin or E-Cad with CIB and MyoII with CRY2 would allow unprecedented efficiency of MyoII re-localization to the cell junctions and thus control of the apical cell constriction. In Appendix 1, we describe the attempts to create such MyoII-CRY2 fusion protein. To dissect the exact role of apico-medial MyoII the opposite could be applied by excluding MyoII solely from the junctions.

Next critical step in testing junctional noise hypothesis is assessing the strengths of individual junctions *in vivo*. While fluorescence intensity of Sqh-GFP at the junctions might correlate with increased contractility, at some point fluorescent signal becomes saturated asking for a different way in assessing junctional strengths. Since AS cell population is very heterogeneous in recAS-SqhKO embryos, recoil parameter estimation after laser incisions will most likely be contaminated by secondary indirect effects arising from the neighbouring junctions as it is in the wild-type. Therefore, a force-sensor would be highly advantageous.

Even though several FRET-based force sensors exist, their efficiency and readout is further to be tested[198,199].

To rule out E-cadherin endocytosis as a mechanism for autonomous junction shortening, we plan to introduce E-cadherin labelled with red fluorophores into our genetic set-up to quantitatively assess E-cadherin content in the cells. This would allow us to perform photo-bleaching/FRAP of individual junctions and simultaneously measure E-cadherin turnover rates in shrinking vs non-shrinking junctions.

Even though we show that Dpp target gene activation in AS cells is not needed for DC, several AS nuclei still show residual *dad*>GFP^{NLS} reporter signal. Ideally, a combination of 2-3 very early enhancer elements driving Gal4 is needed to completely remove input of Dpp in AS cells. Alternatively, Dad over-expression could be used in combination with recently developed Morphotrap that immobilizes Dpp next to its source[200].

Finally, if the proposed Dpp signalling gradient in AS tissue is relevant at all for DC, it would be interesting to know if and how such gradient scales up with increasing cell number. It was demonstrated that the number of nuclei that would give rise to AS cells scales up with increasing copies of Dpp during the blastoderm stage[201]. We managed to confirm this by introducing 2 extra copies of Dpp in the embryo. By visualizing apical cell areas with arm-GFP we detected many more AS cells that also were smaller (data not shown). It could be possible that Dpp gradient in AS cells is needed as a mechanism to ensure developmental robustness similarly to its role in epidermis cells. In such a case embryos with more or less AS cells would complete DC on time before the other developmental processes start.

4.5. Summary of the key findings/hypotheses of Chapter 4

- AS cell can undergo apical constriction only with junctional MyoII
- AS cell-cell junctions can contract autonomously without the need of apico-medial MyoII
- Apico-medial MyoII pulses might equilibrate noise in the junction strengths arising during apical AS cell constriction
- AS tissue has an intrinsic spatio-temporal Dpp gradient information, which is provided prior to DC
- Dpp information gradient and sequential MyoII accumulation in AS cells are most likely two independent phenomena

- First two rows of AS cells are sensing Dpp during the course of wild-type DC
- Dpp target gene activation is not needed in AS cells to drive DC

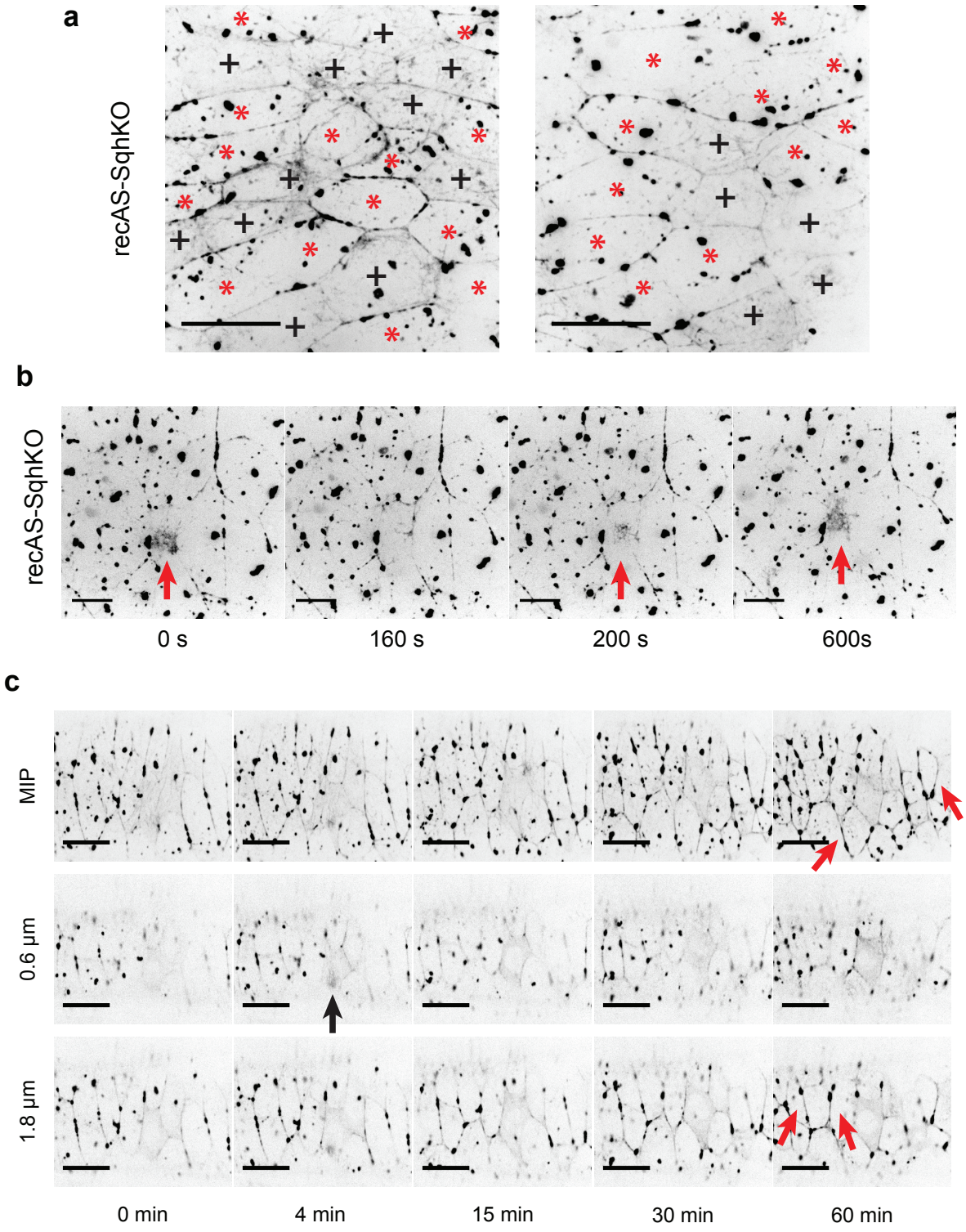

Figure 26. Recovery from MyoII inactivation leads to heterogeneous AS cell population. (a) AS tissue regions in two recAS-SqhKO embryos. Star denotes deGradFP-affected cells, cross denotes cells not affected by deGradFP. Scale bar: 20µm. **(b)** Selected movie frames showing apical Sqh-GFP foci (red arrow) in deGradFP-unaffected AS cell in recAS-SqhKO embryo. Scale bar: 10µm. **(b)** Selected movie frames embryo showing DC in recAS-SqhKO embryos. Sqh-GFP gradually re-appear at the cell-cell junctions (red arrows), but not apico-medially. Black arrow shows apical Sqh-GFP foci in the AS cell unaffected by deGradFP. MIP shows maximum intensity z projection, 0.6µm and 1.2µm shows single planes that are 0.6µm and 1.2µm from the apical cell surface respectively. Scale bar: 20µm.

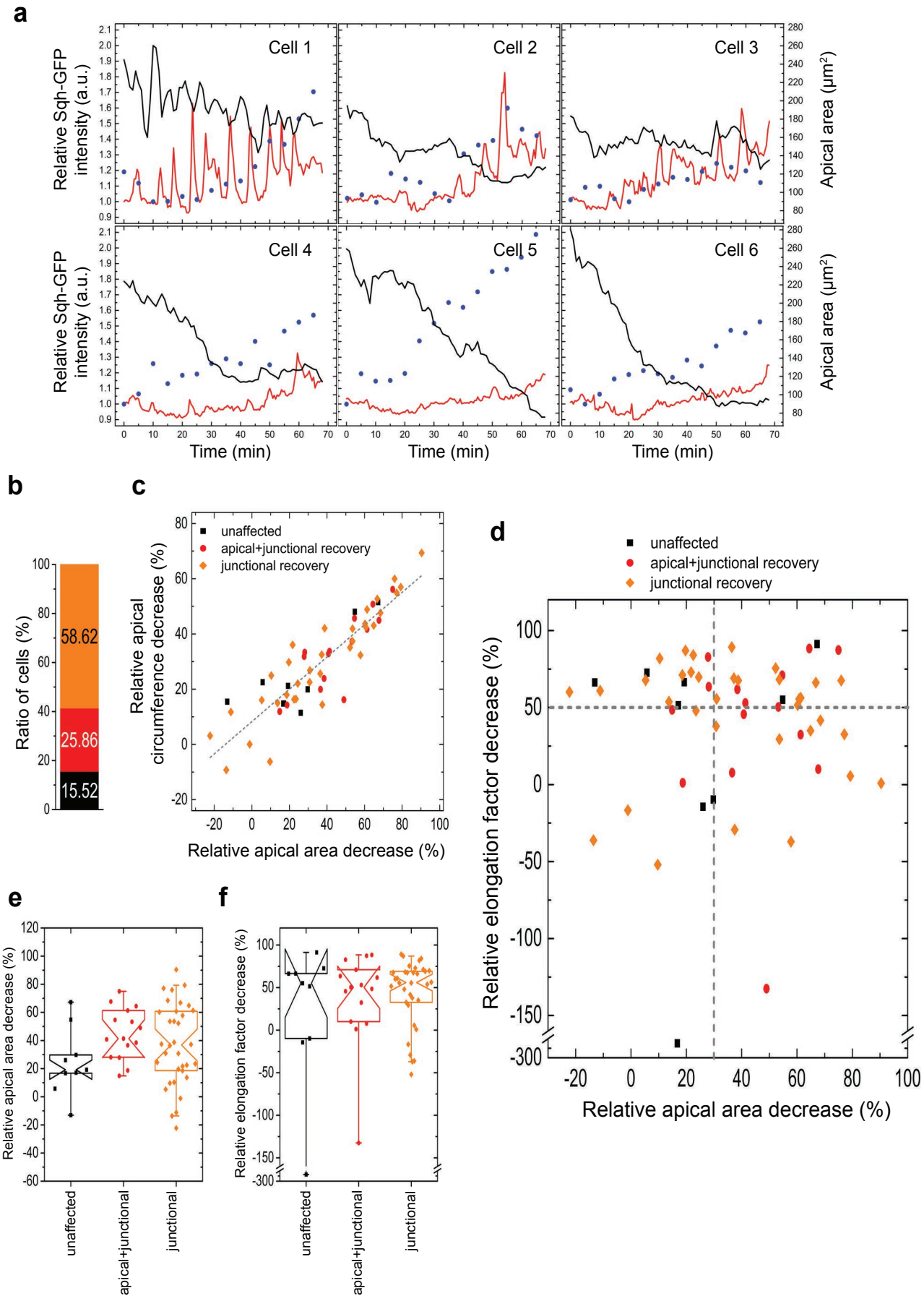
a
Cell 1
Cell 2
Cell 3
Cell 4
Cell 5
Cell 6
Relative Sqh-GFP intensity (a.u.)
Apical area (μm²)
Time (min)
b
Ratio of cells (%)
58.62
25.86
15.52
c
unaffected
apical+junctional recovery
junctional recovery
Relative apical circumference decrease (%)
Relative apical area decrease (%)
d
unaffected
apical+junctional recovery
junctional recovery
Relative elongation factor decrease (%)
Relative apical area decrease (%)
e
Relative apical area decrease (%)
unaffected
apical+junctional
junctional
f
Relative elongation factor decrease (%)
unaffected
apical+junctional
junctional

Figure 27. Junctional MyoII alone can drive AS apical constriction. (a) Representative curves of apical cell area (black line), apico-medial Sqh-GFP intensity (red line) and junctional Sqh-GFP intensity (blue dots) in AS cells in recAS-SqhKO embryos. Three main types of cells are found in recAS-SqhKO embryos. Type 1: deGradFP-unaffected cells (cell 1), where apico-medial Sqh-GFP oscillates and junctional Sqh-GFP increases reducing the apical cell area in a step-wise fashion. Type 2: deGradFP-affected cells (cells 2-3), where apico-medial Sqh-GFP recovers and junctional Sqh-GFP increases reducing the apical cell area. Type 3: deGradFP-affected cells (cells 4-6), where apico-medial Sqh-GFP does not recover, but junctional Sqh-GFP increases reducing the apical cell area. **(b)** Relative ratio of different types of AS cells from (a) in recAS-SqhKO embryos. Black – type 1 (deGradFP-unaffected), red – type 2 (deGradFP-affected with apico-medial and junctional Sqh-GFP recovery), orange – type 3 (deGradFP-affected with only junctional Sqh-GFP recovery). **(c)** Scatter plot showing relationship between the apical AS cell area and circumference change in recAS-SqhKO embryos during the 80min of DC. Different cell types are labelled with appropriate colour (see a-b). Dashed grey line shows the best-fit line (R^2=0.797). **(d)** Scatter plot showing relationship between the apical AS cell area change and the elongation factor change in recAS-SqhKO embryos during the 80min of DC. Different cell types are labelled with appropriate colour (see a-b). Horizontal grey dashed line separates cells with more/less than 50% change in the elongation factor, vertical grey dashed line separates cells with more/less than 30% change in the apical area. **(e)** Standard notched box plots depicting average apical AS cell area decrease in recAS-SqhKO embryos during the 80min of DC. Different cell types are labelled with appropriate colour (see a-b). **(f)** Standard notched box plots depicting average apical AS cell area elongation factor change in recAS-SqhKO embryos during the 80min of DC. Different cell types are labelled with appropriate colour (see a-b).

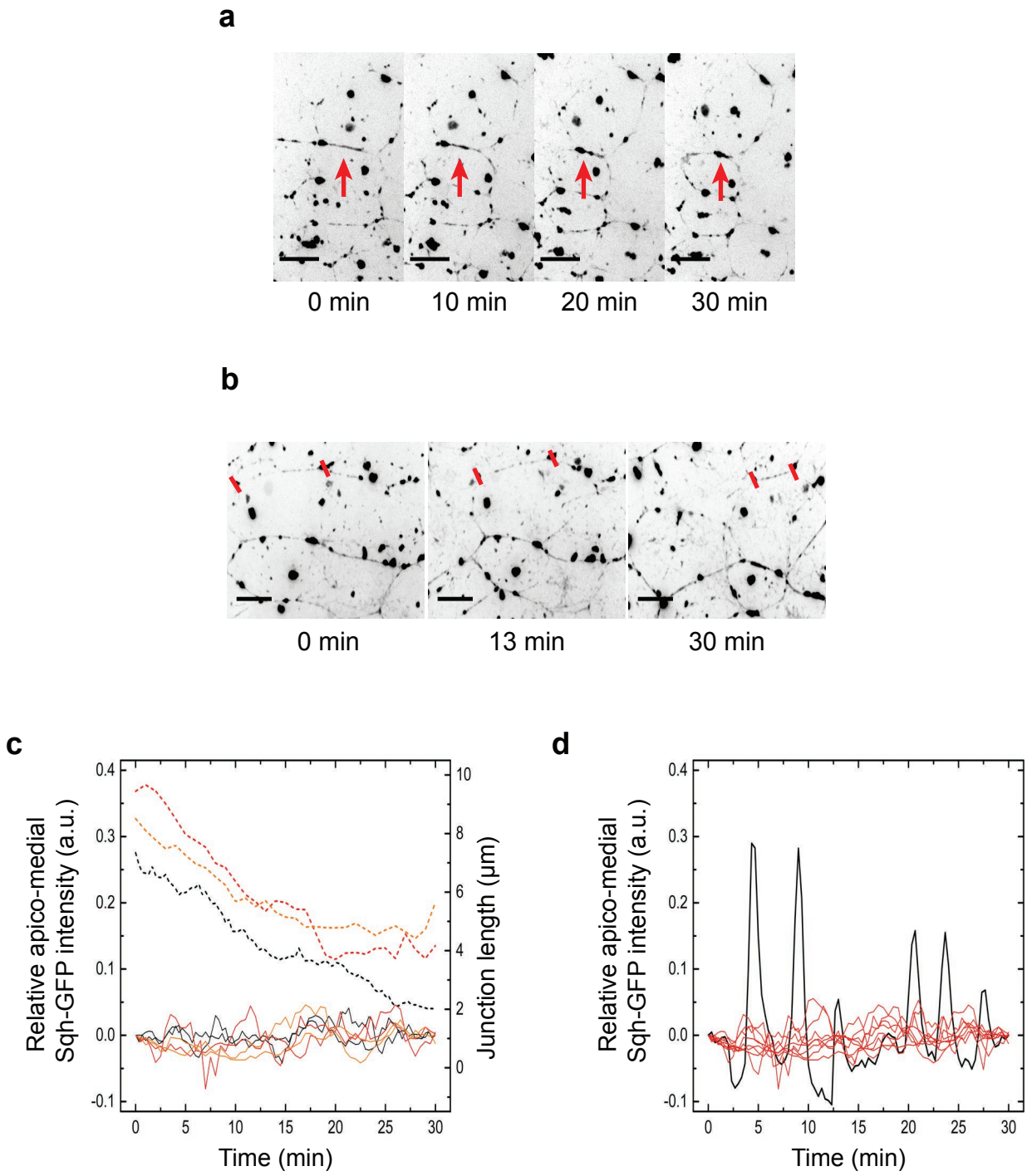

Figure 28. Individual AS cell-cell junctions shorten autonomously without the apico-medial MyoII. (a) Selected movie frames showing an example of AS cell-cell junction that shortens in recAS-SqhKO embryos. Scale bar: 10µm. **(b)** Selected movie frames showing an example of unusually long (~25µm) AS cell-cell junction that shortens in recAS-SqhKO embryos. Scale bar: 10µm. **(c)** Representative curves of AS cell-cell junction length (dashed lines) and apico-medial Sqh-GFP intensity (solid lines) in recAS-SqhKO embryos. 3 different colours represent a single junction in 3 different embryos. **(d)** Representative curves of apico-medial Sqh-GFP intensity in deGradFP-affected AS cells from c (red lines) and deGradFP-unaffected AS cell (black line) in recAS-SqhKO embryo.

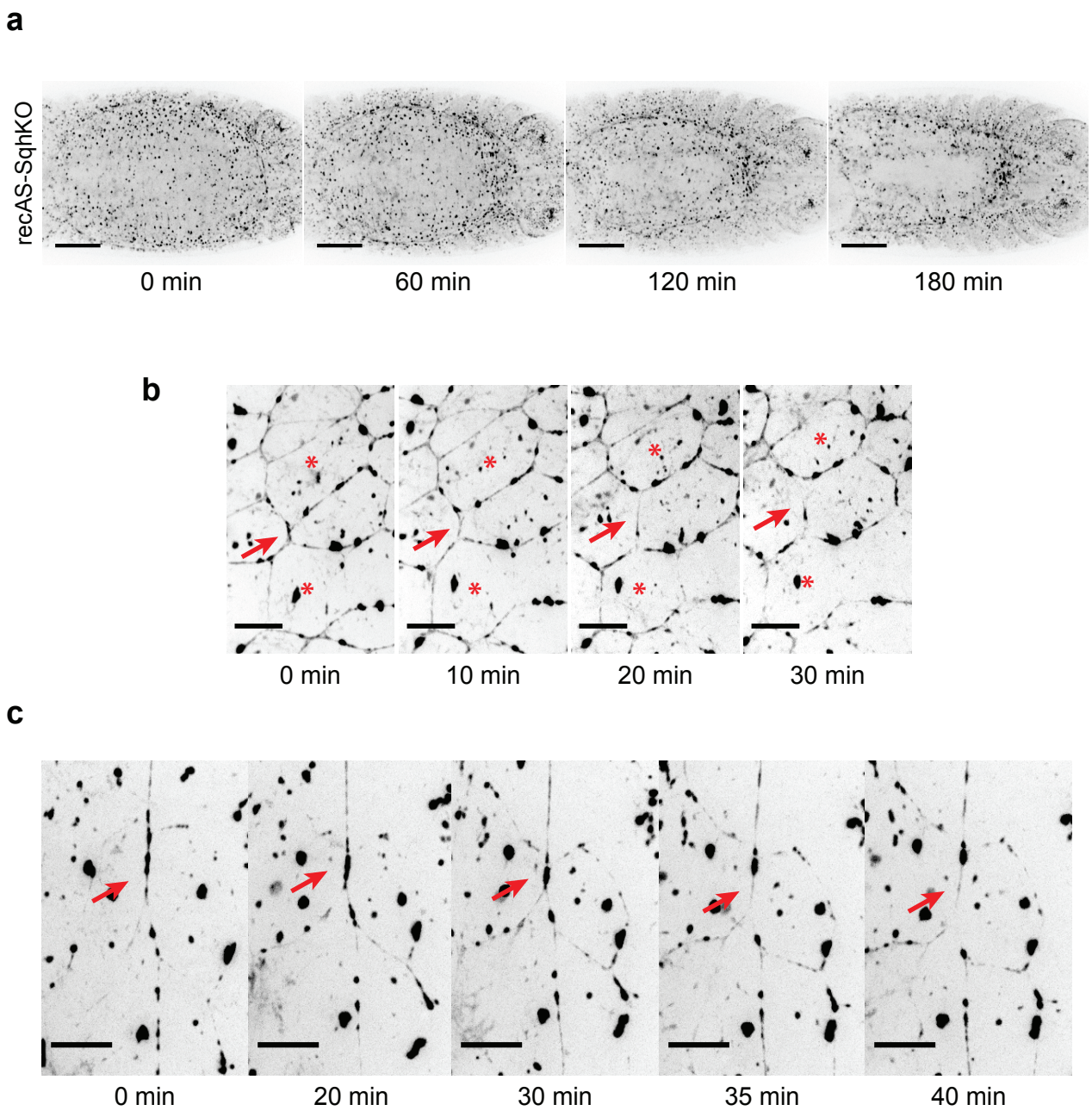

Figure 29. AS cell-cell junctions undergo tug-of-war situation if AS cells constrict by junctional MyoII only. (a) Selected movie frames showing DC in recAS-SqhKO embryos over-expressing deGradFP with *dpp* enhancer elements. MyoII inactivation aggregates appear in the AS cells and DC fails. 0 min depicts the end of germ band retraction. Scale bar: 50µm. **(b)** Selected movie frames showing an example of single AS cell-cell junction (red arrow) that is ripped open by the two contracting AS cells (red stars) in recAS-SqhKO embryos. Scale bar: 10µm. **(c)** Selected movie frames showing an example of single AS cell-cell junction (red arrow) that shortens (time: 0-30min) and then is ripped open (time: 30-40min). Scale bar: 10µm.

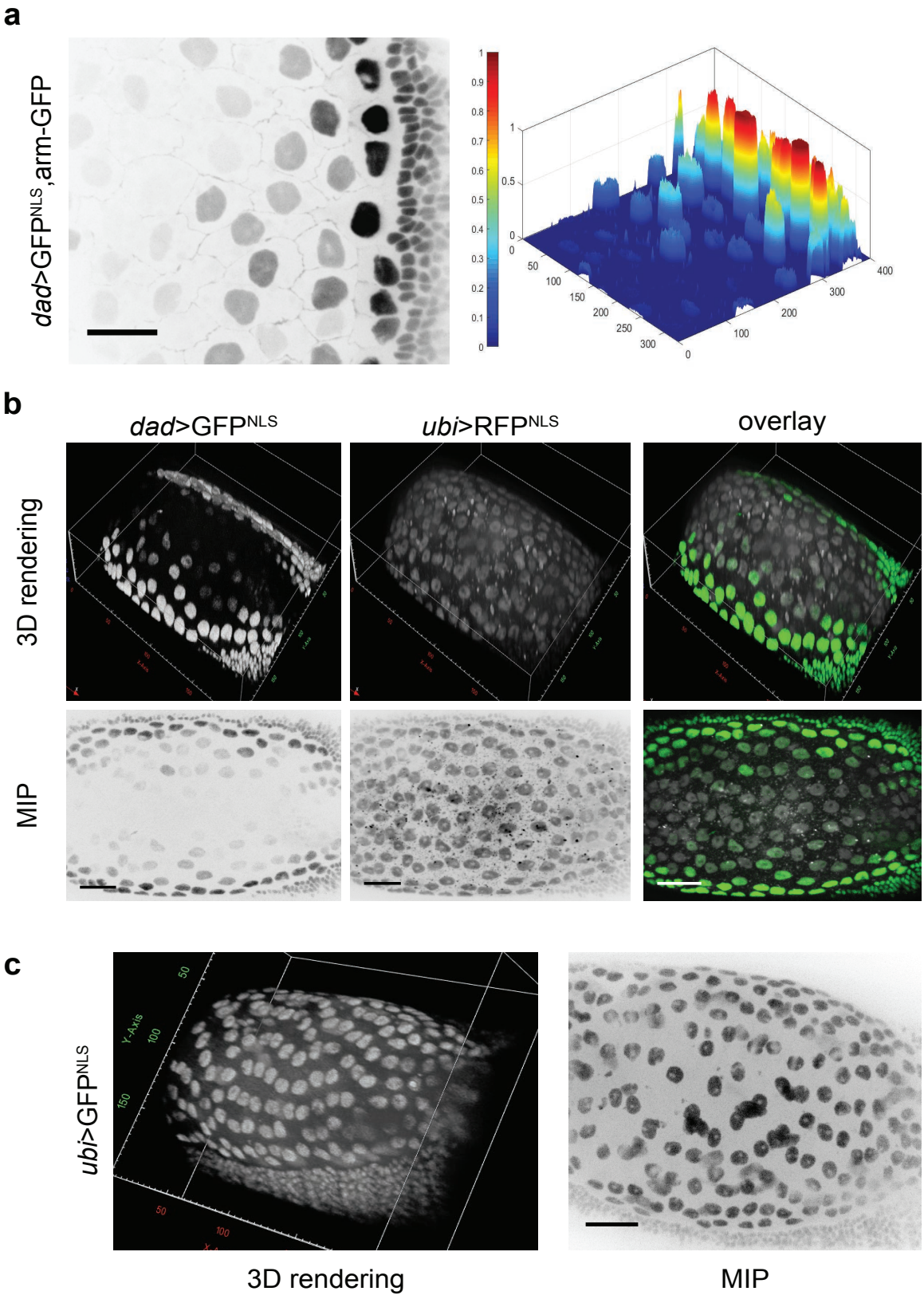

Figure 30. Live reporter reveals graded Dpp signaling activity in AS cells. (a) Left: Region of AS cells showing nuclear Dpp signaling reporter *dad*>GFP^{NLS}. arm-GFP outlines the apical areas of AS cells. Scale bar: 20µm. Right: Surface plot of *dad*>GFP^{NLS} fluorescence signal intensity of the same AS region. **(b)** 3D reconstitution (top panels) and maximum intensity *z* projections (MIP, bottom panels) of embryos carrying *dad*>GFP^{NLS} Dpp signaling reporter and ubiquitously expressed *ubi*>RFP^{NLS} . In overlay: *dad*>GFP^{NLS} is green, *ubi*>RFP^{NLS} is gray. Scale bar in MIP: 30µm. **(c)** 3D reconstitution (left) and maximum intensity **z** projection (MIP, right) of ubiquitously expressed *ubi*>GFP^{NLS} embryo. Scale bar in MIP: 30µm.

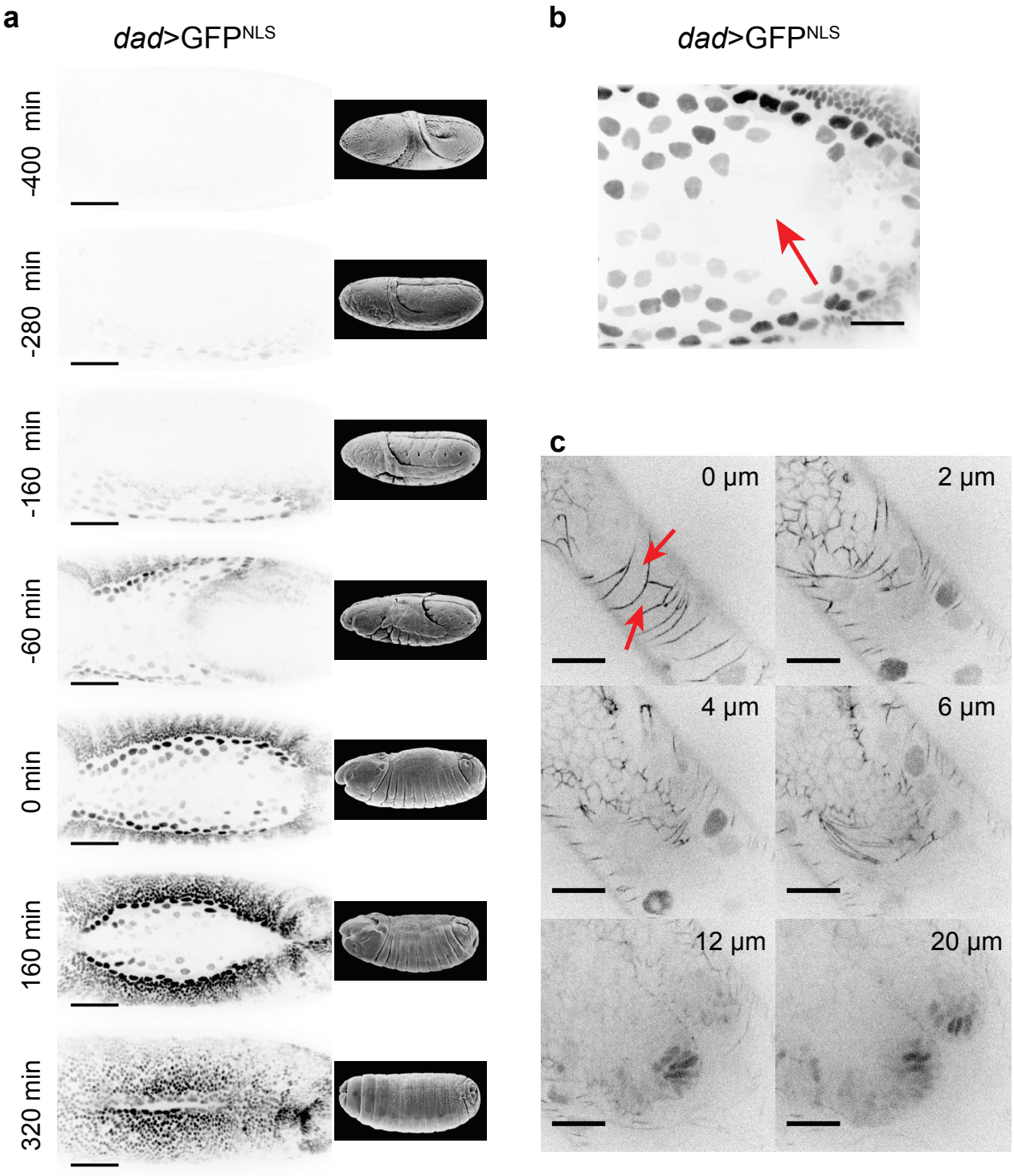

Figure 31. Dpp signaling gradient in AS cells is established prior to DC. (a) Selected movie frames showing *dad*>GFP^{NLS} signal appearance during the *Drosophila* embryogenesis from Bownes stage 8 until stage 16. 0 min depicts the end of germ band retraction. Scale bar: 50µm. Representative embryo stages (right) adapted from Flybase. **(b)** *dad*>GFP^{NLS} signal in the posterior region of AS tissue. Nuclear signal is absent in the small region above the hindgut (red arrow). Scale bar: 30µm. **(c)** Selected single Z stack planes of *dad*>GFP^{NLS}, arm-GFP embryos at the extended germ-band stage (Bownes stage 10). *dad*>GFP^{NLS} signal is absent in the AS cells located above the germ-band (red arrows). 0µm depicts the apical surface of AS cells. Scale bar: 20µm.

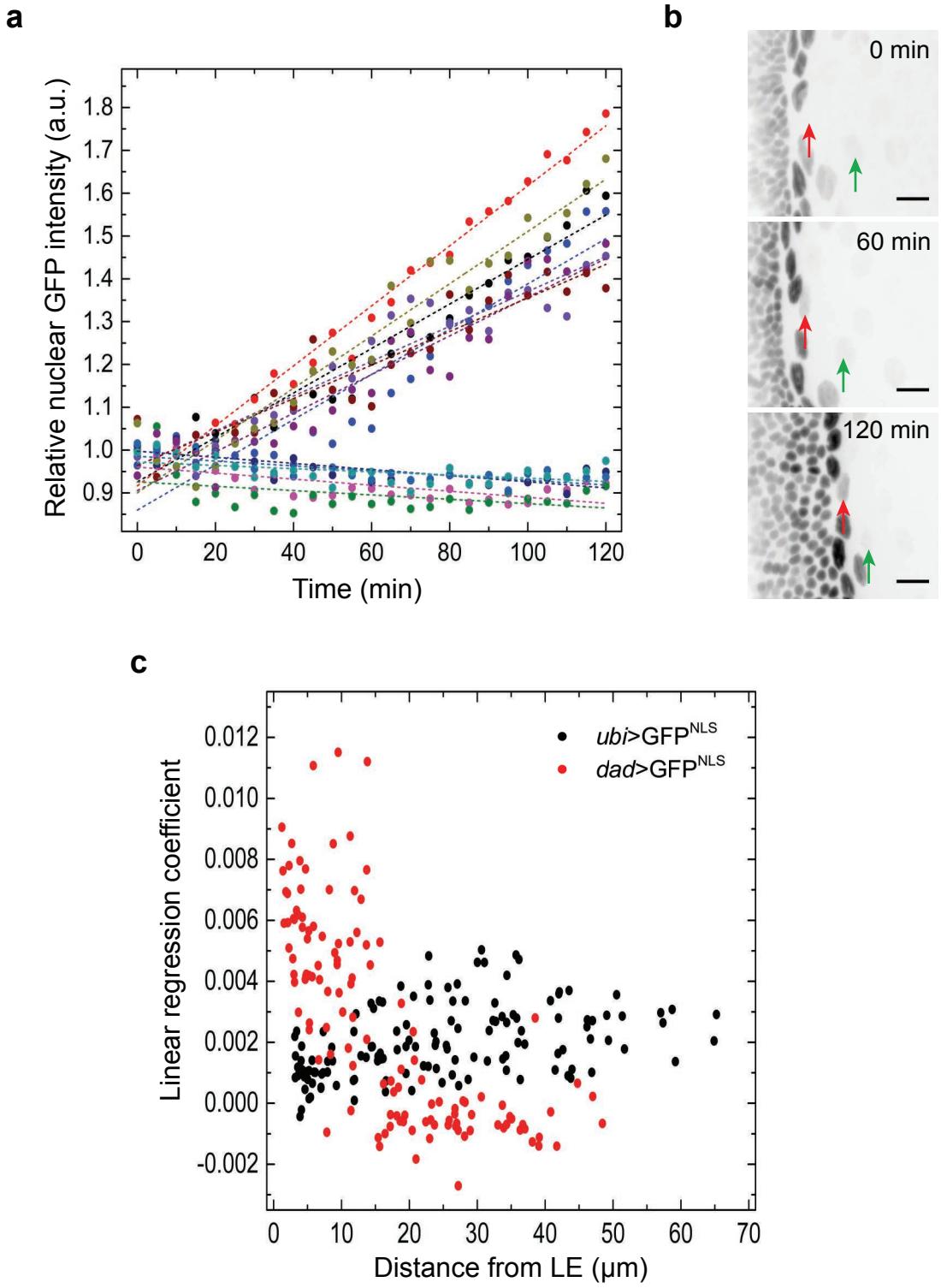

Figure 32. AS cells are responsive to Dpp, but the signalling gradient does not change over the course of DC. (a) Representative scatter plots with best-fit lines (dashed lines) showing fluorescence intensity over time in AS cell nuclei of *dad*>GFP^{NLS} embryos during the 120min of DC. Different color represents a single nucleus. **(b)** Selected movie frames of DC in *dad*>GFP^{NLS} embryos. 0 min depicts the start of analysis shown in (a) and (c). Nuclear GFP^{NLS} fluorescence increases in some AS cell nuclei (red arrow), but not in the others (green arrow). Scale bar: 10μm. **(c)** Scatter plot showing a relationship between the linear regression coefficients obtained from (a) and the initial distance of AS cell nuclei from the leading edge (LE) of the epidermis. Black dots depict nuclei from *ubi*>GFP^{NLS} embryos (n=125 nuclei from 3 embryos) and red dots depict nuclei from *dad*>GFP^{NLS} embryos (n=125 nuclei from 3 embryos).

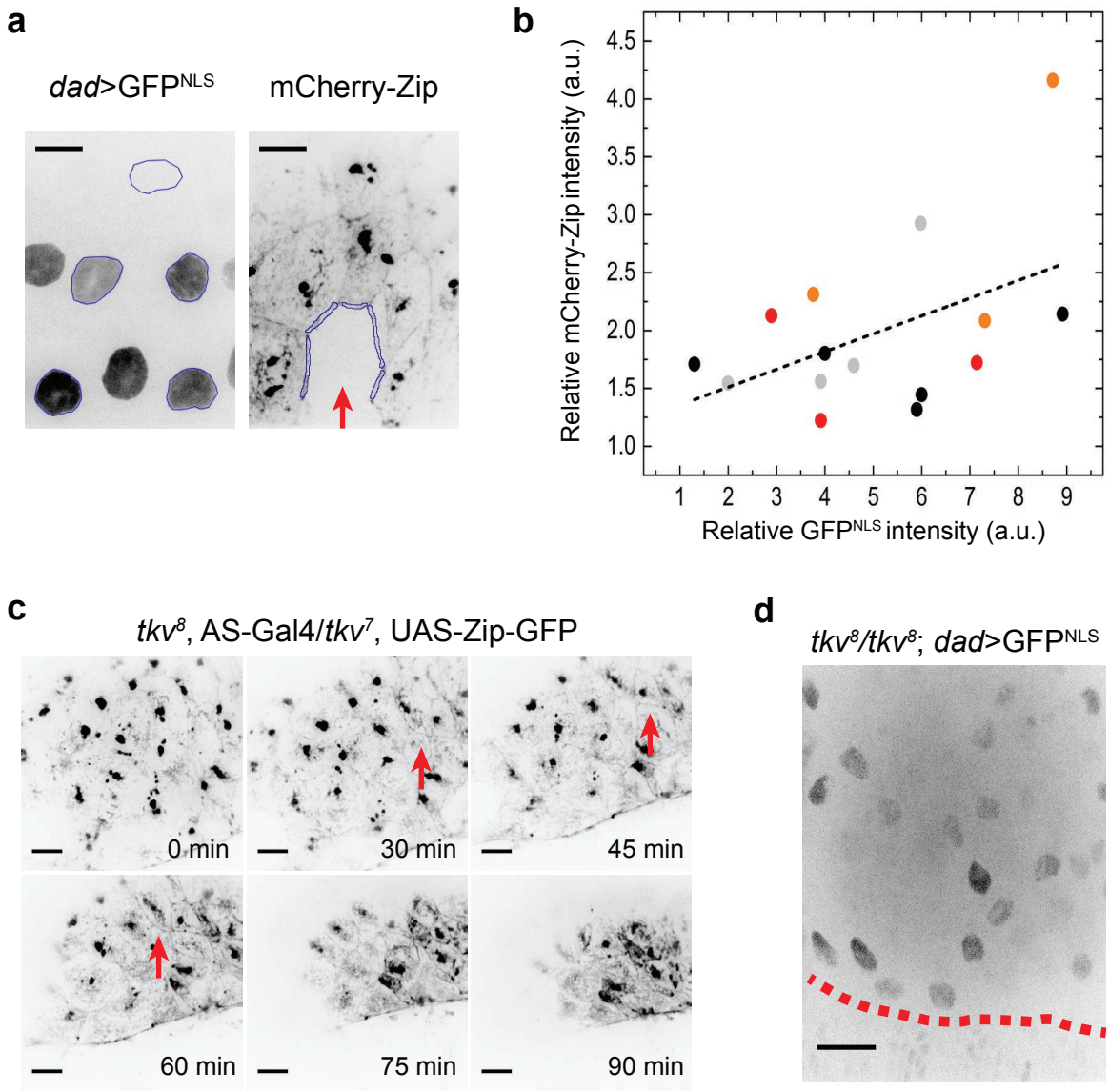

Figure 33. Dpp signaling gradient and junctional MyoII accumulation in the AS cells do not correlate. (a) Example of fluorescence intensity measurements of nuclear *dad*>GFP^{NLS} and junctional mCherry-Zip signals in the AS cells. All the neighbors next to the cell that did not express mCherry-Zip (red arrow) were chosen for analysis. Scale bar: 10µm. **(b)** Scatter plot showing a relationship between the nuclear *dad*>GFP^{NLS} and junctional mCherry-Zip fluorescence intensities. Dashed line depicts the best-fit line from all data points ($R^2 = 0.226$). Different colors represent cells from independent embryos (n=15 cells from 4 embryos). **(c)** Selected movie frames showing transheterozygote *tkv*^{8}/*tkv*^{7} mutant embryos expressing Zip-GFP in the AS cells. Zip-GFP accumulates at the AS cell-cell junctions (red arrows) in these embryos. Scale bar: 10µm. **(d)** *dad*>GFP^{NLS} signal in *tkv*^{8}/*tkv*^{7} mutant embryos. Dashed red line depicts the leading edge of epidermis. Scale bar: 20µm.

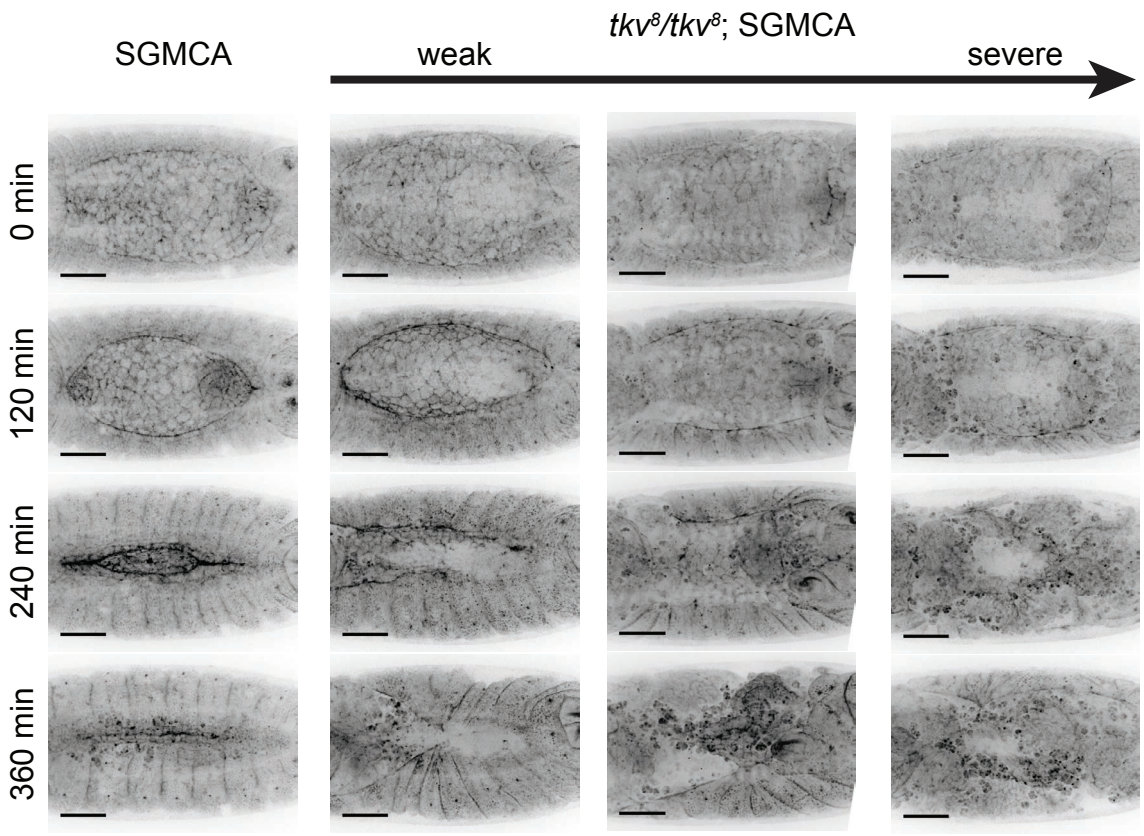

Figure 34. Zygotic mutants for Dpp receptor *tkv* exhibit differentially penetrant phenotypes during DC. Selected movie frames showing DC in control and tkv^8/tkv^8 zygotic mutant embryos. Phenotypic penetrance in tkv^8/tkv^8 embryos is highly variable. In the weak mutants, DC is nearly completed and in the severe mutants DC fails early due to multiple tissue ruptures. 0 min depicts the end of germ-band retraction. SGMCA is used to label F-actin. Scale bar: 50µm.

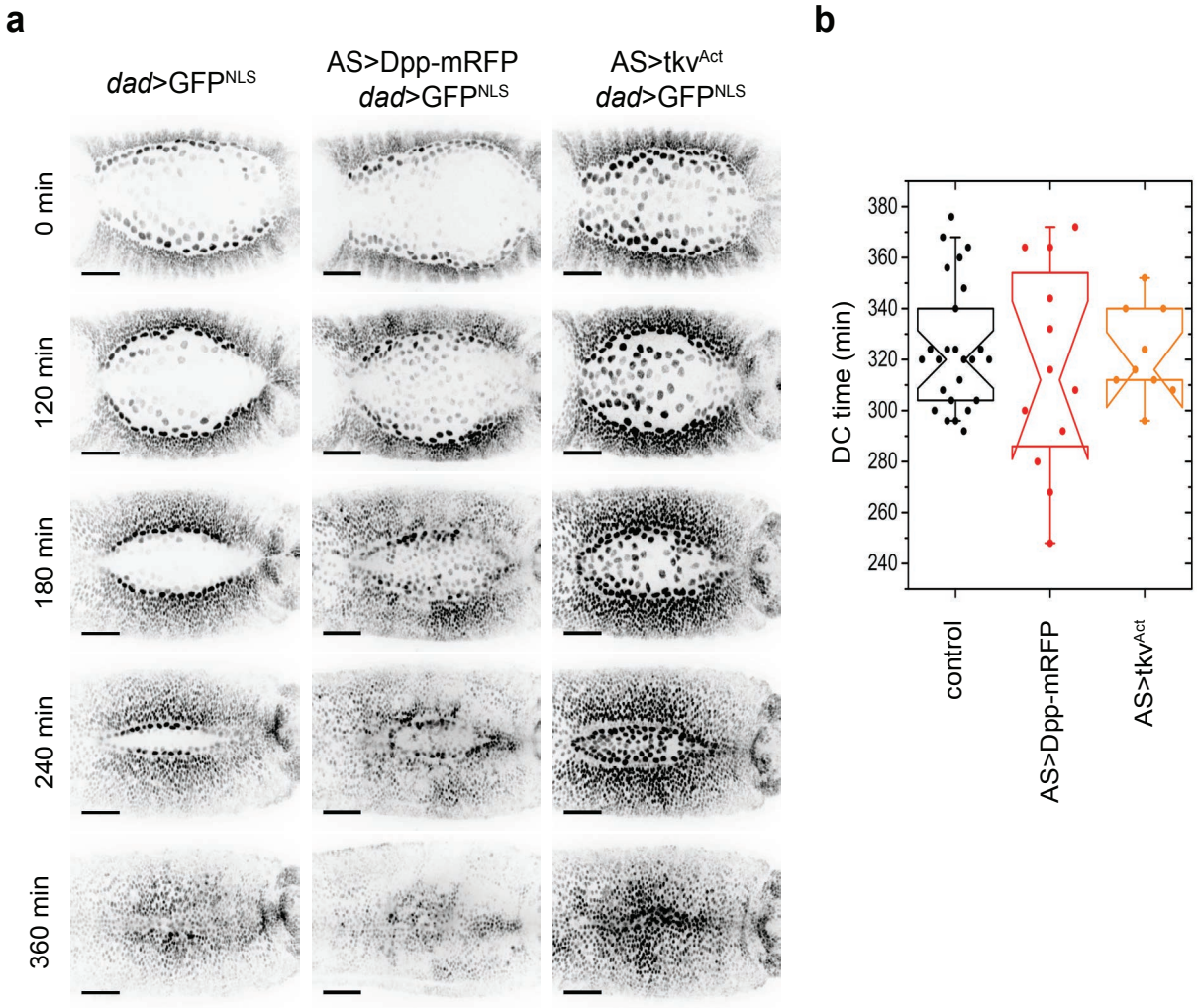

Figure 35. Ectopic activation of Dpp signaling in the AS cells does not affect DC. (a) Selected movie frames showing DC and *dad*>GFP^{NLS} signal in control embryos and embryos over-expressing Dpp-mRFP or tkv^{Act} (constitutively active Tkv) in the AS cells. 0 min depicts the end of germ-band retraction. Scale bar: 50µm. **(b)** Standard notched box plots depicting DC closure times in control embryos and embryos over-expressing Dpp-mRFP or tkv^{Act} (constitutively active Tkv) in the AS cells.

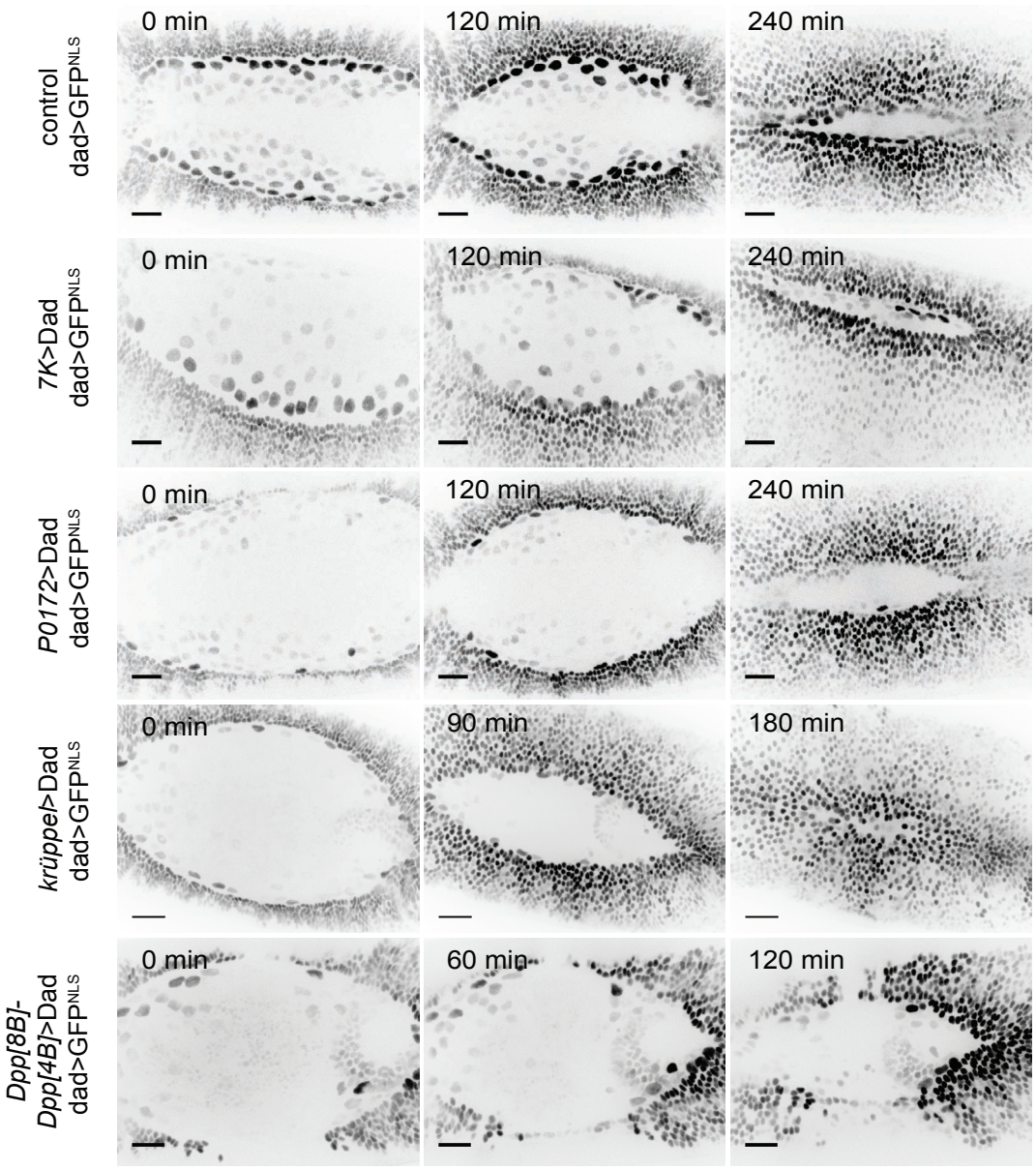

Figure 36. Inhibition of Dpp signaling in the AS cells does not affect DC. Selected movie frames showing DC and *dad*>GFP^{NLS} signal in control embryos and embryos over-expressing Dad with different AS-specific enhancer elements (EEs). 4 different EEs were used: *7K*, *P0172*, *krüppel* and tandem *Dpp[8B]-Dpp[4B]*. *dad*>GFP^{NLS} signal gradient in the AS cells is reduced or eliminated in embryos over-expressing Dad. 0 min depicts the end of germ-band retraction in control, *7K* and *P0712* embryos and the onset of DC in *krüppel* and *Dpp[8B]-Dpp[4B]* embryos. Scale bar: 20µm.

Chapter 5. The active role of the yolk cell during midgut closure in *Drosophila melanogaster*

This chapter is a manuscript in preparation.

Pasakarnis, L., Frei, E., Brunner, D.

LP and DB conceived and planned the experiments; LP performed the experiments; LP and EF generated fly strains used in the study; LP and DB analysed the data and wrote the manuscript.

5.1. Introduction

Around the same time as DC, two other closure events occur in the *Drosophila* embryo - dorsal vessel closure and midgut closure[24]. The former event involves fusion of two primordia and formation of the tubular future heart-like organ of the larva. Here, we describe in great detail, the so far neglected closure of the midgut progenitor cells (MPCs) over the large yolk cell (YC) forming the midgut of hatched larva.

Midgut closure (MC) is an essential morphogenetic event required to form the future intestinal tract of the *Drosophila* larva. So far, the process has only been roughly outlined as MPC migration over the YC that is situated in the center of the embryo[202] and therefore difficult to study. MPCs originate from the endoderm during gastrulation when the three germ-layers are formed[24]. After gastrulation, the posterior pole of the embryo shifts dorsally, initiating the process of germ-band extension. The subsequent posterior ingression internalizes the posterior midgut and hindgut primordia, whereas at the anterior pole, part of the anterior midgut primordia, invaginates together with the ventral furrow[24]. The formation of the midgut primordia from the primary endoderm is initiated by an epithelial-mesenchymal transition (EMT) and leads to cell migration along the underlying mesoderm[203,204]. Once the migrating endoderm from the anterior and posterior poles contact each other, they undergo a mesenchymal to epithelial conversion[24,204]. This leads to the formation of two cell rows that extend dorsally and ventrally to enclose the yolk cell, forming the midgut sac. After the formation of the midgut sac, three circumferential constrictions take place that generate four midgut lobes, which rotate relative to each other according to the left-right polarity cues[205].

The YC, over which the MPCs migrate, is an extra-embryonic tissue. It is consumed after midgut sac formation and will not give rise to any structures in the hatched larva[24]. Yolk-enriched cytoplasm is the main constituent of the fertilized *Drosophila* zygote, in which the maternal and paternal nuclei are embedded. The importance of yolk cytoplasm is well recognized in the early embryonic stages where syncytial nuclear divisions and genetic patterning programs take place[206]. This sets up the future body axis and segment boundaries of

the embryo[206]. During cellularization, the yolk cytoplasm is separated from the future embryonic cells by inward growing cell membranes forming the YC[24]. Post cellularization, the few dozen remaining nuclei in the YC are transcriptionally active and the expressed genes contribute to the increased metabolism that is needed to release nutrients for the developing embryo[24]. During the subsequent developmental stages, the YC is gradually re-shaped by the morphogenetic movements and squeezed towards the center of the embryo. This implicated the YC as a passive substrate for the MPC migration and overall embryogenesis.

Several studies concluded that *Drosophila* YC is only a plasma membrane–bound sack that appears to have little if any mechanical integrity when compared to epithelia like the epidermis[43]. This was concluded from piercing the embryo with a micropipette. YC content flows freely out of the wound, whereas piercing the epithelium generates a constrained wound, as expected for a mechanically robust epithelium[43]. Furthermore, the same study concluded that the mechanical forces responsible for DC reside in the AS tissue and epidermis, but not in the underlying tissues, including the YC and the endoderm. Earlier studies on *Drosophila* embryogenesis revealed that most of the AS cells lie directly above the YC[24]. The YC connection with the AS tissue is important for proper germ-band retraction and DC[105]. Several studies implicated cell surface receptors - integrins – as the key molecules holding the AS cells and YC together[97]. Loss of the integrin-dependent connection between the two extra-embryonic tissues during germ-band retraction leads to premature AS cell apoptosis[105]. The MPCs in contrast, reside 10-15µm below the basal side of the lateral epidermis on either side of the embryo as shown by electron microscopy on sectioned embryo samples[24]. This suggests that the endoderm does not interact with the AS tissue or the lateral epidermis. Even though the importance of the YC in late *Drosophila* embryogenesis is recognized, so far the behaviour of this cell has not been studied.

During embryogenesis of higher organisms, in particular zebrafish and *Xenopus*, the yolk plays a crucial role in several developmental processes[207]. A well-studied example is epiboly in zebrafish. After an initial, cell division-mediated expansion of the embryonic animal pole, the cells of the enveloping layer (EVL) migrate over the yolk to the opposite, vegetal pole of the embryo[207]. In this process, a distinct cytoplasmic layer forms in the yolk that is called the yolk syncytial layer (YSL). The YSL forms in front of the EVL and pulls on the migrating cells[208]. Two contractile acto-myosin (AM) structures are formed in the yolk during epiboly. The first is a dynamic, contractile AM network that generates a retrograde flow towards the EVL cells. The second is a contractile AM belt that later forms in the YSL in between the migrating cell front and the AM network. The former structure was suggested to be sufficient

to drive epiboly on its own if the embryo is artificially forced to become a cylinder rather than the typical sphere[111]. However, the AM belt contributes significantly once the migrating EVL cells pass the equator of the yolk[111]. It was recently suggested that cell movements similar to epiboly contribute to patterning and tissue re-arrangements in early mouse embryos[209]. In summary, in higher organisms the embryonic yolk is actively contributing to embryogenesis.

The *in vivo* study of the YC past the cellularization stage of *Drosophila* embryogenesis is a challenge. Several thick tissues obstruct the view to the inside of the embryo and light scattering induces a substantial loss of fluorescence signals. Due to these reasons it is virtually impossible to visualize the ventral side of the YC past the gastrulation stages. Therefore, previously, the YC and midgut formation were mainly analysed by electron microscopy using serial sections of fixed samples[24]. In contrast, the dorsal side of the YC is only obscured from observation by the AS tissue and the basal lamina, which makes it potentiall suitable for observation. In many of our movies with deGradFP-mediated AS tissue inactivation, which resulted in a considerable reduction of fluorescence signal and signal dynamics, we consistently imaged a second closure event below the AS tissue that had to be MC and that was barely visible in the wild type. Therefore, we decided to make use of this situation to explore MC and the role of the YC in this process using confocal microscopy. Due to the lack of efficient Gal4 enhancer elements driving gene expression in the YC, we established a method to visualize transgenes by express the Gal4 transcriptional activator from injected DNA plasmids. Live fluorescence imaging revealed a highly dynamic and active YC surface that was not observed before. We demonstrate and analyze a contractile activity of the cortical acto-myosin network that creates travelling waves of contractility along the YC surface. We also show that such contractile activity is able to transiently displace the tissues above the YC. Furthermore, we demonstrate an active role of the YC in MC and a striking overall similarity of *Drosophila* MC with zebrafish epiboly. Our observations show that the YC is not as mechanically inert as previously thought. Consequently, our study considerably revises the role of the YC during *Drosophila* morphogenesis.

5.2. Results

5.2.1. The yolk cell contributes to midgut closure

As several tissue closure events occur at the dorsal surface of the *Drosophila* embryo[24], we wanted to track the progression of these events in wild-type embryos using live imaging. To visualize DC, we used a light chain of non-muscle myosin II (MyoII) tagged with GFP (Sqh-GFP), which marks the acto-myosin cable (AMC) at the leading edges (LEs) of the epidermis. In movies showing maximum-intensity *z*-projections of DC, we noticed intense Sqh-GFP signal emmitted from tissues underneath the epidermis and AS tissues (Fig. 37A). Over time, this signal moved towards the dorsal midline very much reminiscent of a second closure event below the AS tissue. It was previously shown that dorsal vessel- and midgut closure (MC) occur during the same developmental stages as DC[24,210]. In an attempt to discriminate between these two closure events, we inhibited DC since dorsal vessel closure is known to depend on DC while a dependence of MC on DC remains to be shown[210]. We used embryos expressing deGradFP to acutely remove MyoII function selectively in AS cells (AS-SqhKO). This arrests DC, as the AMC alone does not produce enough force to complete DC on its own (Chapter 2, Fig. 4C). In AS-SqhKO embryos, we still observed the second closure event, which completed with similar kinetics as in wild-type embryos (Fig. 37A-37B). We conclude that MC occurs independently from DC and can be visualized using a live MyoII reporter.

Although in both cases a tissue closes an opening, conceptually, MC and DC appear to differ fundamentally. In DC the central AS tissue pulls the surrounding epidermis tissue together and then folds down inside the embryo to allow the latter to close over it. In MC the surrounding tissue moves over the dorsal surface of a single, large cell that does not seem to contribute much. While in DC the AS tissue is the key force provider, it is not known where the relevant forces are produced during MC. Intuitively, the most likely possibility seems that the midgut primordium actively moves over the yolk cell surface. Detailed analysis of the MC-associated Sqh-GFP fluorescence revealed that MyoII outlined an eye-shaped opening that seemed to close very similar to the opening in DC. Intriguingly, we observed an outer ring of dot-like Sqh-GFP assemblies that were aligned in a “beads-on-a-string” arrangement very much like the epidermal "pearl-string" of MyoII in DC (Fig. 38A). This suggests that the LE-cells of the closing midgut primordium form an AMC very similar to the epidermal LE-cells.

This raises the possibility that unlike DC, MC is driven by such a contractile AMC that contracts the tissue fronts, thereby closing the opening across the YC surface. Since the YC membrane can be considered a fluid surface, one can easily imagine that the connections between LE cells and YC membranes are freely movable and that little contractile force of an AMC would suffice. To further investigate this possibility, we used the *P48Y*Gal4 enhancer element in Sqh-GFP expressing embryos to express deGradFP and deplete MyoII function selectively in the cells of the midgut primordium. This led to the disappearance of the AMC in the LE cells of the midgut but did not arrest MC (Fig. 37C). This means that similar to DC the AMC is dispensable for closure of the midgut and that other crucial forces are driving the process.

Another possibility that is compatible with a passive role of the YC in MC would be autonomous expansion of the midgut primordium tissue. However, besides the MyoII pearl-string at the lE of the closing tissue, our initial analysis of Sqh-GFP fluorescence revealed two more MyoII structures. This was an additional Sqh-GFP band aligning the inside of the AMC structure and dynamic MyoII foci what appeared to form on the YC surface within the closing midgut primordium (Fig. 38A). This raised the possibility that the YC actively participates in MC. To investigate this possibility, we tried to find Gal4 enhancer elements that would allow selective deGradFP expression in the YC. Unfortunately, two enhancer elements *P0180*Gal4 and *P0181*Gal4 that were previously reported to drive YC expression, did not express UAS-driven transgenes in the YC (data not shown). As an alternative means to inactivate MyoII in the YC, we used the *P0172*Gal4 enhancer element. *P0172*Gal4 simultaneously drives Gal4 expression in the AS tissue and the YC, which should not be a problem since we have shown that MC occurs independent of MC. As expected, in such embryos (hereafter termed AS-yolk-SqhKO) we detected large Sqh-GFP aggregates in AS cells and the YC (Fig. 37A). Importantly, MC no longer occurred. Over time the AS tissue and the YC ruptured due to the developmental arrest. From this we conclude that MyoII activity in the YC is essential for MC.

5.2.2. MyoII forms dynamic contractile structures on the YC surface

In wild-type embryos, MC is optically obstructed by the AS tissue and epidermis. However, our experiments in AS-yolk-SqhKO embryos showed that the concentration of MyoII into aggregates in the overlying AS tissue made it much more transparent and significantly improved imaging the imaging of MC. Thus, we used AS-SqhKO embryos as an optimized background to visualize and explore MC with maximum-intensity *z* projections. As

aforementioned, we recognized two distinct MyoII structures on the YC: 1) large coalescing Sqh-GFP foci that moved in waves across the YC surface and 2) a thick intense band of Sqh-GFP aligning with the front of the midgut primordia and moving right ahead of it (Fig. 38A). Based on cross-sections of fixed embryos, MC was previously described as a process in which the cells of the midgut primordium move over the sphere-like YC[24]. To visualize the YC live in 3D, we again removed Sqh-GFP in both AS tissue and imaged the underlying tissues. 3D reconstructions of such embryos, confirmed the high curvature of the YC in agreement with previous electron microscopy data (Fig. 38B). Thus, we conclude that MyoII activity in the YC occurs on a highly curved cell surface.

Next, we wanted to describe the dynamics of MyoII behaviour in more detail and performed live imaging of AS-SqhKO embryos with a high spatio-temporal resolution. Sqh-GFP signal intensity in the YC was not uniform, but showed a grainy background distribution (Fig. 39A). This indicated an intricate MyoII network at the YC surface. Our analysis confirmed that the observed contractile Sqh-GFP foci and moving waves were situated below the AS cells and within the YC: When not apically constricted, as in AS-SqhKO embryos, AS cells are typically ~3µm in thickness[42]. The Sqh-GFP foci/waves however, appeared >4µm below the apical surface of AS cells (Fig. 39B). deGradFP-induced Sqh-GFP degradation in the YC abolished the formation of these foci and moving waves, confirming that these structures are dependent on MyoII (Fig. 39C). Since MyoII processivity depends on the MyoII heavy chain Zipper[5], we also looked at Zip-GFP localization in wild-type embryos. Similar to Sqh-GFP, Zip-GFP produced foci and waves ~4-5µm below the apical MyoII foci of the AS cells (Fig. 39D). This suggests that, as expected, both subunits of MyoII are involved in YC surface network contractions.

Live imaging of the YC surface over longer time periods revealed a highly dynamic behaviour of the MyoII network. We detected local accumulations of Sqh-GFP signal that in some cases occupied a substantial part of the YC (Fig. 40A). In other instances, we found travelling waves of Sqh-GFP signal that transversed long distances on the YC surface before disappearing again (Fig. 40A). Since MyoII structures are very dynamic and appear in a rather stochastic manner, we quantified their main characteristics. To measure the periodicity of foci appearance, we defined 20µm x 20µm regions on the YC surface in AS-SqhKO embryos and measured Sqh-GFP intensity over time (Methods, section 6.5.3). Since the intensity of the Sqh-GFP signal that appeared in the YC was significantly higher than the Sqh-GFP degradation aggregates in AS cells, we could obtain fluorescence profiles with intensities oscillating over time. We then measured the periods between the peaks in the auto-correlation function of the

signal. On average, MyoII structures on the YC surface appear approximately once every 10min (Fig. 40B). However, the distribution is Gaussian-like and in some regions and time windows higher or lower wave frequencies exist (Fig. 40B). Next, we measured the average travelling speed of the MyoII waves. We defined a travelling wave as Sqh-GFP accumulation that travelled from one point on the YC surface to another. The average speed of travelling MyoII waves is ~0.25µm/sec (Fig. 40C), yet there is also a certain level of variability.

During development, pulsed, contractile MyoII foci were shown to produce mechanical forces that cause cell surface deformation[16,22]. Thus, we hypothesized that Sqh-GFP foci in the YC are also generating mechanical forces and are under tension. To estimate the extent of such forces, we performed laser ablations of the coalescing Sqh-GFP foci. When ablating the central area of the focus, we detected that outer parts rapidly recoiled, away from the laser ablation site (Fig. 41A). This confirms that the whole coalescing structure is under contractile tension.

We similarly used laser incisions to probe the second MyoII structure we had observed in the YC, the thick cable next to the leading edge of the midgut cells (Fig. 41B). Since the cable surrounds the YC opening, we reasoned that it should transmit tension anisotropically around the circumference of the opening. When ablating this MyoII cable, the released free ends recoiled away from the cut site along the leading edge of the closing primordium (Fig. 41B)[42]. The response is strikingly similar to cutting the supra-cellular acto-myosin cable in the LE of the dorsal epidermis (Chapter 2, Fig. 11C). Within several minutes following laser ablation, the MyoII cable was repaired (Fig. 41B). This demonstrates that the MyoII cable in the YC provides line tension all along the entire opening outlined by the midgut cells.

5.2.3. Contractile MyoII activity in the YC affects AS tissue and the dorsal epidermis

Previous mechanical jump experiments that ablated large tissue areas suggested that mechanical properties of the YC or the endoderm do not contribute to DC[43]. This is inconsistent with the results that MyoII foci on the YC surface are contractile and under tension (Fig. 41A). In addition, MyoII contractility dramatically alters the shape of the YC, especially towards the final stages of MC (Fig. 41C). Thus, we reasoned that the contractile forces from YC MyoII foci can be transduced to other tissues. In principle, force transduction is possible since the AS tissue and the YC are separated only by the basal lamina (BL)[97]. Moreover, both extraembryonic tissues are connected to the BL via integrins that are able to transduce

mechanical forces[97]. To unambiguously follow MyoII foci in the YC, we used AS-SqhKO embryos. The AS cells in these embryos should be mechanically passive, as they do not produce any apical surface contractions (Chapter 2, Fig. 8A). We observed transient displacement of AS cells after Sqh-GFP waves on the YC surface passed below them (Fig. 42A). AS cell junctions were pulled towards the approaching Sqh-GFP wave and moved back after the wave dissolved (Fig. 42A). Thus, we conclude that the AS tissue is distorted as a result of the mechanical forces produced by the contractile MyoII waves in the YC.

To quantify the extent of such transiently applied forces, we tracked the movement of apical AS cell surface area centroids in AS-SqhKO embryos (Methods, section 6.5.4). To outline cell adherens junctions, we used mCherry-moesin that labels F-actin and is enriched at the junctions. Cell centroids were transiently displaced on average about every 5-6min (Fig. 42B). The observed frequencies were in line with those of MyoII foci appearance (Fig. 40B). In ~55% of cases, the area centroids were displaced by >0.5μm and in ~15% of cases by >1μm (Fig. 42D). In wild-type embryos, AS cells undergo pulsed contractions that change the cell's apical surface area[36]. To compare centroid displacement values in the AS-SqhKO embryos with the wild-type AS cells, we measured AS cell area centroid displacements in the control embryos. The sudden displacements were more irregular and the overall values were higher than in AS-SqhKO embryos (Fig. 42C). In ~82% of cases centroids were displaced by >0.5μm and in ~51% of cases by >1μm (Fig. 42D). To confirm that centroid displacements in AS-SqhKO embryos are due to the contractile MyoII activity in the YC, we tracked them in AS-yolk-SqhKO embryos. The average centroid displacement values were significantly lower than in control and AS-SqhKO embryos (Fig. 42C). Only in ~16% of cases, centroids were displaced by >0.5μm in AS-yolk-SqhKO embryos (compared to ~55% and ~82% in control and AS-SqhKO embryos respectively) (Fig. 42D). Only in ~1% of cases, centroids were displaced by >1μm in AS-yolk-SqhKO embryos (compared to ~15% and ~51% in control and AS-SqhKO embryos, respectively) (Fig. 42D). Thus, we conclude that contractile MyoII foci in the YC are able to transmit mechanical forces via the BL to transiently deform the overlying AS tissue.

Next, we hypothesized that MyoII foci in the YC would also exert mechanical forces on the dorsal epidermis. To exclude any influence from the contractile AS tissue, we used AS-SqhKO embryos, in which AS tissue tension is severely reduced such that AS cells do not pull on the epidermis (Chapter 2, Fig. 8D-8F). To track and quantify the displacement of the dorsal epidermis LE, we used particle image velocimetry (PIV, Methods, section 6.5.5). Upon MyoII foci appearance in the YC, the LE was suddenly pulled towards these foci (Fig. 43A). After

the foci in the YC disassembled, the LE moved back to its initial place (Fig. 43A). In AS-SqhKO embryos the AMC of the LE is under tension (Chapter 2, Fig. 4D). To exclude that the observed transient LE movements in AS-SqhKO embryos are due to AMC contractility, we inactivated MyoII in both AS and epidermis tissues. Using PIV, we still detected LE movements that correlated with the appearance of contractile MyoII foci in the YC (Fig. 43B). Overall, this demonstrates that the LE of the dorsal epidermis is affected by YC contractility in addition to the AS tissue.

5.2.4. Contractile MyoII waves in the YC do not need concomitant actin polymerization waves

So far we had used *P0172*Gal4 to drive gene expression in the yolk cell, which always included co-expression in the AS tissue. Attempts to use this construct for ectopic expression of a GFP-tagged form of the MyoII heavy chain Zipper (Zip-GFP) caused massive aggregation of the protein (data not shown). We reasoned that constitutive transcription in the multiple YC nuclei leads to a massive amount of overexpressed protein that eventually aggregates. To be more YC-specific with transgene expression and to have more options to control the amount of expressed Gal4 protein, we changed strategy and decided to inject plasmids carrying *gal4* under the control of the ubiquitous tubulin promoter (*tub*>Gal4) into syncytial blastoderm stage embryos and imaged during DC (Methods, section 6.5.6). Unfortunately, after injecting *tub*>Gal4 plasmid into embryos expressing Zip-GFP under UAS promoter control, Zip-GFP still aggregated (Fig. 44A). In contrast, in embryos expressing Sqh-GFP under UAS promoter control, we could detect only very weak MyoII fluorescence in the YC (data not shown). This indicates that different P-element based UAS promoters have different accessibilty for the Gal4 transcriptional activator. Nonetheless, we conclude that plasmid injection into the YC in principle allows selective expression and visualization of proteins in the YC.

Due to the weak Sqh-GFP signal resulting from *tub*>Gal4 plasmid injections we bypassed the Gal4-UAS system altogether by injecting a plasmid that contained GFP-tagged Sqh expressed under the control of the endogenous *sqh* regulatory sequences (*sqh*:Sqh-GFP)[211]. In the injected embryos we observed good Sqh-GFP signal in the YC although it was less intense than the Sqh-GFP signal in AS-SqhKO embryos (Fig. 44B). Having established YC-specific labelling in wild-type embryos, we went on to describe YC dynamics further. Force generation by MyoII motors depends on filamentous actin networks[6,7]. A good example is the

aforementioned apical MyoII foci during pulsed AS cell surface contractions, which correlate with the F-actin foci[38,39]. Thus, we hypothesized that the acto-myosin network should behave similarly during YC surface contractions. Unfortunately, over-expression of F-actin reporters such as lifeAct-GFP or mCherry-moesin with YC-specific enhancer elements did not reveal any F-actin (data not shown). We reasoned that either the amount of expressed actin reporter was too low to clearly visualize F-actin or that the UAS-driven transgenes were not accessible to the endogenous Gal4 transcriptional activator. Thus, we injected *tub*>Gal4 plasmids at a needle tip concentration of 1mg/1µl into the embryos carrying the UAS-LifeAct-GFP transgene[212]. In this way, we could detect F-actin structures. Quite striking was a dense and dynamic network of filopodia at the surface of the YC (Fig. 44C). However, we did not observe any apparent actin nucleation bursts (ANBs) on the surface of the YC as seen in AS cells (Chapter 3, Fig. 13A). Also, we could not detect any travelling waves even in the deeper *z* planes below the filopodia. The only dynamic changes we observed were transient local concentrations of the filopodia, revealing YC surface deformations as could only be caused by MyoII-induced contractions of the YC surface (Fig. 44C). These observations suggest that the contractile MyoII foci and waves we observed, do not require concomitant actin nucleation and indicate that MyoII acts on a stable F-actin network.

When imaging YCs expressing LifeAct-GFP towards the final stages, the geometry of the system allowed imaging part of the YC that lie below the moving endoderm. This revealed that in this region the YC surface became remodelled. Thereby, the dense filopodia network switched to what looked like an "imprint" of the midgut cells (Fig. 44C). The change was apparent along the putative boundary between the YC and the midgut. This shows that the YC surface consists of different functional domains. Consistently, we did not observe Sqh-GFP foci or waves on the YC surface that passed beyond the thick MyoII cable next to the leading edge. These observations suggest that the LE of the endoderm somehow generates a boundary that divides the YC surface and restricts its activities into different domains.

5.2.5. MyoII contractility and midgut closure occur on the basal YC membrane

Despite generating very similar contractile MyoII foci and waves that transiently deform the cell surface in a pulsed fashion the underlying actin dynamics differ significantly between the YC and AS cell surfaces. To explore what might cause this difference we investigated YC polarity. To visualize the apical surface of the YC, we injected *tub*>Gal4

plasmid into a *Drosophila* strain expressing the apical membrane reporter Bazooka-GFP (*baz*), a Par-3 homologue, under the control of the UAS promoter. In AS cells, Baz-GFP localized mainly to the adherens junctions separating apical and baso-lateral cell surfaces and was present also in a few small punctae on the apical cell surface (Fig. 45A). In contrast, in the YC all Baz-GFP accumulated into numerous small punctae present in a high density all over the visible YC surface (Fig. 45A). The appearance and distribution resembles the endocytic Baz punctae being endocytosed from the basal cell surface in numerous epithelial tissues[213]. Thus, we used *tub*>Gal4 plasmid injection to express and visualize a GFP-tagged version of the basolateral membrane reporter Discs-large (Dlg-GFP) in the YC. Dlg-GFP fluorescence labelled the entire visible YC cell surface (Fig. 45B). Because of tissue-induced light scattering, we were unable to simultaneously image the ventral side of the YC. Nevertheless, our results provide strong evidence that dorsal MC is driven by YC membrane with basal/basolateral identity. This provides an explanation for the differences in F-actin organization.

5.2.6. The YC membrane is endocytosed towards the end of MC

The reduction of exposed YC surface during MC posed the question what happens to the membrane over time. It could either fold up, flow past the boundary defined by the moving LE of the endoderm, or it could diminish by endocytosis. To check for evidence of endocytic activity, we followed the appearance of dlg-GFP labelled YC membrane throughout MC. Only towards the final stages of MC we detected multiple blebs of YC membrane with reduced dlg-GFP intensity, reminiscent of cell membrane invaginations associated with endocytosis (Fig. 45C)[214]. This suggests that a membrane remodelling process occurs towards the end of MC. In addition to membrane blebs, we detected "imprints" of the midgut cells similar to those we had seen with LifeAct-GFP (Fig. 44C). Thus, we conclude that towards the end of MC, YC membrane undergoes remodelling and likely shows increased endocytosis.

5.3. Discussion

Tissue closure events are found throughout the development of numerous metazoan species. Here, we describe in detail one such closure event in *Drosophila* where midgut cells are closing over the large YC surface. For the first time, we demonstrate the contractile activity of the YC and its role in facilitating the midgut closure (MC).

Cell movements over the large cell surfaces are described in processes like epiboly in zebrafish and gastrulation in *Xenopus*[215]. In both cases cell re-arrangements occur on the huge yolk that forms the scaffold on which the embryo develops. Here, we describe a similar instance in *Drosophila* embryo, whereby midgut cell movements occur on the large YC. In contrast to zebrafish and *Xenopus*, MC occurs inside the embryo. Consequently, the previous analysis was hampered by the tissues covering the YC - mainly the AS and dorsal epidermis. We show that clear visualization of MC only becomes possible when MyoII activity and fluorescence was depleted in the epithelial tissues above the YC. Similar to the epiboly in zebrafish, we find two distinct populations of MyoII on the YC surface - a rapidly re-arranging cortical AM network and a constricting AM cable next to the moving endoderm. Furthermore, both MyoII waves and the thick cable are under tension, which is comparable to the tensioned structures observed in the zebrafish YSL. In contrast, we did not detect a clear directionality or the flow of actin/MyoII in the YC towards the moving midgut. In epiboly, a retrograde AM contractility flow was shown to act against the frictional force provided by YSL, to drive the movement of epithelia on top[111,208]. Interference with the AM network contractility perturbs the epithelial movement[111]. Similarly, we show that depletion of MyoII activity in the YC prevents the MC. At the moment, we cannot rule out any of the two MyoII populations in the YC as being not essential for producing closure forces. We conclude that the midgut closure over the yolk cell in *Drosophila* is morphologically similar to epiboly in zebrafish embryos.

Several mechanisms alternative to AM contractility were suggested to drive cell movements during zebrafish epiboly[207,216]. In particular, a polarized gradient of cortical tension combined with cytoplasmic flows were observed in the yolk, which contribute to pulling forces as epiboly progresses[216]. In addition, a reduction in the yolk membrane surface was proposed to contribute to the advancement of the EVL front[207]. We observe similar endocytic activity of the YC membrane during the last stages of the MC (Fig. 45C). Whether this activity contributes to the closing force in *Drosophila* is yet to be shown.

Cross-sections through embryos at the DC stage revealed that most AS cells lie directly on top of the YC[24]. However, the YC was thought to be inert and not to contribute to the tension and mechanical properties of the embryo. Such a conclusion is inconsistent with the excessive contractile activity of the YC surface. First, the extreme curvature of its spherical surface should apply pressure to the AS tissue situated on top. Second, contractile MyoII waves on the YC surface move the AS cells and the epidermis suggesting that the YC applies external forces to DC tissues. Third, we have previously suggested that the entities below the apical AS cell surface contribute to the superficial tissue tension directionality, which are observed if a clean

laser ablation is done through the AS monolayer[86]. Interestingly, contractile MyoII wave patterns on the YC surface could account for such directionality. Further detailed quantitative analysis is required to probe the exact YC contribution to DC. Nevertheless, our results require the revisiting of the role of the YC during *Drosophila* morphogenesis and stresses the necessity of a holistic view of the embryonic development.

MC (i.e. midgut closure over the YC) resembles DC (i.e. epidermis closure over the AS tissue). We showed that the YC provides pulling force on the midgut cells and is needed for MC to take place (Fig. 37A). Thus, conceptually, the YC re-capitulates the function of AS tissue, but instead of multiple cells providing the pulling forces, a single YC is doing that. Similarly, contractile MyoII waves on the YC surface resemble the contractile MyoII foci on the apical AS cell surface. However, one interesting difference emerges - in the latter, actin nucleation bursts (ANBs) are also present, whereas we could not detect them in the YC. This suggests that MyoII organization into travelling contractile waves or foci can occur on either the pre-existing actin cortex or via the concomitant *de novo* polymerization of actin. In the case of the YC, MyoII could merely contract the pre-existing F-actin network without the need of transient and excessive actin polymerization. Whether the apico-basal cell polarity cues are instructing differing AM dynamics and can be generalized to all the other tissues is yet to be shown. Interestingly, recent studies on *Drosophila* oocyte maturation revealed MyoII-dependent contractions of the basal cell surfaces that involve very little *de novo* actin polymerization[217]. This bears a striking resemblance to the AM dynamics in the YC.

Discovery and easy visualization of YC contractile activity and MyoII surface waves opens up opportunities to study AM dynamics on a much larger scale than was done before. The YC is huge compared to a typical epithelial cell like the AS, and one can investigate the AM network structure (Fig. 39A) and behaviour much clearer. In collaboration with Rajaa Boujemaa-Paterski, we have already started to explore the activity of the AM network and its constituents in reconstituted *in vitro* actin systems[10,218]. Vice versa, the injection of various compounds or purified AM constituents is relatively straightforward. The YC could become a natural *in vivo* test-tube for the development and validation of novel compounds. In summary, MC is a unique model system for studying closure events and tissue biomechanics *in vivo*.

5.4. Future directions

MC greatly resembles epiboly in higher organisms, where the two main AM structures in the yolk drive the migration of EVL cells (see Section 5.3). To probe the importance of similar AM structures – the thick AMC band and MyoII waves - in the YC, it is essential to acutely remove one structure leaving the other intact and functional. In a way, it would be similar to the tissue-specific MyoII depletion during DC that we have performed (Chapter 2). Yet the YC is a single cell and, thus, tools for subcellular MyoII inactivation are needed.

We have shown that mechanical forces from the contractile YC surface are transduced to the epidermis and the AS tissue (Fig. 42-43). However, all the experiments involved MyoII depletion in these tissues and did not allow testing their resistance against these mechanical forces. Thus, it is important to determine the contribution of the YC to wild-type AS and epidermis tissue behaviour. For this, quantitative analysis of AS cell behaviour is needed to discriminate between the effects of the YC and those produced by mechanical forces of the apical AS cell surfaces. Pulsed AS surface contractions dominate the apical plane of the tissue. However, the basal AS cell behaviour is not well understood and could provide a link to study YC effects on the AS tissue and DC. For this, acute inactivation of MyoII either with pharmacological drugs or protein inactivation methods exclusively in the YC is necessary.

In addition, we have suggested that the directionality of AS tissue tension when cut through the cell monolayer depends either on the basal lamina or the YC. Contractile MyoII waves in the YC often occur in a pattern-like appearance (data not shown). Thus, the next critical step would be to quantitatively analyse wave pattern formation in the YC and systematically induce laser ablations through the AS monolayer. This would allow correlation analysis between local YC contractions and the tension anisotropy in the AS cells. Quantitative analysis also revealed a heterogeneity in the foci appearance and their spreading. Thus, a more elaborate investigation is needed to probe the spatio-temporal differences in MyoII behaviour on the YC surface.

Towards the end of MC, we have observed a likely endocytic activity of the YC membrane. To confirm this, endocytic reporters need to be introduced into the YC. During epiboly in zebrafish, endocytic activity of the YSL was shown to contribute to the pulling forces on the EVL cells[207]. Whether YC membrane endocytosis provides closing forces during MC is yet to be shown. Classical zygotic mutants affecting endocytosis could provide a hint if this is the case. However, these mutants are generally very severe and embryos fail to reach the DC

stage. Thus, an acute inactivation of endocytic activity is required - either with pharmacological compounds or protein inactivation tools.

MC is a 3D process, yet so far we have only described the dorsal part of it. Light scattering properties of the ventral *Drosophila* embryo tissues prevent analysing the ventral closure of the midgut. However, with the advancement of new light microscopy techniques, in particular, SPIM (single-plane illumination microscopy), it is feasible to capture the complete midgut closure. If the ventral midgut and the YC behave the same as dorsally, it would be interesting to understand how such bi-polarity is established in the single cell provided it only has a single surface of the basolateral identity.

5.5. Summary of the key findings/hypotheses of Chapter 5

- MC can be visualized by depleting Sqh-GFP fluorescence signal in the AS and epidermis tissues.
- MyoII activity in the YC is required for MC
- Several contractile MyoII structures form on the dorsal YC surface
- MyoII foci and travelling waves transverse the YC surface during the MC
- Mechanical forces from the YC are transmitted to the AS and epidermis tissues above
- MyoII foci do not need concomitant actin polymerization bursts, but rather contract the pre-existing network
- The YC membrane and the actin network form an "imprint" of the midgut cells
- MC is a closure over the basal surface of the YC
- YC membrane endocytosis is increased towards the late stages of MC
- The YC could be exploited as a novel *in vivo* test-tube for studying AM dynamics

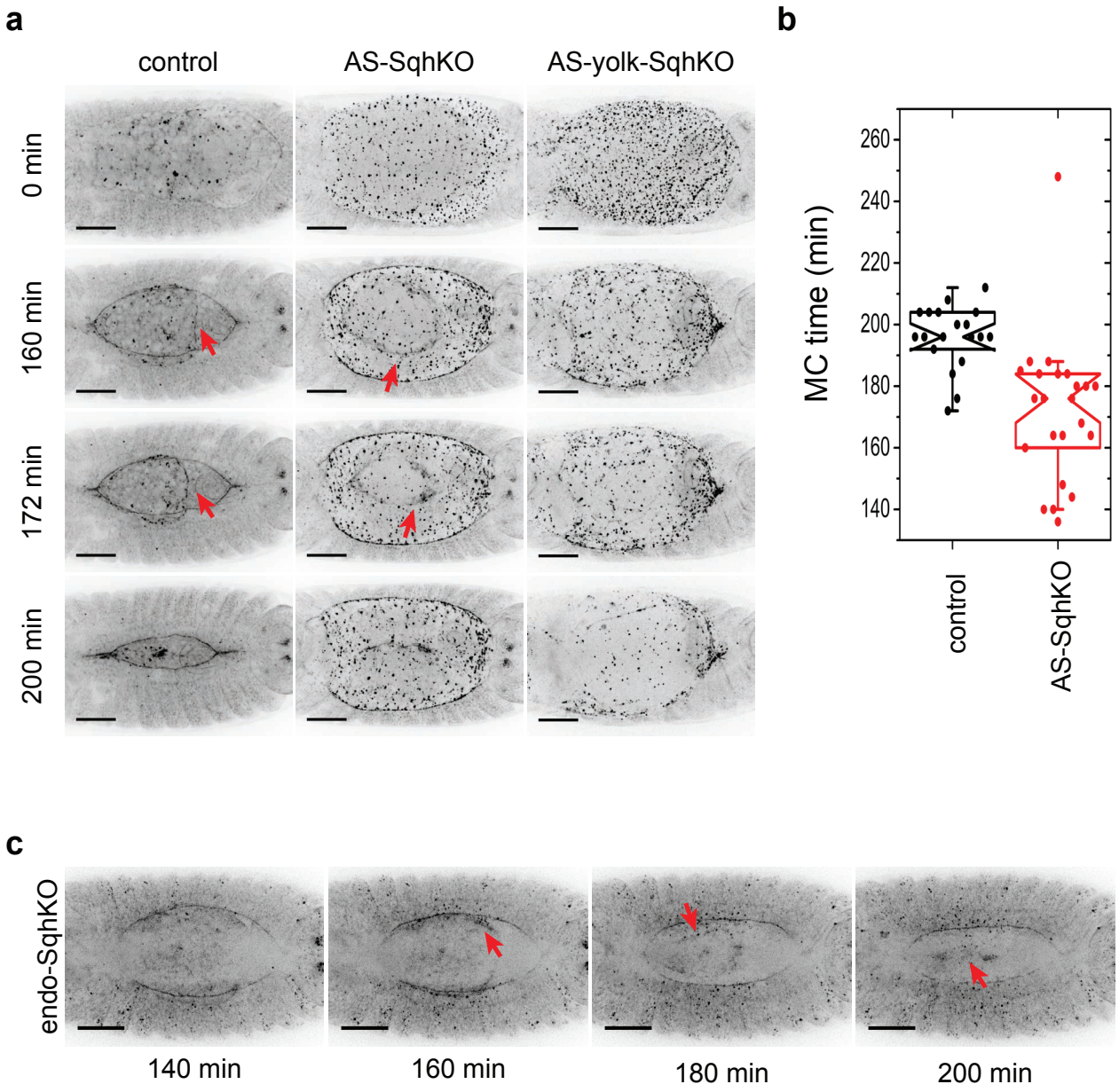

Figure 37. Midgut closure (MC) occurs independently of dorsal closure (DC) and requires MyoII activity in the yolk cell (YC). (a) Selected movie frames showing DC stage and progression in control, AS-SqhKO and AS-yolk-SqhKO embryos. A secondary closure event (red arrows) occurs beneath the AS tissue in control and AS-SqhKO embryos, but not in AS-yolk-SqhKO embryos. Scale bar: 50µm. **(b)** Standard notched box plots showing relative MC times in control (black, n=19) and AS-SqhKO embryos (red, n=23). **(c)** Selected movie frames showing DC in endo-SqhKO embryos. First frame depicts 140min after the end of germ-band retraction. Scale bar: 50µm.

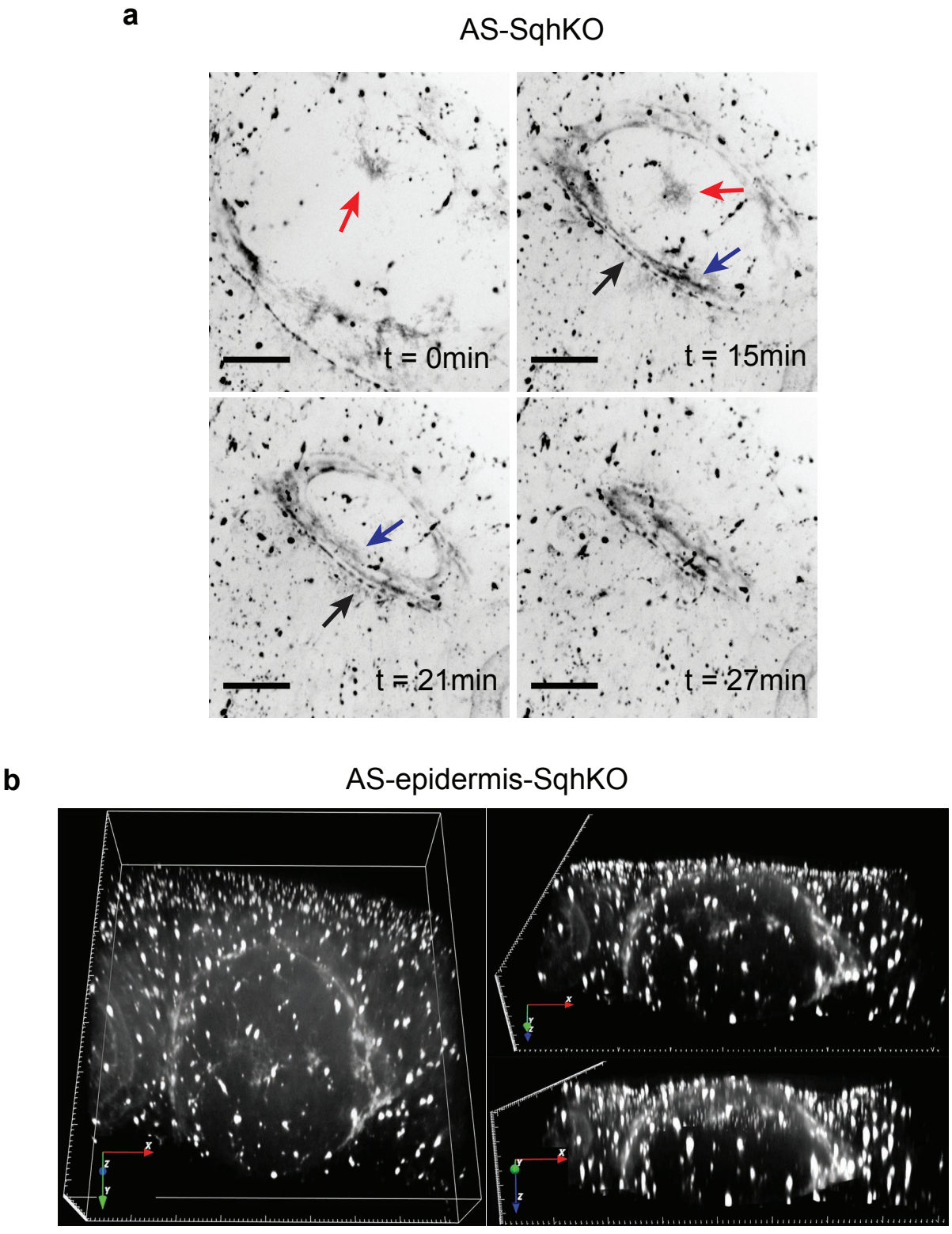

Figure 38. MC can be visualized in detail by depleting Sqh-GFP fluorescence in the AS and epidermis tissues. (a) Selected movie frames showing MC in AS-SqhKO embryos. Several Sqh-GFP structures are seen in the yolk cell (YC): coalescing foci (red arrows) and a thick band next to the leading edge of the midgut (blue arrows). In the midgut cells Sqh-GFP localizes as a "beads-on-a-string" pattern (black arrows). 0min depicts an arbitrary movie frame used as reference. Scale bar: 20μm**. (b)** 3D reconstruction of the YC in AS-epidermis-SqhKO embryos. Different 3D orientations are depicted and illustrate the curvature of the YC

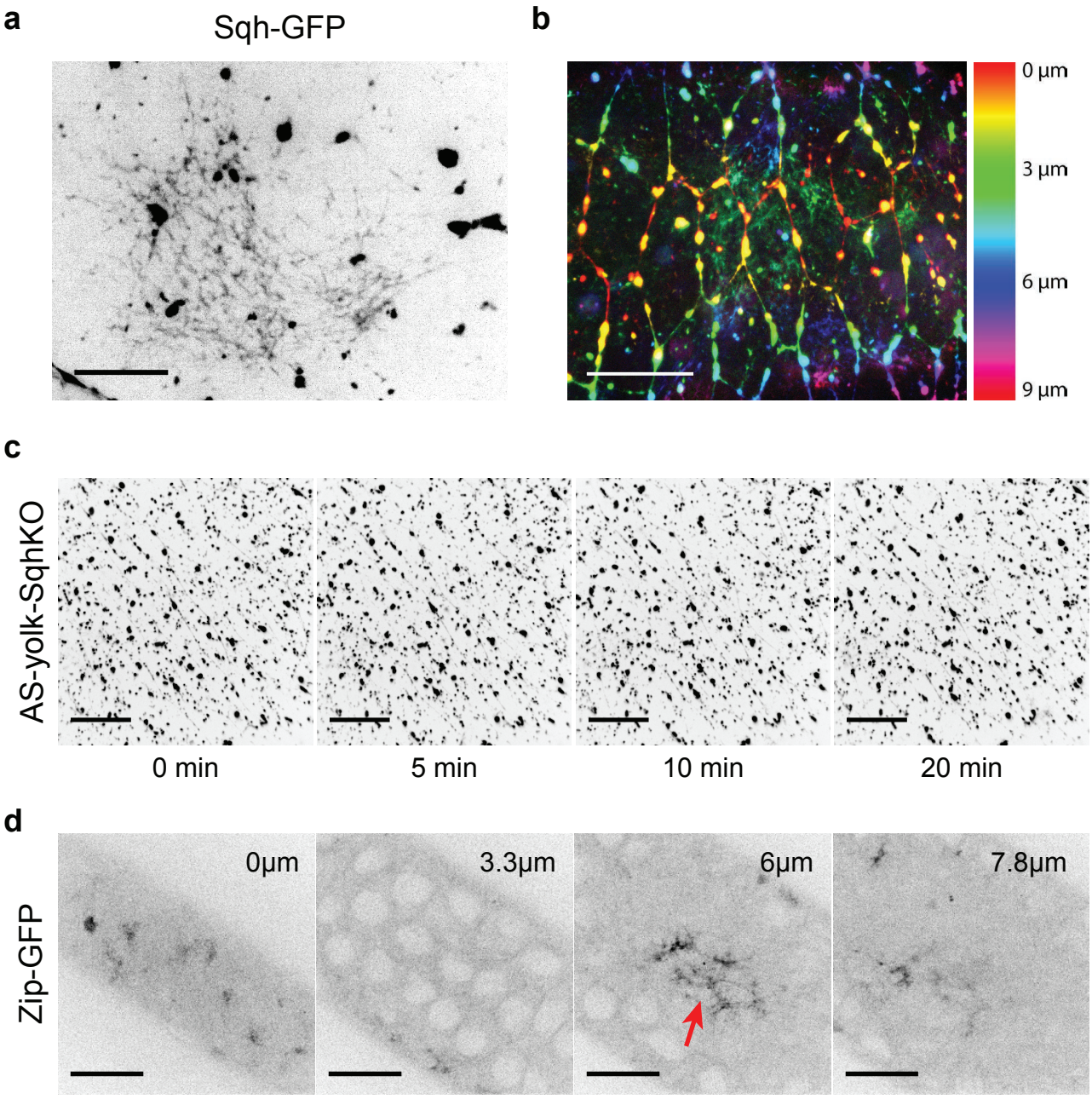

Figure 39. Network-like MyoII appearance in the YC depends on its light chain, but also incorporates the heavy chain. (a) Image from AS-SqhKO embryos showing Sqh-GFP localizing into an intricate network. Scale bar: 10µm. **(b)** Image from AS-SqhKO embryos showing differently color-coded planes of the confocal Z stack. The planes representing apical surface of AS cells are labelled in red/orange (0-1µm) and the coalescing Sqh-GFP foci in the YC are labelled in green/blue (4-5 µm). Scale bar: 20µm. **(c)** Selected movie frames showing the YC in AS-yolk-SqhKO embryos. The coalescing Sqh-GFP foci are absent in the YC. Scale bar: 20µm. **(d)** Selected single planes of confocal Z stack showing apical Zip-GFP foci in the AS cells (0µm) and coalescing Zip-GFP foci in the YC (6µm). 0µm depicts the apical AS cell surface. Scale bar: 20µm..

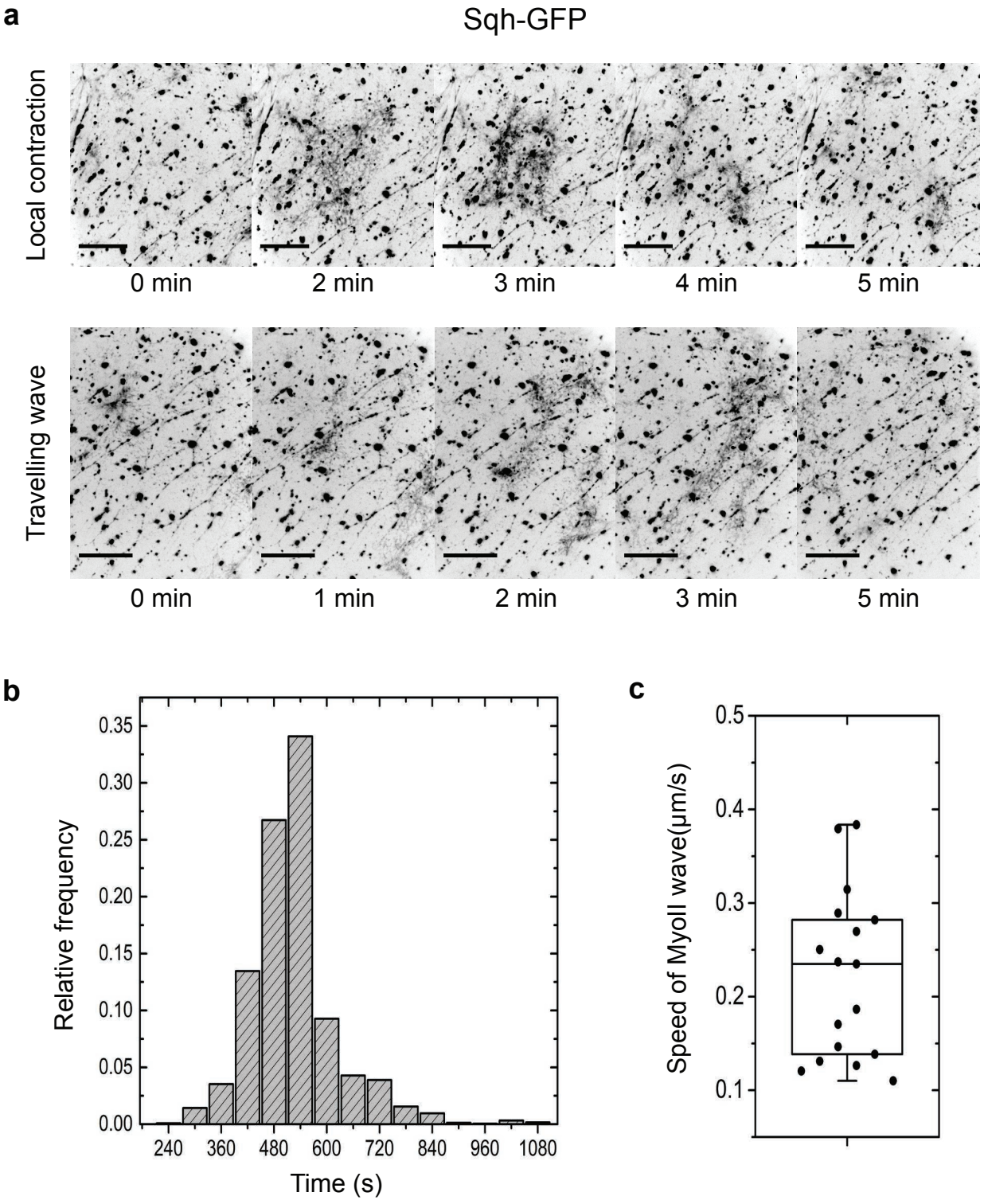

Figure 40. MyoII forms local transient foci and travelling waves in the YC. (a) Selected movie frames showing transient Sqh-GFP structures in the YC in AS-SqhKO embryos. Top: an example of the appearance and dissolution of a local Sqh-GFP focus. Bottom: an example of a travelling Sqh-GFP wave. **(b)** Relative frequency histogram of MyoII foci appearance in the YC. n=2526 periods from 42 regions in 3 embryos. **(c)** Box plot showing the speed of travelling MyoII waves in the YC. Middle line represents median, box represents 25-75 percentiles, whiskers represent 5-95 percentiles. n=17 waves from 3 embryos.

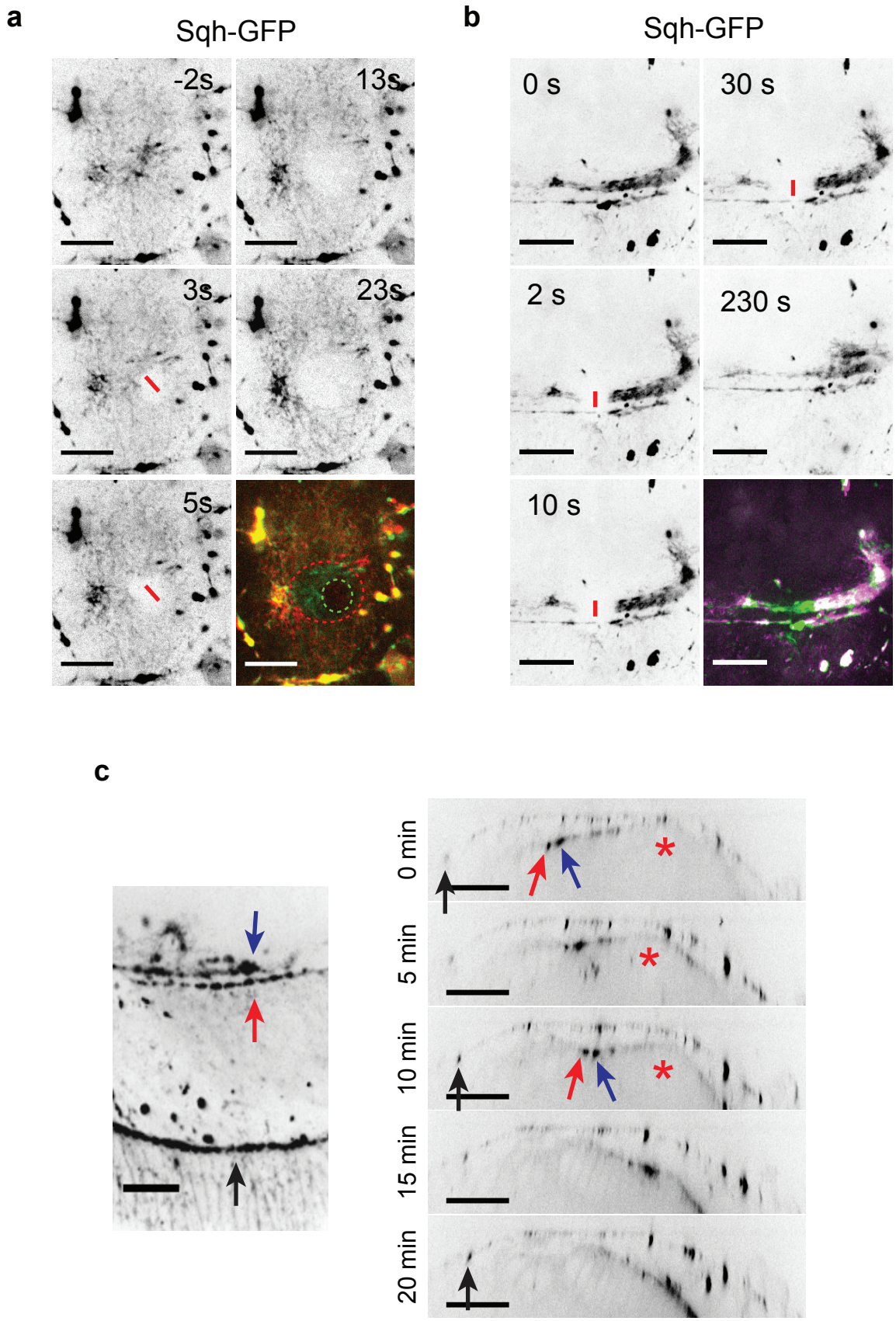
a
Sqh-GFP
-2s
13s
3s
23s
5s
b
Sqh-GFP
0 s
30 s
2 s
230 s
10 s
c
0 min
5 min
10 min
15 min
20 min

Figure 41. MyoII structures in the YC deform the cell surface and are under tension. (a) Selected movie frames showing a laser incision (red line) in the Sqh-GFP focus. The ablated area expands over time (overlay image). The first frame shows 2s before the incision is made, the subsequent frames shows 3, 5, 13 and 23s after the incision. Green in the overlay depicts the frame taken at 3s, red in the overlay - 23s after the incision was made. The green dashed line depicts the ablated area at 3s, the red dashed line depicts the ablated area 23s after the laser incision. **(b)** Selected movie frames showing laser ablation (red line) of the Sqh-GFP band in the YC next to the leading edge of the midgut. 0s shows the frame before the laser ablation, the subsequent frames shows 2, 10, 30 and 230s after the laser ablation. Green in the overlay depicts the frame taken at 0s, magenta in the overlay - 30s after the laser ablation. **(c)** Left: image showing Sqh-GFP during MC in AS-SqhKO embryos. Right: Selected movie frames showing MC progression in the z dimension in AS-SqhKO embryos. YC is deformed (red star) during the MC. Black arrow depicts the LE of the lateral epidermis, red arrow depicts the LE of the midgut, blue arrow depicts the thick Sqh-GFP cable in the YC. Scale bar: left - 10μm, right - 20μm.

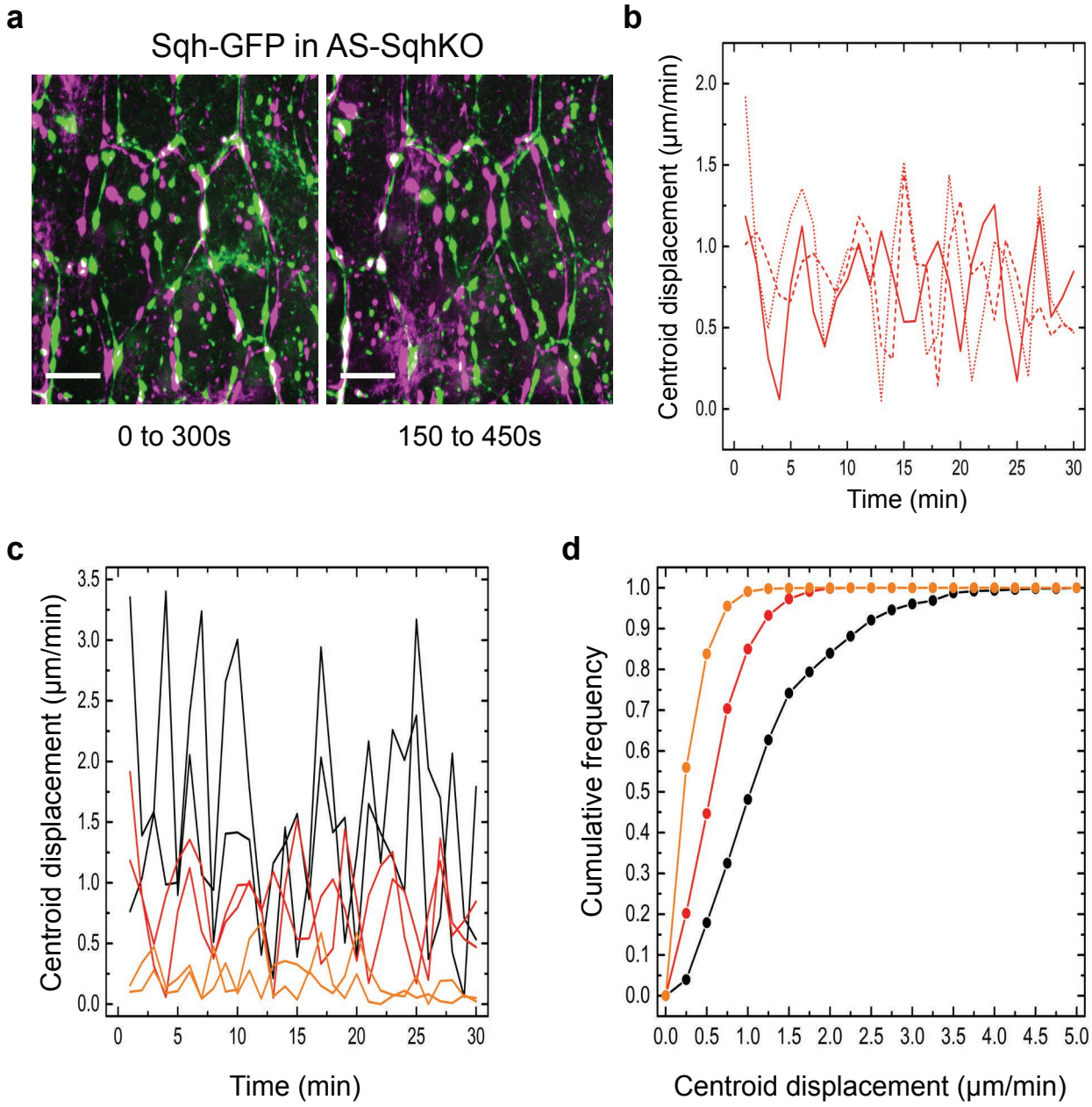

Figure 42. Contractile MyoII waves in the YC transiently displace AS cells situated above them. **(a)** Selected movie frames comparing AS cell location in discrete time windows (green=beginning; magenta=endpoint) in AS-SqhKO embryos. Scale bar: 10µm. **(b)** Representative curves of AS apical area centroid displacement over time in AS-SqhKO embryos. Solid, dashed and dotted lines represent 3 different cells from a single embryo. 3 cells shown of 43 from 5 embryos. **(c)** Representative curves of AS apical area centroid displacement over time in control (black lines), AS-SqhKO (red lines) and AS-yolk-SqhKO (orange lines) embryos. Control: 3 cells shown of 16 from 2 embryos; AS-SqhKO: 3 cells shown of 43 from 5 embryos; AS-yolk-SqhKO: 3 cells shown of 29 from 4 embryos. **(d)** Cumulative frequency diagram of AS apical area centroid displacement over time in control (black lines), AS-SqhKO (red lines) and AS-yolk-SqhKO (orange lines) embryos. Control: n=480 displacements of 16 cells from 2 embryos; AS-SqhKO: n=1404 displacements of 43 cells from 5 embryos; AS-yolk-SqhKO: n=870 displacements of 29 cells from 4 embryos.

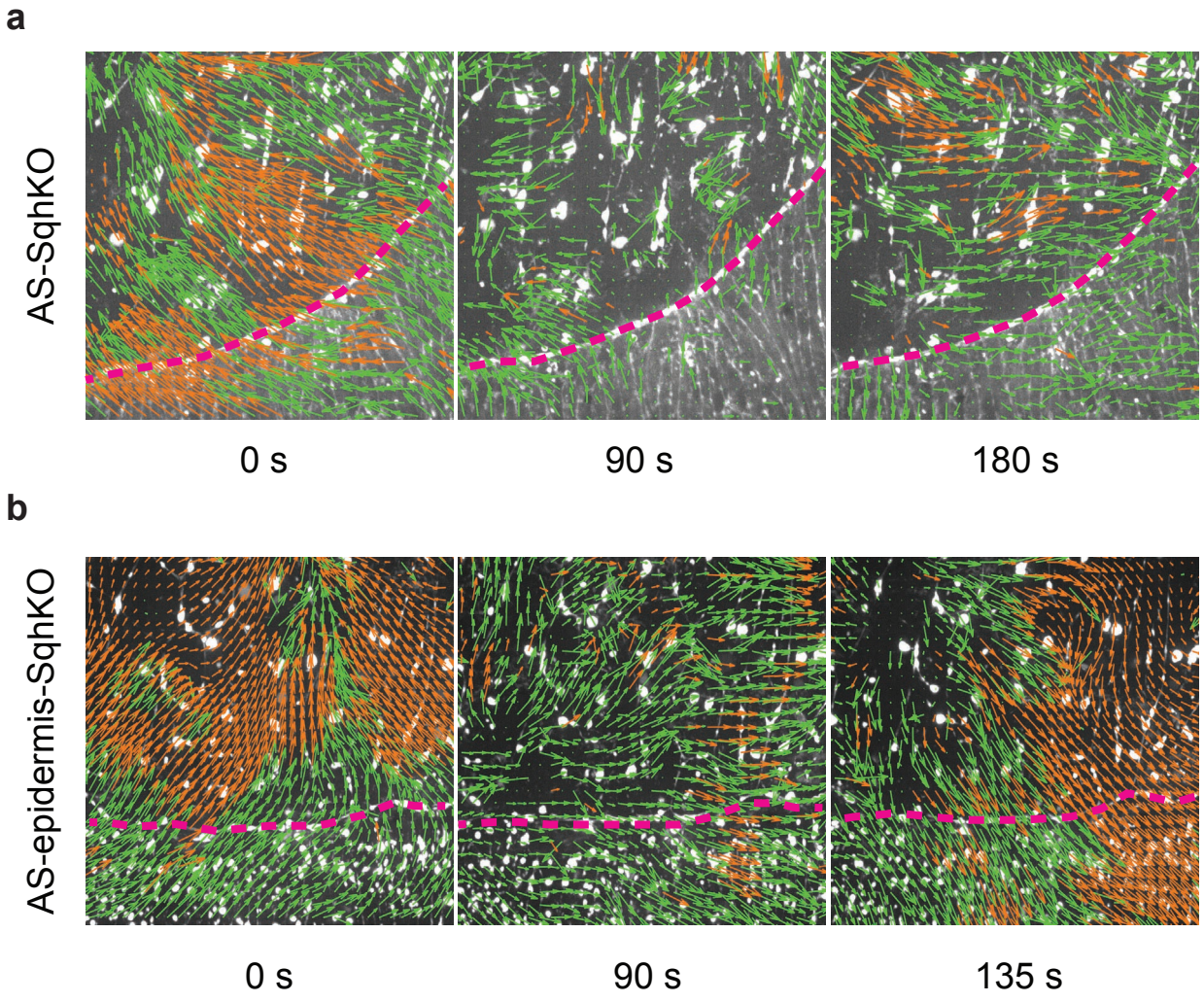

Figure 43. Contractile MyoII waves in the YC transiently displace the LE of the lateral epidermis. **(a)** Selected movie frames showing particle image velocimetry (PIV) analysis of the Sqh-GFP signal in AS-SqhKO embryos. **(b)** Selected movie frames showing PIV analysis of the Sqh-GFP signal in AS-epidermis-SqhKO embryos. In a-b, arrows indicate speed vectors that show particle velocities less than 0.66μm/s (green) or more than 0.66μm/s (orange). The red dashed line depicts the LE.

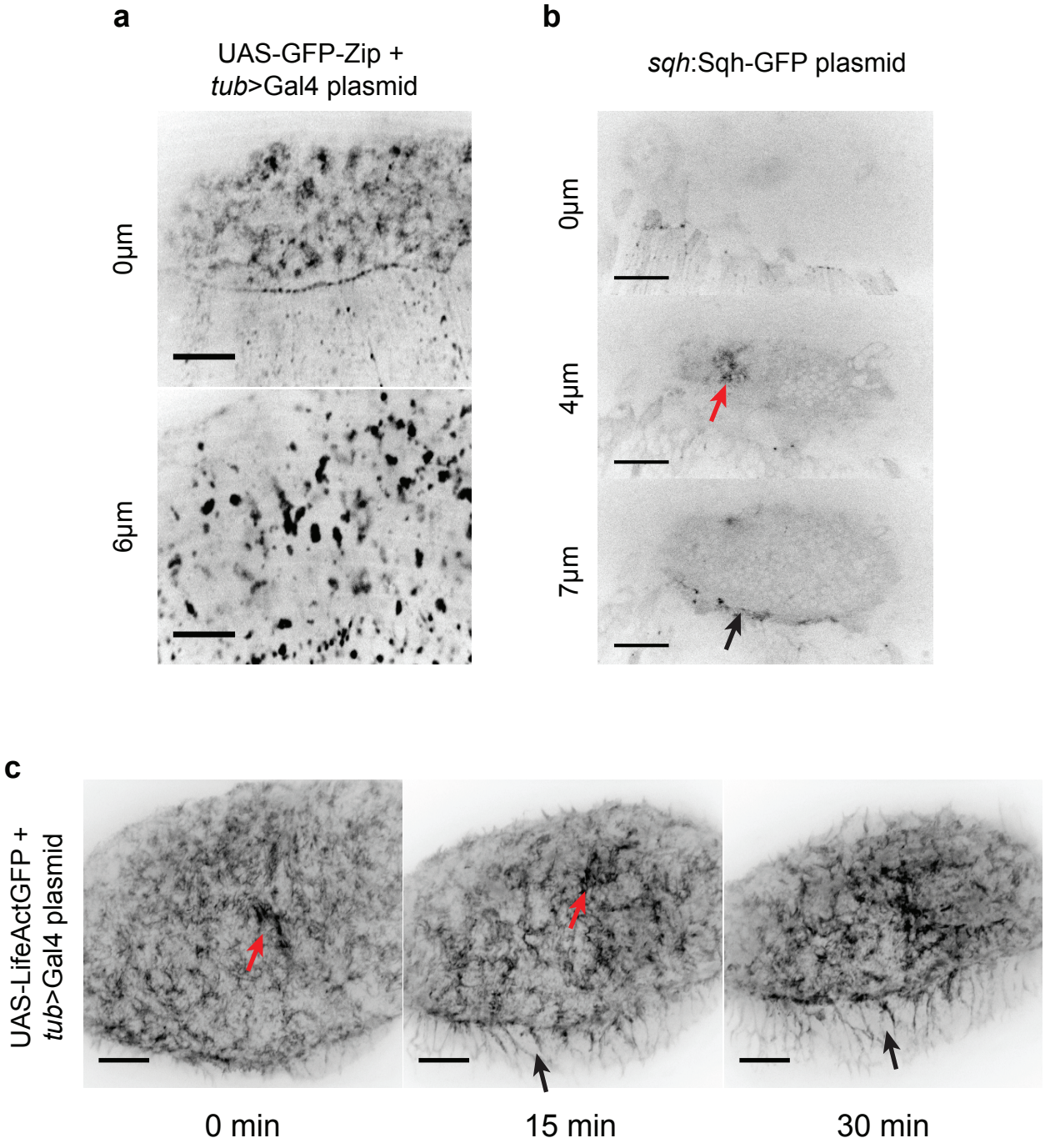

Figure 44. Plasmid injections allow visualization of the YC acto-myosin components in wild-type embryos. (a) Selected single planes of a confocal Z stack showing *tub*>Gal4-injected embryos expressing UAS-GFP-Zip. Zip localizes to the typical actin-based structures in the AS cells and epidermis (0µm), but aggregates in the YC (6µm). 0µm depicts the apical AS cell surface. Scale bar: 20µm. **(b)** Selected single planes of a confocal Z stack showing *sqh*:Sqh-GFP-injected embryos. Sqh localizes to coalescing foci (6µm) and the thick cable (6µm) in the YC. 0µm depicts the apical AS cell surface. Scale bar: 20µm. **(c)** Selected movie frames showing *tub*>Gal4-injected embryos expressing UAS-LifeActGFP in the YC. Transient concentrations of filopodia (red arrows) are visible on the YC surface. As MC proceeds, an "imprint" of putative midgut cells appears on the YC (black arrows). Scale bar: 20µm.

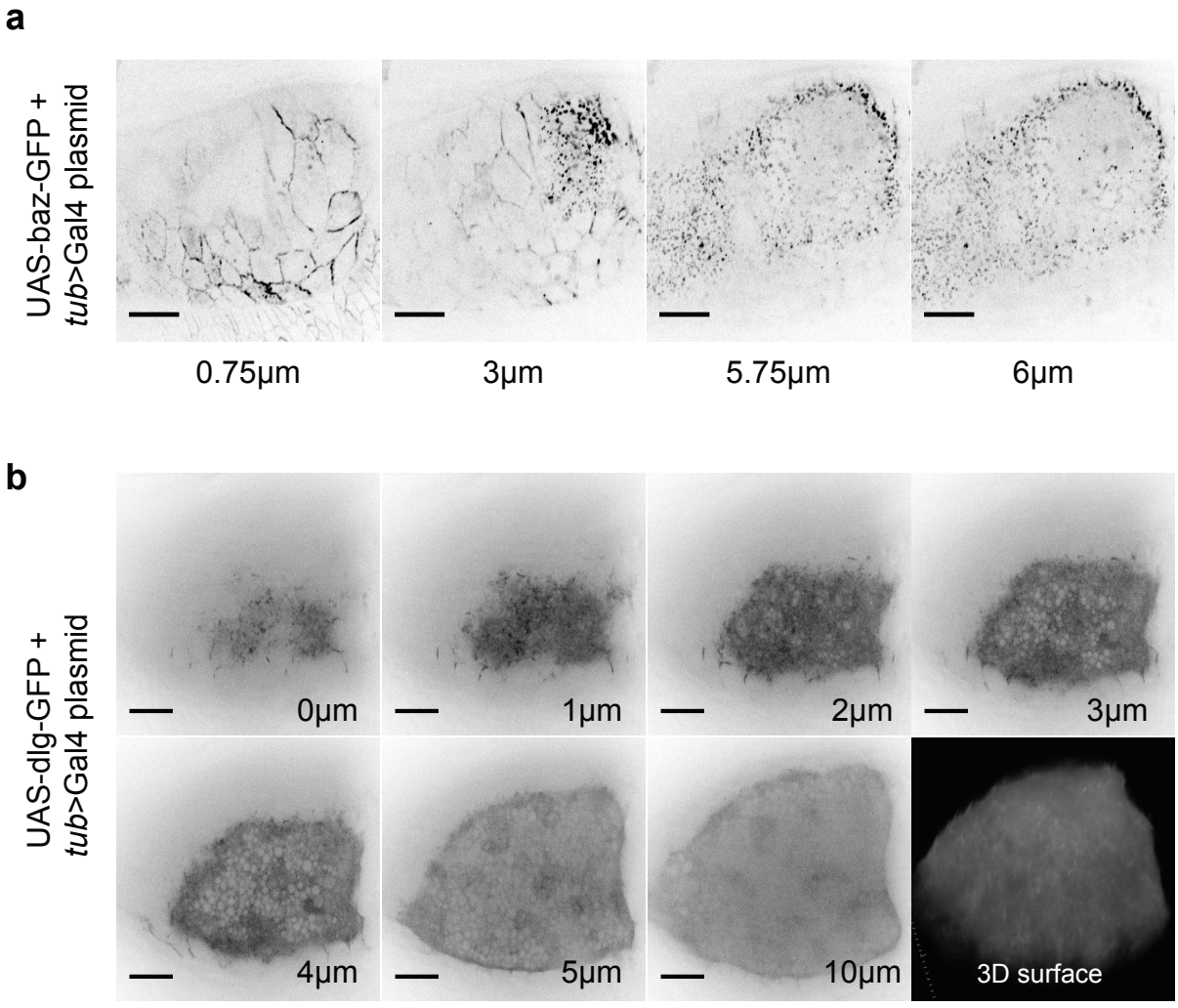
a
UAS-baz-GFP +
tub>Gal4 plasmid
0.75µm
3µm
5.75µm
6µm
b
UAS-dlg-GFP +
tub>Gal4 plasmid
0µm
1µm
2µm
3µm
4µm
5µm
10µm
3D surface
c
early MC
late MC
UAS-dlg-GFP +
tub>Gal4 plasmid
-110 min
-34 min
-95 min
-25 min

Figure 45. The YC membrane has basolateral identity and is endocytosed towards the end of MC. **(a)** Selected single planes of a confocal Z stack showing *tub*>Gal4-injected embryos expressing UAS-baz-GFP. Baz localizes to the apical adherens junctions in the AS cells (0.75μm), but forms numerous punctae in the YC (3-6μm). 0.75μm depicts the plane of adherens junctions in the AS cells. Scale bar: 20μm. **(b)** Selected single planes of a confocal Z stack showing *tub*>Gal4-injected embryos expressing UAS-dlg-GFP. Dlg localizes to the YC surface (0-4μm) and outlines the spherical shape of the YC (3D reconstruction). 0μm depicts the most dorsal plane of the YC. 3D reconstruction depicts rendering of 24μm confocal Z stack with single planes spaced 1μm apart. Scale bar in 0-10μm planes: 20μm. **(c)** Selected movie frames showing *tub*>Gal4-injected embryos expressing UAS-dlg-GFP. As MC progresses, membrane blebs/vesicles appear in the YC membrane (red arrows). Time depicts minutes until the completion of MC (0 min as reference). Scale bar: 20μm.

Chapter 6. Materials and Methods

6.1. General Materials and Methods

6.1.1. *Drosophila melanogaster* strains

All *D. melanogaster* strain genotypes reported in the text or shown in the figures are listed in Table 2. All the original stocks that were used to obtain the analysed genotypes are listed in Table 3. Reproducibility and sample sizes of every panel or experiment performed in this study are listed in Table 4.

All *Drosophila* strains were kept, handled and crossed using standard genetic practices. Recombinant chromosomes were generated after a standard female cross with the balancer flies. The correct recombinant offspring were selected according to *white*$^{+}$ eye colour intensity, appearance of reporter fluorescence in Leica MZ FLIII stereo microscope or by screening at the spinning-disk confocal microscope Leica DM IRBE. For Leica MZ FLIII stereo microscope HBO 105 (Osram) lamp and the following filters were used (GFP2 – Leica10446223, GFP3 – Leica10446244, mCherry - Leica10450098).

All recessive lethal alleles used for live imaging were kept over the balancer chromosomes with the fluorescent reporters (*FM7, KrGal4, UAS-GFP; CyO, KrGal4, UAS-GFP; CyO, sqh-mCherry; TM3, Ser, Sb, sqh-mCherry; TM3, KrGal4, UAS-GFP*). During the image acquisition those embryos without the fluorescent balancer chromosomes were categorized as homozygous recessive for a particular allele (examples include *sqh*^{AX3}, *zip*^{1}, *zip*^{2}, *zip*$^{dsRED(M)}$, *tkv*^{8}, *tkv*^{7}, *inx2*^{G0118}, *Δinx3*^{dsRED}, *Df(1)BSC867*). All the other chromosomes that did not have a fluorescent reporter were determined in the same way (examples include UAS-Mbs.N300, UAS-tsrCA, UAS-Dad, UAS-Dpp-mRFP, UAS-tkv^{Act}).

Genotype analysed/shown	Short name	Chapter	Figure	Notes
y w cv sqh^{AX3}/Y; *sqh*:Sqh-GFP/*332.3*Gal4; UAS-NSlmb-vhhGFP4/+	AS-SqhKO	2; 5; A2	4; 7D; 8A, D-H; 9E-H; 12A, D-E; 37A-B; 39A; 40; 41; 43; 52B, E;	
y w cv sqh^{AX3}/*yw*/Y; *sqh*:Sqh-GFP/+; UAS-NSlmb-vhhGFP4/+	control	2; 5; A2	4; 5A, D-F; 6A; 9E-H; 11D-E; 37A-B; 50; 51; 52B, E;	
y w cv sqh^{AX3}; *sqh*:Sqh-GFP; UAS-NSlmb-vhhGFP4	control	2; A1; A3	4D; 5D; 7A-B, D; 8D-H; 9E; 11D; 12A, E-F; 47C; 60;	
w; ; *pnr*Gal4, UAS-mCherry-moesin/TM6, Tb	control	2	4D; 5C-D; 6B-C; 10D; 11A-C; 12G;	
y w cv sqh^{AX3}/Y; *sqh*:Sqh-GFP/*332.3*Gal4; UAS-NSlmb-	AS-ES-SqhKO	2; 5; A2	4F; 43B; 52A-B;	

vhhGFP4/*pnr*Gal4, UAS-mCherry-moesin				
y w cv sqh^{AX3}/Y; *sqh*:Sqh-GFP/*332.3*Gal80; UAS-NSlmb-vhhGFP4/*pnr*Gal4, UAS-mCherry-moesin	ES-SqhKO	2; A2	5; 6A-C; 7C; 10D; 11A-D, F-G; 54;	
w; *sqh*:Sqh-GFP/*332.3*Gal80; *pnr*Gal4, UAS-mCherry-moesin/+	control	2	5B;	
w; *332.3*Gal80/UAS-Mbs.N300; *pnr*Gal4, UAS-mCherry-moesin/+	ES+Mbs.N300	2; A2	5C; 10E; 12G; 54;	
y w cv sqh^{AX3}/Y; *sqh*:Sqh-GFP/*en*Gal4, UAS-mCherry-moesin; *UAS*-NSlmb-vhhGFP4/+	*en*ES-SqhKO	2	6D;	
*y w cv sqhAX3/+; sqh:*Sqh-GFP/*en*Gal4, UAS-mCherry-moesin; UAS-NSlmb-vhhGFP4/+	control	2; A2	6D; Table 6;	
sqh:Sqh-GFP, Shg-dTomato/+		2	7A;	
w/+; *332.3*Gal4, UAS-mCherry-Zipper/+		2	8B;	
y w cv sqh^{AX3}/Y; *sqh*:Sqh-GFP/*332.3*Gal4, UAS-mCherry-Zipper; UAS-NSlmb-vhhGFP4/+	AS-SqhKO	2	8C;	
w/+; *332.3*Gal4, UAS-mCherry-moesin/+		2	9A;	
w/+; *c381*Gal4, UAS-mCherry-moesin/arm-GFP		2	9A;	
y w cv sqh^{AX3}/+/Y; *sqh*:Sqh-GFP/TRE-dsREDattP40; UAS-NSlmb-vhhGFP4/+	Control	2	9B; 11E;	
y w cv sqh^{AX3}/Y; *sqh*:Sqh-GFP/332.3Gal4, TRE-dsREDattP40; UAS-NSlmb-vhhGFP4/+	AS-SqhKO	2	9B;	
w/+; *c381*Gal4, UAS-mCherry-moesin/+		2; 3; 5	8A; 12B-C; 14; 15; 42B-D;	
w; *332.3*Gal4, arm-GFP/UAS-Mbs.N300	AS+Mbs.N300	2	9C;	
w; *332.3*Gal4, *sqh*:Sqh-GFP, Shg-dTomato/UAS-Mbs.N300		2	9D;	
y w cv sqh^{AX3}/Y; *sqh*:Sqh-GFP/+; UAS-NSlmb-vhhGFP4/*pnr*Gal4, UAS-mCherry-moesin	*pnr*ES-SqhKO	2; 5	10A-B; 38B;	
y w cv sqh^{AX3}/Y; *sqh*:Sqh-GFP/TRE-dsREDattP40; UAS-NSlmb-vhhGFP4/*pnr*Gal4	ES-SqhKO	2	11E	
y w cv sqh^{AX3}/Y; *sqh*:Sqh-GFP/*c381*Gal4, UAS-mCherry-moesin; *UAS*-NSlmb-vhhGFP4/+	AS-SqhKO	2; 3	8A; 12B-C; 13; 14; 15; 16D; 17C; 18A;	
y w cv sqh^{AX3}/Y; *sqh*:Sqh-GFP/*332.3*Gal4, UAS-mCherry-moesin; *UAS*-NSlmb-vhhGFP4/+	AS-SqhKO	2	12D;	
y w cv sqh^{AX3}/+; *sqh*:Sqh-GFP/*c381*Gal4, UAS-mCherry-moesin; UAS-NSlmb-vhhGFP4/+		3; 5	13A; 14; 15; 42B-D;	

y w cv sqh^{AX3}/Y; *sqh*:Sqh-GFP/*P0172*Gal4, UAS-mCherry-moesin; UAS-NSlmb-vhhGFP4/+	AS-yolk-SqhKO	3; 5	13A, C; 14; 17E; 24G; 42B-D;	
w; *c381*Gal4, UAS-mCherry-moesin/UAS-Mbs.N300	AS+Mbs.N300	3	13B;	
w; sp^{1} *zip*^{1}/*sp*^{1} *zip*^{1}; SGMCA		3	13B;	
w; zip$^{dsRED(M)}$/ *zip*$^{dsRED(M)}$; SGMCA		3	13B;	
w; ; sChMCA		3	16A, C;	
w; ; SGMCA		3; 4	16B; 17F; 34;	
w; *c381*Gal4, UAS-mCherry-moesin; UAS-myr-GCaMP V		3; A3	17A-B, D; 18; 19; 20; 21; 24E-F; 62; 63;	
w; *c381*Gal4, UAS-mCherry-moesin, zip^{1}/+; UAS-inx3-GFP/arm-GFP		3	22A-B;	
w; *c381*Gal4, UAS-mCherry-moesin/+; UAS-inx3-GFP/+		3	Section 3.2.4.	
w; *c381*Gal4, UAS-mCherry-moesin, zip^{1}/ *c381*Gal4, UAS-mCherry-moesin, zip^{1}; UAS-inx3-GFP/+		3	22C;	
w; ; *Δinx3*^{dsRED}, SGMCA/TM3, Sb		3	23B;	
w; ; *Δinx3*^{dsRED}, SGMCA/*Δinx3*^{dsRED}, SGMCA		3	23B;	
inx2^{G0118}/ *inx2*^{G0118}; ; *Δinx3*^{dsRED}, SGMCA/*Δinx3*^{dsRED}, SGMCA		3	23C, E;	
Df(1)BSC867/ Df(1)BSC867; ; *Δinx3*^{dsRED}, SGMCA/*Δinx3*^{dsRED}, SGMCA		3	23D;	
w; *332.3*Gal4/UAS-Arp1GFP		3	24A;	
*w; c381*Gal4, UAS-mCherry-moesin/+; UASp-GFP.Rho1/+		3	24B;	
*w; c381*Gal4, UAS-mCherry-moesin/+; UASp-Rok.RBD-GFP/+		3	24B;	
*w; 332.2*Gal4/sqh:WASpRBD-GFP		3	Section 3.2.5.	
*w; c381*Gal4, UAS-mCherry-moesin/UAS-tsrCA		3	24C;	
*w; c381*Gal4, UAS-mCherry-moesin/UAS-tsrDN		3	24D;	
*w; c381*Gal4, UAS-mCherry-moesin/ UAS- Pi3KDN		3	Section 3.2.5.	
y w cv sqh^{AX3}/Y; *sqh*:Sqh-GFP/+; UAS-NSlmb-vhhGFP4/*dpp*GAL4.PS[4B], *dpp*GAL4.PS[8B]Gal4		4; A2	26; 27; 28; 29; Table 6;	
w; ; *dad*GFP^{NLS}	*dad*>GFP^{NLS}	4	31A-B;	
w; *332.3*Gal4, arm-GFP/+; *dad*GFP^{NLS}/+		4	30A; 31C;	
w; ; *dad*GFP^{NLS}/*ubi*RFP^{NLS}	*ubi*>RFP^{NLS}	4	30B;	
w; ; His2Av-mRFP		4	Section 4.2.2.	
w; *ubi*GFP^{NLS}	*ubi*>GFP^{NLS}	4	30C;	
w; ; *dad*GFP^{NLS}/+		4	32;	
w; *ubi*GFP^{NLS}/+		4	32;	
w; *332.3*Gal4, UAS-mCherry-Zip/+; *dad*GFP^{NLS}/+		4	33A-B;	

w; *tkv*^{8}, *c381*Gal4/*tkv*^{7}, UAS-Zip-GFP		4	33C;	
w; *tkv*^{8}/*tkv*^{8}; *dad*GFP^{NLS}		4	33D;	
w; *tkv*^{8}/*tkv*^{8}; SGMCA		4	34;	
w; *332.3*Gal4/CyO, *sqh*-mCherry; *dad*GFP^{NLS}/+	*dad*>GFP^{NLS}	4	35; 36;	
w; *332.3*Gal4/UAS-Dpp-mRFP; *dad*GFP^{NLS}/+	AS>Dpp-mRFP*;* *dad*>GFP^{NLS}	4	35;	
w; *332.3*Gal4/UAS-tkv^{Act}; *dad*GFP^{NLS}/+	AS> UAS-tkv^{Act}*;* *dad*>GFP^{NLS}	4	35;	
*W; 332.3*Gal4, arm-GFP/UAS-tkvDN		4	Section 4.2.2.	
w; *7K*Gal4/UAS-Dad; *dad*GFP^{NLS}/+	*7K*>Dad; *dad*GFP^{NLS}/+	4	36;	
w; *P0172*Gal4/UAS-Dad; *dad*GFP^{NLS}/+	*P0172*>Dad; *dad*GFP^{NLS}/+	4	36;	
w; +/UAS-Dad; *dad*GFP^{NLS}/*krüppel*Gal4	*krüppel*>Dad; *dad*GFP^{NLS}/+	4	36;	
w; UAS-Dad/+; *dad*GFP^{NLS}/*dpp*GAL4.PS[4B], *dpp*GAL4.PS[8B]Gal4	*Dpp[8B]-Dpp[4B]*>Dad; *dad*GFP^{NLS}/+	4	36;	
w; arm-GFP; Dp(2;3)CH321-23O18		4	Section 4.4.	
y w cv sqh^{AX3}/Y; *sqh*:Sqh-GFP/*P48Y*Gal4, *332.3*Gal80; UAS-NSlmb-vhhGFP4/+	endo-SqhKO	5	37C;	
y w cv sqh^{AX3}/Y; *sqh*:Sqh-GFP/*332.3Gal4*, Zip:GFP; UAS-NSlmb-vhhGFP4/+	AS-SqhKO	5	38A;	
y w cv sqh^{AX3}/Y; *sqh*:Sqh-GFP/*332.3Gal4*, *arm-GFP*; UAS-NSlmb-vhhGFP4/+	AS-SqhKO	5	39B; 40B-C; 42;	
w; Zip:GFP/CyO		5	39D;	
w; UAS-GFP-Zip		5	44A;	Injected
y w		5	44B;	Injected
w; UAS-mCherry-moesin/+; *P0180*Gal4/+		5	Section 5.2.2.	
w; UAS-GFP-Zip/*P0172*Gal4/+		5	Section 5.2.3.	
w; UAS-Life-ActGFP		5	44C;	Injected
w; UAS-mCherry-moesin		5	Section 5.2.4.	Injected
w, UAS-baz-GFP		5	45A;	Injected
w; ; UAS-dlg-GFP		5	45B-C;	Injected
*w; 332.2*Gal4, UAS-mCherry-moesin/*332.3*Gal80		5	Section 6.2.1.	
actin5C>TEVdegr-M-EGFP-Zipper/SM6A		A1	46B;	
actin5C>TEVdegr-M-EGFP-Zipper, *zip*^{1}/SM6A		A1	46B;	
actin5C>TEVdegr-F-EGFP-Zipper/SM6A		A1	Section A1.1.1.	
actin5C>TEVdegr-F-EGFP-Zipper, *zip*^{1}/SM6A		A1	Section A1.1.1.	

actin5C>TEVdegr-M-EGFP-FRT[attP86F]		A1	Section A1.1.1.	
actin5C>TEVdegr-F-EGFP-FRT[attP86F]		A1	Section A1.1.1.	
y w; Cry2-tRFP-Sqh		A1	47D;	
y w, nos>Cas9^{mRFP}		A1	48A;	
Δinx3^{dsRED}/+		A1	48A;	
y w, nos>Cas9		A1	48B;	
Δzip^{dsRED}/SM6A		A1	Section A1.1.3.	
y w cv sqh^{AX3}/Y; *sqh*:Sqh-GFP/*332.3*Gal4; UAS-NSlmb-vhhGFP4/*sqh:*Sqh-mCherry		A2	50	
y w cv sqh^{AX3}/Y; *sqh*:Sqh-GFP/*c381*Gal4; UAS-NSlmb-vhhGFP4/*sqh:*Sqh-mCherry		A2	Section A2.1.	
y w cv sqh^{AX3}/Y; *sqh*:Sqh-GFP/*7K*Gal4; UAS-NSlmb-vhhGFP4/+	*7K*AS-SqhKO	A2	51	
y w cv sqh^{AX3}/Y; *sqh*:Sqh-GFP/*actin5c*Gal4; UAS-NSlmb-vhhGFP4/+	*act5C*-AS-epidermis-SqhKO	A2	52C	
y w cv sqh^{AX3}/Y; *sqh*:Sqh-GFP/*P0172*Gal4; UAS-NSlmb-vhhGFP4/+	AS-yolk-SqhKO	5; A2	37A-B; 39C; 52D-E;	
y w cv sqh^{AX3}/Y; *sqh*:Sqh-GFP/*e22c*Gal4; UAS-NSlmb-vhhGFP4/+	e22c-ES-SqhKO	A2	53A	
y w cv sqh^{AX3}/Y; *sqh*:Sqh-GFP/*LE*Gal4; UAS-NSlmb-vhhGFP4/+	LE-ES-SqhKO	A2	53B	
w; UAS-GFP-Zip/+; *GMR34B11*Gal4/+		A2	53C; Table 6;	
w; UAS-GFP-Zip/+; *GMR26F04*Gal4/+		A2	53C; Table 6;	
w; UAS-GFP-Zip/+; *GMR24H01*Gal4/+		A2	53C; Table 6;	
w; UAS-GFP-Zip/+; *69BGal4/*+		A2	Table 6;	
w; UAS-GFP-Zip/+; *GMR11C02*Gal4/+		A2	Table 6;	
w; UAS-GFP-Zip/+; *GMR39B10*Gal4/+		A2	Table 6;	
y w cv sqh^{AX3}/Y; *sqh*:Sqh-GFP/+; UAS-NSlmb-vhhGFP4/*GMR27H09*Gal4		A2	Table 6;	
w; UAS-GFP-Zip/*c1003Gal4;*		A2; A3	59A; Table 6;	
y w cv sqh^{AX3}*/Y; sqh:*Sqh-GFP/+; UAS-NSlmb-vhhGFP4*/P0161Gal4*		A2	Table 6;	
y w cv sqh^{AX3}*/Y; sqh:*Sqh-GFP/*btl*Gal4; UAS-NSlmb-vhhGFP4/+		A2	Table 6;	
w; UAS-GFP-Zip/*P0181*Gal4		3; A2	Table 6; Section 5.2.2.	

y w cv sqh^{AX3}*/Y; sqh:*Sqh-GFP/+; UAS-NSlmb-vhhGFP4/*Kr*Gal4		A2	Table 6;	
y w; *332.3*Gal80[*yellow*$^{+}$]		A2	53D;	
y w; *332.3*Gal4; Sb/TM3, Ser, UAS-yellow^{+}		A2	53D;	
w; *332.3*Gal4; *pnr*Gal4, UAS-mCherry-moesin/TM6, Tb	AS-ES-Mbs.N300	A2 A2	54;	
w; *332.3*Gal4, UAS-mCherry-moesin/UAS-Mbs.N300	AS+Mbs.N300		54;	
w; *332.3*Gal4/UAS-Mbs.N300; *pnr*Gal4, UAS-mCherry-moesin/+	AS-ES+Mbs.N300	A2	54;	
w; ; arm-GFP		A1; A2	49; 55; 56;	
y w cv sqh^{AX3}/Y; *sqh*:Sqh-GFP/*en*Gal4, UAS-Eb1-mCherry; UAS-NSlmb-vhhGFP4/+	*en*ES-SqhKO	A2	57	
w; *332.3*Gal4/UAS-GFP-Zip		A3	58;	
w; Septin2-GFP		A3	59B;	

Table 2. *Drosophila* genotypes analysed in the study.

***Drosophila* Strain**	**Short name**	**Donor**
y w cv sqh^{AX3}; *sqh*:Sqh-GFP	*sqh*:Sqh-GFP rescue construct in the homozygous *sqh*^{AX3} mutant background	Donor R. Karess
w; ; UAS-NSlmb-vhhGFP (III)	deGradFP nanobody expressed under UAS enhancer element (EE)	Donor M. Affolter
w; ; *pnr*Gal4 /TM6, Tb	*pnr* EE expressing Gal4 in the epidermis	BL#3039
w; ; UAS-mCherry-moesin/TM6, Tb	Moesin tagged with mCherry to label F-actin	Donor P. Martin
y w; *332.3*Gal80 (II)	*332.3* EE expressing Gal80 in the amnioserosa; also contains *yellow*$^{+}$	This study, Brunner lab
w; UAS-Mbs.N300 (II)	Constitutively active MyoII phosphatase	Donor J. Treisman
*en*Gal4, UAS-mCherry-moesin/CyO	*engrailed* EE expressing Gal4 in the epidermis stripes; mCherry-moesin labels F-actin	Donor P. Martin
w; Shg-dTomato (II)	Shotgun (DE-cadherin) tagged with dTomato to outline cell adherens junctions	BL#58789
w; UAS-mCherry-Zipper (II)	Zipper isoform C cDNA tagged with mCherry	This study, Brunner Lab
w; UAS-mCherry-moesin/CyO	Moesin tagged with mCherry to label F-actin	Donor P. Martin
w; *332.3*Gal4 (II)	*332.3* EE expressing Gal4 in the amnioserosa	BL#5398
w; *c381*Gal4 (II)	*332.3* EE expressing Gal4 in the amnioserosa	BL#3734

w; arm-GFP (II and III)	Armadillo tagged with GFP to outline cell adherens junctions	B#8555, BL#8556
*w; ; sqh:*Sqh-mCherry (III)	Sqh tagged with mCherry expressed under endogenous *sqh* EE	Donor A. Martin
*y w; 7K*Gal4/CyO	*7K* EE expressing Gal4 in the peripheral AS cells	Donor S. Hayashi
*w; actin5c*Gal4/CyO	*Actin5C* EE expressing Gal4 ubiquitously	BL#4414
*w; P0172*Gal4 (II)	P0172 EE expressing Gal4 in amnioserosa and the yolk cell	Münster Gal4 *Drosophila* Library (No. P0172)
*w; e22c*Gal4/SM5	*engrailed* EE expressing Gal4 in the epidermis stripes	BL#1973
*w; LE*Gal4 (II)	*puckered* EE expressing Gal4 in the leading edge of epidermis	BL#58801
w; UAS-GFP-Zip (II)	Zipper tagged with GFP under UAS EE	Donor D. Kiehart
w; UAS-sqh-GFP/SM6a, sp^1	Sqh tagged with GFP under UAS EE	Donor M. Affolter
w; ; *GMR34B11*Gal4 (III)	EE expressing Gal4 in the epidermis	BL#49774
w; ; *GMR26F04*Gal4 (III)	EE expressing Gal4 in the epidermis	BL#49191
w; ; *GMR24H01*Gal4 (III)	EE expressing Gal4 in the epidermis	BL#48054
*w; ; 69B*Gal4 (III)	*69B* EE expressing Gal4 in the ectoderm	BL#1774
*w; ; GMR11C02*Gal4 (III)	EE expressing Gal4 in the epidermis	BL#45011
*w; ; GMR39B10*Gal4 (III)	EE expressing Gal4 in the epidermis	BL#45260
*w; ; GMR27H09*Gal4 (III)	EE expressing Gal4 in the epidermis	BL#45537
*w; c1003*Gal4 (II)	*c1003* EE expressing Gal4 in the ectoderm	BL#2735
*w; ; P0161*Gal4 (III)	P0161 EE expressing Gal4 in the ectoderm	Münster Gal4 *Drosophila* Library (No. P0161)
*w; btl*Gal4/CyO	*breathless* EE expressing Gal4 in the amnioserosa	Donor S. Luschnig
*w; ; P0181*Gal4 (III)	*P0181* EE expressing Gal4 in the ectoderm	DGRC Kyoto (No.: 103-184Gal4)
w; ; KrGal4/TM3,Ser	*krüppel* EE expressing Gal4 in the amnioserosa and mesoderm	BL#58800
y w; ; Sb/TM3, Ser, UAS-yellow$^+$	WT copy of *yellow* expressed under UAS EE	Brunner Lab
*w; en*Gal4, UAS-Eb1-mCherry/CyO	*engrailed* EE expressing Gal4 in the epidermis stripes; EB1	Brunner Lab

	tagged with mCherry labels plus tips of microtubules	
w; SGMCA (II and III)	Moe-GFP under *sqh* EE to label F-actin	Donor D. Kiehart
w; ; sChMCA (III)	Moe-mCherry under *sqh* EE to label F-actin	BL#35521
w; sp^1 zip^1/SM6a, sp^1	zip^1 is amorphic allele of *zipper*	BL#4199
w; $zip^{dsRED(M)}$/ SM6a, sp^1	$zip^{dsRED(M)}$ is a full knock-out (KO) allele of *zipper*	Brunner lab
w; ; UAS-myr-GCaMP V	Membrane-tethered GCaMP V Ca^{2+} biosensor	Donor M. Müller
w; ; UAS-inx3-GFP (III)	Inx3 tagged with GFP	Donor M. Hoch
w; ; $\Delta inx3^{dsRED}$/TM6B,Tb	$\Delta inx3^{dsRED}$ is a full KO allele of *innexin3 (inx3). inx3* ORF is replaced with loxP-dsRED-loxP-attP	This study, Brunner lab
$inx2^{G0118}$/FM7c	$inx2^{G0118}$ is loss-of-function (LOF) allele of *innexin2*	BL#11826
*Df(1)BSC867/*Binsinscy	*Df(1)BSC867* is a deficiency of X chr. region X:6,981,859; X:7,041,515 that harbours *inx1* and *inx2* genes	BL#29990
w, UAS-Arpc1GFP/FM6, *w*	Arp1 tagged with GFP to label Arp2/3 complex under UAS EE	BL#26629
w; ; UASp-GFP.Rho1 (III)	Rho1 tagged with GFP under UAS EE	BL#9393
w; ; UASp-Rok.RBD-GFP (III)	GFP-tagged Rho1 activity biosensor under UAS EE	BL#52290
w; ; sqh:WASpRBD-GFP/+ (III)	GFP-tagged Cdc42 activity biosensor under UAS EE	BL#56745
w; UAS-tsr[S3A]CA (II)	Constitutively active cofilin (*tsr*) under UAS EE	BL#9237
w; ; UAS-tsr[S3E]DN (III)	Dominant negative form of cofilin (*tsr*) under UAS EE	BL#9239
w; ; UAS- Pi3KDN[92EA2860C] (III)	Dominant negative form of PI-3 kinase (*Dp110*) under UAS EE	BL#8289
*w; ; dpp*GAL4.PS[4B], *dpp*GAL4.PS[8B]Gal4/TM6, Tb	Tandem of *dpp* EEs expressing Gal4	BL#7008
w; ; *dad*GFP^{NLS} (III)	*dad* EE expressing GFP with nuclear localization signal (NLS)	Donor M. Affolter
w; ; *ubi*RFP^{NLS} (III)	*ubiquitin (ubi)* EE expressing RFP with NLS	BL#30555
w; ; His2Av-mRFP (III)	Histone H2A variant tagged with mRFP	BL#23650
w; *ubi*GFP^{NLS} (II)	*ubiquitin (ubi)* EE expressing GFP with NLS	Donor K. Basler
w; tkv^7/CyO	tkv^7 is a loss-of-function allele of *thickveins*	Donor K. Basler
w; tkv^8/CyO	tkv^8 a loss-of-function allele of *thickveins*	Donor K. Basler
w; UAS-Dpp-mRFP/CyO	Dpp tagged with mRFP under UAS EE	Donor C.Bökel
w; UAS-tkv^{Act} (II)	Constitutively active *tkv* under UAS EE	Donor J.P. Vincent

w; UAS-tkvDN (II)	Dominant negative form of *tkv* under UAS EE	Donor J.P. Vincent
w; UAS-Dad/CyO	WT copy of *dad* under UAS promoter sequences	Donor K. Basler
w; arm-GFP; Dp(2;3)CH321-23O18	Duplication of II chr. region 2L:2399554;2L:2486451 including Dpp	BL#54589
*w; P48Y*Gal4 (II)	*P48Y* EE expressing Gal4 in the endoderm and AS	BL#4935
w; Zip:GFP/SM6a	Zipper tagged with GFP at the endogenous locus	FlyTrap collection (No. CC01626)
y w	Mutant alleles for *yellow*$^{+}$ and *white*$^{+}$ genes	Brunner lab
*w; ; P0180*Gal4 (III)	*P0180* EE expressing Gal4 in the yolk cell	Münster Gal4 *Drosophila* Library (No. P0180)
w; UAS-Life-ActGFP (II)	LifeAct tagged with GFP under UAS EE	Donor F. Schnorrer
w, UAS-baz-GFP (I)	Bazooka (*baz*) tagged with GFP under UAS EE	BL#29037
w; ; UAS-dlg-GFP (III)	Dlg (*dics-large, dlg*) tagged with GFP under UAS EE	Brunner lab
actin5C>TEVdegr-M-EGFP-Zipper/SM6A	*actin5C* EE expressing TEVdegr-M-EGFP-Zipper	This study, Brunner lab
actin5C>TEVdegr-F-EGFP-Zipper/SM6A	*actin5C* EE expressing TEVdegr-F-EGFP-Zipper	This study, Brunner lab
actin5C>TEVdegr-M-EGFP-FRT[attP86F]	*actin5C* EE expressing TEVdegr-M-EGFP-FRT	This study, Brunner/Basler lab
actin5C>TEVdegr-F-EGFP-FRT[attP86F]	*actin5C* EE expressing TEVdegr-F-EGFP-FRT	This study, Brunner/Basler lab
y w; Cry2-tRFP-Sqh (II and III)	*sqh* EE expressing Cry2-tRFP-Sqh ubiquitously	This study, Brunner lab
y w, *nos*>Cas9^{mRFP}	*nanos (nos)* EE expressing Cas9. *white*$^{+}$ and mRFP are present	BL#54591
y w, *nos*>Cas9	*nanos (nos)* EE expressing Cas9. *white*$^{+}$ and mRFP are removed	This study, Brunner lab
w; Septin2-GFP (II)	Septin2 tagged with GFP	BL#26257
Df(3R)BSC789/TM3, Sb	*Df(1)BSC789* is a deficiency of III chr. region 3R:28820134;3R:29040507 around the *inx3* gene	BL#27361
w; TRE-dsRED-attP40 (II)	Live Jnk signalling reporter	BL#59011

Table 3. Original *D. melanogaster* strains used in this study.

Figure panel	**Reproducibility**
4A-C	Control: n>30; AS-SqhKO: n>30
4D	Control: n=53 LE ends, 29 embryos; AS-SqhKO: n=44 LE ends, 22 embryos
4F	Control: n=19 embryos; AS-SqhKO: n=23 embryos; AS-ES-SqhKO: n=7 embryos
4G	Control: n=19 embryos; AS-SqhKO: n=23 embryos
5A	Control: n>30; ES-SqhKO: n>30
5B	Control: n>10; ES-SqhKO: n>30
5C	Control: n=364, 7 embryos; ES-SqhKO: n=743, 11 embryos; Mbs.N300: n=454, 9 embryos

5D	Control: n=53 LE ends, 29 embryos; ES-SqhKO: n=19 LE ends, 10 embryos
5E-F	Control: n=19 embryos; ES-SqhKO: n=26 embryos
5F	Control: n=19 embryos; ES-SqhKO: n=26 embryos
6A	Control: n=19 embryos; ES-SqhKO: n=26 embryos
6B	Control: n>30; ES-SqhKO: n>30
6C	Control: n>10; ES-SqhKO: n>10
6D	Control: n>10; *en*ES-SqhKO: n>20
7A	n>30
7B	Apical near LE: n=56 cells, 5 embryos; apical far LE: 54 cells, 5 embryos. Junctional near LE: n=23 junctions, 5 embryos; junctional far LE: n=29 junctions, 5 embryos
7C	n>20
7D	Control: n>10; AS-SqhKO: n>10
8A	Control: n=16 cells, 2 embryos; AS-SqhKO: n=29 cells, 4 embryos
8B	n>5
8C	n=4
8D-H	Control: 157 vertices, 22 embryos; AS-SqhKO: 104 vertices, 17 embryos
9A	332.3Gal4, UAS-mCherry-moesin: n>10; c381Gal4, UAS-mCherry-moesin/arm-GFP: n>20
9B	n>12
9C	n=14
9D	n=4
9E	Control: n=29 lasercuts; AS-SqhKO: n=22 lasercuts
9F-H	Control: n=19 embryos; AS-SqhKO: n=23 embryos
10A	n>10
10B	n>10
10D	*pnr*Gal4: n>10; *pnr*Gal4+332.3Gal80: n>10
10E	n=11
11A	Out of n=89 embryos, no puckering: 7, weak puckering: 58, severe puckering: 24
11B	n=39 (out of 95)
11C	Control: n=29 lasercuts; ES-SqhKO: n=10 lasercuts
11D	Control: n=4; ES-SqhKO: n=3
11E	Control: n=14; ES-SqhKO: n=10
11F-G	Control: n=19 embryos; ES-SqhKO: n=26 embryos
12A-C	Control: 12 cells, 2 embryos; AS-SqhKO: 24 cells, 5 embryos
12D	n>10
12E-F	Control: 157 vertices, 22 embryos; AS-SqhKO: 104 vertices, 17 embryos
12G	Control: n=364, 7 embryos; ES-SqhKO: n=743, 11 embryos; Mbs.N300: n=454, 9 embryos
13A	Control: n>10; AS-yolk-SqhKO: n>10
13B	AS-SqhKO: n>10; AS-Mbs.N300: n=12; zip^{1}/ zip^{1}: n=3; zip^{dsRED}/ zip^{dsRED}: n=4;
13C	AS-SqhKO: n>10; AS-yolk-SqhKO: n>10
14A	Control: n=6389 periods, 72 cells, 3 embryos; AS-SqhKO: n=11386 periods, 106 cells, 5 embryos; AS-yolk-SqhKO: n=5709 periods, 90 cells, 4 embryos
14B-C	Control: n=13508 CCFs, 155 unique cell pairs, 3 embryos; AS-SqhKO: n=22712 CCFs, 205 unique cell pairs, 5 embryos; AS-yolk-SqhKO: n=11738 CCFs, 177 unique cell pairs, 4 embryos
15	Control: n=35 cells, 5 lasercuts/embryos; AS-SqhKO: cells 31, 5 lasercuts/embryos
16A	n=6
16B	n=14
16C	n=6 cells, 1 embryo
16D	n=3
17A	n>20
17B	n=6
17C	n=5
17D	n=6
17E	n>6
17F	n=3
18A	Control: n=5; AS-SqhKO: n=3

18B	n= 6 cells, 3 embryos
19A	n>30
19B	n=46 cells, 3 lasercuts/embryos
19C	n>5 lasercuts in 2 embryos
19D	n=10 lasercuts in 3 embryos
19E	n=1 lasercut in 1 embryo
19F	n=3 lasercuts in 2 embryos
19G	n=1 lasercut in 1 embryo
20A	n>30 lasercuts/cells in >10 embryos
20B	n>10 lasercuts/cells in >5 embryos
20C	n=10 lasercuts in 3 embryos
20D	n>20 lasercuts/cells in 3 embryos
20E	n>10 lasercuts/cells in >5 embryos
20F	n>5 lasercuts/cells in >3 embryos
21	n>10 lasercuts in >7 embryos
22A	n>20
22B	n>20
22C	n=5
23A	n=3
23B	Control: n=8; Mutant: n=7
23C	n>30
23D	n>20
23E	n>20 cells in >5 embryos
24A	n=1
24B	GFP-Rho1: n=4; Rho1.RBD-GFP: n=7
24C	Control: n=6389 periods, 72 cells, 3 embryos; DN-tsr: n=5549 periods, 65 cells, 4 embryos
24D	Control: n=6389 periods, 72 cells, 3 embryos; CA-tsr: n=2294 periods, 25 cells, 2 embryos
24E	n>30
24F	n=4
24G	n=9
26A	n=427 cells, 27 regions/embryos
26B	n>10
26C	n>10
27A	n=8 cells, 1 embryo
27B-F	n=58 cells, 4 embryos
28A	n>30 junctions >7 embryos
28B	n>10 junctions >5 embryos
28C-D	n=3 junctions, 6 cells, 3 embryos
29A	n>20
29B	n>30 junctions >7 embryos
29C	n>10 junctions >5 embryos
30A	n>30
30B	n=11
30C	n=18
31A-B	n>30
31C	n>5
32A	n=125 nuclei, 3 embryos
32B	n>30
32C	*ubi*>GFP^{NLS}: n=135 nuclei, 3 embryos; *dad*>GFP^{NLS}: n=125 nuclei, 3 embryos
33A-B	n=15 cells, 4 embryos
33C	n=19
33D	n=5
34	n>10
35	Control: n=25: AS>Dpp-mRFP: n=12; AS>tkv^{Act}: n=9
36	Control: n>30: *7K*>UAS-Dad: n=5; *P0172*>UAS-Dad: n=7; *krüppel*>UAS-Dad: n=4; *Dpp[8B]-Dpp[4B]* >UAS-Dad: n=1;
37A	Control: n>30; AS-SqhKO: n>30; AS-yolk-SqhKO: n>20;
37B	Control: n=19; AS-SqhKO: n=23

37C	n>5
38A	n>20 embryos
38B	n>10 embryos
39A-B	n>30 embryos
39C	n>20 embryos
39D	n=7
40A	n>20 embryos
40B	n=2526 periods, 42 regions, 3 embryos
40C	n=17 waves, 3 embryos
41A	n>10
41B	n=8
41C	n>10 embryos
42A	n>10 embryos
42B	n=43 cells, 5 embryos
42C	Control: n=16 cells, 2 embryos; AS-SqhKO: n=43 cells, 5 embryos; AS-yolk-SqhKO: n=29 cells, 4 embryos
42D	Control: n=480 displacements of 16 cells from 2 embryos; AS-SqhKO: n=1404 displacements of 43 cells from 5 embryos; AS-yolk-SqhKO: n=870 displacements of 29 cells from 4 embryos.
43A	n=7
43B	n=3
44A	n=6
44B	n=4
44C	n=4
45A	n=11
45B	n=11
45C	n=11
46B	n=5
47B	n=10
47C	n=6
47D	n>10
48A-B	n>30
49A	n>10
49B	n=4
50	Control: n>30; AS-SqhKO with sqh-mCherry: n>10
51	Control: n>30; *7K*AS-SqhKO: n>20
52A	n=16
52B	Control: n=19 embryos; AS-SqhKO: n=22 embryos; AS-epidermis-SqhKO: n=7
52C	n=10
52D	n>20
52E	Control: n=19 embryos; AS-SqhKO: n=22 embryos; AS-yolk-SqhKO: n=12
53A	n=6
53B	n>10
53C	n=4-5
53D	n>30
54	AS-ES -Mbs.N300: n>10; AS+Mbs.N300: n=12; ES+Mbs.N300: n=12; AS-ES+Mbs.N300:n=10
55A	n=2
55B	n=8 lasercuts, 2 embryos
56A-B	Uncut: n=22; LE cuts: n=16; Epidermis+LE cuts n=26
56C	n=2
57	n=7
58	n>20
59A	n>30 bursts, 1 embryo
59B	n>30 bursts, 2 embryos
60	n>30
61	n>30
62	n>30 lasercuts, 10 embryos

63	n>30 waves, 4 embryos

Table 4. Reproducibility and sample sizes of the experiments. n is the number of analysed embryos unless indicated otherwise.

6.1.2. Important notes on the following fly strains/genotypes:

1) *c381*Gal4 (BL#3734) was described before as IV chromosome EE, but we found it to be on the II chromosome. We confirmed this multiple times by segregating it from CyO balancers and creating recombinant chromosomes with UAS-mCherry-moesin or sp^1 zip^1 that are on the II chromosome.

2) We noticed that expression of AS-specific *332.3*Gal4 EE (BL#5398) is temperature-sensitive. If kept at 18°C only several AS cells show expression of fluorescently labelled markers (e.g. mCherry-moesin), while at 25°C all AS cells are highly expressive. Thus, the full extent of *332.3*Gal4 and *332.3*Gal80 effects are only visible at 25°C.

3) The original *pannier* (*pnr*) EE shows varying ectopic expression in AS cells. The number of AS cells ectopically expressing *pnr* ranges from several to almost all AS cells (Chapter 2, Fig. 10). As a first attempt to clean the chromosomes, we outcrossed the EE with the wild-type chromosomes, but this did not help to eliminate the ectopic expression.

6.1.3. deGradFP crosses/imaging:

For tissue-specific Sqh-GFP depletion *ywcvsqh^{AX3}; sqh:*Sqh-GFP; UAS-NSlmb-vhhGFP4 virgin females were crossed with appropriate Gal4-expressing males. All progeny after the cross that contained Gal4 enhancer element showed degradation aggregates. However, half of them (i.e. female progeny) also contained untagged Sqh. Thus, only the male progeny would show the phenotypes, since they would have *ywcvsqh^{AX3}/Y* and Sqh-GFP depleted according to Gal4 expression pattern[68]. To clearly distinguish between the male/female progeny for AS-SqhKO and ES-SqhKO genotypes we also performed the following crosses:

AS-SqhKO: *ywcvsqh^{AX3}; sqh:*Sqh-GFP; UAS-NSlmb-vhhGFP4 ***X*** FM7, GFP/Y; *332.3*Gal4

ES-SqhKO: *ywcvsqh^{AX3}; sqh:*Sqh-GFP, *332.*3Gal80; UAS-NSlmb-vhhGFP4 ***X*** FM7, GFP/Y; ; *pnr*Gal4, UAS-mCherry-moesin/TM3, Ser.

For rescue of AS-SqhKO with mCherry-tagged Sqh, *ywcvsqh^{AX3}; sqh:*Sqh-GFP; *sqh:*Sqh-mCherry females were crossed to *w/Y; 332.3*Gal4; UAS-NSlmb-vhhGFP4 males. As additional confirmation, *ywcvsqh^{AX3}; sqh:*Sqh-GFP; UAS-NSlmb-vhhGFP4 females were crossed to *w/Y; 332.*3Gal4; *sqh:*Sqh-mCherry or *w/Y; c381*Gal4; *sqh:*Sqh-mCherry males.

For visualizing the Jnk activity reporter TRE-dsREDattP40, the following strains were crossed: **Control** and **ES-SqhKO**: ywcvsqhAX3; sqhSqh-GFP, 332.3Gal80; UAS-NSlmb-vhhGFP4 virgins were crossed to TRE-dsREDattP40/+; pnrGal4/+. Embryos without pnrGal4 expression were used as control (n=14 embryos analyzed) and with pnrGal4 expression as ES-SqhKO (n=10 embryos analyzed).

AS-SqhKO: ywcvsqhAX3; sqhSqh-GFP; UAS-NSlmb-vhhGFP4 virgins were crossed to w; 332.3Gal4, TRE-dsREDattP40 (n=12 embryos analyzed).

6.1.4. Live imaging/confocal microscopy

D. melanogaster embryos were collected and aged at 21-25°C, dechorionated with 50% bleach for 3-4min, aligned and transferred onto on a glass slide with glue. Embryos were covered with Voltalef Halocarbon oil 10S (Sigma-Aldrich) to avoid dehydration. Depending on the experiment embryos were imaged from any stage past syncytium until the end of DC or later. In cases where DC failed, embryos were imaged at least for 30-60min after DC failure.

Imaging of all embryos was performed at 23-25ºC using spinning-disk confocal microscopes (Zeiss Axio Observer.Z1 or custom-modulated Leica DM IRBE) equipped with iXon3/888 or Neo sCMOS cameras and controlled by ANDOR IQ software. Objectives used: 25X (for DC overview and DC parameter analysis at 25ºC), 40X, 63X and 100X. With 25X objective, usually, z-planes were acquired every 2µm and maximum-intensity z projections were analysed. For higher resolution images (40X, 63X, 100X objectives) z-planes were acquired every 0.25-1µm, and single planes or maximum-intensity z projections of relevant planes were analysed.

6.1.5. Image Processing and Analysis

Image processing and maximum intensity z-projections were done using ImageJ or MATLAB (MathWorks). All signal intensity and region-of-interest (ROI) measurements were done using ImageJ or Icy. In few cases image brightness/contrast was adjusted on images as a whole for better visualization. 3D reconstructions were done with Icy using Raycaster Mapping, Cubic Interpolation and Composite Blending. Data were quantified and plotted using Excel (Microsoft), MATLAB (MathWorks) and Origin Pro (Origin Labs). All statistical tests and descriptive statistics were performed with Origin Pro (Origin Labs). Detailed description of individual analysis is found in the respective Methods sections below.

6.2. Materials and Methods specific for Chapter 2

6.2.1. Generation of the AS-specific 332.3Gal80 insertion

To selectively repress the Gal4/UAS system in AS cells we replaced Gal4 in the enhancer trap P{GawB} insertion 332.3 with the Gal80 repressor expressing P{ET-GAL80}. Swapping was triggered by expressing P-element transposase[92]. For this, yw; UAS-hid/CyO virgins were crossed to *P{y[+t7.7]=ET-GAL80}1, y[1] w[1118]; P{w[+mW.hs]=GawB}332.3/CyO ; ry[506] Dr[1] P{ry[+t7.2]=Delta2-3}99B/+* males[219]. Since the activation of hid by 332.3Gal4 is lethal, we selected for surviving yellow$^+$ males, which had lost Gal4 expression. Their offspring was individually crossed to w; pnrGal4, UAS-mCherry-moesin/TM3, Ser virgins, which express ectopic mCherry in the AS tissue. The progeny of one male was lacking such mCherry expression suggesting that it was expressing Gal80 in the AS tissue (Fig. 10D). We named this P{ET-GAL80}332.3 insertion 332.3Gal80 (Fig. 10C). To further confirm Gal80-mediated Gal4 suppression in the AS tissue we crossed w; 332.2Gal4, UAS-mCherry-moesin/CyGFP virgins to yw/Y; 332.3Gal80 males and found that all 332.2Gal4, UAS-mCherry-moesin/332.3Gal80 offspring had suppressed mCherry-moesin expression in the AS tissue.

We noticed that 332.3Gal80 adults had dark, yellow$^+$ pigmentation in the antennae and circling the eyes (Fig. 53D). Obviously, yellow$^+$ transcription was induced in the respective cells by tissue-specific enhancers. The same enhancers should also be driving Gal4 and white$^+$ transcription in the original P{GawB}332.3 insertion. To test this, we analysed adults of the genotype *yw; P{w[+mW.hs]=GawB}332.3/+; TM3, P{w[+mC]=UAS-y.C}MC2, Ser[1]/+* for Gal4-mediated expression of UAS-yellow$^+$. The yellow$^+$ pigmentation pattern was identical to that driven by P{ET-GAL80}332.3, but even stronger than in homozygous yw; P{ET-GAL80}332.3 flies (Fig. 53D).

6.2.2. Generation of mCherry-tagged Zipper under UAS control

We cloned full-length zipper cDNA from two sources. The 5'-end (first 2725bp of the *zipper* ORF, isoform C) was obtained from the Berkeley Drosophila Genome Project library (Plasmid No. IP15404). The 3'-end (last 3191bp) was obtained from a cDNA Matchmaker library (gift from Markus Noll). A unique XbaI restriction site in the middle of the cDNA was used to fuse the two cDNA fragments. The full length *zipper* cDNA (isoform C) was cloned into the P-element P{UASp} transformation vector (5XUAS) and a sequence encoding mCherry was

added at the 5' end with a "GAGAGAGAGAGAGPTENSSMISDP" linker sequence. Transgenic flies were generated as described in[220].

6.2.3. Image analysis

The apical AS cell surface areas in Fig. 8A and Fig. 12C were measured using polygonal selection tool in ImageJ, by outlining the apical actin belt next to the adherens junctions and following the change of belt shape over time. 16 cells from 2 embryos were tracked for control embryos and 29 cells from 4 embryos were tracked for AS-SqhKO embryos. The relative apical area change was normalized as follows:

$$\mathbf{N(t_x)=(ASarea(t_x)-ASarea(t_{x+1}))/ASarea(t_x);}$$

where "$N(t_x)$" is the normalized AS apical area change of a given frame t_x, "$ASarea(t_x)$" is the absolute AS apical area of a given frame t_x and "$ASarea(t_{x+1})$" is the absolute AS apical area of a given frame at the next following time point t_{x+1}.

Intensities of apical and junctional Sqh-GFP in Fig. 7B were measured from time-lapse movies after subtracting background illumination (Gaussian filtering (imgaussfilt), sigma value=150, MATLAB). The intensity of the apical Sqh-GFP signal was measured by selecting regions in the middle of individual AS cells and following the respective area over time. Since apical Sqh-GFP signal intensity oscillates (i.e. cells are pulsing), we normalized the signal to the minimum intensity value measured in the first 45min of the movie. For junctional Sqh-GFP signal intensity measurements, a 3 pixel-wide line was drawn along the junction length and average intensity values were measured over time. Junctional intensity was normalized against the minimum intensity measured in the first 5 frames of a movie. Intensities were measured until apical- and junctional Sqh-GFP pools could no longer be discriminated.

6.2.4. DC parameter analysis

The relative dorsal opening area was measured on maximum intensity z-projections using polygon selection tool in ImageJ. Time-point zero was defined as the end of germ-band retraction (GBR) with an error margin of ± 4min (1 movie frame). The end of dorsal closure was defined as complete sealing of the opening. In AS-SqhKO embryos, we tracked the area of the dorsal opening until tissue rupturing made the epidermal edges disappear in the maximum intensity projection.

The relative area of the dorsal opening was tracked as follows:

$$\mathbf{S(t_x)=area(t_{0+x})/area(t_0)}$$

where "$S(t_x)$" is the relative area of the dorsal opening at a given time-point x, "$area(t_{0+x})$" is the area of the dorsal opening at a given time-point x and "$area(t_0)$" is the area of the dorsal opening at time-point zero (i.e. end of germ band retraction).

The relative dorsal opening area change (% per min) was measured as follows:

$$\mathbf{\Delta S(t_x) = (area(t_x)-(area(t_{x+1}))/area(t_x))/\Delta t}$$

where "$\Delta S(t_x)$" is the relative area change of the dorsal opening in a given frame, "$area(t_x)$" is the area of the dorsal opening in the given frame, "$area(t_{x+1})$" is the area of the dorsal opening in the following frame and "Δt" is the time interval between frames.

The length of the dorsal opening was defined as the maximum distance between epidermal fronts in parallel to the anterior-posterior axis of the embryo. This procedure was applied to every frame in the time-lapse movies. The maximal length axis of the dorsal opening as defined at time-point zero was used to define the gap width. For this a perpendicular line through the middle-point of the length axis was drawn (± 1º). The distance change over time between the crossing points of this line with the LEs of the two epidermis fronts defined the gap width change. Once the dorsal opening is re-shaped from initial shape at the end of germ band retraction, such a line would mark the maximum distance between the two LEs. Such line is commonly denoted as the starting height of the opening in most studies that focus on later stages of DC[39,42,45–47,54].

The convergence speed of the LEs was calculated as follows:

$$\mathbf{v(t_x)=(width(t_x)-width(t_{x+1}))/\Delta t}$$

where "$v(t_x)$" is the convergence speed of LEs, "$width(t_x)$" is the width of the dorsal opening in a given frame, "$width(t_{x+1})$" is the width of the dorsal opening in the following frame and "Δt" is the time interval between frames. The speed of the approaching LEs is defined as zero when they do not move in either direction in the two consecutive frames. Initially, speed is negative due to a ventral-ward movement of the LEs. DC onset was defined as the time-point when the speed of the approaching LEs became positive and stayed positive in the following 2 frames.

6.2.5. AC cable intensity analysis

For actin cable intensity analysis, we defined 80 neighbouring lines, 30-pixel in length, which together formed a 30x80px rectangle (~5x12µm). The rectangle was placed on the LE with the long axis perpendicular to the LE, such that the 2 middle 30px lines centered on the LE as shown in Supplementary Figure 3f. In control embryos the LE position was given by the AMC, and a fictive line through the base of the cell protrusions (lamellipodia and filopodia) was used

in ES-SqhKO and UAS-Mbs.N300 embryos. The rectangle was then moved along the entire LE, ensuring a 10-15px overlap and perpendicular orientation to the LE. At each position, the average intensity of each 30-pixel line was defined. The signal intensities were then normalized against the background signal, which we defined as the average value of the outer-most 20 of all 30-pixel lines that were positioned above the AS tissue, which did not express any fluorescent signal. Intensities were then assembled into an intensity profile as shown in Fig. 11F.

6.2.6. Laser microsurgery and analysis

Laser microsurgery was done on a spinning disc confocal microscope (Zeiss Axio Observer.Z1) equipped with a MicroPoint pulsed nitrogen pumped dye laser (5ns pulse width, 10Hz, λ=435nm; Andor Technology). Objectives used: 63X and 100X. All ablations were carried out to ensure consistent and complete ablation of the adherens junctions, but without damaging underlying tissues. Therefore, laser cuts in the AS tissue were carefully monitored for not having damaged the underlying yolk cell (and the basal lamina connecting the yolk cell with the basal AS cell membrane). A damaged yolk cell is easily detectable due to the appearance of a ring of Sqh-GFP signal around the wounded area[123].

After laser ablation of individual adherens junctions connecting AS cells time-lapse image series were acquired and the displacements of all neighbouring AS tissue vertices that could be discriminated, were tracked over time in 1-2 sec intervals. For laser incisions of the LE, the distance between the free ends generated by the incisions were tracked over time in 0.5-1 sec intervals.

For angle measurements, the smaller angle between the anterior-posterior embryo axis and a line following the junction was measured and defined as junction orientation angle. The angle of each cell-cell vertex with respect to the ablated junction was defined as follows: A first line was drawn along the ablated junction up to the cutting point. A second line was then drawn from this point to the vertex of interest and the angle between the two lines was measured (Fig. 12E).

Canthi removal in Appendix 2, section A2.1. was performed with 40X objective as described in Wells et al. 2014 and embryos were imaged for 120min. Then laser incisions in the LEs were performed with 63X objective as described above.

6.3. Materials and Methods specific for Chapter 3

6.3.1. Injections of pharmacological compounds

For all injections, prior to covering embryos with Halocarbon oil they were desiccated for 10-15min in the air. Injections were carried out at two different places – directly at the Zeiss Axio Observer.Z1 spinning-disk confocal microscope using Leitz injection micromanipulator or at the upright Zeiss Axiovert X35 microscope using Narishige MO-11 injection manipulator (Narishige Scientific Instrument lab, Japan). In the former case image acquisition started within <30s, in the latter – within <2min after the injection. To generate the injection needles, boro-silicate capillaries (GC100TF-10, Harvard Instruments) were pulled using Narishige needle puller PN-3 (Narishige Scientific Instrument lab, Japan). Needles were broken against the glass slide and fluid was expelled using an air syringe. All injected compounds are listed in Table 5 together with solvents used and concentrations in the needle. Injection place is also noted in Table 5. Laser incisions were performed on Zeiss Axio Observer.Z1 spinning-disk confocal microscope after injecting the compounds directly at the microscope.

Compound (Company)	**Tip concentration**	**Solvent**	**Injection place***	**Action on the target**	**Figure/Section**
DMSO (Sigma-Aldrich)	1%, 10%, 100% v/v	1:10 and 1:100 DMSO:H_2O	SD, UPR	Undefined	17B; 20E, F;
Latrunculin B	100µM, 1mM, 10mM, 1M	DMSO, 1:100 DMSO:H_2O	SD	Depolymerizes actin	17A; 20A-C; 56A, B;
Cytochalasin D	100µM	DMSO	SD, UPR	Depolymerizes actin	Section 3.2.2;
Blebbistatin	100µM, 1mM, 10mM	DMSO	SD, UPR	Inhibits MyoII	Section 3.2.2;
Ionomycin	100µM, 1mM, 10mM	DMSO, 1:100 and 1:10 DMSO:H_2O	SD	Ca^{2+} ionophore	17D-F;
NG-EGTA	0.5mM	DMSO	SD	Chelates Ca^{2+} (also intracellular)	Section 3.2.2;
Carbenoxolone	100 µM, 1M, 3M, 10M	DMSO	SD, UPR	Prevents electro-chemical coupling of cells via gap junctions	18;

Wortmannin	1mM, 10mM, 60mM	DMSO	SD, UPR	Inhibits PI3-kinase; at high concentrations inhibits MyoII regulatory light chain	24G;
Pannexin	0.8M	H_2O	UPR	Block solute transport via gap junctions	Section 3.2.5;
Sildenafil	100µM, 3mM, 10mM	DMSO	UPR	Inhibits *phosphodiesterase* type 5	Section 3.2.5; 17C;
cAMP	1M	H_2O	UPR	Common cellular secondary messenger	24F;
cGMP	1mM, 10mM	DMSO	UPR	Common cellular secondary messenger	Section 3.2.5;
EDTA	1M	H_2O	SD	Chelates Ca^{2+}	19D;
DMF	100%, 80%, 60%, 40%, 20% v/v	DMSO	SD	Organic solvent, undefined	Section 3.2.5;
H_2O	-	-	UPR	Solvent	Section 3.2.5;
Colchicine	10mM	PBS	UPR	Prevents microtubule polymerization	Section 3.2.5;
Colcemide	10µg/ml w/v	DMSO	SD	Prevents microtubule polymerization	Section 3.2.3;
CK-666	1mM	DMSO	SD	Inhibits Arp2/3 complex	20D;
Adenyl-cyclase inhibitor	0.5mM	H_2O	UPR	Inhibits cAMP production	Section 3.2.5;

Table 5. Pharmacological compounds used in this study. * SD – injected at the Zeiss Axio Observer.Z1 spinning-disk confocal microscope and imaged <30s later; UPR – injected at the upright Zeiss Axiovert X35 and imaged <2min later with Leica DM IRBE spinning-disk confocal microscope;

6.3.2. CO_2/Argon anaesthesia

For CO_2/Argon anaesthesia embryos were prepared same as for live imaging, but were glued on the MatTek imaging dish (MatTek Corporation) and covered with Voltalef Halocarbon oil S10 (Sigma-Aldrich). Imaging dish was then placed into a custom-built gas flow-through chamber. Either CO_2 or Argon gases were saturated with water and applied to the chamber. Final gas flow concentration was at a rate of ~1000ml/min. Upon recovery from anaesthesia,

CO_2/Argon gases were replaced with compressed air at a rate of ~2000ml/min using an inflatable balloon.

6.3.3. Image Processing and Analysis

Fig. 14: To quantify actin nucleation burst (ANB) parameters, mCherry-moesin fluorescence intensities in AS cell ROI were measured every 30s from maximum intensity *z* projections throughout the movie using ImageJ. The intensity oscillations were then detrended by subtracting the mean intensity value individually for every intensity profile.

For finding the periods of ANBs, we divided the movie frames into time windows of 900s that were shifted by 30s. For every 900s window from intensity profile auto-correlation was performed on the intensity profile (*autocorr* function in MATLAB). The average distance between the peaks in the auto-correlation function was taken as a period for that time window. Peaks were found using *findpeaks* function in MATLAB without any threshold in peak height.

For finding phase difference between ANBs in the neighbouring AS cells, we divided the movie frames into time windows of 900s that were shifted by 30s. For every 900s window from intensity profile, cross-correlation was performed on the two neighbouring cell intensity profiles (*xcorr* function in MATLAB). The total number of maxima and minima that were between -60s to +60s time lags in the cross-correlation functions (CCFs) was then obtained from all the time windows and all the possible cell neighbour pairs. Threshold of correlation coefficient of 0.2 were used to distinguish between significant vs non-significant correlation for both minima and maxima. ANBs in the neighbouring cells were categorized as non-correlated if there were neither minima nor maxima in the -60s to +60s time lag of CCF for a given time window. If minima was present in the -60s to +60s time lag of CCF, cells were categorized as being anti-phase for a given time window. If maxima was present in the -60s to +60s time lag of CCF, cells were categorized as being in-phase for a given time window.

Fig. 15 and Fig. 16: For ANB visualization in laser-cut cells and CO_2/Argon anesthetized embryos, mCherry-moesin fluorescence intensity was measured in AS cell ROI. Intensity profile was normalized to minimum/maximum intensity values of every measured ROI (*mat2gray* function in MATLAB).

Fig. 19: Ca^{2+}-induced myr-GCaMP V intensity changes upon laser incisions were measured from single planes of AS cell ROI throughout the movie every 1s using ImageJ. The intensities were normalized to the intensity value at 5s prior to the laser incision.

Fig. 24: ANB periods were obtained in the same way as in Fig. 14.

6.3.4. CRISPR/Cas9-mediated *inx3* knock-out

CRISPR/Cas9 genome engineering was followed according to the protocols on flyCRISPR (http://flycrispr.molbio.wisc.edu/) and CRISPR fly design[149] (http://www.crisprflydesign.org/protocols/).

1) We chose the following two CRISPR target sites - GATTTCTCAATTGCTAAGGT and GCTGGGATCGCTGGTTCCGC - in the vicinity of *inx3* gene using CRISPR optimal target finder (http://tools.flycrispr.molbio.wisc.edu/targetFinder/).
2) Next, we generated tandem-guideRNA plasmid pCFD4-U61-U63 (Addgene plasmid no. 49411) that contained the above mentioned target sequences followed by gRNA core.
   2.1) We used the following primers to amplify DNA fragment from pCFD4-U61-U63 using PCR:
   fwd primer:
   TATATAGGAAAGATATCCGGGTGAACTTCGgatttctcaattgctaaggtGTTTTAGAGCTAGAAATAGCAAG
   rev primer:
   ATTTTAACTTGCTATTTCTAGCTCTAAAACgctgggatcgctggttccgcGACGTTAAATTGAAAATAGGTC
   2.2) We then inserted the obtained PCR fragment into BbsI-digested pCFD4-U61-U63 plasmid using Gibson Assembly Kit (New England Biolabs).
   2.3) We sequenced the obtained pCFD4-U61-U63-gRNAinx3 plasmid using the following primers:
   M13 rev: CAGGAAACAGCTATGAC
   Inx31_anti: CTGGGATCGCTGGTTCCGC
3) Next, we created pHD-DsRed-attP-inx3-HR1-HR2 homologous repair plasmid.
   3.1) Two ~1kb homology regions flanking the *inx3* gene were amplified from *D. melanogaster* strain nosCas9 (BL#54591) using the following primers:
   Homologous arm region 1 (HR1):
   fwd_AarI_HR1: CGTCCACCTGCTACGTCGCctctcagcatgcaaatgg
   rw_AarI_HR1: GCTGCACCTGCTAGCCTACagctggttcccgctccgag
   Homologous arm region 2 (HR2):
   fwd_SapI_HR2: GCTCGCTCTTCGTATggtcggattttccattgtttatg
   rev_SapI_HR2: CGAGGCTCTTCGGACcaagtgctgctcattgttcc
   Single fly PCRs were done according to the following protocol:

i) Single adult fly was squished in 20µl solution consisting of 10mM Tris-HCl (pH 8.2), 25mM NaCl, 1mM EDTA, 0.2% (v/v) TritonX100, 200µg/ml Proteinase K.

ii) Mixture was then incubated for 2h at 37°C and then 15min at 95°C.

iii) 2µl of fly extract was used for standard 50µl PCR reaction using Phusion Polymerase (Thermo Scientific).

3.2) First homologous arm region 1 (HR1) was inserted into pHD-DsRed-attP donor vector (Addgene plasmid no. 51434) using AarI restriction sites to obtain plasmid pHD-DsRed-attP-inx3-HR1.

Next, homologous arm region 2 (HR2) was inserted into pHD-DsRed-attP-inx3-HR1 using SapI restriction sites to obtain pHD-DsRed-attP-inx3-HR1-HR2 plasmid with both inx3-flanking homologous regions present.

3.3) Plasmid maxi-preps of pCFD4-U61-U63-gRNAinx3 and pHD-DsRed-attP-inx3-HR1-HR2 were then obtained using NucleoBond PC 500 DNA purification kit (Macherey-Nagel). The following final concentrations of plasmids were used for injection: pHD-DsRed-attP+HR1/HR2 – 500ng/µl; tandem-guideRNA - 250ng/µl. *D. melanogaster* strain nosCas9 (BL#54591) embryos were injected following standard injection protocol[220].

4) We next screened for successful CRISPR events in *D. melanogaster*.

4.1) Since the original *nos*Cas9 (BL#54591) fly strain contained GMR-mRFP, injected F_0 males were crossed to *yw* females whereas injected F_0 females were crossed to *FM6, w* males. Successful CRISPR events were immediately screened for dsRED signal in F_1 progeny coming from the injected F_0 males. F_1 progeny of injected F_0 females were crossed once more to *FM6, w* and only F_2 were screened for GMR-dsRED. In total, 3 independent CRISPR events from 157 hatched animals generated $inx3^{dsRED}$ alleles.

4.2) We verified dsRED-attP integration into *inx3* locus in the following ways:

i) Using primer pairs so that one primer was inside the dsRED-attP cassette and the other one was outside the HR region.

HR1:

inx3_outHR1_1: GGACTTGGAACTTGAAACTCGAAG

rev_dsRED_1: GTTCACGCCGATGAACTTCACC

and

inx3_outHR1_2: GCTGGCAGATACATTTCTGGCG

rev_dsRED_2: CACCTTGAAGCGCATGAACTC

HR2:

inx3_outHR2_1: GGCGATGTGGCTCCAGTTAG
fwd_dsRED: GGTGAAGTTCATCGGCGTGAAC
and
inx3_outHR2_2: CGGACTAAGTCGAAAGTTGCC
fwd_dsRED: GGTGAAGTTCATCGGCGTGAAC

ii) Using pair of primers that both anneal outside the two HRs. For this we used all possible pair-wise combinations of primers inx3_outHR1_1, inx3_outHR1_2, inx3_outHR2_1 and inx3_outHR2_2 mentioned above.

iii) Crossing all 3 obtained *Δinx3^{dsRED}* alleles over the deficiency *Df(3R)BSC789* (BL#27361) that encompasses *inx3*. Such *Δinx3^{dsRED}*/*Df(3R)BSC789* flies were lethal with occasional escapers that were not fertile and overall very weak.

5) All 3 *Δinx3^{dsRED}* founder lines were then crossed with *ywhsCre* (BL#766) flies to remove dsRED flanked by loxP sites. All obtained *Δinx3^{attP}* chromosomes were lethal over the *Df(3R)BSC789* deficiency.

6.4. Materials and Methods specific for Chapter 4

6.4.1. Image analysis in recAS-SqhKO embryos

AS cells in recAS-SqhKO embryos were classified as not affected by the deGradFP if they showed coalescing Sqh-GFP foci and contained typical diffuse cytoplasmic Sqh-GFP signal. AS cells were classified as affected by the deGradFP if they contained Sqh-GFP aggregates and diffuse cytoplasmic Sqh-GFP signal was not detectable.

For Sqh-GFP intensity analysis in recAS-SqhKO embryos maximum-intensity z projections or relevant z slices were used. All measurements were performed with ImageJ or Icy.

For measuring apical MyoII population in recAS-SqhKO embryos, ROI was chosen at the apical cell surface. For 8 cells, average ROI intensities were measured every 1min and excluded Sqh-GFP degradation aggregates. Cells where these aggregates prevented intensity measurements at the apical surface were analysed qualitatively for appearance of the apical Sqh-GFP bursts outside the aggregates. Apical Sqh-GFP intensity was normalized to the minimum intensity value in the first 10min of the movie.

For junctional Sqh-GFP, 3-pixel-wide line was drawn along the cell-cell junction and average intensity values were measured. For 8 cells, signal intensity was measured in 5min intervals

for 80min. For the remaining 50 cells, qualitative analysis throughout the 80min were performed to confirm junctional Sqh-GFP signal increase. Junctional Sqh-GFP intensity was normalized to the intensity value in the first measured frame.

Cell circumference, area and elongation factor were measured with Icy ROI selection tool and ROI statistics plugin (plugin ID: ICY-W5T6J4) by outlining AS cell area encompassed by the junctions. Cell area and circumference decrease was measured as follows:

$$\Delta AS_{area}=(AS_{area}(t_0)-AS_{area}(t_{80}))/AS_{area}(t_0)*100\%$$

where "ΔAS_{area}" is the relative cell area decrease in 80min, "$AS_{area}(t_0)$" is the cell area at time point 0min, "$AS_{area}(t_{80})$" is the cell area at time point 80min;

$$\Delta AS_{circ}=(AS_{circ}(t_0)-AS_{circ}(t_{80}))/AS_{circ}(t_0)*100\%$$

where "ΔAS_{circ} " is the relative cell circumference decrease in 80min, "$AS_{circ}(t_0)$" is the cell circumference at time point 0min, "$AS_{circ}(t_{80})$" is the cell circumference at time point 80min;

Elongation factor (EF) was determined using ROI statistics plugin (plugin ID: ICY-W5T6J4) and is defined as a ratio between the first and second ellipse diameters drawn on the cell area. The minimum value of EF is 1 for a non-elongated object (i.e. circle or disk). Hence to reflect the change in EF over time, 1 was subtracted from the calculated ratios. The percentage of EF reduction was calculated using the following formula:

$$\Delta AS_{EF}=((AS_{EF}(t_0)-1)-(AS_{EF}(t_{80})-1))/(AS_{EF}(t_0)-1)*100\%$$

where "ΔAS_{EF} " is the relative elongation factor decrease in 80min, "$AS_{EF}(t_0)$" is the cell elongation factor at time point 0min, "$AS_{EF}(t_{80})$" is the cell elongation factor at time point 80min;

Fig. 28: Individual junction length was measured using Icy ROI selection tool by drawing a line between the two neighbouring cell vertices in the movie at 1min intervals. The apical ROI next to the shortening junction was picked not to include Sqh-GFP degradation aggregates. To account for the fluorescence bleaching and equalize the fluorescence intensities across the different embryos and cells (deGradFP-affected vs non-affected), the detrended (*detrend* function in MATLAB) signals were subtracted from the original intensity profiles.

6.4.2. Nuclear *dad*>GFP^{NLS} signal intensity measurements

Surface intensity map of *dad*>GFP^{NLS} signal in Fig. 30B was created from intensity values normalized to the minimum/maximum values of the image field (*mat2gray* function in MATLAB).

For both *dad*>GFP^{NLS} and *ubi*>GFP^{NLS} absolute nuclear intensities in maximum z intensity projections were measured using ROI parameter measurement tool in ImageJ. Intensities were

measured every 5min for 120min, the first frame starting ~45-60min prior to DC onset as defined by the net LE dorsal-ward movement.

As a complementary analysis, nuclear intensities were measured from processed images, where all single z slices were corrected for uneven background illumination by subtracting Gaussian-blurred image (*imgaussfilt* function in MATLAB, Sigma=150) from the original image. ROI intensities in the maximum-intensity z projections obtained from such Gaussian-filtered images were then measured. For consistency, exactly the same ROIs were used for maximum z-intensity projections with and without background illumination subtraction.

After obtaining intensity profiles of every nucleus for 120min, the intensity values were normalized to the starting intensity value at time 0min. Linear fit and regression model was then applied according to the formula:

$$f(x)=a*x+b$$

Coefficients ***a*** and ***b*** were obtained for every nucleus and ***a*** were plotted against a distance of the nucleus from the LE at the beginning of analysis. The distance from LE was defined as the shortest distance in the maximum-intensity z projection from the center of AS cell nucleus to the LE.

6.4.3. *dad*>GFP^{NLS} and Zip-mCherry correlation

For correlating Zip-mCherry and *dad*>GFP^{NLS} intensities w; *332.3*Gal4, UAS-Zip-mCherry/+; *dad*>GFP^{NLS}/+ flies were analysed. AS cells that did not express UAS-Zip-mCherry were chosen as a reference for measuring Zip-mCherry signal intensity at the adherens junction.

Zip-mCherry intensity was measured from maximum-intensity z projections by outlining ROI in a single junction excluding the vertice point shared by 3 neighbouring cells. Outlined ROI was <5px (~0.75µm) wide. As a complementary measurement, 3px-wide line was drawn along the single junction also excluding the vertice point shared by 3 neighbouring cells. To allow comparison of intensities across different embryos, Zip-mCherry intensities for every junction were normalized to the mean background intensity (MBI) of every embryo. MBI was defined as a mean value of least 30 random background areas in the cell that did not express UAS-Zip-mCherry.

Absolute *dad*>GFP^{NLS} nuclear intensities were measured from maximum-intensity z projections by outlining ROI around the nuclei in ImageJ. To allow comparison of intensities between different embryos, *dad*>GFP^{NLS} intensities was normalized to the MBI of every embryo. MBI was defined as a mean value of at least 30 random background areas in between the nuclei.

Correlation coefficients between the normalized Zip-mCherry and *dad*>GFP^{NLS} intensities were obtained using linear fit in Origin Pro.

6.4.4. DC time measurement

DC completion time using *dad*>GFP^{NLS} as a reporter was determined as the time from the end of germ-band retraction (±1-2 frames (4-8min)) until AS nuclei were below the epidermis and no longer visible in the maximum-intensity z projections (±2-3 frames (8-12min)). DC times were measured in this way for all the compared genotypes (Fig. 35). The values were larger than measuring with arm-GFP or Sqh-GFP reporters, since the epidermis seals prior to AS nuclei disappearance.

6.5. Materials and Methods specific for Chapter 5

6.5.1. MC time measurement

MC completion time in control and AS-SqKO embryos was defined as the time from the end of germ-band retraction (±1-2 frames (4-8min)) until the end of the fusion of two midgut sides at the dorsal surface of the embryo (±1-2 frames (4-8min)).

6.5.2. Laser microsurgery of the yolk cell

Laser microsurgery was done on a spinning disc confocal microscope (Zeiss Axio Observer.Z1) equipped with a MicroPoint pulsed nitrogen pumped dye laser (5ns pulse width, 10Hz, λ=435nm; Andor Technology). 100X objective was used.

6.5.3. Analysis of Sqh-GFP wave parameters in the yolk cell

For Sqh-GFP foci parameter analysis in Fig. 40B, fluorescence signal intensity from a rectangle squares (20µ x x20µm) in maximum-intensity z projection was measured. Foci appearance periods were calculated in the same way as for ANBs in AS cells described in section 6.3.3. The only exception was that the sliding window was chosen to be 1650s to encompass 2-3 intensity oscillation peaks.

Average speed of travelling Sqh-GFP waves in Fig. 40C was determined in the following steps:
1) Movie frames where the analysed Sqh-GFP wave appeared and disappeared were selected.
2) The distance (in µm), which the selected wave has travelled, was measured in a maximum-

intensity z projection. 3) The travelled distance was divided by the time between the start- and end-frames.

6.5.4. Measurement of AS cell centroid displacement

The apical AS cell surface areas in Fig. 42 were measured using polygonal selection tool in Icy with ROI selection tool. Apical actin belt next to the adherens junctions was outlined and its centroid location was followed over time. 16 cells from 2 embryos were tracked for control embryos, 43 cells from 5 embryos were tracked for AS-SqhKO embryos and 29 cells from 4 embryos were tracked for AS-yolk-SqhKO embryos.

The co-ordinates of AS cell area centroid were extracted using Icy ROI statistics plugin (plugin ID: ICY-W5T6J4) from a movie frames at 1min interval apart. The distance between the centroid locations in two subsequent frames was calculated as follows:

$$\mathbf{\Delta C(t_a\text{-}t_{a+1}) = sqrt((X(t_a)\text{-}X(t_{a+1}))^2 + (Y(t_a)\text{-}Y(t_{a+1}))^2);}$$

where "$\mathbf{\Delta C(t_a\text{-}t_{a+1})}$" is the distance of centroid displacement between a given frame $\mathbf{t_a}$ and the next following time point $\mathbf{t_{a+1}}$, "$\mathbf{X(t_a)}$" is the centroid coordinate along the X axis of the image at a given frame $\mathbf{t_a}$, "$\mathbf{X(t_{a+1})}$" is the centroid coordinate along the X axis of the image the next following time point $\mathbf{t_{a+1}}$, "$\mathbf{Y(t_a)}$" is the centroid coordinate along the Y axis of the image at a given frame $\mathbf{t_a}$, "$\mathbf{Y(t_{a+1})}$" is the centroid coordinate along the Y axis of the image the next following time point $\mathbf{t_{a+1}}$, "**sqrt**" is the square root.

6.5.5. Particle image velocimetry

Particle image velocimetry was used with PIVlab - time-resolved particle image velocimetry (PIV) tool - plugin in MATLAB. The tool was created by W. Thielicke. For images shown in Fig. 43, the following settings were used:

1st interrogation window: 128x128 pixels; 2nd interrogation window: 64x64 pixels; The obtained vector fields were thresholded for vector speed of 10px/frame (0.66µm/).

6.5.6. Plasmid injection into the YC

For visualizing transgenes in the YC, *tub*>Gal4 and *sqh*:Sqh-GFP plasmids (1µg/µl) were injected into the embryos as described in 6.3.1. The plasmids were injected into the blastoderm stage embryos (Bownes stages 1-4) that were imaged later during the MC stages.

References

1. Pollard, T. D. Regulation of actin filament assembly by Arp2/3 complex and formins. *Annu. Rev. Biophys. Biomol. Struct.* **36,** 451–477 (2007).

2. Campellone, K. G. & Welch, M. D. A nucleator arms race: cellular control of actin assembly. *Nat. Rev. Mol. Cell Biol.* **11,** 237–51 (2010).

3. Ananthakrishnan, R. & Ehrlicher, A. The forces behind cell movement. *Int. J. Biol. Sci.* **3,** 303–317 (2007).

4. Blanchoin, L., Boujemaa-Paterski, R., Sykes, C. & Plastino, J. Actin dynamics, architecture, and mechanics in cell motility. *Physiol. Rev.* **94,** 235–63 (2014).

5. Vicente-Manzanares, M., Ma, X., Adelstein, R. S. & Horwitz, A. R. Non-muscle myosin II takes centre stage in cell adhesion and migration. *Nat. Rev. Mol. Cell Biol.* **10,** 778–90 (2009).

6. Munjal, A. & Lecuit, T. Actomyosin networks and tissue morphogenesis. 1789–1793 (2014). doi:10.1242/dev.091645

7. Pasakarnis, L., Dreher, D. & Brunner, D. SnapShot: Mechanical Forces in Development I. *Cell* **165,** 754–754.e1 (2016).

8. Murrell, M., Oakes, P. W., Lenz, M. & Gardel, M. L. Forcing cells into shape : the mechanics of actomyosin contractility. *Nat. Publ. Gr.* **16,** 486–498 (2015).

9. Reymann, A.-C. *et al.* Turnover of branched actin filament networks by stochastic fragmentation with ADF/cofilin. *Mol. Biol. Cell* **22,** 2541–2550 (2011).

10. Loisel, T. P., Boujemaa, R., Pantaloni, D. & Carlier, M. F. Reconstitution of actin-based motility of Listeria and Shigella using pure proteins. *Nature* **401,** 613–616 (1999).

11. Zaidel-bar, R., Zhenhuan, G. & Luxenburg, C. The contractome – a systems view of actomyosin contractility in non-muscle cells. 2209–2217 (2015). doi:10.1242/jcs.170068

12. Garcia-Mata, R., Boulter, E. & Burridge, K. The 'invisible hand': regulation of RHO GTPases by RHOGDIs. *Nat. Rev. Mol. Cell Biol.* **12,** 493–504 (2011).

13. Hall, A. & Nobes, C. D. Rho GTPases: molecular switches that control the organization and dynamics of the actin cytoskeleton. *Philos. Trans. R. Soc. Lond. B. Biol. Sci.* **355,** 965–70 (2000).

14. Basson, M. A. Signaling in Cell Differentiation and Morphogenesis. 1–22 (2012).

15. Tabata, T. & Takei, Y. Morphogens, their identification and regulation. *Development* **131,** 703–712 (2004).

16. Heisenberg, C. P. & Bellaïche, Y. XForces in tissue morphogenesis and patterning. *Cell* **153,** (2013).

17. Gorfinkiel, N. & Blanchard, G. B. Dynamics of actomyosin contractile activity during epithelial morphogenesis. *Curr. Opin. Cell Biol.* **23,** 531–9 (2011).

18. Lecuit, T. & Lenne, P.-F. Cell surface mechanics and the control of cell shape, tissue patterns and morphogenesis. *Nat. Rev. Mol. Cell Biol.* **8,** 633–644 (2007).

19. LeGoff, L. & Lecuit, T. Mechanical Forces and Growth in Animal Tissues. *Cold Spring Harb. Perspect. Biol.* 1–18 (2015). doi:10.1101/cshperspect.a019232

20. Behrndt, M., Roensch, J., Grill, S. W. & Heisenberg, C. in Zebrafish Gastrulation. **257,** 10–14 (2014).

21. Munro, E., Nance, J. & Priess, J. R. Cortical flows powered by asymmetrical contraction transport PAR proteins to establish and maintain anterior-posterior polarity in the early C. elegans embryo. *Dev. Cell* **7,** 413–424 (2004).

22. Lecuit, T., Lenne, P.-F. & Munro, E. Force generation, transmission, and integration during cell and

tissue morphogenesis. *Annu. Rev. Cell Dev. Biol.* **27,** 157–184 (2011).

23. Edwards, K. a, Demsky, M., Montague, R. a, Weymouth, N. & Kiehart, D. P. GFP-moesin illuminates actin cytoskeleton dynamics in living tissue and demonstrates cell shape changes during morphogenesis in Drosophila. *Dev. Biol.* **191,** 103–17 (1997).

24. Campos-Ortega, J. a. & Hartenstein, V. The Embryonic Development of Drosophila melanogaster. *Springer-Verlag Berlin* 1–405 (1997). doi:10.1007/978-3-662-22489-2

25. Eltsov, M. *et al.* Quantitative analysis of cytoskeletal reorganization during epithelial tissue sealing by large-volume electron tomography. *Nat Cell Biol* **17,** 605–614 (2015).

26. Wada, A., Kato, K., Uwo, M. F., Yonemura, S. & Hayashi, S. Specialized extraembryonic cells connect embryonic and extraembryonic epidermis in response to Dpp during dorsal closure in Drosophila. *Dev. Biol.* **301,** 340–9 (2007).

27. Toyama, Y., Peralta, X. G., Wells, A. R., Kiehart, D. P. & Edwards, G. S. Apoptotic force and tissue dynamics during Drosophila embryogenesis. *Science* **321,** 1683–6 (2008).

28. Muliyil, S., Krishnakumar, P. & Narasimha, M. Spatial, temporal and molecular hierarchies in the link between death, delamination and dorsal closure. *Development* **138,** 3043–54 (2011).

29. Riesgo-Escovar, J. R., Jenni, M., Fritz, a & Hafen, E. The Drosophila Jun-N-terminal kinase is required for cell morphogenesis but not for DJun-dependent cell fate specification in the eye. *Genes Dev.* **10,** 2759–2768 (1996).

30. Sluss, H. K. & Davis, R. J. Embryonic morphogenesis signaling pathway mediated by JNK targets the transcription factor JUN and the TGF-beta homologue decapentaplegic. *J. Cell. Biochem.* **67,** 1–12 (1997).

31. Hou, X. S., Goldstein, E. S. & Perrimon, N. Drosophila Jun relays the Jun amino-terminal kinase signal transduction pathway to the Decapentaplegic signal transduction pathway in regulating epithelial cell sheet movement. *Genes Dev.* **11,** 1728–1737 (1997).

32. Harden, N., Ricos, M., Ong, Y. M., Chia, W. & Lim, L. Participation of small GTPases in dorsal closure of the Drosophila embryo: distinct roles for Rho subfamily proteins in epithelial morphogenesis. *J. Cell Sci.* **112 (Pt 3,** 273–84 (1999).

33. Ricos, M. G., Harden, N., Sem, K. P., Lim, L. & Chia, W. Dcdc42 acts in TGF-beta signaling during Drosophila morphogenesis: distinct roles for the Drac1/JNK and Dcdc42/TGF-beta cascades in cytoskeletal regulation. *J. Cell Sci.* **112 (Pt 8,** 1225–35 (1999).

34. Young, P. E., Richman, a M., Ketchum, a S. & Kiehart, D. P. Morphogenesis in Drosophila requires nonmuscle myosin heavy chain function. *Genes Dev.* **7,** 29–41 (1993).

35. Franke, J. D., Montague, R. A., Kiehart, D. P. & Carolina, N. Article Nonmuscle Myosin II Generates Forces that Transmit Tension and Drive Contraction in Multiple Tissues during Dorsal Closure. **15,** 2208–2221 (2005).

36. Solon, J., Kaya-Copur, A., Colombelli, J. & Brunner, D. Pulsed forces timed by a ratchet-like mechanism drive directed tissue movement during dorsal closure. *Cell* **137,** 1331–42 (2009).

37. Gorfinkiel, N., Blanchard, G. B., Adams, R. J. & Martinez Arias, A. Mechanical control of global cell behaviour during dorsal closure in Drosophila. *Development* **136,** 1889–98 (2009).

38. David, D. J. V, Tishkina, A. & Harris, T. J. C. The PAR complex regulates pulsed actomyosin contractions during amnioserosa apical constriction in Drosophila. *Development* **137,** 1645–55 (2010).

39. Blanchard, G. B., Murugesu, S., Adams, R. J., Martinez-Arias, A. & Gorfinkiel, N. Cytoskeletal dynamics and supracellular organisation of cell shape fluctuations during dorsal closure. *Development* **137,** 2743–52 (2010).

40. Saravanan, S., Meghana, C. & Narasimha, M. Local, cell-nonautonomous feedback regulation of myosin dynamics patterns transitions in cell behavior: a role for tension and geometry? *Mol. Biol. Cell* **24,** 2350–61 (2013).

41. David, D. J. V, Wang, Q., Feng, J. J. & Harris, T. J. C. Bazooka inhibits aPKC to limit antagonism of actomyosin networks during amnioserosa apical constriction. *Development* **140,** 4719–29 (2013).

42. Saias, L. *et al.* Decrease in Cell Volume Generates Contractile Forces Driving Dorsal Closure. *Dev. Cell* **33,** 611–621 (2015).

43. Kiehart, D. P., Galbraith, C. G., Edwards, K. a, Rickoll, W. L. & Montague, R. a. Multiple forces contribute to cell sheet morphogenesis for dorsal closure in Drosophila. *J. Cell Biol.* **149,** 471–90 (2000).

44. Rodriguez-Diaz, A. *et al.* Actomyosin purse strings: renewable resources that make morphogenesis robust and resilient. *HFSP J.* **2,** 220–37 (2008).

45. Hutson, M. S. *et al.* Forces for morphogenesis investigated with laser microsurgery and quantitative modeling. *Science* **300,** 145–9 (2003).

46. Peralta, X. G. *et al.* Upregulation of forces and morphogenic asymmetries in dorsal closure during Drosophila development. *Biophys. J.* **92,** 2583–96 (2007).

47. Wells, A. R. *et al.* Complete canthi removal reveals that forces from the amnioserosa alone are sufficient to drive dorsal closure in Drosophila. *Mol. Biol. Cell* **25,** 3552–68 (2014).

48. Jacinto, A. & Baum, B. Actin in development. *Mech. Dev.* **120,** 1337–1349 (2003).

49. Scuderi, A. & Letsou, A. Amnioserosa is required for dorsal closure in Drosophila. *Dev. Dyn.* **232,** 791–800 (2005).

50. Jacinto, A. *et al.* Dynamic analysis of actin cable function during Drosophila dorsal closure. *Curr. Biol.* **12,** 1245–50 (2002).

51. Franke, J. D., Montague, R. a & Kiehart, D. P. Nonmuscle myosin II is required for cell proliferation, cell sheet adhesion and wing hair morphology during wing morphogenesis. *Dev. Biol.* **345,** 117–32 (2010).

52. Magie, C. R., Meyer, M. R., Gorsuch, M. S. & Parkhurst, S. M. Mutations in the Rho1 small GTPase disrupt morphogenesis and segmentation during early Drosophila development. *Development* **126,** 5353–64 (1999).

53. Watanabe, N., Kato, T., Fujita, A., Ishizaki, T. & Narumiya, S. Cooperation between mDia1 and ROCK in Rho-induced actin reorganization. *Nat. Cell Biol.* **1,** 136–143 (1999).

54. Azevedo, D. *et al.* DRhoGEF2 regulates cellular tension and cell pulsations in the Amnioserosa during Drosophila dorsal closure. *PLoS One* **6,** e23964 (2011).

55. Jankovics, F. *et al.* A functional genomic screen combined with time-lapse microscopy uncovers a novel set of genes involved in dorsal closure of Drosophila embryos. *PLoS One* **6,** e22229 (2011).

56. Wilson, R. C. & Doudna, J. A. Molecular Mechanisms of RNA Interference. *Annu. Rev. Biophys.* **42,** 217–239 (2013).

57. Zenklusen, D., Larson, D. R. & Singer, R. H. Single-RNA counting reveals alternative modes of gene expression in yeast. TL - 15. *Nat. Struct. Mol. Biol.* **15 VN - r,** 1263–1271 (2008).

58. Caussinus, E., Kanca, O. & Affolter, M. Protein knockouts in living eukaryotes using degradFP and green fluorescent protein fusion targets. *Curr. Protoc. Protein Sci.* 1–13 (2013). doi:10.1002/0471140864.ps3002s73

59. Jay, D. G. Selective destruction of protein function by chromophore-assisted laser inactivation. *Proc. Natl. Acad. Sci.* **85,** 5454–5458 (1988).

60. Surrey, T. *et al.* Chromophore-assisted light inactivation and self-organization of microtubules and motors. *Proc. Natl. Acad. Sci. U. S. A.* **95,** 4293–8 (1998).

61. Shu, X. *et al.* A genetically encoded tag for correlated light and electron microscopy of intact cells, tissues, and organisms. *PLoS Biol.* **9,** (2011).

62. Bulina, M. E. *et al.* Chromophore-assisted light inactivation (CALI) using the phototoxic fluorescent

protein KillerRed. *Nat. Protoc.* **1,** 947–53 (2006).

63. Takemoto, K. *et al.* SuperNova, a monomeric photosensitizing fluorescent protein for chromophore-assisted light inactivation. *Sci Rep* **3,** 2629 (2013).

64. Kennedy, M. J. *et al.* Rapid blue light induction of protein interaction in living cells. *Nat. Methods* **7,** 973–975 (2010).

65. Yu, X. *et al.* Formation of nuclear bodies of Arabidopsis CRY2 in response to blue light is associated with its blue light-dependent degradation. *Plant Cell* **21,** 118–130 (2009).

66. Taslimi, A. *et al.* An optimized optogenetic clustering tool for probing protein interaction and function. *Nat. Commun.* **5,** 4925 (2014).

67. Renicke, C., Schuster, D., Usherenko, S., Essen, L. O. & Taxis, C. A LOV2 domain-based optogenetic tool to control protein degradation and cellular function. *Chem. Biol.* **20,** 619–626 (2013).

68. Caussinus, E., Kanca, O. & Affolter, M. Fluorescent fusion protein knockout mediated by anti-GFP nanobody. *Nat. Struct. Mol. Biol.* **19,** 117–21 (2012).

69. Brauchle, M. *et al.* Protein interference applications in cellular and developmental biology using DARPins that recognize GFP and mCherry. *Biol. Open* **3,** 1252–61 (2014).

70. Rothbauer, U. *et al.* A Versatile Nanotrap for Biochemical and Functional Studies with Fluorescent Fusion Proteins. *Mol. Cell. Proteomics* **7,** 282–289 (2007).

71. Schornack, S. *et al.* Protein mislocalization in plant cells using a GFP-binding chromobody. *Plant J.* **60,** 744–754 (2009).

72. Harder, B. *et al.* TEV protease-mediated cleavage in Drosophila as a tool to analyze protein functions in living organisms. *Biotechniques* **44,** 765–772 (2008).

73. Taxis, C., Stier, G., Spadaccini, R. & Knop, M. Efficient protein depletion by genetically controlled deprotection of a dormant N-degron. *Mol. Syst. Biol.* **5,** 267 (2009).

74. Nishimura, K., Fukagawa, T., Takisawa, H., Kakimoto, T. & Kanemaki, M. An auxin-based degron system for the rapid depletion of proteins in nonplant cells. *Nat. Methods* **6,** 917–922 (2009).

75. Jungbluth, M., Renicke, C. & Taxis, C. Targeted protein depletion in Saccharomyces cerevisiae by activation of a bidirectional degron. *BMC Syst. Biol.* **4,** 176 (2010).

76. Dohmen, R. J., Wu, P. & Varshavsky, A. Heat-inducible degron: a method for constructing temperature-sensitive mutants. *Science* **263,** 1273–6 (1994).

77. Tan, G., Chen, M., Foote, C. & Tan, C. Temperature-sensitive mutations made easy: Generating conditional mutations by using temperature-sensitive inteins that function within different temperature ranges. *Genetics* **183,** 13–22 (2009).

78. Sandler, A. D. Children with Spina Bifida: Key Clinical Issues. *Pediatr. Clin. North Am.* **57,** 879–892 (2010).

79. Watkins, S. E., Meyer, R. E., Strauss, R. P. & Aylsworth, A. S. Classification, epidemiology, and genetics of orofacial clefts. *Clin. Plast. Surg.* **41,** 149–163 (2014).

80. Mizuno, T., Tsutsui, K. & Nishida, Y. Drosophila myosin phosphatase and its role in dorsal closure. *Development* **129,** 1215–23 (2002).

81. Wodarz, A., Hinz, U., Engelbert, M. & Knust, E. Expression of crumbs confers apical character on plasma membrane domains of ectodermal epithelia of drosophila. *Cell* **82,** 67–76 (1995).

82. Manseau, L. *et al.* GAL4 enhancer traps expressed in the embryo, larval brain, imaginal discs, and ovary of Drosophila. *Dev. Dyn.* **209,** 310–322 (1997).

83. Chatterjee, N. & Bohmann, D. A versatile φC31 based reporter system for measuring AP-1 and NRF2 signaling in Drosophila and in tissue culture. *PLoS One* **7,** (2012).

84. Fischer, S. C. *et al.* Contractile and mechanical properties of epithelia with perturbed actomyosin

dynamics. *PLoS One* **9,** e95695 (2014).

85. Lee A, T. J. Excessive Myosin activity in mbs mutants causes photoreceptor movement out of the Drosophila eye disc epithelium. *Mol. Biol. Cell* **15,** 3285–95 (2004).

86. Ma, X., Lynch, H. E., Scully, P. C. & Hutson, M. S. Probing embryonic tissue mechanics with laser hole drilling. *Phys. Biol.* **6,** 036004 (2009).

87. Herranz, H. & Morata, G. The functions of pannier during Drosophila embryogenesis. *Development* **128,** 4837–46 (2001).

88. Brand, A. H. & Perrimon, N. Targeted gene expression as a means of altering cell fates and generating dominant phenotypes. *Development* **118,** 401–15 (1993).

89. Glise, B. & Noselli, S. Coupling of Jun amino-terminal kinase and Decapentaplegic signaling pathways in Drosophila morphogenesis. *Genes Dev.* **11,** 1738–1747 (1997).

90. Pfeiffer, B. D. *et al.* Tools for neuroanatomy and neurogenetics in Drosophila. *Proc. Natl. Acad. Sci. U. S. A.* **105,** 9715–9720 (2008).

91. Takaesu, N. T., Johnson, a N. & Newfeld, S. J. Posterior spiracle specific GAL4 lines: new reagents for developmental biology and respiratory physiology. *Genesis* **34,** 16–18 (2002).

92. Sepp, K. J. & Auld, V. J. Conversion of lacZ enhancer trap lines to GAL4 lines using targeted transposition in Drosophila melanogaster. *Genetics* **151,** 1093–1101 (1999).

93. Martín-blanco, E. *et al.* puckered encodes a phosphatase that mediates a feedback loop regulating JNK activity during dorsal closure in Drosophila. *Genes Dev.* **12,** 557–670 (1998).

94. Jankovics, F. & Brunner, D. Transiently reorganized microtubules are essential for zippering during dorsal closure in Drosophila melanogaster. *Dev. Cell* **11,** 375–85 (2006).

95. Sokolow, A., Toyama, Y., Kiehart, D. P. & Edwards, G. S. Cell ingression and apical shape oscillations during dorsal closure in Drosophila. *Biophys. J.* **102,** 969–79 (2012).

96. Jayasinghe, A. K., Crews, S. M., Mashburn, D. N. & Hutson, M. S. Apical oscillations in amnioserosa cells: basolateral coupling and mechanical autonomy. *Biophys. J.* **105,** 255–65 (2013).

97. Narasimha, M. & Brown, N. H. Novel functions for integrins in epithelial morphogenesis. *Curr. Biol.* **14,** 381–5 (2004).

98. Machado, P. F. *et al.* Emergent material properties of developing epithelial tissues. *BMC Biol.* **13,** 98 (2015).

99. Lehmann, R. & Nüsslein-Volhard, C. Abdominal segmentation, pole cell formation, and embryonic polarity require the localized activity of oskar, a maternal gene in Drosophila. *Cell* **47,** 141–152 (1986).

100. Wang, Q., Feng, J. J. & Pismen, L. M. A cell-level biomechanical model of Drosophila dorsal closure. *Biophys. J.* **103,** 2265–74 (2012).

101. Martin, A. C., Kaschube, M. & Wieschaus, E. F. Pulsed contractions of an actin-myosin network drive apical constriction. *Nature* **457,** 495–9 (2009).

102. Rauzi, M., Lenne, P.-F. & Lecuit, T. Planar polarized actomyosin contractile flows control epithelial junction remodelling. *Nature* **468,** 1110–4 (2010).

103. Gorfinkiel, N. & Arias, A. M. Requirements for adherens junction components in the interaction between epithelial tissues during dorsal closure in Drosophila. *J. Cell Sci.* **120,** 3289–98 (2007).

104. Kaltschmidt, J. a *et al.* Planar polarity and actin dynamics in the epidermis of Drosophila. *Nat. Cell Biol.* **4,** 937–44 (2002).

105. Reed, B. H., Wilk, R., Schöck, F. & Lipshitz, H. D. Integrin-dependent apposition of Drosophila extraembryonic membranes promotes morphogenesis and prevents anoikis. *Curr. Biol.* **14,** 372–80 (2004).

106. Homsy, J. G. *et al.* JNK signaling coordinates integrin and actin functions during Drosophila

embryogenesis. *Dev. Dyn.* **235,** 427–34 (2006).

107. Martin, A. C. & Goldstein, B. Apical constriction: themes and variations on a cellular mechanism driving morphogenesis. *Development* **141,** 1987–1998 (2014).

108. Rauzi, M. & Lecuit, T. Closing in on mechanisms of tissue morphogenesis. *Cell* **137,** 1183–5 (2009).

109. Martin, A. C. Pulsation and stabilization: Contractile forces that underlie morphogenesis. *Dev. Biol.* **341,** 114–125 (2010).

110. Dierkes, K., Sumi, A., Solon, J. & Salbreux, G. Spontaneous Oscillations of Elastic Contractile Materials with Turnover. *Phys. Rev. Lett.* **113,** 148102 (2014).

111. Behrndt, M. *et al.* Forces driving epithelial constriction in zebrafish gastrulation.

112. Bretschneider, T. *et al.* The three-dimensional dynamics of actin waves, a model of cytoskeletal self-organization. *Biophys. J.* **96,** 2888–2900 (2009).

113. Reig, G., Pulgar, E. & Concha, M. L. Cell migration: from tissue culture to embryos. *Development* **141,** 1999–2013 (2014).

114. Hunter, G. L., Crawford, J. M., Genkins, J. Z. & Kiehart, D. P. Ion channels contribute to the regulation of cell sheet forces during Drosophila dorsal closure. *Development* **141,** 325–34 (2014).

115. Wu, M., Wu, X. & De Camilli, P. Calcium oscillations-coupled conversion of actin travelling waves to standing oscillations. *Proc Natl Acad Sci U S A* **110,** 1339–1344 (2013).

116. Oertner, T. G. & Matus, A. Calcium regulation of actin dynamics in dendritic spines. *Cell Calcium* **37,** 477–482 (2005).

117. Markova, O., Sénatore, S., Chardès, C. & Lenne, P.-F. Calcium Spikes in Epithelium: study on Drosophila early embryos. *Sci. Rep.* **5,** 11379 (2015).

118. Antunes, M., Pereira, T., Cordeiro, J. V., Almeida, L. & Jacinto, A. Coordinated waves of actomyosin flow and apical cell constriction immediately after wounding. *J. Cell Biol.* **202,** 365–379 (2013).

119. Razzell, W., Evans, I. R., Martin, P. & Wood, W. Report Calcium Flashes Orchestrate the Wound Inflammatory Response through DUOX Activation and Hydrogen Peroxide Release. *Curr. Biol.* **23,** 424–429 (2013).

120. Redd, M. J., Cooper, L., Wood, W., Stramer, B. & Martin, P. Wound healing and inflammation: embryos reveal the way to perfect repair. *Philos. Trans. R. Soc. Lond. B. Biol. Sci.* **359,** 777–84 (2004).

121. Cordeiro, J. V & Jacinto, A. The role of transcription-independent damage signals in the initiation of epithelial wound healing. *Nat. Rev. Mol. Cell Biol.* **14,** 249–62 (2013).

122. Sieger, D., Moritz, C., Ziegenhals, T., Prykhozhij, S. & Peri, F. Long-Range Ca2+ Waves Transmit Brain-Damage Signals to Microglia. *Dev. Cell* **22,** 1138–1148 (2012).

123. Abreu-Blanco, M. T., Verboon, J. M. & Parkhurst, S. M. Cell wound repair in Drosophila occurs through three distinct phases of membrane and cytoskeletal remodeling. *J. Cell Biol.* **193,** 455–64 (2011).

124. Schroth-Diez, B. *et al.* Propagating waves separate two states of actin organization in living cells. *HFSP J.* **3,** 412–27 (2009).

125. Munjal, A., Philippe, J., Munro, E. & Lecuit, T. A self-organized biomechanical network drives shape changes during tissue morphogenesis. (2015). doi:10.1038/nature14603

126. Gurtovenko, A. a & Anwar, J. Modulating the structure and properties of cell membranes: the molecular mechanism of action of dimethyl sulfoxide. *J. Phys. Chem. B* **111,** 10453–10460 (2007).

127. Notman, R., Noro, M., O'Malley, B. & Anwar, J. Molecular basis for dimethylsulfoxide (DMSO) action on lipid membranes. *J. Am. Chem. Soc.* **128,** 13982–13983 (2006).

128. Van Lierop, J. E. *et al.* Activation of smooth muscle myosin light chain kinase by calmodulin. Role of LYS30 and GLY40. *J. Biol. Chem.* **277,** 6550–6558 (2002).

129. Melom, J. E., Akbergenova, Y., Gavornik, J. P. & Littleton, J. T. Spontaneous and Evoked Release Are Independently Regulated at Individual Active Zones. *J. Neurosci.* **33,** 17253–17263 (2013).

130. Verheugen, J. A., Vijverberg, H. P., Oortgiesen, M. & Cahalan, M. D. Voltage-gated and Ca(2+)-activated K+ channels in intact human T lymphocytes. Noninvasive measurements of membrane currents, membrane potential, and intracellular calcium. *J. Gen. Physiol.* **105,** 765–94 (1995).

131. Nakajima, T., Shearer, T. R. & Azuma, M. Involvement of calpain 2 in ionomycin-induced cell death in cultured mouse lens epithelial cells. *Curr. Eye Res.* **36,** 930–6 (2011).

132. McCollum, A. T., Jafarifar, F., Chan, R. & Guttmann, R. P. Oxidative Stress Inhibits Ionomycin-Mediated Cell Death in Cortical Neurons. *J. Neurosci. Res.* **76,** 104–109 (2004).

133. Bennett, M. V. L. & Spray, D. C. Gap Junctions. (1985).

134. Evans, W. H. & Martin, P. E. M. Gap junctions: structure and function (Review). *Mol. Membr. Biol.* **19,** 121–136 (2002).

135. Rozental, R., Srinivas, M. & Spray, D. C. How to Close a Gap Junction Channel. *Connexin Methods Protoc.* **154,** 447–476 (2001).

136. Palani, D., Ghildyal, P. & Manchanda, R. Effects of carbenoxolone on syncytial electrical properties and junction potentials of guinea-pig vas deferens. 207–214 (2006). doi:10.1007/s00210-006-0109-7

137. Saltman, A. E. *et al.* Gap junction uncoupling protects the heart against ischemia. *J. Thorac. Cardiovasc. Surg.* **124,** 371–376 (2002).

138. Jabr, R. & Chowdhury, R. The Relationship between Gap Junction Conductance and Conduction Velocity in Mammalian Myocardium. **44,** (2016).

139. Wood, W. Wound healing: Calcium flashes illuminate early events. *Curr. Biol.* **22,** R14–R16 (2012).

140. Salameh, A. & Dhein, S. Effects of mechanical forces and stretch on intercellular gap junction coupling. *Biochim. Biophys. Acta - Biomembr.* **1828,** 147–156 (2013).

141. Zhao, H. B. & Santos-Sacchi, J. Effect of membrane tension on gap junctional conductance of supporting cells in Corti's organ. *J. Gen. Physiol.* **112,** 447–455 (1998).

142. Wang, T. L., Tseng, Y. Z. & Chang, H. Regulation of connexin 43 gene expression by cyclical mechanical stretch in neonatal rat cardiomyocytes. *Biochem. Biophys. Res. Commun.* **267,** 551–557 (2000).

143. Falk, M. M., Kells, R. M. & Berthoud, V. M. Degradation of connexins and gap junctions. *FEBS Lett.* **588,** 1221–1229 (2014).

144. Solan, J. L. & Lampe, P. D. NIH Public Access. **588,** 1423–1429 (2015).

145. Hetrick, B., Han, M. S., Helgeson, L. A. & Nolen, B. J. NIH Public Access. **20,** 701–712 (2014).

146. Giuliani, F., Giuliani, G., Bauer, R. & Rabouille, C. Innexin 3, a new gene required for dorsal closure in Drosophila embryo. *PLoS One* **8,** e69212 (2013).

147. Bauer, R. *et al.* Intercellular communication: The Drosophila innexin multiprotein family of gap junction proteins. *Chem. Biol.* **12,** 515–526 (2005).

148. Lehmann C, Lechner H, Löer B, Knieps M, Herrmann S, Famulok M, Bauer R, H. M. Heteromerization of Innexin Gap Junction Proteins Regulates Epithelial Tissue Organization in Drosophila. *Mol Biol Cell.* **17,** 351–1676–85 (2066).

149. Port, F., Chen, H.-M., Lee, T. & Bullock, S. L. Optimized CRISPR/Cas tools for efficient germline and somatic genome engineering in Drosophila. *Proc. Natl. Acad. Sci. U. S. A.* **111,** E2967–76 (2014).

150. Narasimha, M., Uv, A., Krejci, A., Brown, N. H. & Bray, S. J. Grainy head promotes expression of septate junction proteins and influences epithelial morphogenesis. *J. Cell Sci.* **121,** 747–52 (2008).

151. Gates, J. *et al.* Enabled plays key roles in embryonic epithelial morphogenesis in Drosophila. *Development* **134,** 2027–39 (2007).

152. Baek, S. H., Kwon, Y.-C., Lee, H. & Choe, K.-M. Rho-family small GTPases are required for cell polarization and directional sensing in Drosophila wound healing. *Biochem. Biophys. Res. Commun.* **394,** 488–92 (2010).

153. Chen, J. *et al.* Cofilin / ADF is required for cell motility during Drosophila ovary development and oogenesis. **3,** (2001).

154. Wymann, M. P. *et al.* Wortmannin inactivates phosphoinositide 3-kinase by covalent modification of Lys-802, a residue involved in the phosphate transfer reaction. *Mol. Cell. Biol.* **16,** 1722–1733 (1996).

155. Mason, F. M. & Martin, A. C. Tuning cell shape change with contractile ratchets. *Curr. Opin. Genet. Dev.* **21,** 671–679 (2011).

156. Gorfinkiel, N., Schamberg, S. & Blanchard, G. B. Integrative Approaches to Morphogenesis : Lessons From Dorsal Closure. **533,** 522–533 (2011).

157. Razzell, W., Wood, W. & Martin, P. Recapitulation of morphogenetic cell shape changes enables wound re-epithelialisation. *Development* **141,** 1814–20 (2014).

158. Hunter, G. The Role of Mechanically Gated Ion Channels in Dorsal Closure During. (2012).

159. Houslay, M. D. Underpinning compartmentalised cAMP signalling through targeted cAMP breakdown. *Trends Biochem. Sci.* **35,** 91–100 (2010).

160. Saucerman, J. J., Greenwald, E. C. & Polanowska-Grabowska, R. Perspectives on: Cyclic nucleotide microdomains and signaling specificity: Mechanisms of cyclic AMP compartmentation revealed by computational models. *J. Gen. Physiol.* **143,** 39–48 (2013).

161. Harrisingh, M. C., Wu, Y., Lnenicka, G. A. & Nitabach, M. N. Intracellular Ca2+ Regulates Free-Running Circadian Clock Oscillation In Vivo. *J. Neurosci.* **27,** 12489–12499 (2007).

162. Guglielmi, G., Barry, J. D., Huber, W. & DeRenzis, S. An Optogenetic Method to Modulate Cell Contractility during Tissue Morphogenesis. *Dev. Cell* **35,** 646–660 (2014).

163. Roh-Johnson, M. *et al.* Triggering a cell shape change by exploiting preexisting actomyosin contractions. *Science* **335,** 1232–5 (2012).

164. Mason, F. M., Tworoger, M. & Martin, A. C. Apical domain polarization localizes actin-myosin activity to drive ratchet-like apical constriction. *Nat. Cell Biol.* **15,** 926–36 (2013).

165. Xie, S. & Martin, A. C. Intracellular signalling and intercellular coupling coordinate heterogeneous contractile events to facilitate tissue folding. *Nat. Commun.* **6,** 7161 (2015).

166. Lowery, L. A. & Sive, H. Strategies of vertebrate neurulation and a re-evaluation of teleost neural tube formation. **121,** 1189–1197 (2004).

167. Eom, D. S., Amarnath, S., Fogel, J. L. & Agarwala, S. Bone morphogenetic proteins regulate neural tube closure by interacting with the apicobasal polarity pathway. *Development* **138,** 3179–3188 (2011).

168. Ernst, S. *et al.* Shroom3 is required downstream of FGF signalling to mediate proneuromast assembly in zebrafish. *Development* **139,** 4571–81 (2012).

169. Ebrahim, S. *et al.* NMII forms a contractile transcellular sarcomeric network to regulate apical cell junctions and tissue geometry. *Curr. Biol.* **23,** 731–736 (2013).

170. Ishiuchi, T. & Takeichi, M. Willin and Par3 cooperatively regulate epithelial apical constriction through aPKC-mediated ROCK phosphorylation. *Nat. Cell Biol.* **13,** 860–6 (2011).

171. Ratheesh, A. *et al.* Centralspindlin and α-catenin regulate Rho signalling at the epithelial zonula adherens. *Nat. Cell Biol.* **14,** 818–828 (2012).

172. Verkhovsky, A. B. & Borisy, G. G. Non-sarcomeric mode of myosin II organization in the fibroblast lamellum. *J. Cell Biol.* **123,** 637–652 (1993).

173. Kerridge, S. *et al.* Modular activation of Rho1 by GPCR signalling imparts polarized myosin II activation during morphogenesis. *Nat. Cell Biol.* **18,** (2016).

174. Ciruna, B., Jenny, A., Lee, D., Mlodzik, M. & Schier, A. F. Planar cell polarity signalling couples cell division and morphogenesis during neurulation. *Nature* **439,** 220–4 (2006).

175. Tanegashima, K., Zhao, H. & Dawid, I. B. WGEF activates Rho in the Wnt-PCP pathway and controls convergent extension in Xenopus gastrulation. *EMBO J.* **27,** 606–17 (2008).

176. Kinoshita N, Sasai N, Misaki K, Y. S. Apical accumulation of Rho in the neural plate is important for neural plate cell shape change and neural tube formation. *Mol. Biol. Cell* **19,** 2289–99 (2008).

177. Zeitlinger, J. *et al.* Defective dorsal closure and loss of epidermal decapentaplegic expression in Drosophila fos mutants. *EMBO J.* **16,** 7393–401 (1997).

178. Ducuing, A., Keeley, C., Mollereau, B. & Vincent, S. A DPP-mediated feed-forward loop canalizes morphogenesis during. **208,** (2015).

179. Beira, J. *et al.* The Dpp/TGF??-dependent corepressor schnurri protects epithelial cells from JNK-induced apoptosis in drosophila embryos. *Dev. Cell* **31,** 240–247 (2014).

180. Bragdon, B. *et al.* Bone Morphogenetic Proteins: A critical review. *Cell. Signal.* **23,** 609–620 (2011).

181. Matsuda, S., Harmansa, S. & Affolter, M. BMP morphogen gradients in flies. *Cytokine Growth Factor Rev.* **27,** 119–127 (2015).

182. Affolter, M. & Basler, K. The Decapentaplegic morphogen gradient: from pattern formation to growth regulation. *Nat. Rev. Genet.* **8,** 663–674 (2007).

183. Chizhikov, V. V & Millen, K. J. Mechanisms of roof plate formation in the vertebrate CNS. *Nat. Rev. Neurosci.* **5,** 808–812 (2004).

184. Liu, A. & Niswander, L. A. Bone morphogenetic protein signalling and vertebrate nervous system development. *Nat. Rev. Neurosci.* **6,** 945–54 (2005).

185. Akiyama, T. *et al.* Dally regulates Dpp morphogen gradient formation by stabilizing Dpp on the cell surface. *Dev. Biol.* **313,** 408–419 (2008).

186. Kornberg, T. B. & Roy, S. Cytonemes as specialized signaling filopodia. *Development* **141,** 729–736 (2014).

187. Jackson, P. D. & Hoffmann, F. M. Embryonic expression patterns of the Drosophila decapentaplegic gene: separate regulatory elements control blastoderm expression and lateral ectodermal expression. *Dev. Dyn.* **199,** 28–44 (1994).

188. Garcı, B., Martinez, A. & Jacinto, A. Dpp signalling orchestrates dorsal closure by regulating cell shape changes both in the amnioserosa and in the epidermis. **124,** 884–897 (2007).

189. Zahedi, B. *et al.* Leading edge-secreted Dpp cooperates with ACK-dependent signaling from the amnioserosa to regulate myosin levels during dorsal closure. *Dev. Dyn.* **237,** 2936–46 (2008).

190. Irish, V. F. & Gelbart, W. M. The decapentaplegic gene is required for dorsal-ventral patterning of the Drosophila embryo. *Genes Dev.* **1,** 868–879 (1987).

191. Penton, A. *et al.* Identification of two bone morphogenetic protein type I receptors in Drosophila and evidence that Brk25D is a decapentaplegic receptor. *Cell* **78,** 239–250 (1994).

192. Affolter, M., Nellen, D., Nussbaumer, U. & Basler, K. Multiple requirements for the receptor serine/threonine kinase thick veins reveal novel functions of TGF beta homologs during Drosophila embryogenesis. *Development* **120,** 3105–17 (1994).

193. Martin-Blanco, E., Pastor-Pareja, J. C. & Garcia-Bellido, a. JNK and decapentaplegic signaling control adhesiveness and cytoskeleton dynamics during thorax closure in Drosophila. *Proc. Natl. Acad. Sci. U. S. A.* **97,** 7888–93 (2000).

194. Raftery, L. a & Sutherland, D. J. TGF-beta family signal transduction in Drosophila development: from Mad to Smads. *Dev. Biol.* **210,** 251–68 (1999).

195. Levayer, R. & Lecuit, T. Oscillation and Polarity of E-Cadherin Asymmetries Control Actomyosin Flow Patterns during Morphogenesis. *Dev. Cell* **26,** 162–175 (2013).

196. Widmann, T. J. & Dahmann, C. Dpp signaling promotes the cuboidal-to-columnar shape transition of Drosophila wing disc epithelia by regulating Rho1. *J. Cell Sci.* **122,** 1362–73 (2009).

197. Milan, M. Sculpting a fly leg: BMP boundaries and cell death. *Nat Cell Biol* **9,** 17–18 (2007).

198. Cai, D. *et al.* Mechanical feedback through E-cadherin promotes direction sensing during collective cell migration. *Cell* **157,** 1146–1159 (2014).

199. Cost, A. L., Ringer, P., Chrostek-Grashoff, A. & Grashoff, C. How to Measure Molecular Forces in Cells: A Guide to Evaluating Genetically-Encoded FRET-Based Tension Sensors. *Cell. Mol. Bioeng.* **8,** 96–105 (2015).

200. Harmansa, S., Hamaratoglu, F., Affolter, M. & Caussinus, E. Dpp spreading is required for medial but not for lateral wing disc growth. *Nature* **527,** 317–322 (2015).

201. Wharton, K. a, Ray, R. P. & Gelbart, W. M. An activity gradient of decapentaplegic is necessary for the specification of dorsal pattern elements in the Drosophila embryo. *Development* **117,** 807–822 (1993).

202. Pert, M., Gan, M., Saint, R. & Murray, M. J. Pert et al. (2015) - Netrins and FrazzledDCC promote the migration and mesenchymal to epithelial transition of Drosophila midgut cells. 1–11 (2015). doi:10.1242/bio.201410827

203. Reuter, R., Grunewald, B. & Leptin, M. A role for the mesoderm in endodermal migration and morphogenesis in Drosophila. **1145,** 1135–1145 (1993).

204. Tepass, U. & Hartenstein, V. Epithelium formation in the Drosophila midgut depends on the interaction of endoderm and mesoderm. *Development* **120,** 579–90 (1994).

205. Hozumi, S. *et al.* An unconventional myosin in Drosophila reverses the default handedness in visceral organs. *Nature* **440,** 798–802 (2006).

206. Stathopoulos, A. & Levine, M. Whole-genome analysis of Drosophila gastrulation. *Curr. Opin. Genet. Dev.* **14,** 477–484 (2004).

207. Lepage, S. E. & Bruce, A. E. E. Zebrafish epiboly: mechanics and mechanisms. *Int. J. Dev. Biol.* **54,** 1213–28 (2010).

208. Carvalho, L. & Heisenberg, C.-P. The yolk syncytial layer in early zebrafish development. *Trends Cell Biol.* **20,** 586–92 (2010).

209. Panousopoulou, E., Hobbs, C., Mason, I., Green, J. B. A. & Formstone, C. J. Epiboly generates the epidermal basal monolayer and spreads the nascent mammalian skin to enclose the embryonic body. 1915–1927 (2016). doi:10.1242/jcs.180703

210. Chartier, A., Zaffran, S., Astier, M., Sémériva, M. & Gratecos, D. Pericardin, a Drosophila type IV collagen-like protein is involved in the morphogenesis and maintenance of the heart epithelium during dorsal ectoderm closure. *Development* **129,** 3241–53 (2002).

211. Royou, A., Field, C., Sisson, J. C., Sullivan, W. & Karess, R. Reassessing the Role and Dynamics of Nonmuscle Myosin II during Furrow Formation in Early Drosophila Embryos □. **15,** 838–850 (2004).

212. Morais-de-Sá, E. & Sunkel, C. Adherens junctions determine the apical position of the midbody during follicular epithelial cell division. *EMBO Rep.* **14,** 696–703 (2013).

213. Nelson, W. J. Remodeling Epithelial Cell Organization : Transitions Between Front – Rear and Apical – Basal Polarity. 1–20 (2016).

214. Doherty, G. J. & Mcmahon, H. T. Mechanisms of Endocytosis. (2009). doi:10.1146/annurev.biochem.78.081307.110540

215. Bruce, A. E. E. Zebrafish epiboly: Spreading thin over the yolk. *Dev. Dyn.* 244–258 (2015). doi:10.1002/dvdy.24353

216. Hernández-vega, A., Marsal, M. & Pouille, P. Polarized Movements Cortical Tension drives Zebrafish Epiboly. (2015).

217. He, L., Wang, X., Tang, H. L. & Montell, D. J. Tissue elongation requires oscillating contractions of a

basal actomyosin network. **12,** (2010).

218. Reymann, A.-C. *et al.* Nucleation geometry governs ordered actin networks structures. *Nat. Mater.* **9,** 827–832 (2010).

219. Igaki, T. *et al.* Drob-1, a Drosophila member of the Bcl-2/CED-9 family that promotes cell death. *Proc. Natl. Acad. Sci. U. S. A.* **97,** 662–667 (2000).

220. Rubin, G. M. & Spradling, a C. Genetic transformation of Drosophila with transposable element vectors. *Science* **218,** 348–353 (1982).

221. Morin, X., Daneman, R., Zavortink, M. & Chia, W. A protein trap strategy to detect GFP-tagged proteins expressed from their endogenous loci in Drosophila. *Proc. Natl. Acad. Sci. U. S. A.* **98,** 15050–15055 (2001).

222. Karess, R. E. *et al.* The regulatory light chain of nonmuscle myosin is encoded by spaghetti-squash, a gene required for cytokinesis in Drosophila. *Cell* **65,** 1177–1189 (1991).

223. Bischof, J., Maeda, R. K., Hediger, M., Karch, F. & Basler, K. An optimized transgenesis system for Drosophila using germ-line-specific phiC31 integrases. *Proc. Natl. Acad. Sci. U. S. A.* **104,** 3312–7 (2007).

224. Port, F., Muschalik, N. & Bullock, S. L. Systematic Evaluation of Drosophila CRISPR Tools Reveals Safe and Robust Alternatives to Autonomous Gene Drives in Basic Research. *G3 (Bethesda).* **5,** 1493–502 (2015).

225. Desprat, N., Supatto, W., Pouille, P. A., Beaurepaire, E. & Farge, E. Tissue Deformation Modulates Twist Expression to Determine Anterior Midgut Differentiation in Drosophila Embryos. *Dev. Cell* **15,** 470–477 (2008).

226. Kumar, A. & Shivashankar, G. V. Mechanical force alters morphogenetic movements and segmental gene expression patterns during drosophila embryogenesis. *PLoS One* **7,** 1–10 (2012).

227. Guglielmi, G. *et al.* An Optogenetic Method to Modulate Cell Contractility during Tissue Morphogenesis Resource An Optogenetic Method to Modulate Cell Contractility during Tissue Morphogenesis. *Dev. Cell* **35,** 646–660 (2015).

228. Caussinus, E., Colombelli, J. & Affolter, M. Tip-Cell Migration Controls Stalk-Cell Intercalation during Drosophila Tracheal Tube Elongation. *Curr. Biol.* **18,** 1727–1734 (2008).

229. Frasch, M. Induction of visceral and cardiac mesoderm. *Nature* **374,** 464–467 (1995).

230. Jacinto, a *et al.* Dynamic actin-based epithelial adhesion and cell matching during Drosophila dorsal closure. *Curr. Biol.* **10,** 1420–6 (2000).

231. Lu, H., Sokolow, A., Kiehart, D. P. & Edwards, G. S. Remodeling Tissue Interfaces and the Thermodynamics of Zipping during Dorsal Closure in Drosophila. *Biophys. J.* **109,** 2406–2417 (2015).

232. Swope, D., Kramer, J., King, T. R., Cheng, Y. S. & Kramer, S. G. Cdc42 is required in a genetically distinct subset of cardiac cells during Drosophila dorsal vessel closure. *Dev. Biol.* **392,** 221–232 (2014).

233. Mostowy, S. & Cossart, P. Septins: the fourth component of the cytoskeleton. *Nat. Rev. Mol. Cell Biol.* **13,** 183–94 (2012).

234. VanHook, A. & Letsou, A. Head involution in Drosophila: genetic and morphogenetic connections to dorsal closure. *Dev. Dyn.* **237,** 28–38 (2008).

235. Bloch Qazi, M. C., Heifetz, Y. & Wolfner, M. F. The developments between gametogenesis and fertilization: Ovulation and female sperm storage in Drosophila melanogaster. *Dev. Biol.* **256,** 195–211 (2003).

236. Menant, A. & Karess, R. E. Inducing 'cytokinesis' without mitosis in unfertilized Drosophila eggs. *Cell Cycle* **11,** 2856–2863 (2012).

Acknowledgements

First and foremost, I thank you, Damian, for accepting me into your group and giving me the opportunity to work and develop all the projects that we have. Thank you for constant optimism and motivation during the tough times. Thank you for allowing me to think out-side the box and develop ideas even if you were not convinced by them immediately. My words cannot express the gratitude I will always have for you for supporting me throughout this PhD both scientifically and personally.

I will always be indebted to the two persons in the lab – Erich Frei and Werner Boll - without whom this PhD would not have moved forward. Thank you, Erich, not only for helping me with *Drosophila* genetics and generating critical strains needed for the projects, but also for challenging me to look at things from a different angle. Thank you for the mutual respect that we shared at the fly bench and outside it. Thank you, Werner, for continuous support with the never-ending struggles in the lab - be it microscopes, laser-cutting, DNA cloning or anything else. I admire how quickly and efficiently you dealt with the problems and were always at hand if needed.

I thank all current and former members of Brunner lab – Maria, Magdalene, Mandy, Marisa, Michelle, Martina, Mirjam, David, Francesco, Stephen, Wolfgang, Arne, Lara, Martin, Nadia, Arina, Daniel, Fiona, Kristian for wonderful atmosphere in the lab and a lot of great times to remember.

I especially thank two PhD students in the lab – Maria and Adam – for all the unforgettable moments that we had. With you two, riding a PhD rollercoaster was so much more fun.

I thank Lara Selvaggi for patience in establishing magnetic bead injections into the embryos. I thank Daniel Fürst and Erich Brunner for valuable insights into "CRISPRering" field. I thank Wolfgang Helmhart and Werner Boll for valuable advice on "CRY2ing" strategies. I am also grateful to all the people, particularly, to Sara Caviglia, Ludovic Baillon, Stephan Luschnig, Erich Brunner and Christian Lehner who provided critical suggestions to our projects.

I thank all our collaborators who steered or helped with some of the projects I was involved in: Markus Affolter, Rajaa Boujemaa-Paterski, Christof Aegerter, Michael Eltsov and Achilleas Frangakis. I also thank the members of my thesis advisory committee - Markus Affolter, Konrad Basler and Christof Aegerter – for valuable input during the course of this PhD.

I am indebted to all those who proofread the thesis and provided valuable comments: Damian, Marisa, Mandy, Martin and Steve. Thank you, Mandy, for the Zusammenfassung.

I also thank my partner Eglė and our little one – Algirdas – for being patient with me through the tough times and supporting me during this PhD.

I will always be grateful to my parents that my fostered curiosity and supported me unconditionally throughout whatever I did.

Thank you all!

Curriculum Vitae

Surname: PASAKARNIS

First name: Laurynas

Date of birth: November 4th, 1987

Nationality: Lithuanian

Education:

2007	Vilnius Lyceum Cum Laude Brandos Atestatas
2007-2011	Undergraduate student Department of Biology and Biochemistry, University of Bath, Bath, UK Study group: Mollecular and Cellular Biology
2009-2010	Undergraduate Research Assistant MRC National Institute for Medical Research, London, UK Advisor: Prof. Dr. Jean-Paul Vincent Project: Characterization of novel genes involved in the phenomenon of cell competition
2011	Undergraduate Research Assistant Department of Biology and Biochemistry, University of Bath, Bath, UK Advisor: Dr. Andrew Chalmers Project: Effect of ESCRT component loss on epithelial cell polarity and tissue morphology
2011	Master of Biology in Molecular and Cellular Biology Department of Biology and Biochemistry, University of Bath, Bath, UK Title of diploma thesis: Effect of ESCRT component loss on epithelial cell polarity and tissue morphology
2011-2016	PhD student Institute of Molecular Life Sciences, University of Zürich, Zürich, Switzerland Advisor: Prof. Dr. Damian Brunner PhD thesis title: Analysis of Acto-myosin Network Remodelling - Towards a Comprehensive Understanding of Tissue Closure Events

Publications:

Eltsov, M., Dubé N., Yu Z., Pasakarnis L., Haselmann-Weiss U., Brunner D., Frangakis AS. Quantitative analysis of cytoskeletal reorganization during epithelial tissue sealing by large-volume electron tomography. *Nat Cell Biol* **17,** 605–614 (2015).

Pasakarnis L., Dreher D., Brunner D. SnapShot: Mechanical Forces in Development I. Cell. 2016 Apr 21;165(3):754-754.

Dreher D., Pasakarnis L., Brunner D. SnapShot: Mechanical Forces in Development II. Cell. 2016 May 5;165(4):1028-1028.

Appendix 1. Generation of molecular tools for studying mechanical forces during morphogenesis

This chapter consists of experiments and strategies for developing novel molecular tools to acutely interfere with the protein function. It also provides an improved strategy to current CRISPR/Cas9 protocols established in the lab.

The work described here was done by L. Pasakarnis in collaboration with the following persons:

TIPI method: with **N. Dubè**, D. Brunner lab and **J. Bischoff**, K. Basler lab

CRY2 method: with **W. Boll**, D. Brunner lab

CRISPR/Cas9 improvement: with **E. Frei** and **D. Fürst**, D. Brunner lab

Magnetic bead injections: with **L. Selvaggi**, D. Brunner and C. Aegerter labs

A1.1. Results

A1.1.1. TEV-induced protein inactivation (TIPI) method in Drosophila

TEV-induced protein inactivation (hereafter, TIPI) was successfully applied in *S. cerevisiae* to acutely eliminate protein function[73]. The method was recently introduced into *Drosophila* to study different aspects of DC (Dubè and Brunner, unpublished). TIPI protein tag is relatively short and contains TEV-recognition domain, SF3B1-p14 binding partner motif and EGFP, which in total is 382 amino acids (a.a). Thus, we took advantage of available plasmids in *S. cerevisiae* and generated TIPI-tagged Zipper (MyoII heavy chain). Two protein open-reading frames (ORFs) were generated that will reveal either stabilizing a.a. Met or destabilizing a.a. Phe at the N-terminus after TEV-induced cleavage (Fig. 46A; Methods, section A1.4.1). Both ORFs were ubiquitously driven by *actin5C* promoter.

Using P-element transposition we successfully obtained transgenic flies with TIPI-tagged Zipper (hereafter, TIPI-Zip). After recombining TIPI-Zip with amorphic zip^1 allele, we observed typical pearl-necklace localization of Zip in the AMC of epidermis (Fig. 46B). Signal in the AS cells was also localized to the appropriate structures such as apical MyoII foci and adherens junctions (Fig. 46B). Consistently, the signal intensity of TIPI-Zip was similar to the endogenous protein trap Zip-GFP, where one copy of untagged Zipper was still present[35,98,221]. Yet for acute protein inactivation all available copies must be TIPI-tagged. Unfortunately, we could not obtain homozygous *TIPI-Zip,* zip^1 flies even though *TIPI-Zip* flies in otherwise wild-type background are homozygous viable. We also could not complement *TIPI-Zip,* zip^1 with the endogenous *Zip-GFP* trap chromosome as *Zip-GFP* is homozygous lethal on its own[221].

We hypothesized that the failure of *TIPI-Zip* to rescue other lethal *zip* alleles is due to *actin5C* promoter being either under-expressed or over-expressed at certain stages during *Drosophila* development. Since complete promoter/enhancer region is not defined for *zipper*, we thus tagged light chain Sqh with TIPI-tag and flanked such ORF by both 5' and 3' ends of genomic *sqh* regions (Fig. 46C). These regions are sufficient to rescue amorphic sqh^{AX3} mutant allele with GFP-tagged Sqh[222]. With such TIPI-tagged Sqh we will be able to apply TIPI during DC and inactivate MyoII even more acutely than with deGradFP.

To facilitate fast and efficient tagging of any protein of interest for TIPI, in collaboration with J. Bischoff (K. Basler lab), we have created transgenic flies bearing the TIPI-tag followed by FRT5 sequence (Fig. 46D). Using attP landing site sequences developed by K. Basler and colleagues, ORFs of interest can now be efficiently introduced into Drosophila genome[223]. A simple cross of the flies would attach TIPI-tag to these ORFs via Flipase-mediated FRT-recombination. Such approach would tremendously reduce the time needed to engineer TIPI-tagged proteins using standard molecular cloning techniques.

A1.1.2. CRY2 oligomerization as a tool to mis-localize MyoII

Plant cytochrome CRY2-CIB system was recently used in cell culture to mis-localize proteins of interest in a light-inducible manner[64]. Such approach was successfully brought into Drosophila providing the ability to deplete cells of actin cortex[162]. Thus we wanted to create light-inducible tool to acutely control MyoII-dependent contractility in the cells. We tagged MyoII light chain Sqh with PHR domain of CRY2. PHR domain was found to be sufficient for CRY2 oligomerization upon exposure to blue light[64] (Fig. 47A). To visualize Sqh without exposing CRY2 to the blue light we added tagRFP that is excited with the green light (Fig. 47A). We chose not to use mCherry as a red fluorophore since currently available Sqh-mCherry reporter is hardly visible, shows considerable amount of aggregates and cannot be used effectively during DC-stage embryos[39,54] (Chapter 2). The whole ORF of CRY2-tRFP-Sqh was flanked by endogenous *sqh* genomic regions[222]. Next, we transfected *Drosophila* Schneider's S2 cells with such CRY2-tRFP-Sqh plasmid and observed the signal in cell lamellae and the cytoplasm (Fig. 47B). When the cells were exposed to the blue light (λ=465nm), within a few minutes CRY2-tRFP-Sqh coalesced into discrete aggregates at the same time depleting the signal from the cytoplasm (Fig. 47B). Such CRY2 behaviour was consistent with the other

tissue culture experiments[64]. We conclude that Sqh can be mis-localized using CRY2 aggregation in insect cell culture.

Next, we tested if CRY2-tRFP-Sqh works in *Drosophila* embryos by injecting the plasmid into the yolk cell during the syncytial stage and then imaging later during DC. Without the blue light, we did not detect any clear CRY2-tRFP-Sqh signal, but after the blue light illumination bright aggregates appeared in the yolk cell (Fig. 47C). This confirms that CRY2 is able to coalesce in *Drosophila* embryos. Therefore, we wanted to integrate CRY2-tRFP-Sqh into Drosophila genome. For this, we used II chromosome attP landing site 22A. Even though integration into attP site is very efficient, two injection rounds (~400-500 animals in total) did not yield any transgenic fly. As the size of CRY2-tRFP is 4 times bigger than the Sqh protein, we hypothesized that when expressed at high levels, CRY2-tRFP-Sqh protein acts as a dominant negative form and impedes normal *Drosophila* development. Therefore, we cloned CRY2-tRFP-Sqh into a P-element transformation vector and successfully obtained 6 independent integrations into the genome. After mapping transgene locations, we looked at DC stage embryos either heterozygous or homozygous for CRY2-tRFP-Sqh. In all cases, we observed only very faint fluorescence signal in the epidermis and AS tissue (Fig. 47D). The signal was clearly visible in the AMC of epidermis, but did not reveal any apical foci in the AS cells (Fig. 47D). Upon blue light illumination we could not detect any additional obvious accumulation of CRY2-tRFP-Sqh aggregates (data not shown). We also could not complement the amorphic sqh^{AX3} allele with such CRY2-tRFP-Sqh even by keeping *Drosophila* constantly in the dark. Thus, we conclude that CRY2-tRFP-Sqh impedes the functionality of MyoII even in the dark state, where high levels of fusion protein could act as a dominant negative form.

A1.1.3. Optimizing the existing protocols for a fast and efficient CRISPR/Cas9-mediated genome engineering

Although several protocols exist to introduce any genome modification into Drosophila genome using CRISPR/Cas9 system, some of these protocols work better for different purposes. Earlier we showed a successful generation of complete knock-out (KO) allele of *innexin-3* (*inx3*) using a gene replacement strategy (Chapter 3, Fig. 23A). The protocol was first introduced by S. Bullock and colleagues in an attempt to replace a gene of interest (GOI) in *Drosophila*[149]. Similarly to standard *Drosophila* transgenics, guideRNA plasmids together with homologous recombination (HR) donor are injected into the pole cells that express Cas9

nuclease under the *nanos* promoter (*nos*>Cas9). In our case, HR donor plasmid contained attP-loxP-dsRED-loxP cassette flanked by the two homologous regions outside the *inx3* (Chapter 3, Fig. 23A). Typically, the injected embryos (F_0) do not show eye-specific dsRED fluorescence, however, when crossed to *yw* (or any other) flies, the progeny (F_1) can be already screened for the successful targeting events in 2^{nd}-3^{rd} instar larvae (Fig. 48A). Typically the signal of dsRED, which is controlled by *GMR* enhancer, is present in the larval brain, gut and the last body segment (Fig. 48A). If GOI is silenced in any of these locations one or the other fluorescent signal might be missing. In the case of $\Delta inx3^{dsRED}$, larvae lacked the signal in the brain suggesting a possible silencing of *inx3*, which was not yet reported (Fig. 48A). Once such F_1 adults hatch, dsRED is strongly expressed in the eyes, but several additional areas like ocelli or parts of abdomen are also dsRED positive (Fig. 48B).

Even though the basic CRISPR/Cas9 transgenesis protocol was introduced by Port et al., we noticed that the original *nos*>Cas9 strain had already showed fluorescence signal in the adult flies (Fig. 48A). The reason behind was *nos*>Cas9 integration into one of the attP landing sites, which is marked by GMR-mRFP expression. As it is impossible to distinguish between GMR-mRFP and GMR-dsRED, the screen for successful CRISPR events is only by possible in F_1 males and F_2 females. We, therefore, removed GMR-mRFP using Cre recombinase. *white*$^+$ marker from *nos*>Cas9 can also be removed in order to improve further addition of transgenes. Upon injecting guideRNA and HR donor plasmid mix into the embryos (Fig. 48C), PCR can be performed on some injected F_0 embryos to confirm that CRISPR targets GOI in the zygotic tissues[224]. We then recommend to cross all the hatched adults to *yw* flies, where F_0 females can be pooled together at this step. Since already 2^{nd}-3^{rd} instar larvae of such cross show very prominent dsRED expression (Fig. 48C), we recommend to screen for successful CRISPR events already at this stage as it easier to screen within the wondering larvae in the tube than within anesthetized adults. In the case CRISPR is not efficient, this would allow saving time before performing another injection round. If successful events can be detected in the F_1 larvae, the hatched adult can then be crossed to flies carrying balancer chromosomes in case recessive lethal allele is generated (Fig. 48C). Successful CRISPR/Cas9 targeting of non-essential genes (like *white, yellow, ebony*) were reported to occur at rates above 75%[224]. In agreement with few other studies on CRISPR/Cas9 efficiency for cell and organism lethal genes[224], we observed very low rates (~2% for *inx3* and <1% for *zipper*; Fürst and Brunner, unpublished). For such a low rates screening at the larval stages becomes more preferable than screening through hundreds of adult animals. Hence, we conclude that our modifications to the

typical CRISPR/Cas9 transgenesis protocol allow faster and more efficient screening for successful CRISPR events.

A1.1.4. Optimizing magnetic bead injection into *Drosophila* embryos to study mechanical forces using magnetic tweezers

During AS cell surface contractions, cells produce transient pulling forces on their neighbours[36]. As to date there is no data on the magnitude of such cellular forces, we attempted to investigate them by using magnetic tweezers[225,226]. The custom magnetic tweezer set-up was built by L. Selvaggi (C. Aegerter and D. Brunner labs) by deploying copper solenoids onto the epifluorescence microscope stage. After applying electric current through the solenoids, they would magnetize metal iron core inside them. The core would then create magnetic field in the vicinity of the objective lens. Such magnetic field can be exploited to pull magnetic beads present inside the embryo or single cells. If such beads are pulled against the cell cortex or adherens junctions, this will deform the cell and allow estimating the applied force needed for such deformation. Thus, the key prerequisite is that AS cells contain magnetic beads inside the cytoplasm.

Since AS cells are relatively large (~10-15µm in XY dimensions), first we used 2.8µm diameter paramagnetic beads that allow generation up to 140pN forces when magnetic field is applied in solution. Since AS cells are formed just after the cellularization of the blastoderm, we injected magnetic beads into syncytial stage embryos and used permanent magnet to pull them to the dorsal side of the embryo. When imaged later during the DC stage, we detected the beads in the yolk cell just below the AS cell monolayer (Fig. 49A). We reasoned that when AS nuclei are cellularized, the magnetic beads are pushed upwards by the basally growing membrane and actin cortex. Thus, we injected 1µm diameter magnetic beads that allow generation of only 20pN forces when magnetic field is applied in solution. Following the same procedure and using permanent magnet, we pulled the beads dorsally in the blastoderm stage embryos. When imaging these embryos later during DC stage, in several of them (4 out 18 injected embryos) we detected magnetic beads inside the AS cells at 1-2µm below their adherens junctions (Fig. 49B). However, most embryos still contained the beads only in the yolk cell. Nevertheless, we conclude that 1µm magnetic beads can be successfully introduced into AS cells to be used for magnetic tweezers.

A1.2. Discussion and future directions

Upon the advent of novel molecular tools, depletion of gene function at the protein level became a reality. Numerous methods exist that allow precise spatio-temporal and reversible control of the protein function (Chapter 1, Table 1). In this study, we have successfully used one such method – deGradFP – to acutely deplete MyoII function during tissue closure events. In this Chapter, we have attempted to create several other protein inactivation methods targeting MyoII.

deGradFP effectively inactivates MyoII in AS, epidermis and the YC (Chapters 2 and 5). However, GFP-positive aggregates in the cells suggest that inactivation could be a consequence of sequestering away MyoII rather than degrading it. Such idea is further supported by our observation that MyoII heavy chain Zip is present in the aggregates of light chain Sqh (Chapter 2, Fig. 8C). We thus attempted to complement MyoII inactivation using TEV-induced protein inactivation (TIPI) method. Conceptually, the design of TIPI is similar to deGradFP where GOI is labelled with a certain tag and either TEV or deGradFP nanobody is over-expressed to recognize such tagged protein. One key difference in our case was that TIPI-tagged Zipper was expressed under *actin5C* promoter, whereas Sqh-GFP was under endogenous *sqh* promoter[222]. Different promoter is the most likely reason why TIPI-Zipper could not rescue the mutant zip^{1} allele to adulthood. For both TIPI and deGradFP it is crucial that all protein copies including the maternally-deposited ones are labeled with the appropriate tag. Since minimal promoter region was not mapped for *zipper*, the next step would be introducing TIPI protein tag at the endogenous *zipper* locus. Such approach could be done exploiting Δzip^{dsRED} allele containing the attP landing site that was generated in our lab using CRISPR/Cas9 genome engineering (Fürst and Brunner, unpublished). Alternatively, transgenic flies with TIPI-tagged Sqh under the endogenous promoter could be generated.

To get unprecedented control over MyoII inactivation, we also generated Sqh tagged with a plant chromophore CRY2 and tagRFP. It was demonstrated that in insect and few mammalian cell lines CRY2 forms aggregates or photobodies upon blue light illumination[64]. Consistently, we also observed such photobody formation within minutes after exposure to the blue light in *Drosophila* S2 cells and injected embryos. However, after experiencing difficulties in generating stable transgenic strains carrying CRY2-tRFP-Sqh, we suspect that CRY2-tRFP affects the functionality of Sqh, as the former is almost 3 times larger than Sqh protein. At high levels such CRY2-tRFP-Sqh fusion protein might even act as a dominant-negative form. In

support of such conclusion, only the weakly expressed P-element CRY2-tRFP-Sqh insertions are viable. Even though the ORF is under the endogenous Sqh promoter and localizes to the AMC in the dorsal epidermis neither of the P-element insertions can rescue mutant sqh^{AX3} allele. Weak expression levels also does not allow to detect significant increase of CRY2-tRFP-Sqh upon blue light illumination as CRY2 oligomerization depends on initial high concentration of available proteins[66]. Unfortunately, it is not possible to reduce CRY2-tRFP tag any further as we have already used the minimal PHR domain of CRY2 in our plasmids[64]. Thus, the next reasonable option would be to label Zip with CRY2-tRFP as MyoII heavy chain is ~12 times larger than the light chain Sqh and is likely not to be perturbed by CRY2-tRFP tag. However, this could pose additional challenges as so far even the GFP-tagged version of Zip that could rescue the mutant alleles was not reported.

The need of generating light-induced MyoII inactivation is indispensable as it would allow relieving tissue tension acutely and without externally damaging the tissue. Currently, the only acute way of releasing tissue tension is laser-mediated ablation, which also causes wound healing responses[44,118,119]. Thus, it is of great importance to delineate tissue tension effects on cell behaviour from the ones induced by wound healing. CRY2-CIB association was recently applied to inhibit cell contractility of gastrulating *Drosophila* cells[227]. This was achieved by targeting CRY2-tagged phosphoinositide-phosphatase to the actin cortex of the cells upon blue light illumination. Yet the effect there is highly non-specific as cells lose the whole actin cortex and not only the MyoII contractility. Nonetheless, a successful application of CRY2-CIB interaction *in vivo* opens up possibilities to engineer various MyoII mis-localization strategies. We discussed one such important approach in Chapter 4 with the aim to deplete apical MyoII pool and to specifically recruit MyoII to adherens junctions. This, for example, could be achieved by coupling cytoplasmic domain of E-cadherin or α-catenin with CIB and MyoII with CRY2. Whether MyoII would be fully functional fused with CRY2 and junctional proteins fused with CIB is yet to be shown.

CRISPR/Cas9-mediated genome engineering has become a pivotal tool in the advance of life sciences. Genomes of any model organism including *Drosophila* are being altered for use in cell and developmental biology. Several different protocols exist to efficiently obtain single base pair mutation, label the GOI with any protein tag or completely remove it. In this work we stress the importance to screen for CRISPR events as soon as possible since success rate is very low for cell/organism-lethal genes as opposed to non-essential ones. By modifying the original *nos*>Cas9 *Drosophila* strain and removing *GMR*-mRFP, we could now pool the injected F_0 females to reduce the burden of single fly crosses and easily screen for successful

CRISPR events in the 2nd-3rd instar larvae of F_1 generation. Insertion of dsRED cassette in the replaced gene allows following and recombining such allele easily with various reporters for the desired analysis. Furthermore, a presence of attP-landing site sequence in the removed GOI allows inserting modified protein versions at the endogenous locus. Even though we successfully used deGradFP, the method does not work efficiently with all GFP-tagged proteins. As neither protein inactivation method is perfect for all the possible targets (Chapter 1, Table 1), ability to quickly label target protein with different tags would allow finding the most efficient method for every case. The versatility of combining fast CRISPR/Cas9 genome engineering together with acute protein inactivation paves a way to elucidating gene/protein function that was limited by classical genetics approaches.

A1.3. Summary of the key findings/hypothesis of Appendix 1

- Light and heavy chains of MyoII (Sqh and Zip) were fused with TIPI protein tag
- Sqh was fused with cytochrome CRY2 for light-inducible protein aggregation
- CRY2-Sqh aggregates appear within minutes after the blue light exposure in *Drosophila* S2 cells and injected embryos
- Neither TIPI-Zipper nor CRY2-Sqh rescued the appropriate mutant alleles
- Existing CRISPR/Cas9 gene knock-out (KO) protocol was optimized for quick and easy screening of rare CRISPR events
- Embryo injection protocol was optimized to introduce 1µm beads into single AS cells to be used with magnetic tweezers or other applications

A1.4. Materials and Methods specific for Appendix 1

A1.4.1. TIPI-M/F-Zipper

To generate TIPI-tagged Zipper, we used the following strategy:

1) We first amplified full-length zipper cDNA (isoform C, 5916bp) by PCR from a cDNA Matchmaker library (gift from Markus Noll) using primers that contained sites for EcoRI and KpnI restriction enzymes at 5'-end and 3'-end respectively:
   ecoI5zip: GCATGAATTCATGTCGGAGGAAGTAGATC

kpn3zip: CAGGGTACCTCAATTGGCAGAATCCTCTC

Next, we inserted Zipper cDNA into pBluescript SK- vector using EcoRI and KpnI restriction enzymes to obtain plasmid pBluescript SK-cDNA-Zipper.

2) Next, we used Gateway MultiSite Cloning Kit (Thermo Scientific) to produce pENTR plasmids to be fused into the final ptAW destination vector (see Thermo Scientific for detailed protocols).

   i) The following plasmids were made earlier by Nadia Dubè in the lab: pENTR-TEV-degr(M/F)-SF3B1, pENTR-EGFP and pENTR-Actin5C. Thus, we only made pENTR-HL-Zipper plasmid to be fused with the ones above. For this we amplified Zipper cDNA from pBluescript SK-cDNA-Zipper plasmid with the following primers:

   attBlinkzipST:

   GGGGACAACTTTGTATAATAAAGTTGCTCATATGGATCGAATTCCT GCAGCCCGGACGACAGAGAATTCATCGATGATATCAGATCCAATGT CGGAGGAAGTAGATCGCAACG

   attB2Rzip:

   GGGGACCACTTTGTACAAGAAAGCTGGGTATCAATTGGCAGAATCC TCT

   We then cloned the obtained PCR fragment into pDONR vector (Thermo Scientific) to obtain pENTR-HL-Zipper plasmid.

   ii) Next, we cloned the following 4 pENTR plasmids together with ptAW destination vector: pENTR-Actin5C, pENTR-TEV-degr(M/F), pENTR-EGFP and pENTR-HL-Zipper. Therefore, we obtain the final expression clones ptAW-TEVdeg(M)-SF3B1-EGFP-Zipper and ptAW-TEVdeg(F)-SF3B1-EGFP-Zipper

   iii) Plasmid maxi-preps of expression clones were injected in to *yw D. melanogaster* embryos at 750ng/µl concentration following a standard injection protocol[220]. F_1 progeny of injected animals were screened for appearance of mini-*white*$^+$ eye marker, which was present in expression clone plasmid backbone. Obtained transgenic lines were mapped by crossing two times with *yw; Sp/SM6B, sp*^{1}*, Roi; MKRS/TM6B, Tb, Hu* flies. Transgenic insertions that were mapped to II chromosome, were then recombined with *zip*^{1} *sp*^{1} chromosome, by screening the recombinants for mini-*white*$^+$ and *sp*^{1} over *SM6B, Roi, sp*^{1}.

A1.4.2. TIPI-M/F-Sqh

For all constructs with Sqh, Sqh ORF and 5'-3' genomic regions were amplified using PCR from *sqh*Sqh-GFP rescue plasmid (a gift from R. Karess).

1) **TIPI-(M/F)-Sqh** plasmids were generated with Gibson Assembly Kit (New England Biolabs) by ligating the following components:
   1.1) **5'-*sqh*-genomic region** that was amplified from *sqh*Sqh-GFP rescue plasmid with primers:
   5pr_HindIII: GAAGTTATGCTAGCGGATCCAAGCTTcccgattcgatttttcactcg
   5pr_gen_TEVDGR: GAAGGGGGCGGCCGCggttgctgttggattggtgg
   1.2) **3'-*sqh*-genomic region** that was amplified from *sqh*Sqh-GFP rescue plasmid with primers:
   sqh_3pr_gen: GGATGAGCAGTAGCATTCGTAGAATTGACTAG
   GIB_3pr_gen_Kpn: CTTCACAAAGATCCTCTAGAggtacctttttcaaatgttcgtg
   1.3) **Sqh ORF** that was amplified from *sqh*Sqh-GFP rescue plasmid with primers:
   3pr_gen_sqh: CAATTCTACGAATGCTACTGCTCATCCTTGTC
   TEVDGR_sqh: GATGATATCAGATCCAATGTCATCCCGTAAGACCG
   1.4) **TIPI-(M/F)-SF3B1-EGFP** that was amplified from ptAW-TEVdeg(M/F)-SF3B1-EGFP-Zipper plasmid described earlier with primers:
   TEVDGR_5pr_gen: caatccaacagcaaccGCGGCCGCCCCCTTC
   sqh_TEVDGR:
   CTTACGGGATGACATTGGATCTGATATCATCGATGAATTC
   1.5) **pTWBattB vector** that was linearized with HindIII and KpnI restriction enzymes

All matching PCR fragments contained ~30bp overlapping overhangs needed for Gibson Assembly.

A1.4.3. CRY2-tRFP-Sqh

1) **CRY2-tRFP-Sqh** construct in pTWBattB vector was generated with Gibson Assembly Kit (New England Biolabs) by ligating the following components:
   2.1) **5'-*sqh*-genomic region** (same as for TIPI-(M/F)-Sqh, see above)
   2.2) **3'-*sqh*-genomic region** (same as for TIPI-(M/F)-Sqh, see above)
   2.3) **Sqh ORF** that was amplified from *sqh*Sqh-GFP rescue plasmid with primers:

tagRFP_HL_sqh:
CTAAATTAGGTCATAAAGGAGCTCCCTCCGGAGGCGGTGCTACTGC
TGGCGCTGGTGGAGCCGGTGGACCTGCGGGGTTAATTATGTCATCC
CGTAAGACCGC
3pr_gen_sqh: CAATTCTACGAATGCTACTGCTCATCCTTGTC

2.4) **CRY2 (PHR)** domain that was amplified from pUAST_mCherry_CRY2phr_p14_TEVpN plasmid (made by W. Boll) with primers:
CRY2_5pr_gen: atccaacagcaaccATGAAGATGGACAAAAAG
CRY2_PacI:
TCTTTAATTAATTCAGACATAATTAACCCCGCAGGTCCACCGGC

2.5) **tagRFP** that amplified from pTWBattB_Pact_Dia_RFP_LOV2_cODC plasmid (made by W. Boll) with primers:
GIB_tagRFP_PacI:
GGTTAATTATGTCTGAATTAATTAAAGAAAATATGCATATG
CRY2_PacI:
TCTTTAATTAATTCAGACATAATTAACCCCGCAGGTCCACCGGC

2.6) **pTWBattB vector** that was linearized with HindIII and KpnI restriction enzymes

All matching PCR fragments contained ~30bp overlapping overhangs needed for Gibson Assembly. Plasmid maxi-prep of pTWBattB-CRY2-tRFP-Sqh (500ng/µl) was injected into two different *D. melanogaster* strains carrying attP landing site sequences at 22A (II chromosome) and 86F (III chromosome). F_1 progeny of injected flies were screened for mini-*white*$^+$ appearance, but no transgenic flies were obtained.

2) CRY2-tRFP-Sqh construct in p{UAST} P-element vector was generated by amplifying Cry2-tRFP-Sqh together with 5' and 3' genomic *sqh* regions from pTWBattB-CRY2-tRFP-Sqh plasmid using the following primers:
GIB_5pr_gen: ATGAGCTCGGATCCAAGCTTgcatgcctcttttcattcagg
GIB_3pr_gen_Kpn: CTTCACAAAGATCCTCTAGAggtacctttttcaaatgttcgtg

The obtained PCR product was cloned into p{UAST} vector that was digested with SphI and KpnI. This replaced 5XUAS sequence with 5'-CRY2-tRFP-Sqh-3' sequence. Plasmid maxi-

prep of p{UAST}-CRY2-tRFP-Sqh (750ng/µl) was injected into *yw D. melanogaster* strain. F_1 progeny of injected flies were screened for mini-*white*$^+$ appearance and 6 independent transgenic lines were found. Obtained transgenic lines were mapped by crossing two times with *yw; Sp/SM6B, sp*^{1}*, Roi; MKRS/TM6B, Tb, Hu* flies.

A1.4.4. TIPI-(M/F)-FRT *D. melanogaster* generation

For introducing TIPI-protein tag into *D. melanogaster* genome, the Actin5C-TEVDegr(M/F)-SF3B1-EGFP sequence was amplified using PCR from TIPI-(M/F)-Dia expression plasmid (provided by N. Dubè) with the following primers:

5NheAct5C: gcgagctagcgcatgcaattctatattctaaaaacacaaatg

3TEVdegrKPN: cgtaggtacctggatctgatatcatcgatg

The obtained PCR products were then cloned into pyF5w_attB plasmid (made by J. Bischoff, K. Basler lab) using NheI and KpnI restriction sites. Final pyF5w-attB-actin5C-TEV-degrM and pyF5w-attB-actin5C-TEV-degrF plasmids were injected and integrated into attP landing site 86F on the III chromosome by J. Bischoff. Two D. melanogaster strains were generated: *actin5C*>TEVdegr-M-EGFP-FRT[attP86F] and *actin5C*>TEVdegr-F-EGFP-FRT[attP86F]

A1.4.5. Schneider's S2 cell transfection and light-induced CRY2 aggregation

Schneider's S2 cells were maintained in Schneider's Drosophila Medium (Gibco Life Technologies) supplemented by 10% fetal calf serum (FCS). Transient transfection with pTWBattB-CRY2-tRFP-Sqh plasmid was carried out according to FuGENE (Promega Corporation) cell transfection protocol. S2 cells were grown for 24h in 6-well dishes (MatTek Corporation), transfected with total of 3µg of plasmid and imaged 72h later with custom-modulated Leica DM IRBE spinning-disk confocal microscope.

For light-induced CRY2 aggregation, a circular blue LED dome (custom-built by W. Boll) was used to illuminate transfected S2 cells. ~9.8 mW/cm^2 intensity blue light (λ=465nm) was applied on the entire 6-well dish.

A1.4.6. Light-induced CRY2 aggregation in *D. melanogaster* embryos

For transient expression of pTWBattB-CRY2-tRFP-Sqh plasmid, the embryos were collected for 1h at 18°C and injected into the yolk cell according to standard injection protocol. Embryos were then aged at 18°C until DC stage and imaged with Leica DM IRBE spinning-disk confocal

microscope. For light-induced CRY2 aggregation embryos were simultaneously imaged with 488nm (20% power intensity and 200ms) and 561nm (20% power intensity and 1s) lasers. CRY2 aggregation was monitored in 561nm channel.

Transgenic flies containing P-element CRY2-tRFP-Sqh were prepared for live imaging according to standard protocol. Due to weak expression of CRY2-tRFP-Sqh, embryos were simultaneously imaged with 488nm (20% power intensity and 200ms) and 561nm (30% power intensity and 1-2s) lasers.

A1.4.7. Superparamagnetic bead injection

Two types of superparamagnetic beads (LifeTechnoogies AS, Norway, hereafter, beads) were used for injections - 1µm (MyOne) and 2.8µm (Dynabeads M-270). To avoid bead aggregation, 1mg of beads (~10^9 beads) was incubated with 5µl Tween-20 diluted in 5ml of de-ionized water for 15min. The beads were then washed 3 times with de-ionized water. For final injection solution beads were re-suspended in 200µl in de-ionized water.

Embryos were collected for 1-2h at room temperature and dechorionated with 50% bleach for 3-4min. Two different approaches were used to inject beads in to the embryos that would be imaged with different set-ups:

1. Imaged on a glass slide:

Embryos that will be imaged with spinning-disk confocal microscope were aligned on a nitrocellulose filter dorsal side facing down and transferred on to glass slide with glue. They were desiccated for 10-15min, covered with Voltalef Halocarbon oil 10S (Sigma-Aldrich) and injected with 2.8µm or 1µm magnetic beads. Embryos were then put on a permanent 1T magnet for 1-2h occasionally moving the glass slide in XYZ directions. Embryos were then aged for 14-16h at 18°C and imaged later.

2. Imaged in the glass capillary:

Embryos that will be imaged on magnetic tweezer set-up, were aligned on a glass slide without the glue with dorsal side facing down. They were then desiccated for 7-10min and injected with 2.8µm or 1µm magnetic beads without covering them with Voltalef Halocarbon oil 10S (Sigma-Aldrich). Only after the injections they were covered with oil and put on a permanent 1T magnet for 1-2h occasionally moving the glass slide in XYZ directions. Embryos were then aged for 14-16h at 18°C and transferred with the cut Eppendorf pipette tip to the glass capillary containing Voltalef Halocarbon oil 10S.

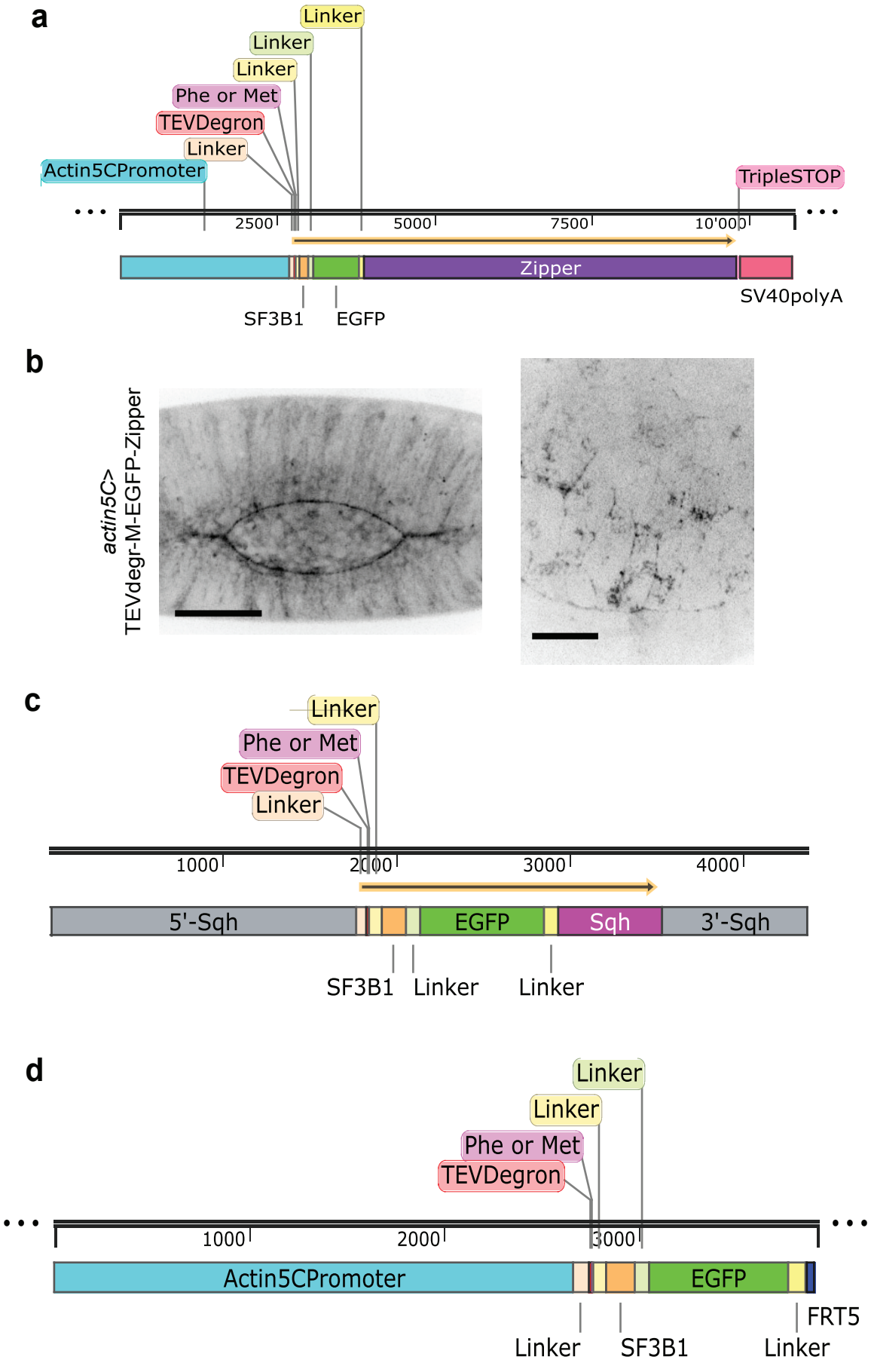
a
Linker
Linker
Linker
Phe or Met
TEVDegron
Linker
Actin5CPromoter
TripleSTOP
2500
5000
7500
10'000
Zipper
SV40polyA
SF3B1
EGFP
b
actin5C>
TEVdegr-M-EGFP-Zipper
c
Linker
Phe or Met
TEVDegron
Linker
1000
2000
3000
4000
5'-Sqh
EGFP
Sqh
3'-Sqh
SF3B1
Linker
Linker
d
Linker
Linker
Phe or Met
TEVDegron
1000
2000
3000
Actin5CPromoter
EGFP
FRT5
Linker
SF3B1
Linker

Figure 46. Strategies of protein tagging for TEV-induced protein inactivation (TIPI). (a) Schematic representation of MyoII heavy chain Zip tagged with TIPI tag. TIPI tag consists of TEV-degron, Met (stabilizing) or Phe (destabilizing) amino acid, SF3B1 TEV-binding partner motif and EGFP. TIPI-tag is followed by cDNA of Zip isoform C and SV40polyA sequence. *Actin5C* promoter ubiquitously expresses the open-reading frame (ORF, yellow arrow) of the fusion protein. **(b)** Image of TIPI-tagged Zip during DC. Zip localizes properly in the LE of epidermis (left) and the apical surface of amnioserosa cells. Scale bar: left - 50µm, right - 20µm. **(c)** Schematic representation of TIPI-tagged MyoII light chain Sqh. TIPI-tag is fused with Sqh ORF and is expressed by the regulatory *sqh* elements (yellow arrow). **(d)** Schematic representation of TIPI-tag engineered for efficient *in vivo* fusion with any ORF or gene of interest. FRT recombination sequence is inserted after the TIPI-tag and integrated into *Drosophila* genome. In the presence of flipase (Flp) protein, the recombination with another FRT tagged ORF leads to fusion of TIPI tag with the ORF.

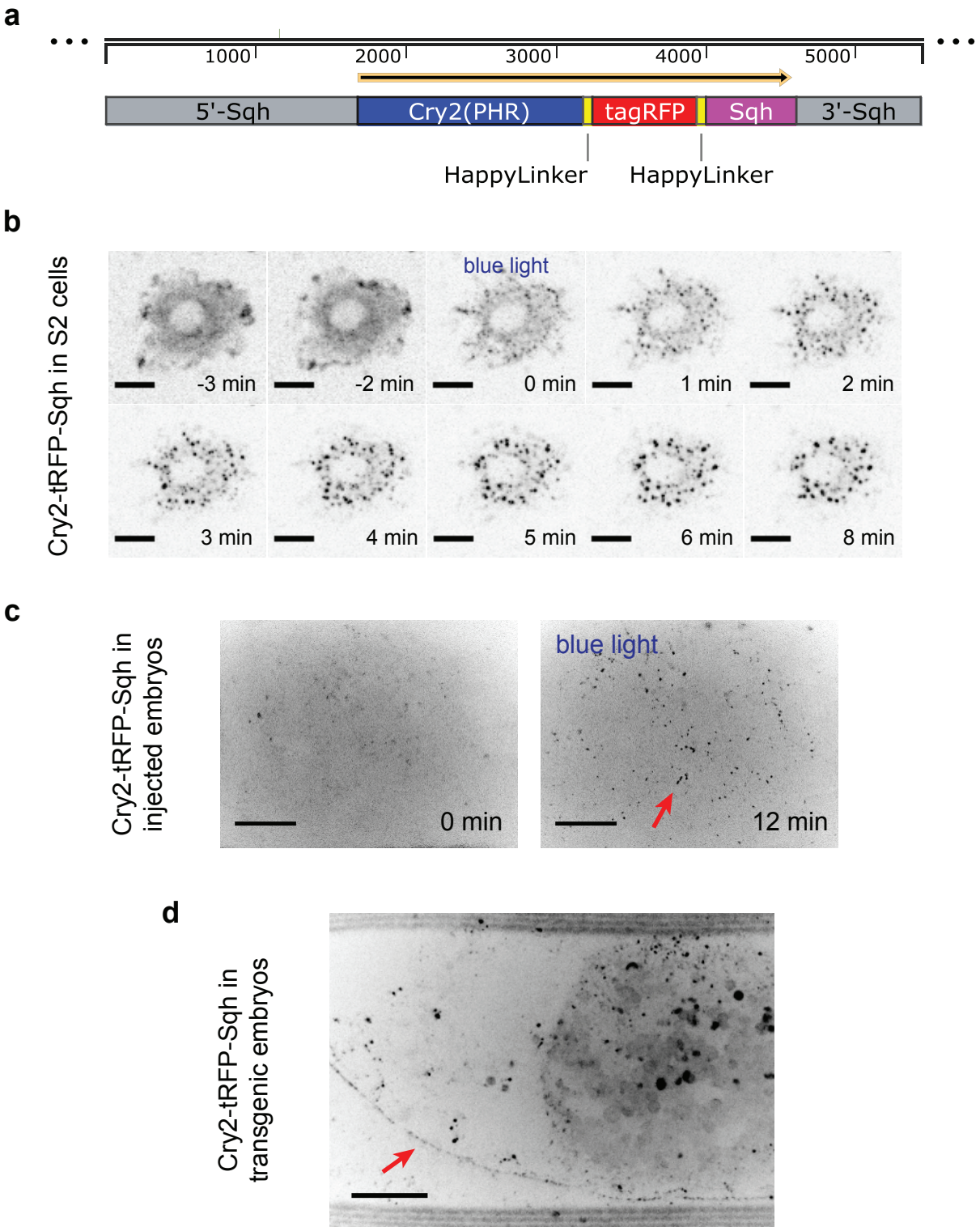

Figure 47. MyoII clustering mediated by light inducible CRY2 photobody aggregation. (a) Schematic representation of MyoII light chain Sqh tagged with PHR domain of CRY2 and tagRFP. ORF (yellow arrow) is expressed by the genomic regulatory sqh elements. **(b)** Blue light (λ=465nm) illumination of *Drosophila* Schneider's S2 cells transfected with CRY2-tagRFP-Sqh plasmid induces rapid photobody aggregation. Scale bar: 10μm. **(c)** *Drosophila* embryo at the DC stage that was injected with CRY2-tagRFP-Sqh plasmid earlier during the blastoderm stage. Blue light (λ=465nm) illumination induces photobody aggregation (red arrow). Scale bar: 20μm. **(d)** *Drosophila* embryo that contains genomic CRY2-tagRFP Sqh P-element at the DC stage. CRY2-tagRFP-Sqh localizes to the leading edge of epidermis (red arrow). Scale bar: 20μm.

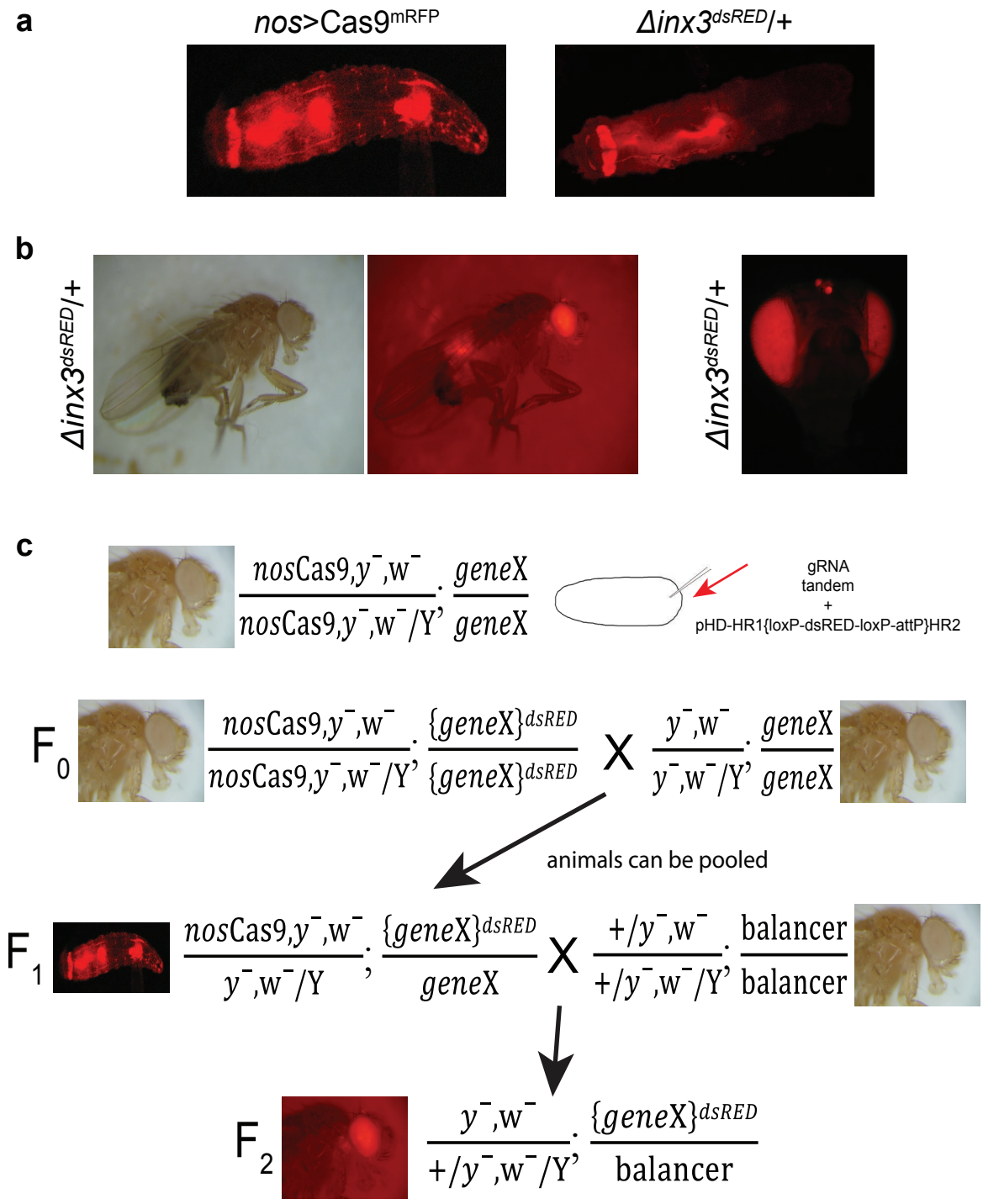

Figure 48. Optimized CRISPR/Cas9 protocol for *Drosophila* transgenesis. (a) GMR-mRFP/dsRED expression pattern in 3rd instar larvae of *nos*>Cas9 strain (left) and *inx3* knock-out (KO) strain (right). dsRED expression is suppressed in the larval brain in the *inx3*^{dsRED} strain (left). **(b)** GMR-dsRED expression pattern in adult *Drosophila* in *inx3*^{dsRED} KO strain. Note the intense expression in the eyes and ocelli. **(c)** Improved scheme of CRISPR/Cas9 transgenesis for creating a loss-of-function or full KO mutant alleles in *Drosophila*. *nos*>Cas9 embryos are injected with guideRNA templates and pHD-HR-dsRED donor plasmid (red arrow). Hatched adults (F_0) are crossed to *yw* strain. Screening for successful CRISPR targeting events can be carried out in 2nd-3rd instar larvae offspring from such a cross. If successful event is detected, the hatched adults (F_1) are crossed to balancer strains.

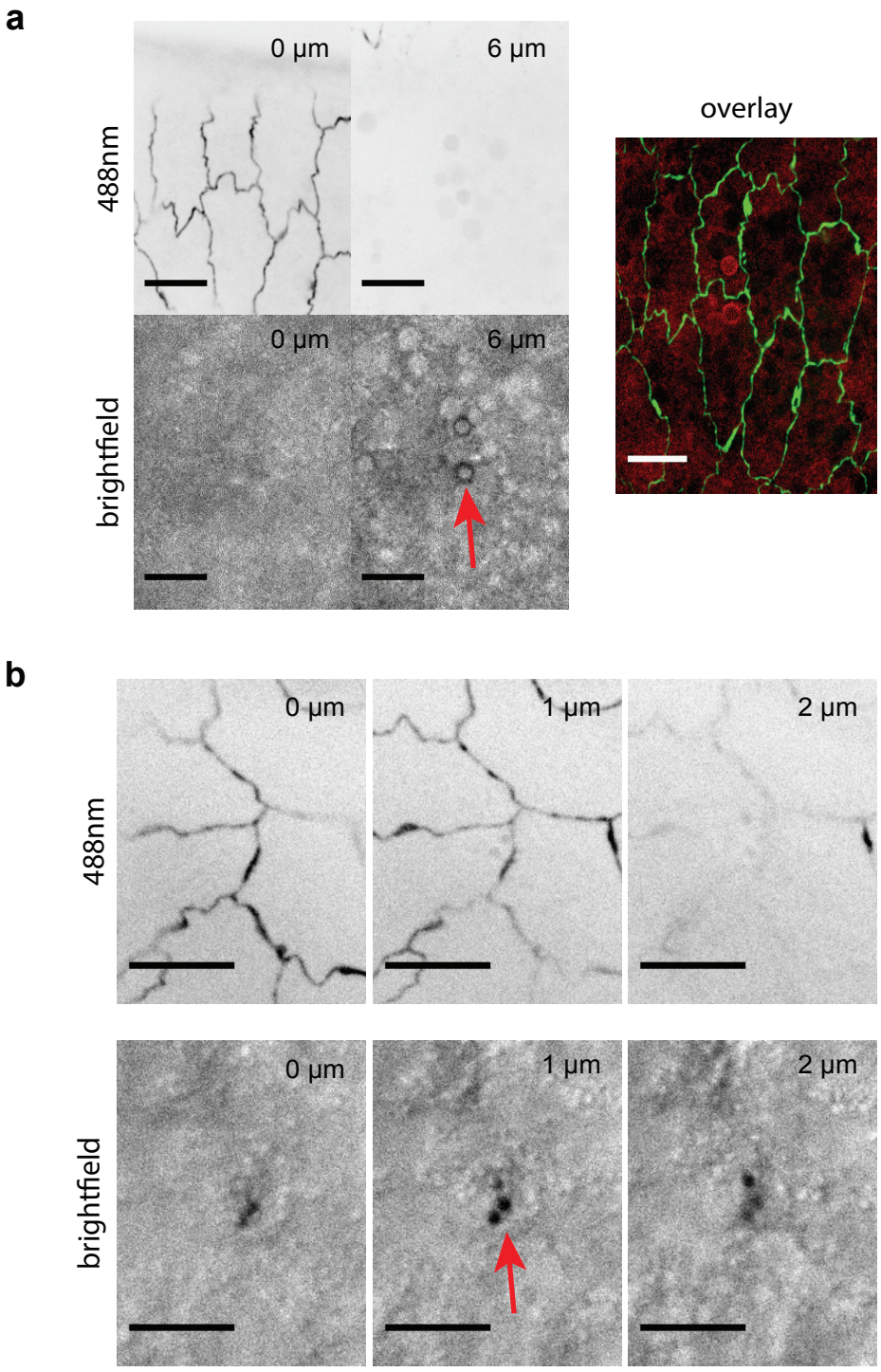

Figure 49. Magnetic beads can be introduced into *Drosophila* embryos and single cells. **(a)** GFP and brightfield images of amnioserosa (AS) tissue region with 2.8µm diameter magnetic beads injected during the blastoderm stage earlier. The beads are not included in the AS cells and are found in the underlying yolk cell (~6µm below the apical AS cell surface). Arm-GFP was used to outline AS cell adherens junctions. Scale bar: 10µm. **(b)** GFP and brightfield images of AS tissue region with 1µm diameter magnetic beads injected during the blastoderm stage earlier. The beads are in the AS cells (~1µm below the apical AS cell surface). Arm-GFP was used to outline AS cell adherens junctions. Scale bar: 10µm.

Appendix 2. Additional data for Chapter 2

Part of the results described here are published in
Eltsov, M., Dube, N., Zhou, Y., Pasakarnis, L., Haselmann-Weiss, U., Brunner, D., Frangakis, A.S. **Quantitative analysis of cytoskeletal reorganization during epithelial tissue sealing by large-volume electron tomography.** *Nat Cell Biol.* 2015 May;17(5):605-14.
LP contributed with latrunculin B injections, Supplementary Figure 5 and unpublished data presented in section A2.2. and Figures 56-57.

A2.1. Additional results and discussion

Earlier we demonstrated that AMC alone cannot complete DC if MyoII is inactivated in AS cells with *332.3*Gal4 (Fig. 4C). Consistently, we observed the same phenotype when deGradFP was expressed with AS-specific enhancer elements (EEs) other than *332.3*. However, there were two groups of AS-specific EEs that were either mosaic in their expression or were ectopically expressed in other tissues (e.g. epidermis or the yolk cell). The first group with sporadic/mosaic expression includes *btl*Gal4 (*breathless* EE), *7K*Gal4 (pAS), *MJ33a*Gal4, *P0181*Gal4 (Table 6)[26,97,228]. The second group with ectopic expression includes *c381*Gal4 (AS+epidermis), *P0172*Gal4 (AS+yolk cell), *Kr*Gal4 (*krüppel* EE, AS+mesoderm)[97,229] (Table 6). Phenotype severity depended on the amount of affected AS cells, with *332.3*Gal4 and *c381*Gal4 producing the most severe DC failures. Next, we wanted to confirm that AS-SqhKO phenotype is due to the specific depletion of Sqh-GFP and not an off-target protein(s). Thus, we introduced *sqh*:Sqh-mCherry transgene that is not targeted by the deGradFP into AS-SqhKO set-up with the two strongest EEs - *332.3*Gal4 and *c381*Gal4. DC and such animals were rescued to the adulthood (Fig. 50).

We showed that AS cell apical constriction is the main driving force of DC (Section 2.2.2). Next, we wanted to know if there is a critical number of AS cells that is necessary to complete DC. For this, we utilized EE *7K*Gal4, which was reported to be expressed in the first row of AS cells next to the LE (pAS)[26]. We could not confirm that every embryo consistently followed the described expression pattern as in majority of cases many more than just pAS cells expressed Gal4. Nevertheless, a fraction of embryos expressed Gal4 in pAS only. In these embryos, the middle AS cells were not affected by the deGradFP and contracted autonomously (Fig. 51A). They did so by stretching those cells where MyoII was inactivated (Fig. 51A). In this genotype AMC was still not able to complete DC (Fig. 51B). Nevertheless, we could not observe any obvious pattern or minimal number of constricting AS cells that are necessary for

DC. We conclude that AS cells contain cell-autonomous apical constriction program, which does not depend on their neighbours being able to constrict.

In AS-SqhKO embryos with *332.3*Gal4 we observed an initial AS area decrease that we attributed to early AS cell volume reduction reported recently[42]. Alternatively, it is possible that the proposed purse-string activity of AMC could account for such area decrease. To discriminate between the cell volume reduction and AMC contractility in AS-SqhKO embryos, we inactivated MyoII in both AS tissue and epidermis simultaneously (Fig. 52A; AS-ES-SqhKO). As expected, DC failed in such embryos (Fig. 52A). Next, we measured AS tissue area outlined by mCherry-moesin in AS-epidermis-SqhKO embryos and detected an initial area decrease (Fig. 52B). This supports our hypothesis that the area decrease is due to AS cell volume loss rather than contractility of the AMC. We observed similar results when MyoII was depleted with ubiquitous *actin5C*Gal4 (Fig. 52C). However, due to lack of fluorescent reporter other than Sqh-GFP, we could not track the LEs unambiguously to quantify the area decrease. Interestingly, in all SqhKO genotypes that we have analysed, we observed that posterior spiracles of the embryo were rotating without the MyoII being present in the nearby cells (Fig. 52A). Thus, we hypothesize, that the torque forces provided by the spiracle rotation could be contributing to the initial re-shaping of the dorsal opening. It is also likely that spiracle rotation facilitates the initial AS tissue area reduction as some AS cells could be squeezed next to the future posterior canthus.

In AS-SqhKO embryos we also detected a contractile activity of the yolk cell below the AS tissue (see Chapter 5). We show later that such activity is able to move epidermis LE (see Chapter 5, Fig. 43). Thus, we wanted to check if yolk cell contractility contributes to the initial AS tissue area decrease in AS-SqhKO embryos. We over-expressed deGradFP and depleted MyoII in both the AS tissue and the yolk cell simultaneously (Fig. 52D). Measurements of AS tissue area revealed no significant difference in the initial relative AS tissue area decrease between the control, AS-SqhKO and AS-yolk-SqhKO embryos (Fig. 52E). Therefore, we conclude that the initial AS tissue area reduction is dependent neither on AMC nor the yolk cell contractility.

As we have just described, the most EE expression patterns were variable in AS cells. We also observed similar heterogeneity with the epidermis-specific EEs (Table 6). To obtain strictly epidermis-specific Gal4 expression needed for the acute MyoII inactivation, we screened through all commonly reported epidermis-specific EEs and, additionally, included new EEs from the JaneliaFarm Gal4 collection[90]. All of the tested epidermis-specific EEs either showed mosaic ectopic expression in the AS cells or were not expressed in the whole epidermis

(Table 6). Surprisingly, even though the commonly used *engrailed*-derived EE e22Gal4 is reported to cover the whole epidermis[50,230], the expression of deGradFP was limited only to the *engrailed* stripes and sporadic AS cells (Fig. 53A). deGradFP expression by LE-specific EE based on JNK target *puckered* (LEGal4) showed disruption of AMC only towards the end of DC (Fig. 53B). After screening through several epidermis-specific EEs from JaneliaFarm library, we found that all of them were either ectopically expressed in the AS cells or showed mosaic or no signal at all in the epidermis (Fig. 53C).

To overcome such major drawback of ectopic EE expression, we generated AS-specific Gal80. We showed earlier that *332.3*Gal80 eliminated the ectopic deGradFP expression in the AS cells caused by *pnr*Gal4 EE (Fig. 10D). Since *332.3*Gal80 also contains *yellow*$^{+}$ transgene, we also noticed a dark pigmentation around the eyes and antennae in *332.3*Gal80 homozygous adult flies (Fig. 53D). To check if this pigmentation is due to EEs near the *332.3* locus, we over-expressed UAS-*yellow*$^{+}$ with the original *332.3*Gal4 EE. Consistently, in such flies we observed an even stronger pigmentation around the adult eyes and antennae (Fig. 53D). Thus, we conclude that *332.3*Gal80 is under the same regulatory sequences as *332.3*Gal4.

Name	Genotype tested	BSC ID*	Expression pattern**	Notes
69BGal4	*w;* UAS-GFP-Zip/+; *69B*Gal4/+	BL#1774	Epidermis and AS	Strong expression in the ectoderm
GMR11C02 Gal4	*w;* UAS-GFP-Zip /+; *GMR11C02*Gal4/+	BL#45011	Mosaic epidermis	JaneliaFarm strain
GMR39B10-GAL4	*w;* UAS-GFP-Zip /+; *GMR39B10*Gal4/+	BL#45260	Sporadic/no signal in epidermis	JaneliaFarm strain
GMR27H09-GAL4	*w;* UAS-GFP-Zip /+; *GMR27H09*Gal4/+	BL#45537	Epidermis and yolk cell	JaneliaFarm strain
GMR12D10-GAL4	*w;* UAS-GFP-Zip /+; *GMR12D10Gal4/+*	BL#48504	Epidermis and sporadic AS	JaneliaFarm strain
GMR26F04-GAL4	*w;* UAS-GFP-Zip /+; *GMR26F04Gal4*/+	BL#49191	Mosaic epidermis and sporadic AS	JaneliaFarm strain
GMR34B11-GAL4	*w;* UAS-GFP-Zip /+; *GMR34B11*Gal4/+	BL#49774	Epidermis and mosaic AS	JaneliaFarm strain
C1003Gal4	*w;* UAS-GFP-Zip /*C1003*Gal4;	BL#2735	Heart primordium, mosaic epidermis	
dpp-GAL4.PS[4B], dpp-GAL4.PS[8B]Gal4	*y w cv sqh*^{AX3}/ Y; *sqh*:Sqh-GFP/+; UAS-NSlmb-vhhGFP4*/dpp-GAL4.PS[4B], dpp-GAL4.PS[8B]Gal4*	BL#7008	Epidermis and mosaic AS	Consists of two *dpp* enhancer elements
LEGal4	*y w cv sqh*^{AX3}/ Y; *sqh*:Sqh-GFP/+; UAS-NSlmb-vhhGFP4/+	BL#58801	Epidermal leading edge (1-2 cells from AS)	Based on *puckered* enhancer element
e22cGal4	*y w cv sqh*^{AX3}/ Y; *sqh*:Sqh-GFP/+; UAS-NSlmb-vhhGFP4/+	BL#1973	Epidermal stripes and sporadic AS	Based on *engrailed* enhancer elements

pnrGal4	*y w cv sqh*^{AX3}/ Y; *sqh*:Sqh-GFP/+; UAS-NSlmb-vhhGFP4/*pnr*Gal4	BL#3039	Dorsal epidermis (3-4 cells from AS) and mosaic AS	Ectopic expression in AS cells variable (from several cells to the whole tissue)
P0161Gal4	*y w cv sqh*^{AX3}/ Y; *sqh*:Sqh-GFP/+; UAS-NSlmb-vhhGFP4/*P0161*Gal4	-	Epidermis and ectopic AS	P0161 from Münster Drosophila library
P0172Gal4	*y w cv sqh*^{AX3}*/Y; sqh:*Sqh-GFP/*P0172*Gal4; UAS-NSlmb-vhhGFP4/+	-	AS and yolk cell, sporadic epidermis	P0172 from Münster Drosophila library
P0180Gal4	*y w cv sqh*^{AX3}/ Y; *sqh*:Sqh-GFP/+; UAS-NSlmb-vhhGFP4/*P0180*Gal4	-	Sporadic AS	P0180 from Münster Drosophila library
c381Gal4	*y w cv sqh*^{AX3}/Y; *sqh:*Sqh-GFP/*c381*Gal4; UAS-NSlmb-vhhGFP4/+	BL#3734	AS and mosaic epidermis	Most commonly used AS-specific Gal4
KrGal4	*y w cv sqh*^{AX3}/Y; *sqh*:Sqh-GFP/+; UAS-NSlmb-vhhGFP4/*krüppel*Gal4	BL#58800	AS and mesoderm	Based on *krüppel* enhancer elements
7KGal4	*y w cv sqh*^{AX3}/Y; *sqh:*Sqh-GFP/*7K*Gal4; UAS-NSlmb-vhhGFP4/+	-	Mosaic in AS, pAS in some embryos	
btlGal4	*y w cv sqh*^{AX3}/ Y; *sqh:*Sqh-GFP/*btl*Gal4; UAS-NSlmb-vhhGFP4/+	-	Mosaic in AS	Based on *breathless* enhancer elements
Act5CGal4	*y w cv sqh*^{AX3}/ Y; *sqh:*Sqh-GFP/*Act5C*Gal4; UAS-NSlmb-vhhGFP4/+	BL#25374	Ubiquitous	Based on *actin5C* enhancer elements
P0181Gal4	*w; UAS-GFP-Zipper/P0181*Gal4	-	Sporadic AS	DGRC Kyoto No.: 103-184Gal4
332.3Gal4	*y w cv sqh*^{AX3}/ Y; *sqh:*Sqh-GFP /*332.3*Gal4; UAS-NSlmb-vhhGFP4/+	BL#5398	All AS	Strongest expression at 25°C, mosaic expression at 18-21ºC
P48YGal4	*y w cv sqh*^{AX3}/ Y; *sqh:*Sqh-GFP /*P48Y*Gal4; UAS-NSlmb-vhhGFP4/+	BL#4935	Sporadic AS and endoderm	
enGal4	*y w cv sqh*^{AX3}/ Y; *sqh:*Sqh-GFP /*en*Gal4, UAS-mCherry-moesin; UAS-NSlmb-vhhGFP4/+	BL#30564	Epidermal stripes and ectopic AS	Based on *engrailed* enhancer elements
MJ33aGal4	N. Dubè, personal communication	BL#6992	Sporadic AS	
C289b11Gal4	N. Dubè, personal communication	BL#6981	Sporadic AS	

Table 6. Gal4 enhancer elements (EEs) used in the study and their expression patterns. *BSC - Bloomington Stock Center; ** expression in ~1-20 cells is classified as sporadic, > 20 cells is classified as mosaic, pAS – peripheral AS cells;

Recently, an alternative way of reducing MyoII activity was described that involved over-expression of constitutively-active MyoII phosphatase (Mbs.N300)[42,84]. Consistent with the published results when over-expressed in AS cells with *332.3*Gal4, Mbs.N300 does not lead to major defects during DC (Fig. 54)[42,84]. Same is true if Mbs.N300 was over-expressed in the epidermis using *pnr*Gal4 (Fig. 54). We showed earlier that the fragments of AMC in the epidermis are still detected upon Mbs.N300 over-expression (Fig. 5C). Even Mbs.N300 over-expression with leaky *pnrGal4* EE that shows ectopic expression in the AS cells did not lead to any major defects during DC (Fig. 52). However, in ~50% embryos we observed anterior ruptures similar like in ~40% of ES-SqhKO embryos (Fig. 11B). This supports our hypothesis that the tissue ruptures occur because of the reduced ability of epidermis to withstand external forces from the involuting head, and not due to the absence of AMC. These results question the use of Mbs.N300 as a tool to interfere with MyoII dynamics. Most likely the over-expression is not sufficient to completely eliminate MyoII function.

Interesting experiment was performed in Wells et al., 2014, whereby the two zipping canthi were ablated away from the dorsal opening[47]. Since LEs straightened after the canthi removal and DC proceeded with normal rates, authors argued that the tissue ratchet mechanism is not acting during DC. However, authors did not provide any evidence for reduced AMC tension. We have recently shown that LE cells interdigitate with finger-like protrusions with the neighbouring cells[25]. This allows connecting the small AMCs inside every epidermis cell into a supracellular AMC surrounding the dorsal opening[25,35,43]. Therefore, we expect that cutting AMC away from the canthi would not affect the tension between the individual LE cells. To check if AMC is still under tension after the canthi removal, we repeated the experiment done in Wells et al, 2014, and, in addition, performed laser incisions in the LE. In agreement with the authors, we observed that the two LEs flattened out (Fig. 55A). Consistently, DC still continued and dorsal opening became a slit-like rather than a typical eye-shaped (Fig. 55A). Within 2 hours after the canthi removal, we performed LE laser incisions at varying distances from the removed canthi. We could not observe any obvious differences in recoil of the free LE ends after such incisions when compared to those done prior to canthi removal (Fig. 55B). Differences were also not evident when laser ablating at different places along the LE – either next to the removed canthi or in the middle of the LE (Fig. 55B). Thus, we conclude that the interpretations by Wells et al., 2014, excluding tissue ratchet are unsupported and canthi removal cannot discriminate between the two DC models.

A2.2. Zipping force in the epidermis is not generated by acto-myosin contractility

Our recent electron tomography data excluded the role of actin in generating the zipping force[25]. Injection of actin-depolymerizing drug latrunculin B (LatB) below the zipping canthi revealed that the canthus is more resistant to the drug treatment than the other acto-myosin structures in DC tissues (SuppFig. 5 in [25]). Upon LatB injection all actin-based structures break down eventually ripping apart all the tissues and the two canthi. Thus, we hypothesized that if the external tension acting on the canthus would be reduced, the canthus might disassemble later after the LatB injection. Therefore, we performed laser incisions either in the AMC next to the canthus or almost completely isolated the canthus from the rest of the epidermis and AMC (see Methods). On average, the isolated canthi stayed intact for longer while other structures like AMC were tearing apart at similar times after the LatB injection (Fig. 56A-56B). Curiously, isolation of the canthus did not have a major effect on its architecture if LatB was not injected, suggesting that the canthus is an autonomous structure of the epidermis (Fig. 56C).

Reconstruction of the canthus using large-volume electron tomography suggested that microtubules (MTs) could generate the zipping force as the actin-rich filopodia are omitted from the plane of the sealing epidermis[25]. Besides actin, we also exclude acto-myosin contractility as the zipping force since MyoII inactivation in the epidermis (ES-SqhKO) did not prevent zipping (Fig. 6C). In support of MT role in zipping, we confirmed that MTs are still dynamic in MyoII-depleted epidermis by visualizing MT plus tip binding protein EB1 tagged with mCherry (Fig. 57). In agreement with the recent thermodynamic model of zipping[231], we suggest that AMC plays a role in relaying and tuning the zipping force transmission along the cable length, but does not generate the actual zipping force.

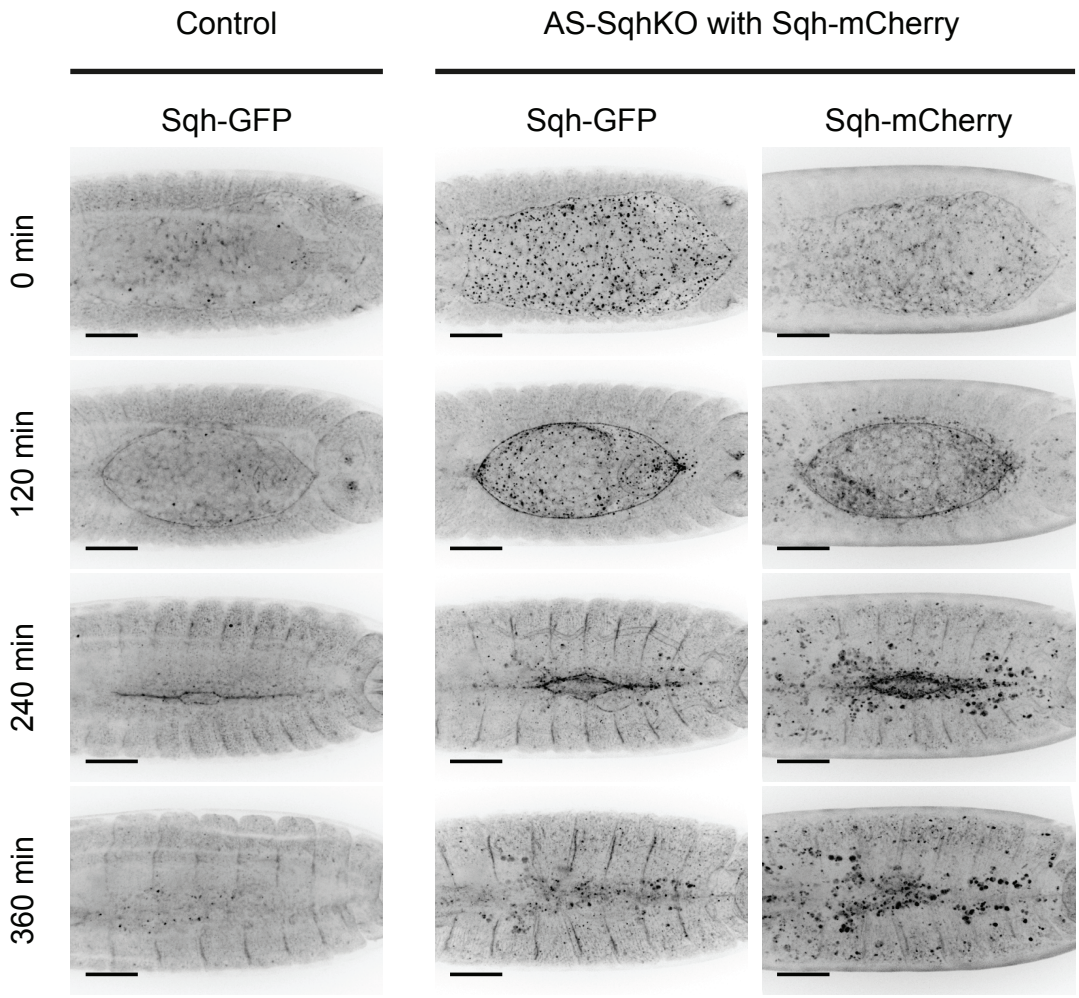

Figure 50. Sqh-mCherry rescues the phenotypes caused by deGradFP-mediated inactivation of Sqh-GFP. Selected movie frames showing DC in control and AS-SqhKO embryos with additional Sqh-mCherry transgene. Sqh-GFP aggregates still form in the AS-SqhKO+Sqh-mCherry embryos, but DC completes normally. 0 min depicts the end of germ-band retraction. Scale bar: 50µm.

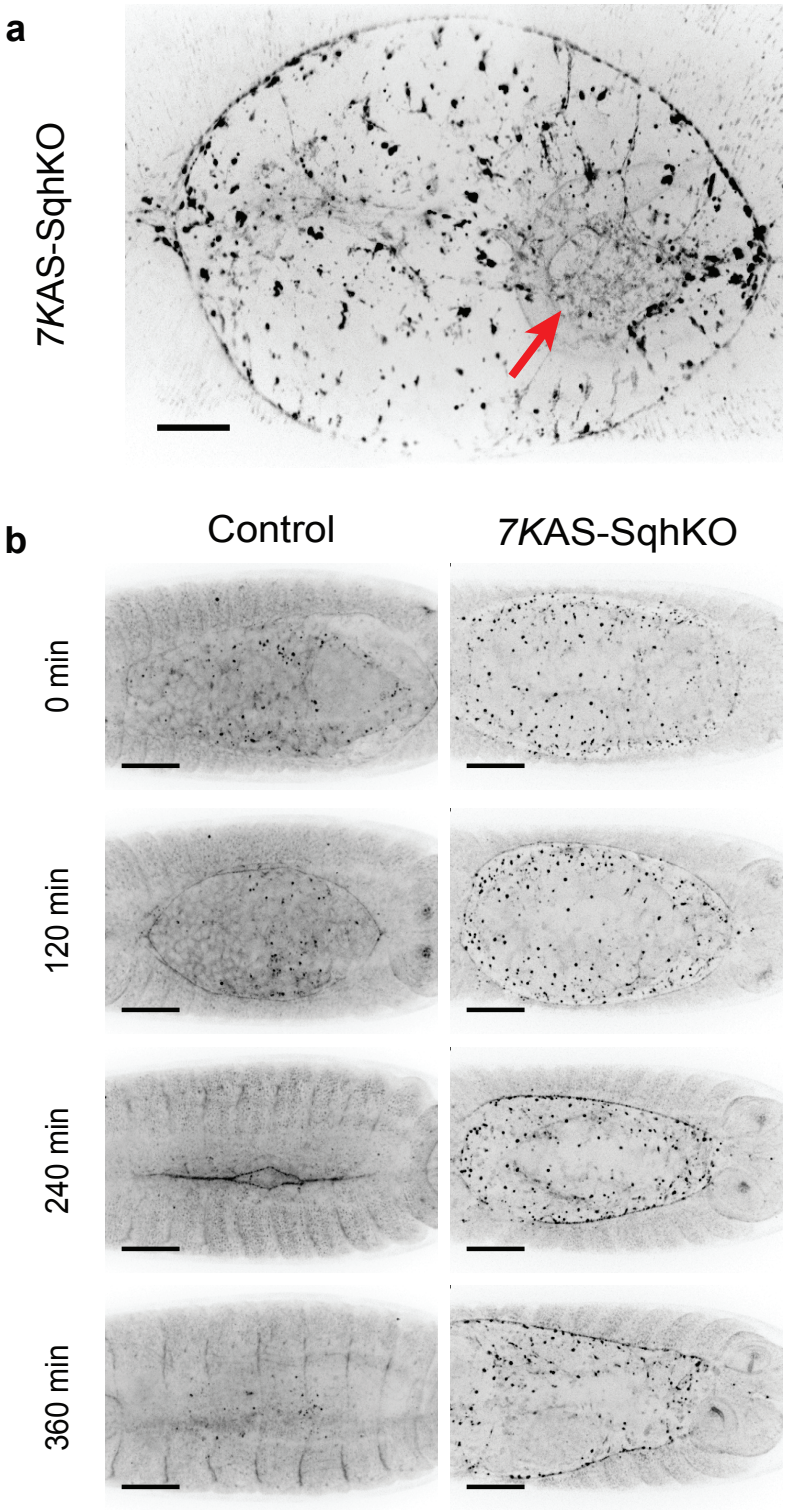

Figure 51. MyoII inactivation in part of the AS tissue leads to DC failure. (a) Image of DC stage embryo expressing deGradFP with *7K*Gal4 enhancer element (*7K*AS-SqhKO). AS cells not affected by MyoII inactivation contract autonomously (red arrow). Scale bar: 20µm. **(b)** Selected movie frames showing DC in control and *7K*AS-SqhKO embryos. 0 min depicts the end of germ-band retraction. Scale bar: 50µm.

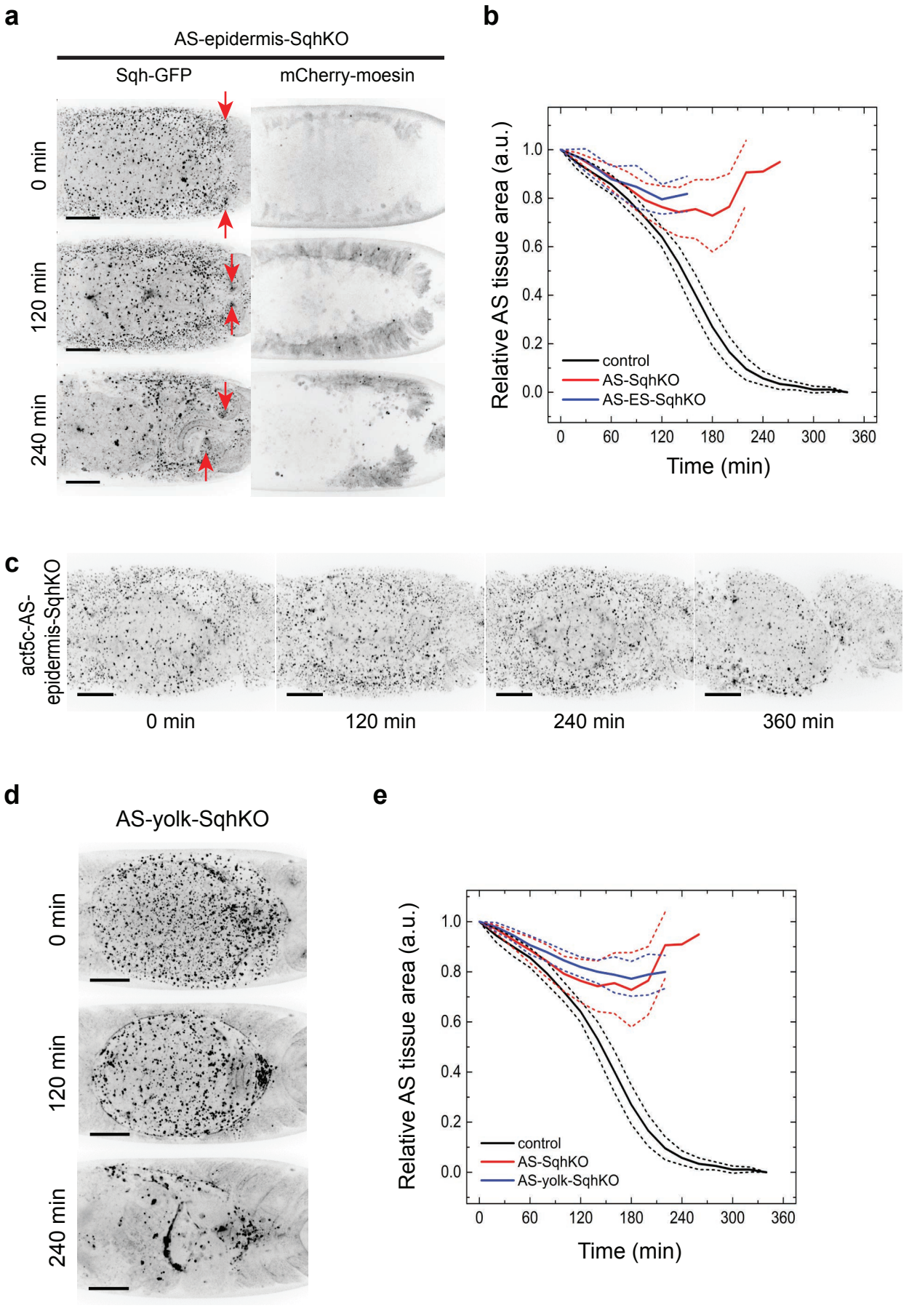
a
AS-epidermis-SqhKO
Sqh-GFP
mCherry-moesin
0 min
120 min
240 min
b
Relative AS tissue area (a.u.)
1.0
0.8
0.6
0.4
0.2
0.0
control
AS-SqhKO
AS-ES-SqhKO
0
60
120
180
240
300
360
Time (min)
c
act5c-AS-epidermis-SqhKO
0 min
120 min
240 min
360 min
d
AS-yolk-SqhKO
0 min
120 min
240 min
e
Relative AS tissue area (a.u.)
1.0
0.8
0.6
0.4
0.2
0.0
control
AS-SqhKO
AS-yolk-SqhKO
0
60
120
180
240
300
360
Time (min)

Figure 52. AS tissue area decrease during the early DC stages is independent of AMC or yolk cell contractility. (a) Selected movie frames showing DC in control and AS-epidermis-SqhKO embryos. Posterior spiracles (red arrows) rotate independently from DC. mCherry-moesin labels F-actin. 0 min depicts the end of germ-band retraction. Scale bar: 50μm. **(b)** Relative area occupied by the AS tissue in control (black line, n=19), AS-SqhKO (red line, n=22) and AS-epidermis-SqhKO (blue line, n=7) embryos. Dashed lines: Standard deviation. **(c)** Selected movie frames showing DC in control and act5C-AS-epidermis-SqhKO embryos. 0 min depicts the end of germ-band retraction. Scale bar: 50μm. **(d)** Selected movie frames showing DC in control and AS-yolk-SqhKO embryos. 0 min depicts the end of germ-band retraction. Scale bar: 50μm. **(e)** Relative area occupied by the AS tissue in control (black line, n=19), AS-SqhKO (red line, n=22) and AS-yolk -SqhKO (blue line, n=12) embryos. Dashed lines: Standard deviation.

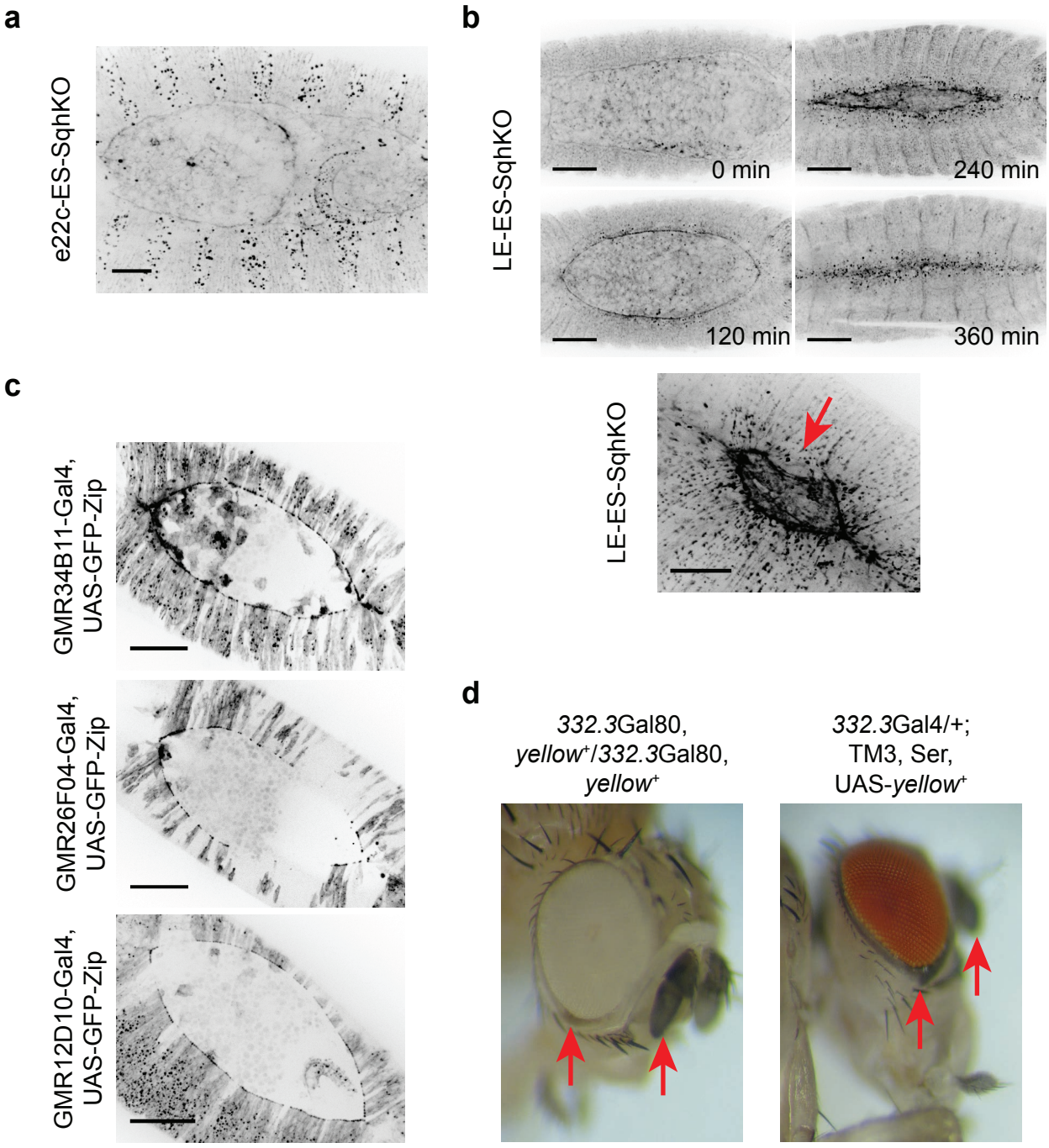

Figure 53. Commonly used and novel epidermis-specific enhancer elements (EEs) are not sufficient to achieve strict tissue-specificity or temporal control. (a) Image of DC stage embryo expressing deGradFP with engrailed-based *e22c*Gal4 EE. Sqh-GFP aggregates accumulate in the *engrailed*-expressing stripes only. Scale bar: 10µm. **(b)** Selected movie frames showing DC in LE-ES-SqhKO embryos. AMC in the epidermis forms (120min), but disassembles later (240min). Scale bar: 50µm. Bottom: Image of LE-ES-SqhKO embryo showing partial depletion of AMC (red arrow). Scale bar: 20µm. (**c)** Image of DC stage embryos expressing UAS-Zip-GFP with three different epidermis-specific EEs from JaneliaFarm Gal4 collection. All EEs either show mosaic expression in the AS cells or do not cover the complete epidermis. Scale bar: 50µm. (**d)** Increased pigmentation in adult *Drosophila* animals expressing y*ellow+* gene with 3*32.3* EE. The pigmentation is obvious around the eyes and the antennae (red arrows). It less prominent in 3*32.3G*al80, y*ellow+* animals (left) than in 3*32.3G*al4, UAS-y*ellow+* animals (right).

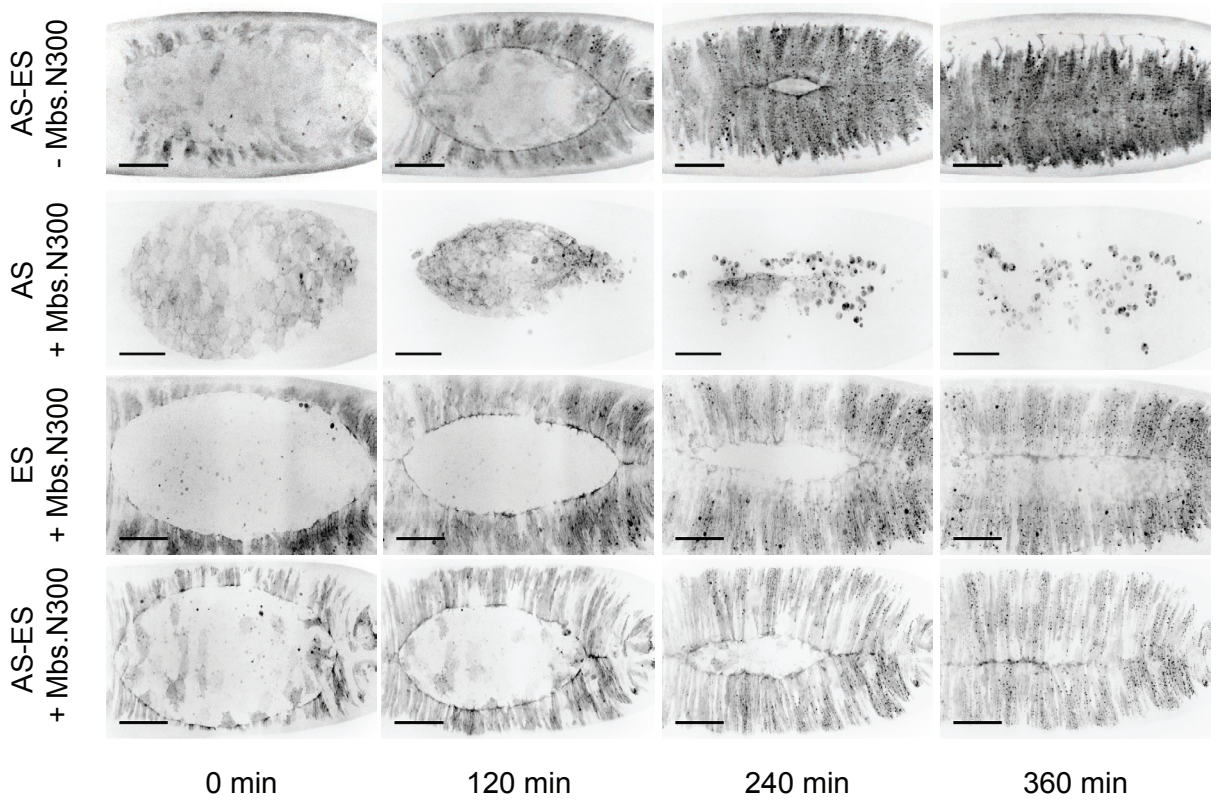

Figure 54. Over-expression of Mbs.N300 in AS and epidermis does not affect DC. Selected movie frames showing DC in control embryos (AS-ES-Mbs.N300) and embryos expressing constitutively active MyoII phosphatase in AS tissue (AS+Mbs.N300), epidermis (ES+Mbs.N300) and both tissues (AS-ES+Mbs.N300). mCherry-moesin labels F-actin. 0 min depicts the end of germ-band retraction. Scale bar: 50μm.

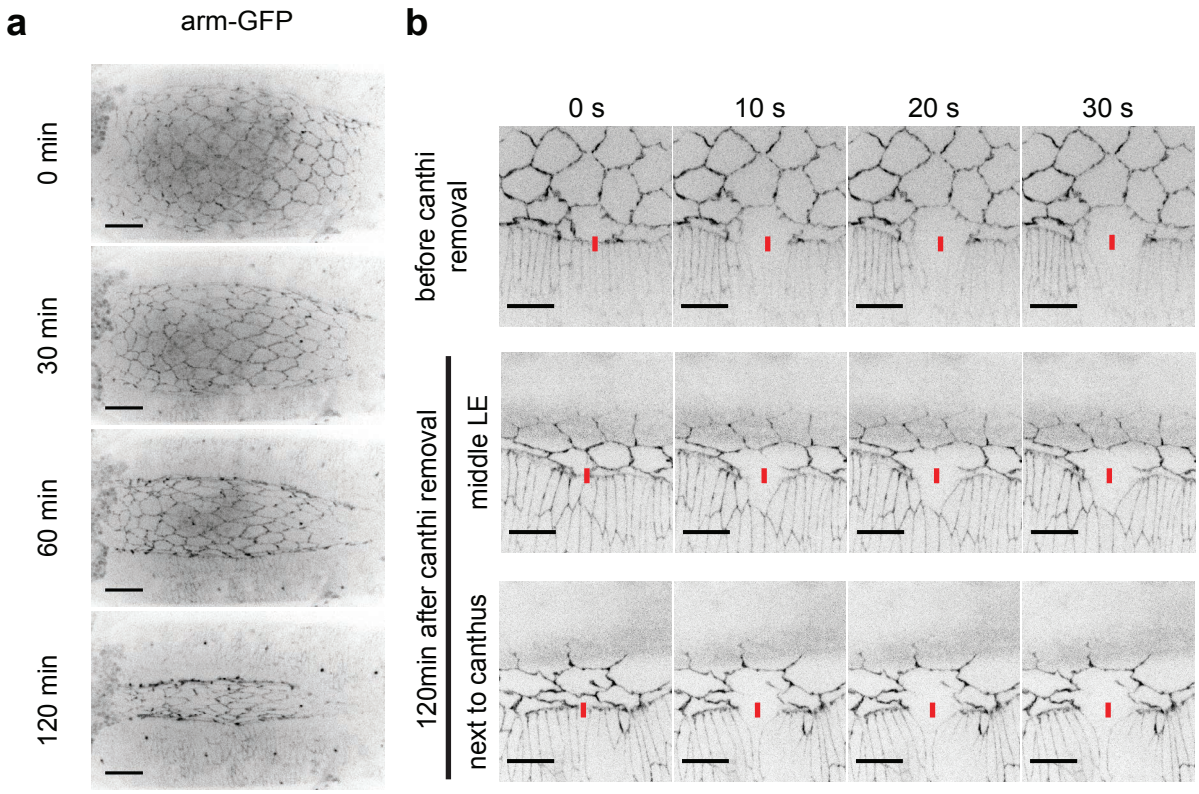

Figure 55. Canthi removal does not affect AMC tension. (a) Selected movie frames showing DC in embryos after the removal of both zipping canthi. Arm-GFP labels cell adherens junctions. Scale bar: 20µm. **(b)** LE recoil after laser-mediated AMC incision (red lines) in the embryos before and 120min after the canthi removal. Examples of laser incisions in the middle of LE and next to the ablated canthi is shown. Scale bar: 10µm.

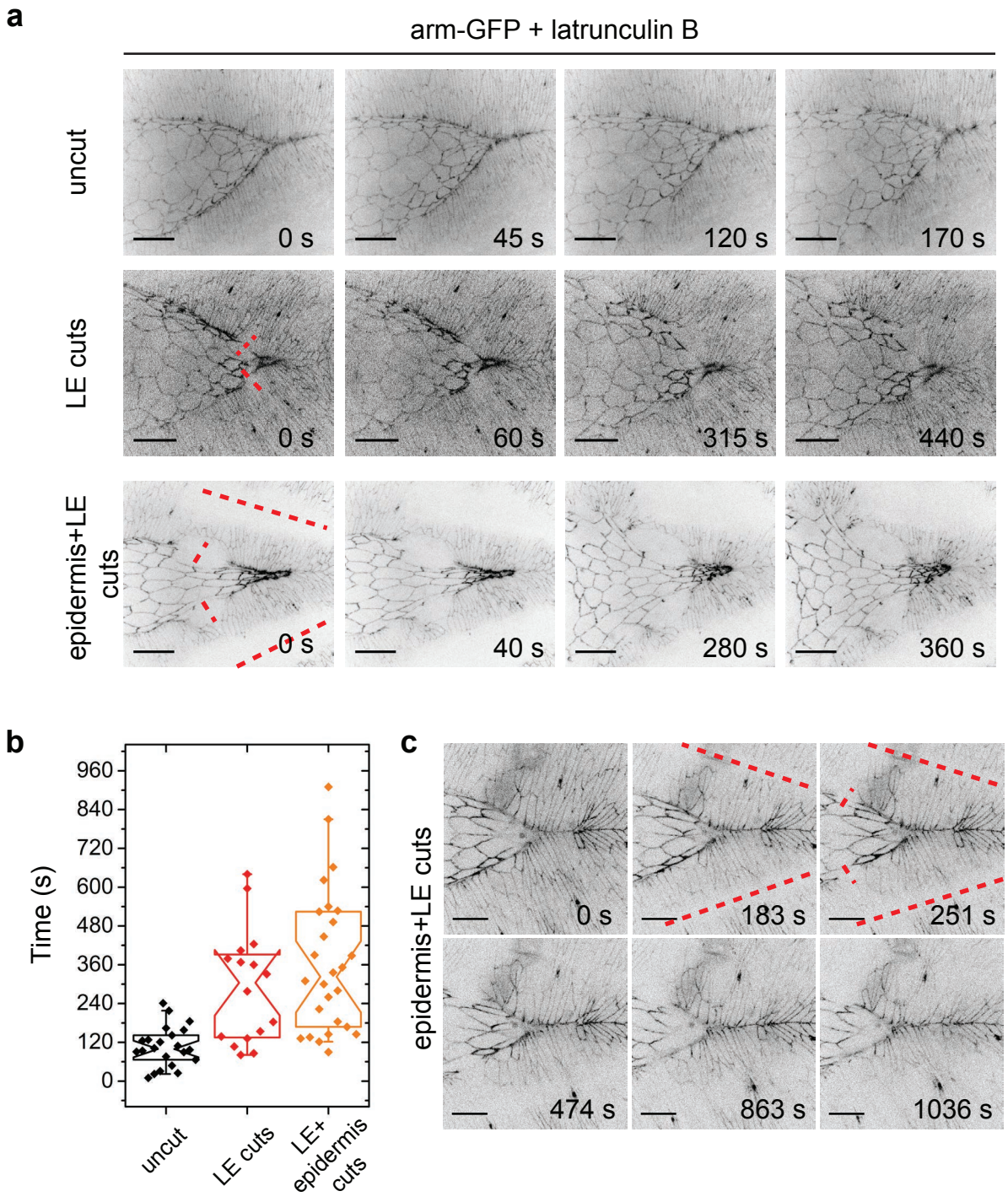

Figure 56. Reducing tension around the zipping canthus increases its resistance to LatB treatment. (a) Selected movie frames showing tissue response after LatB injection in control embryos (uncut) and embryos where LE was cut next to canthus (LE cuts) or canthus was isolated from the ventral epidermis (epidermis+LE cuts). First frame is selected after LatB injection; second frame is selected when the first ruptures appear in the tissues; third frame is selected before the canthus starts to rupture; last frame is selected when the canthus is completely ruptured. Red dashed lines indicate the laser ablations. Scale bar: 20µm. **(b)** Standard notched box plots depicting time when canthus ruptures after LatB injection in 3 embryo types described in (a). n=22 embryos for control, n=16 for LE cuts, n=26 for epidermis+LE cuts. **(c)** Selected movie frames showing canthus progression after isolating it from the tissue in embryos that were not injected with LatB (red lines). Scale bar: 20µm.

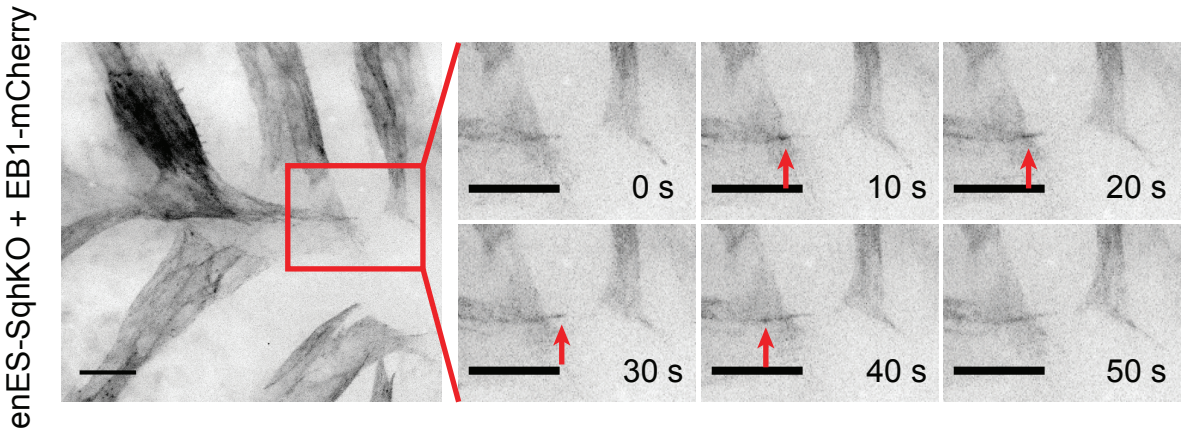

Figure 57. Microtubules in the epidermis are dynamic after the MyoII inactivation. Left: Image of the zipping canthus in the embryo, where EB1-mCherry is expressed and MyoII is inactivated in engrailed epidermis stripes (*en*ES-SqhKO). Right: Selected movie frames showing the dynamics of EB1-mCherry (red arrow) in the epidermis protrusion of *en*ES-SqhKO embryos.

Appendix 3. Omnium Gatherum

This appendix includes preliminary data and observations of various processes during *Drosophila* embryogenesis. Some of these observations might fit in the previous chapters, but they are also very interesting on their own.

A3.1. Basolateral ANBs and contractions in the first row of AS cells

We and other studies described AS cell surface contractions at the apical membrane in great detail[36,37,39,40]. Imaging AS cells with actin or MyoII reporters during the early-to-mid DC did not reveal any actin nucleation bursts (ANBs) or MyoII foci at the basal cell surface[38,39]. Studies focusing on apical AS cell surface revealed that cells next to LEs ingress and bend below the epidermis as DC progresses[95]. When imaging these peripheral AS cells towards the end of DC, we detected ANBs and MyoII foci at the basolateral cell surface (Fig. 58). These foci were able to transiently contract cell surfaces (Fig. 58). AS cells that were in the middle of the dorsal opening did not showed such basolateral pulses. Yet the resolution of the basal surface was greatly limited since the AS tissue was internalized to the interior of the embryo. So far the switch from apical to basolateral AS cell surface contractions was not studied and it would interesting to understand why such a switch happens. Is it a passive consequence of cell-autonomous ANB triggering or an actively controlled AM network re-modelling? One reason why basolateral AS surface contractions could be important is to provide pulling forces for the dorsal vessel primordium that lies below the epidermis. It was shown that dorsal vessel closure requires DC and connection to both epidermis and AS cells in order to fuse at the dorsal midline shortly after DC completes[210].

A3.2. Pulsatile activity of dorsal vessel primordium cells

In addition to peripheral AS cell basal surface contractions, we also observed that dorsal vessel primordium cells show pulsatile behaviour (Fig. 59A). When screening for epidermis-specific Gal4 enhancer elements, we noticed that one of them - *c1003*Gal4 - was expressed below the epidermis in the dorsal vessel primordium. When visualizing GFP-Zipper with *c1003*Gal4, we observed transient contractile foci in these cells. The observation is interesting in a sense that dorsal vessel of *Drosophila* pulsates after the fusion of primordium and towards the end of embryogenesis[232]. Recently, AM network regulator *cdc42* was found to be required for primordium fusion suggesting that AM dynamics is critical in the dorsal vessel fusion as well[232]. It would be interesting to know whether such pulsatile MyoII activity is entirely stochastic or is controlled and have a defined function in dorsal vessel tubulogenesis.

Besides actin, there are three other cytoskeletal components found in the cells: microtubules (MTs), intermediate filaments (IFs) and septins. MTs and IFs have been studied extensively for their essential role in cell division and vesicular transport (MTs) or cell adhesion and stress-transduction (IFs). Recently, it has been shown that septins form filamentous structures in the cytoplasm and are also involved in processes like cytokinesis or movements of cilia and flagella[233]se. As the importance of actin and MTs during DC is clear, we wanted to test whether septins play any role during the process. Thus, we imaged ubiquitously expressed Septin-2 tagged with GFP (Sep2-GFP) during the DC stage embryos. We detected Sep2-GFP signal mainly in the epidermis whereas AS cells showed barely detectable fluorescence (Fig. 59B). Surprisingly, below the epidermis, we noticed a pulsatile activity in what morphologically appeared to be dorsal vessel primordium cells (Fig. 59B). Since Sep2-GFP signal was very weak, to confirm this it necessary to over-express various septin components in these cells with the *c1003Ga4* enhancer element mentioned earlier. It could very fascinating if filamentous septin network would behave similarly to actin/MyoII network and exhibit pulsatile activities during the morphogenesis.

A3.3. Wave of apical constriction during the germ-band extension

Imaging Sqh-GFP from the syncytial stages onwards revealed an interesting behaviour of dorsal ectodermal cells. Around the time when germ-band (GB) convergence and extension occurs at the lateral side of the epidermis, dorsally GB moves and slides below the forming AS layer. Interestingly, such GB movement along the dorsal midline involved considerable MyoII accumulation at the apical cell surface of dorsal cells (Fig. 60). MyoII-mediated constriction of the cells induced bending of the tissue in front of the moving GB. The process resembled rolling or sliding of the two tissues with respect to each other. Similar rolling motion is observed in the involuting head of the *Drosophila* embryo[24,234]. Dorsal GB movement obviously involves various tissue interactions and mechanical forces in action, yet surprisingly it is not studied in great detail. Thus, it would be interesting to understand whether the observed apical constriction wave actively pulls the GB or, alternatively, GB pushes forward due to the ventral epidermis extension. What signals instruct dorsal ectodermal cells to constrict - is it tissue tension, morphogens or emerging AM network behaviour? The process is another striking example of spatio-temporally coordinated apical constriction during morphogenesis and could easily become an additional and novel model system.

A3.4. Sqh-GFP dynamics in unfertilized Drosophila eggs

Embryogenesis and development is at the pinnacle of creating a new organism. However, for this to happen the egg cell of the animal needs to be fertilized. Even though the egg cell is considerably different from a zygote and is primed for fertilization, it is, nevertheless, still a living cell. In the case of *Drosophila*, the egg is fertilized inside the female reproductive tract[235]. Yet the females still extrude the egg cell even if it is not fertilized. When collecting Sqh-GFP embryos and imaging them to study DC, we noticed that some of them did not develop through the syncytial nuclear stages. We assumed that such eggs were the unfertilized ones. Wild-type embryos complete 13 nuclear divisions before the cellularization of the blastoderm starts[24]. During the divisions Sqh-GFP signal accumulates outside the nuclei in the cytoplasm (Fig. 61)[222]. The unfertilized eggs did not undergo any of such divisions (Fig. 61). However, Sqh-GFP signal was still present in the cytoplasm creating waves and contractile flows in the entire egg cell (Fig. 61). Over time Sqh-GFP was localizing to an intricate network throughout the egg, but disappeared after several hours. It was reported that the unfertilized *Drosophila* egg can form a cytokinetic cleavage furrow if certain cyclins are injected externally[236]. Thus, the observed Sqh-GFP waves might prime the embryo for the cell or nuclear divisions. Alternatively, these are just an inevitable process leading towards the cell death.

A3.5. Electro-chemical intracellular connection between the two epidermis sheets

We have shown that AS tissue and epidermis form two electro-chemically separated tissues (Chapter 3, Fig. 19F-19G). If laser incision is performed in either tissue, transient Ca^{2+} wave does not spread into other one. Thus, we wanted to know whether the same happens between the two separate epidermal cell sheets after the zipping sealed them together. We performed laser incision in one of the two sheets during the zipping or shortly after it. Surprisingly, Ca^{2+} wave did not spread into the opposing epidermis sheet (Fig. 62). This shows that electro-chemical coupling between the two epidermis sides does not happen immediately after they form the adherens junctions between each other. Next, we tested when the two sheets become electrochemically coupled. Since the distance from the canthus along the dorsal midline reflects the time that has passed after the zipping, we cut at various distances along the dorsal midline. We observed that the two epidermal sheets became electro-chemically coupled at ~68±26µm (n=6 embryos) away from the canthus (Fig. 62). Such coupling reflects the establishment of gap junctions (GJs) between the two epidermal sheets. Whether such delayed intracellular connection has the underlying function is yet to be shown.

A3.6. Transient Ca^{2+} waves in the dorsal epidermis

Ca^{2+} was proposed to trigger and coordinate ANBs in AS cells during their apical surface contractions[114]. Using the most sensitive membrane-bound Ca^{2+} biosensor myr-GCaMP 5, we did not observe any intensity oscillations in AS cells (Chapter 3, Fig. 24E). However, while making laser incisions in the dorsal epidermis using this biosensor, we noticed that in some regions myr-GCaMP 5 intensities were fluctuating without any laser incisions. These transient fluctuations were often evident near the posterior spiracles and the involuting head. We did not observe any of these Ca^{2+} fluctuations in the epidermis during DC. However, we detected them in the whole dorsal epidermis after the DC was completed (Fig. 63). These fluctuations were transient and lasting only several seconds. Interestingly, they often spread via multiple cells in a wave-like fashion (Fig. 63). Nonetheless, we did not observe any obvious pattern or directionality of such waves.

Similar to dorsal epidermis, occasional transient intracellular Ca^{2+} spikes were already detected in the early stages of *Drosophila* embryos[117]. The authors used 3rd generation GCaMP biosensors, which have longer half-lives and, thus, are less sensitive to oscillating Ca^{2+} levels. As a result, no Ca^{2+} fluctuations in the dorsal epidermis was reported. By contrary, we used plasma membrane-bound GCaMP, which shows Ca^{2+} near the plasma membrane, i.e. as soon as Ca^{2+} enters the cell. Thus, it would be interesting to further investigate whether Ca^{2+} spikes that we observed are exclusively at the plasma membrane or spread through the whole cell volume. Few other questions can also be addressed – 1) Are Ca^{2+} waves cell-autonomous? 2) Why they appear after DC is completed, but not before? 3) Most importantly, what is the function of these Ca^{2+}waves?

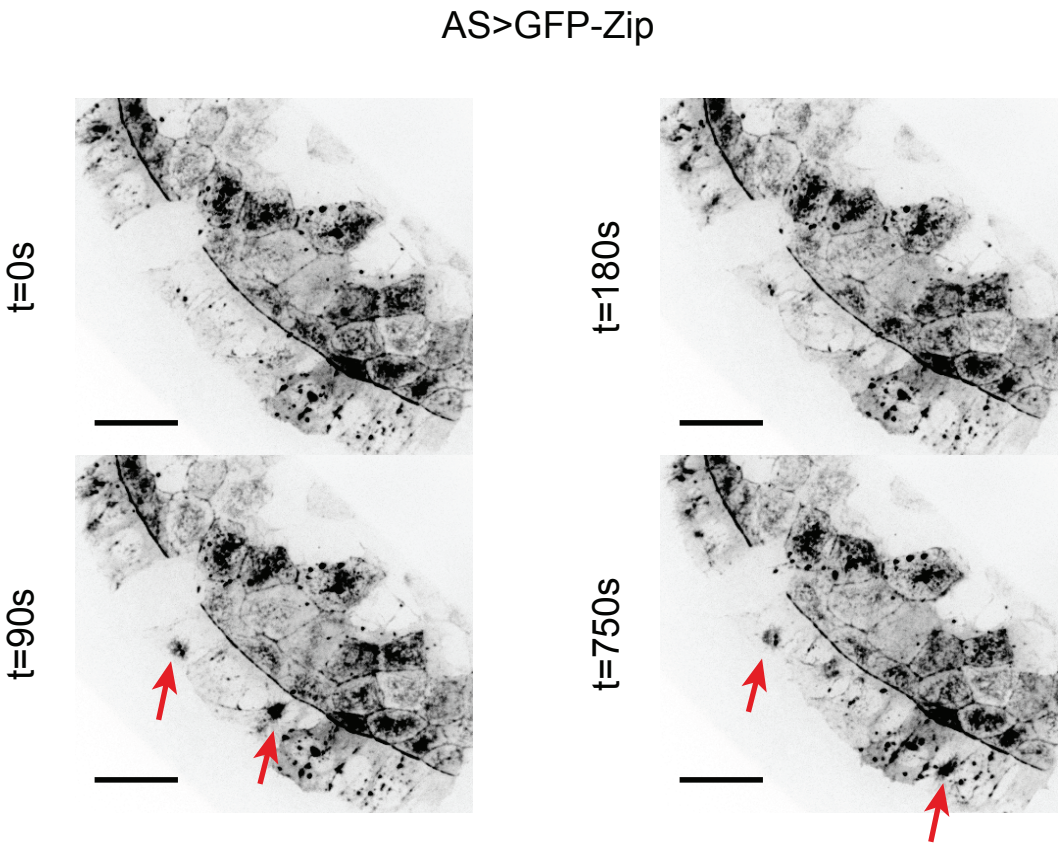

Figure 58. MyoII foci appears at the basolateral cell surface after AS cells are bent under the epidermis during DC. Selected movie frames showing AS cells expressing GFP-Zip during the DC. Zip foci are forming at the basolateral AS cell surface (red arrows). 0s depicts an arbitrary reference time-point. Scale bar: 20µm.

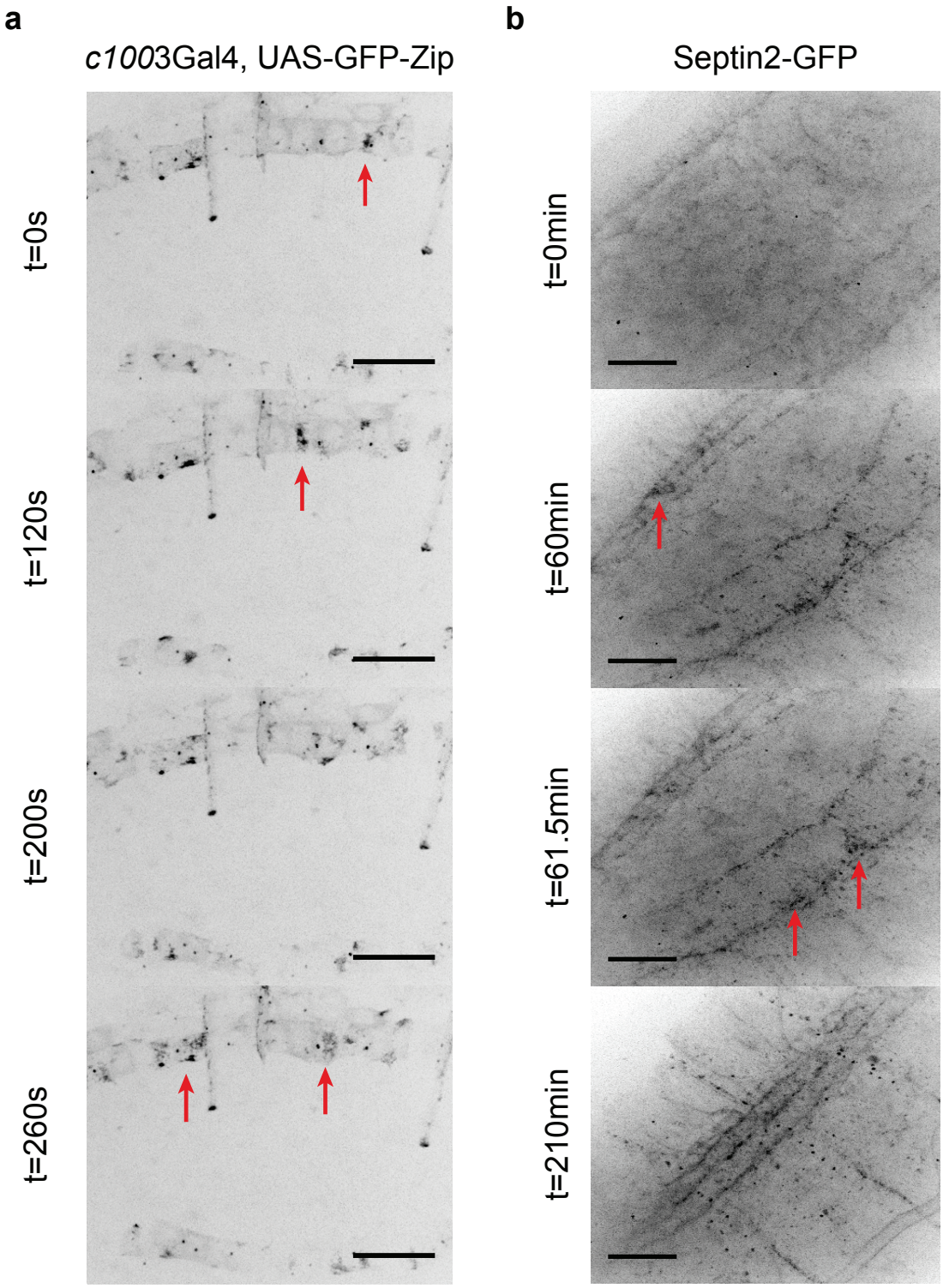

Figure 59. Dorsal vessel primordia undergo cycles of MyoII and septin coalescence. (a) Selected movie frames showing dorsal vessel primordia cells expressing GFP-Zip with *c1003*Gal4 enhancer element during DC stage. Transient Zip foci are forming in the primordia cells (red arrows). 0s depicts a random reference time-point. Scale bar: 20µm. **(b)** Selected movie frames showing Septin2-GFP embryos during DC stage. Transient Septin2 foci are forming in the dorsal vessel primordia cells (red arrows). 0min depicts an arbitrary reference time-point. Scale bar: 20µm.

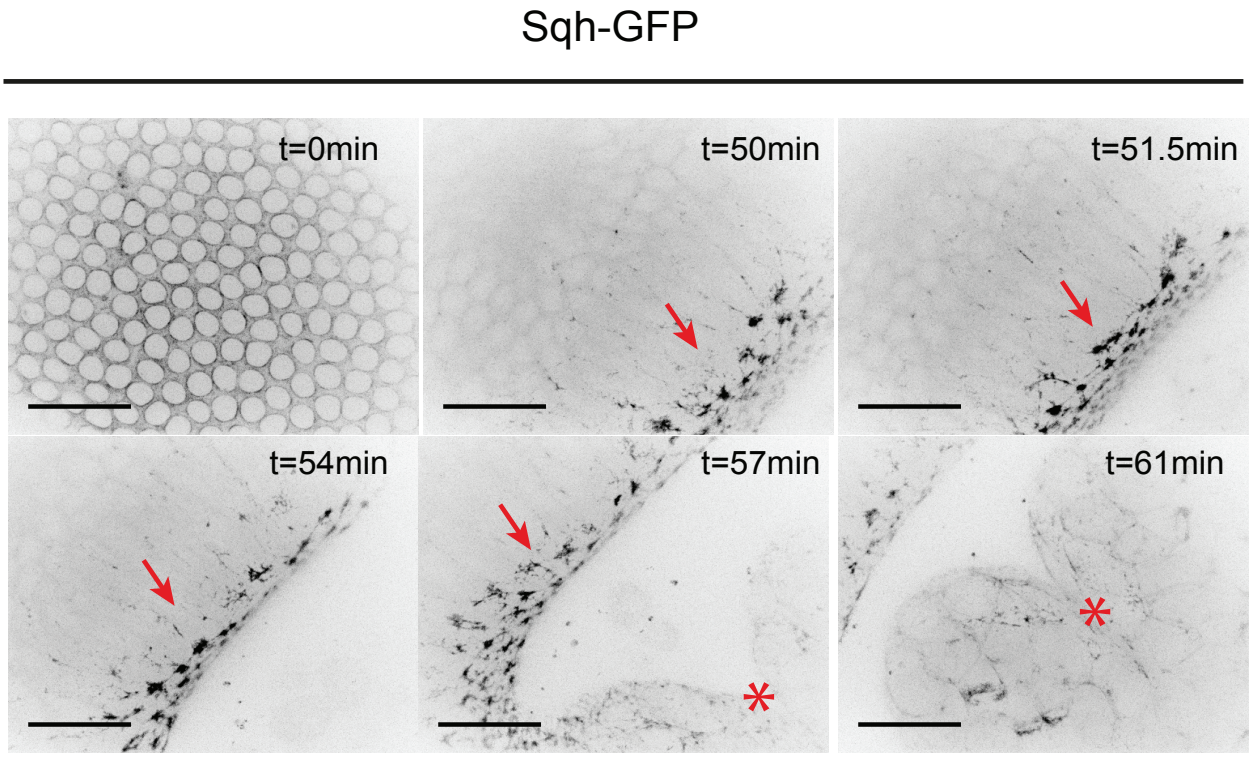

Figure 60. Germ-band extension is preceded by a wave of apical cell constriction along the dorsal midline of the embryo. Selected movie frames showing dorsal region of Sqh-GFP embryos from cellularization stage (Bownes stage 5) during germ-band extension (Bownes stage 8). Wave of apical Sqh-GFP accumulation and apical constriction (red arrows) precedes the extending germ-band (red star). 0min depicts cellularization of the embryo (Bownes stage 5). Scale bar: 20µm.

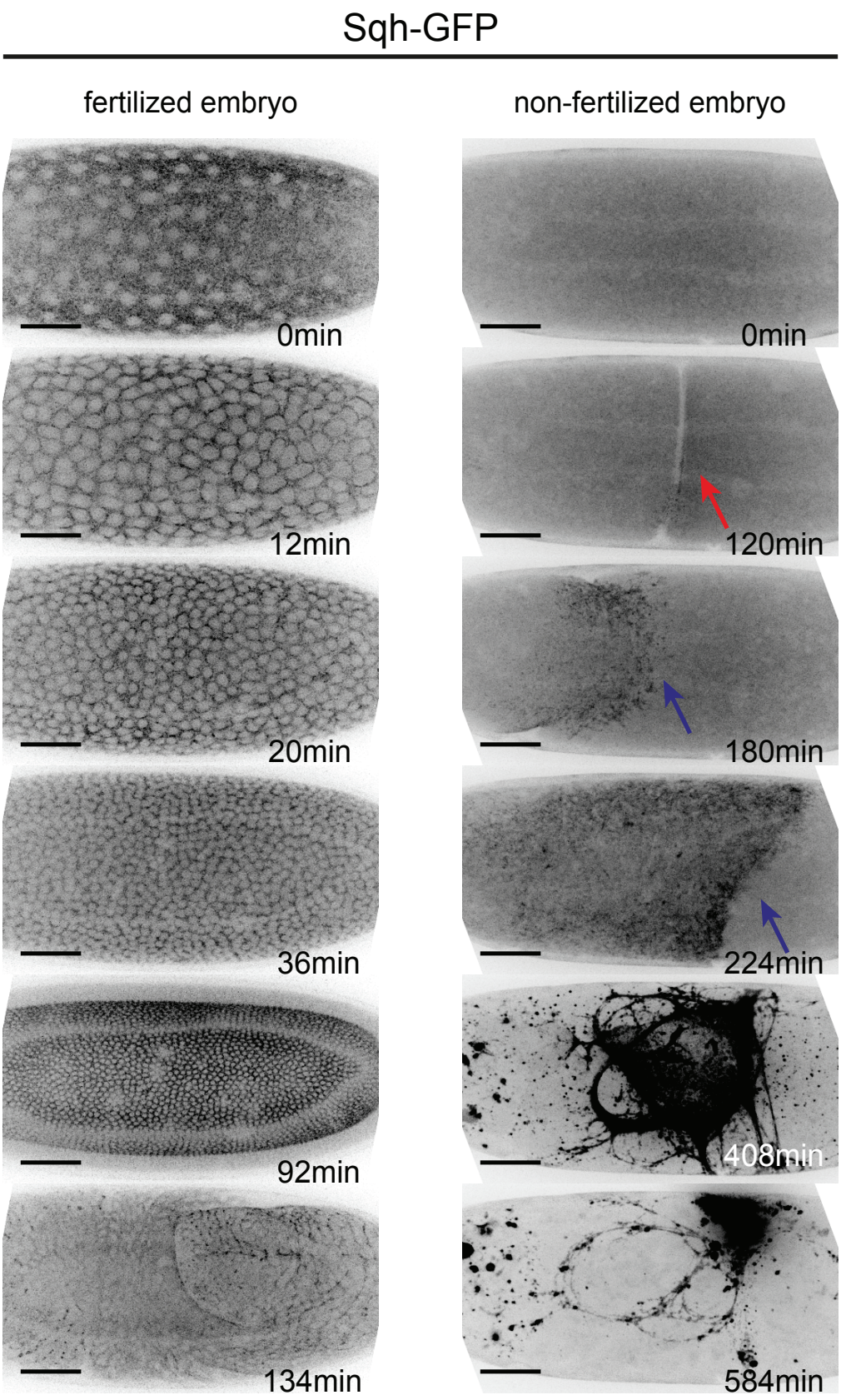

Figure 61. Unfertilized Drosophila eggs undergo dramatic MyoII-driven cell surface changes. Selected movie frames showing fertilized and not-fertilized Sqh-GFP embryos. Furrows on the egg surface (red arrows) and Sqh-GFP waves (blue arrows) are present in the unfertilized Drosophila egg. Left: 0min depicts a nuclear division cycle, 92min depicts cellularization; Right: 0min depicts an arbitrary reference point. Scale bar: 50µm.

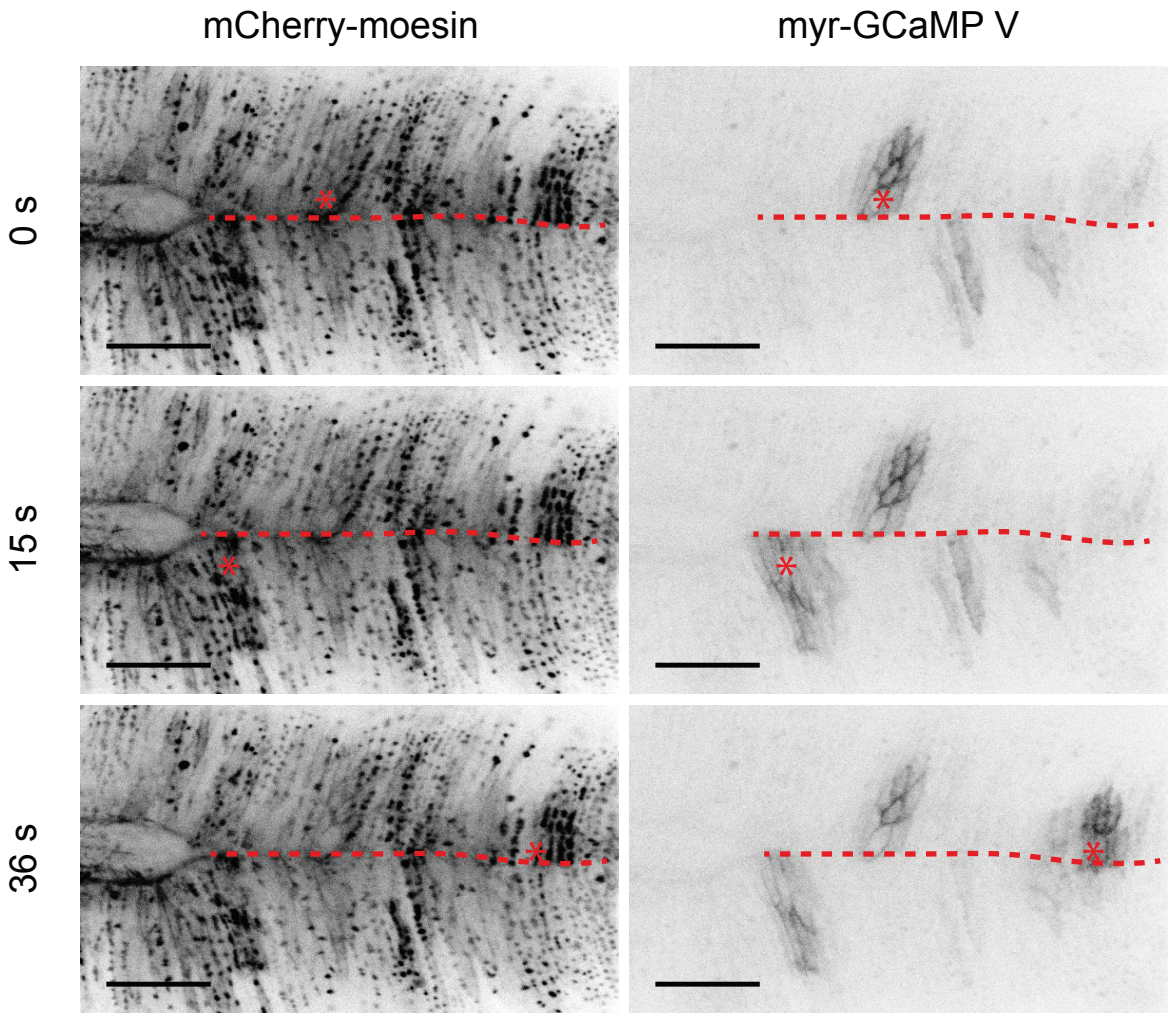

Figure 62. Cell sheets of dorsal epidermis are not coupled electro-chemically immediately after their sealing. Selected movie frames showing laser incisions (red stars) in next the sealing midline of the dorsal epidermis. Ca^{2+} wave induced after the incision does not spread into the opposing epidermal sheet. Time 0s depicts the first incision, 15s and 36s depict the subsequent incisions. mCherry-moesin labels F-actin, Ca^{2+} is monitored by membrane-tethered myr-GCaMP V biosensor. Red dashed line depicts the sealing midline of the epidermis. Scale bar: 20µm.

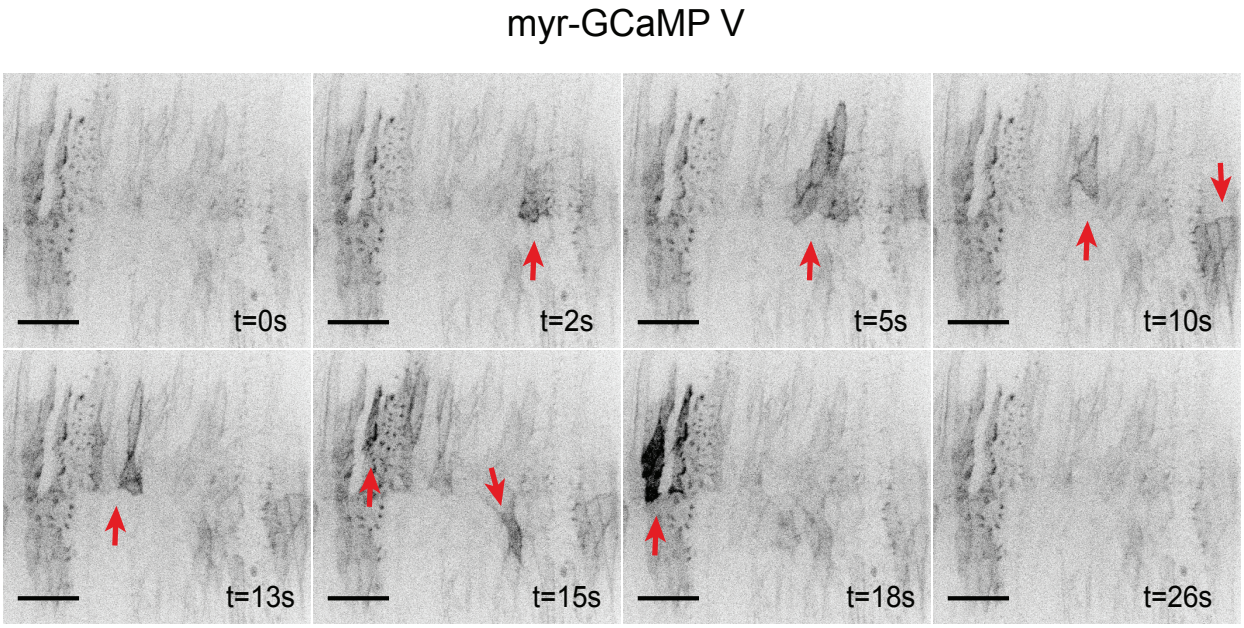

Figure 63. Transient Ca^{2+} waves spontaneously appear in the dorsal epidermis. Selected movie frames showing dorsal epidermis expressing membrane-tethered myr-GCaMP V Ca^{2+} biosensor. Spontaneous myr-GCaMP V intensity spikes appear that also move as waves and transverse multiple cells. 0s depicts an arbitrary reference time-point. Scale bar: 20µm..

Appendix 4. Publications

754 Cell 165, April 21, 2016 ©2016 Elsevier Inc. DOI http://dx.doi.org/10.1016/j.cell.2016.03.044

SnapShot: Mechanical Forces in Development I

Laurynas Pasakarnis, David Dreher, and Damian Brunner
Department of Molecular Life Sciences, University of Zurich, 8057 Zürich, Switzerland

Cell

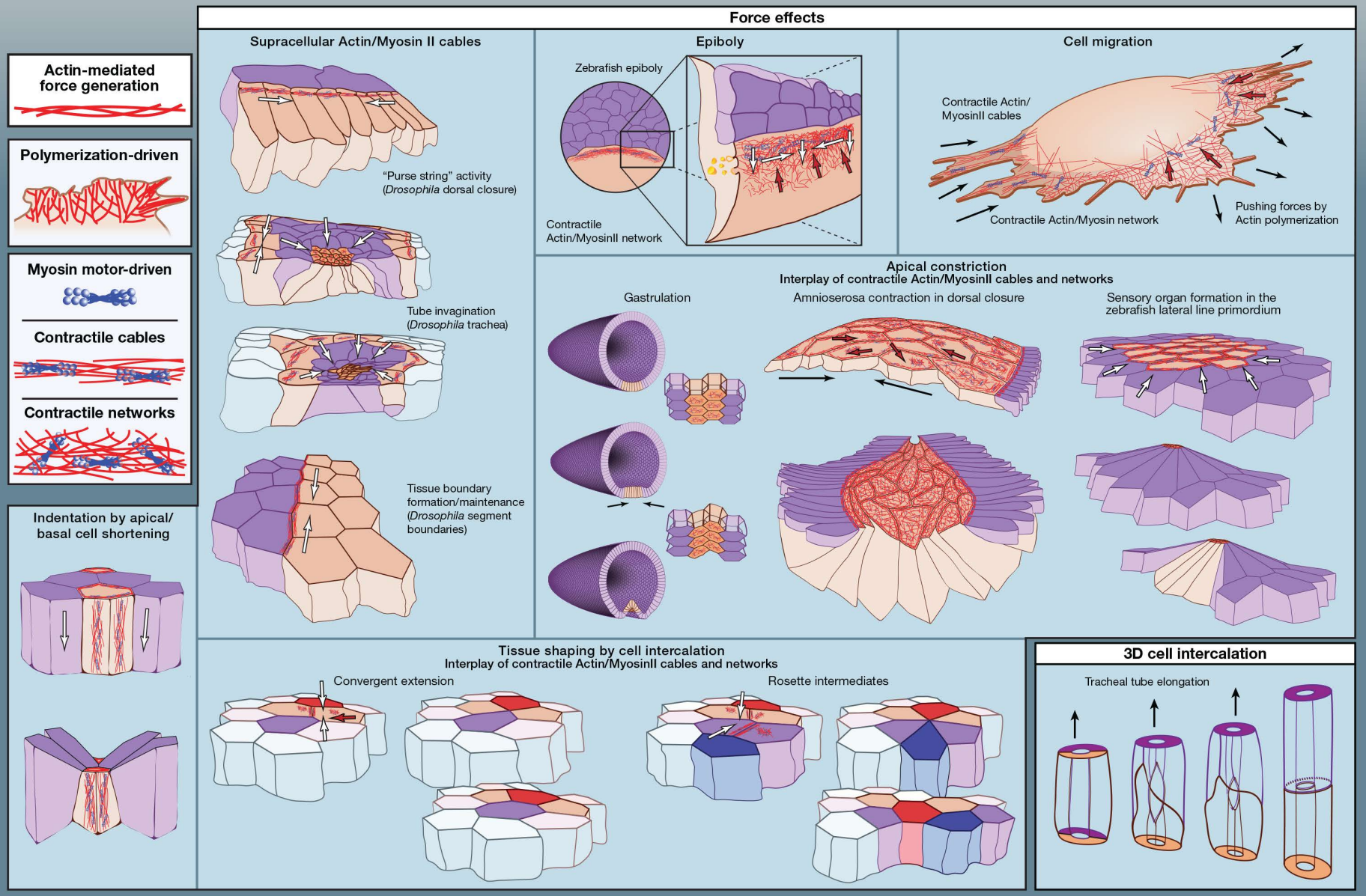

See online version for legend and references

SnapShot: Mechanical Forces in Development I

Laurynas Pasakarnis, David Dreher, and Damian Brunner
Department of Molecular Life Sciences, University of Zurich, 8057 Zürich, Switzerland

Cell-type-specific F-actin structures and myosin motors are key generators of the forces that drive tissue morphogenesis in developing organisms. These cytoskeletal elements mediate defined cell deformation and control the arrangement of cell-cell contacts. This SnapShot presents a selection of morphogenetic processes, the analysis of which has pioneered specific types of F-actin/myosin-mediated force generation in development.

Filamentous F-actin is the element most commonly used to generate the forces that propel the cell shape changes driving tissue morphogenesis. F-actin polymerization alone can produce pushing forces, but more commonly, F-actin provides a scaffold for myosin motors. F-actin/myosin cables produce anisotropic forces that mostly appear to be continuous, while contractile actin/myosin networks generate various forces that can be pulsatile. In many tissues, different force-producing systems act in combination. There remains a major gap in understanding force production at the intersection between the signaling pathways controlling cell fate and the cytoskeleton-associated factors controlling F-actin nucleation and dynamics or myosin activity. This link controls key parameters of cell-type-specific force generation, in particular the exact sub-cellular positioning of F-actin cables and networks, the local control of F-actin dynamics, and localized Myosin activation. Commonly, Rho family GTPases and Rock kinase are involved. Examples of force actions are illustrated. F-actin, red; myosin, blue. Black and white arrows depict force vectors and red arrows actin flows.

Supracellular Actin/Myosin II Cables

During dorsal closure in *Drosophila* embryos, all cells lining the front of an epidermal opening form a tensioned actin/myosin II cable spanning their dorsal, apical edge. Special adhesion structures connect individual cables to generate a supracellular cable all around the opening that is proposed to produce forces acting comparable to a purse-string. The purse-string combines with apical amnioserosa cell constriction. Similar supracellular cables form around small epithelial wounds. Developing tubular structures such as *Drosophila* trachea and salivary glands originate from epithelial invaginations. Thereby, supracellular tensioned actin/myosin II cables form in the surrounding tissue to support apical constriction of groups of cells. The cables generate forces impinging on the invaginating cells and may provide resistance forces preventing invagination of surrounding cells. Actin/myosin II cables maintain tissue boundaries, previously established by signaling networks. Cables enrich at the cell-cell contacts lining the boundary. This produces a line with increased tension as compared to the environment, thereby forming a physical barrier that prevents cells from mingling.

Epiboly

During epiboly, the embryonic blastoderm tissue expands to engulf the large yolk cell. A band of actin/myosin II forming ahead of the blastoderm in the yolk syncytium provides two critical forces. Within the ring, a retrograde flow of actin/myosin II produces traction forces pulling on the tissue front. This mechanism dominates during early epiboly. In addition, the band produces a contractile force that becomes dominant after the blastoderm has passed the yolk cell equator. Surface tension produced by endocytosis of yolk cell membrane is proposed to contribute to the net pulling force.

Cell Migration

Cell migration combines pushing forces generating cell protrusions at the leading front and contractile forces that retract the rear. Cell fronts are pushed forward by a myosin-II-supported, F-actin nucleation front that is balanced by shear stress induced through substrate adhesion. Contractile actin/myosin II bundles move the main cell body and retract the rear of the cell. Cells migrate individually or in dynamic collectives. Neuronal growth cones use similar forces to move forward.

Indentation by Apical/Basal Shortening

Cells produce an actin/myosin II cable structure that pulls the apical cell surface basally, thereby pulling neighboring cell surfaces along. In addition, the cells constrict their apical surfaces (see below) and eventually delaminate and undergo apoptosis, leaving a tissue indent. In this way, rows of cells form furrows separating leg segments in *Drosophila* leg development. Whether other morphogenesis processes involving apoptotic cell delamination (e.g., amnioserosa tissue contraction in *Drosophila* dorsal closure) use such active apical/basal cell shortening remains to be shown.

Apical Constriction

Constriction of the apical cell surface is a very common mechanism driving tissue morphogenesis. The classical example is *Drosophila* gastrulation, where anisotropic apical constriction of a defined subset of ventral blastoderm cells initiates tissue invagination. Another example is dorsal closure, where the cells of the amnioserosa tissue fill an epidermal opening and constrict to bring the surrounding epidermis cells in sufficient proximity for tissue sealing. Both systems generate a tissue indentation and involve pulsed F-actin nucleation bursts at the apical cell membranes, which can propagate as waves across cell surfaces. The F-actin network, and with it the cell surface, contracts by recruiting myosin II, thereby pulling on neighboring cells. Contractions are stabilized by a general, apical F-actin/myosin II enrichment and may mediate reorganization of a peripheral F-actin/myosin II ring below cell adherens junctions that acts as a clutch preventing relaxation. In gastrulation, relaxation after a contraction is negligible, while amnioserosa cell surface areas fluctuate considerably. It is possible that the latter system uses the supracellular epidermal actin/myosin II cable as external clutch mechanism. In the zebrafish lateral line, primordium sensory organs are singled out starting with their apical constriction. In contrast to other apical constriction events that lead to tissue indentation, this generates cell rosettes, which protrude out of the tissue.

Tissue Shaping by Cell Intercalation

Cell intercalation describes a rearrangement of cell-cell boundaries, driven by actin/myosin II cables lining adherens junctions. Cables are particularly strong at certain boundaries, which leads to their shortening. In *Drosophila* germband extension, local bursts of contractile actin/myosin II networks contribute to boundary shortening. Eventually, such boundaries collapse and a new, roughly perpendicular boundary forms between two previously separated cells. If more than four cells are involved, they form an intermediate rosette structure. Intercalation results in tissue elongation along one axis and a corresponding shortening perpendicular to it. It is one of the mechanisms driving convergent extension of tissues.

3D Cell Intercalation

In tubular epithelia cell-cell contact, re-arrangements occur in 3D. In developing *Drosophila* trachea, adherens junction remodeling provides tube elongation. Individual cells reach around the lumen and establish contacts with themselves. These autocellular junctions zip up along the tube length. In tracheal development, the migrating tip cell of a growing tracheal branch mediates junction remodeling by producing a pulling force that stretches the cells attached to its back. Whether cell-autonomous forces contribute is not known.

REFERENCES

Affolter, M., Zeller, R., and Caussinus, E. (2009). Nat. Rev. Mol. Cell Biol. *10*, 831–842.

Blanchoin, L., Boujemaa-Paterski, R., Sykes, C., and Plastino, J. (2014). Physiol. Rev. *94*, 235–263.

Bruce, A.E.E. (2016). Dev. Dyn. *245*, 244–258.

Dahmann, C., Oates, A.C., and Brand, M. (2011). Nat. Rev. Genet. *12*, 43–55.

Ernst, S., Liu, K., Agarwala, S., Moratscheck, N., Avci, M.E., Dalle Nogare, D., Chitnis, A.B., Ronneberger, O., and Lecaudey, V. (2012). Development *139*, 4571–4581.

Heisenberg, C.-P., and Bellaïche, Y. (2013). Cell *153*, 948–962.

Michelot, A., and Drubin, D.G. (2011). Curr. Biol. *21*, R560–R569.

Monier, B., Gettings, M., Gay, G., Mangeat, T., Schott, S., Guarner, A., and Suzanne, M. (2015). Nature *518*, 245–248.

Röper, K. (2013). BioArchitecture *3*, 45–49.

Walck-Shannon, E., and Hardin, J. (2014). Nat. Rev. Mol. Cell Biol. *15*, 34–48.

  DOI http://dx.doi.org/10.1016/j.cell.2016.03.044

1028 Cell 165, May 5, 2016 ©2016 Elsevier Inc. DOI http://dx.doi.org/10.1016/j.cell.2016.04.060

SnapShot: Mechanical Forces in Development II

David Dreher, Laurynas Pasakarnis, and Damian Brunner
Department of Molecular Life Sciences, University of Zurich, 8057 Zürich, Switzerland

Cell

Microtubule/motor-mediated forces

Microtubule pulling by cortical Dynein

Asymmetric spindle positioning
(*C. elegans* embryo)

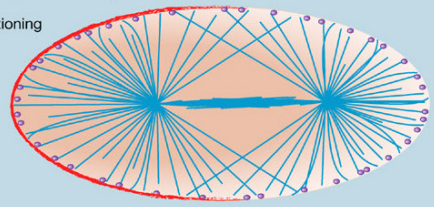

Tissue zipping force
(*Drosophila* dorsal closure)

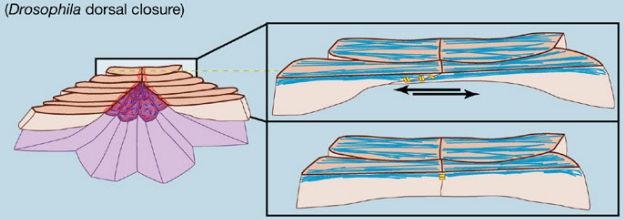

Cilia-driven flows

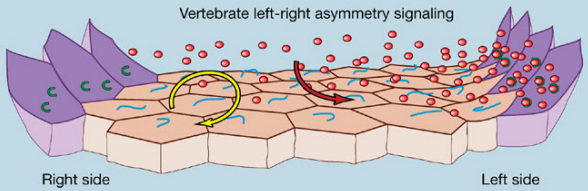

Growth/division-mediated forces

Differential growth rates

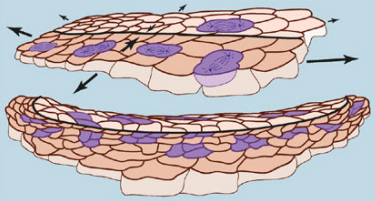

Oriented cell division

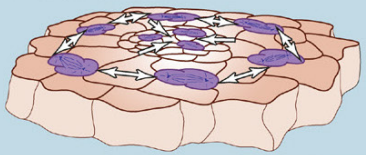

Cell surface tension

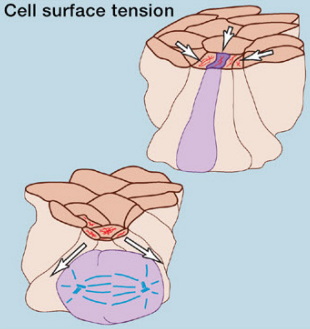

Cell wall (extracellular matrix) modeling

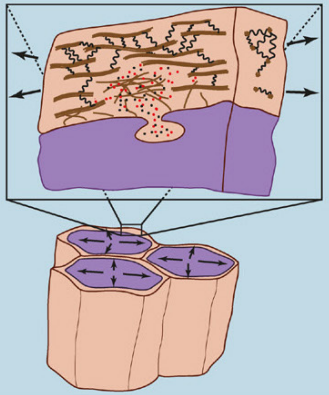

Hydrostatic forces

Hydrostatic pressure

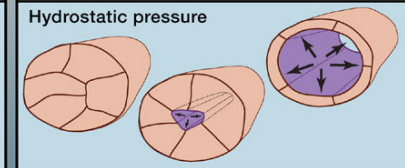

Cell volume reduction by fluid loss

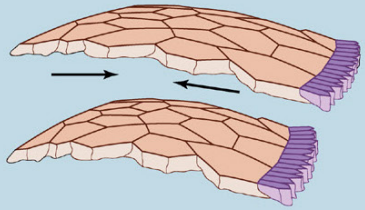

Cell adhesion as force transmission element

Cell to cell/matrix to cell force transmission

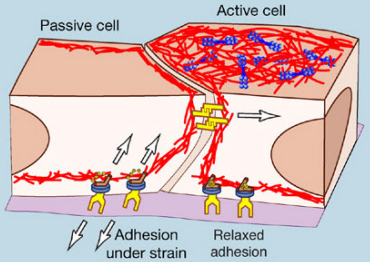

Cell to matrix force transmission

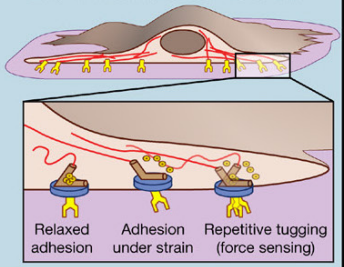

Force analysis tools

Molecular tools

FRET-based
tension sensors

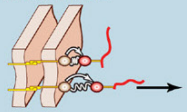

Image analysis-based tools

Cell deformation estimation
(aspect ratio)
Force reporter intensity
(Fluorescent MyoII)
Deformation of
incorporated droplets
Force estimation
(boundary angle and curvature)

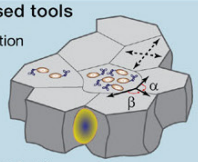

Substrate-based analysis

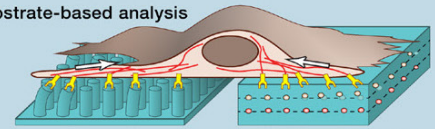

Manipulating tools

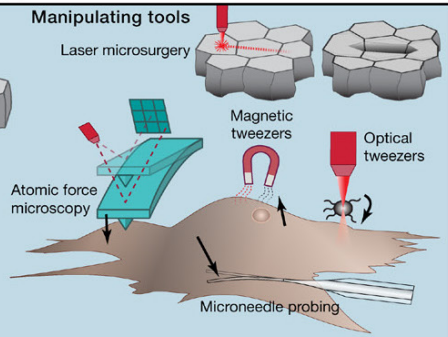

Mechanosensing in development

Pulsed cell surface contraction with mechanically gated ion channels

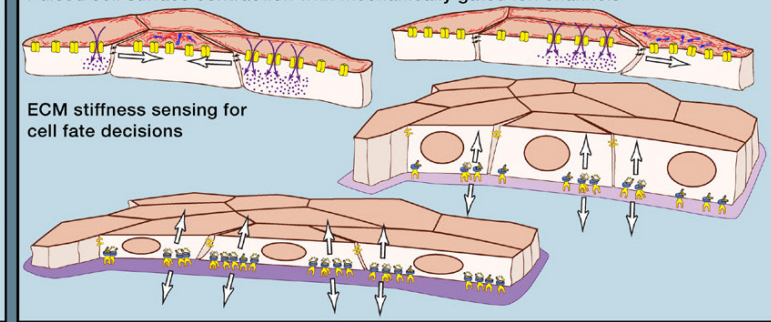

ECM stiffness sensing for cell fate decisions

See online version for legend and references

SnapShot: Mechanical Forces in Development II

David Dreher, Laurynas Pasakarnis, and Damian Brunner
Department of Molecular Life Sciences, University of Zurich, 8057 Zürich, Switzerland

The forces shaping an organism are not exclusively produced by actin/myosin II networks. In part II of this SnapShot, we present various alternative mechanisms. In addition to driving morphogenesis, cells use mechanical forces to sense and react to the specific mechanical properties of their environment. Also, we present a selection of experimental tools commonly used in force analysis.

Microtubule Pulling by Cortical Dynein

Asymmetric cell division such as the first division of the *C. elegans* embryo generates a larger anterior (left) and a smaller posterior (right) cell containing differing determinants. A crucial step in the process is asymmetric spindle positioning by cortically anchored dynein motors (purple) that pull on microtubule (blue) plus ends. Controlled by cell polarity cues, there is more dynein activity at the posterior than at the anterior pole, resulting in net posterior displacement of the spindle and consequently of cytokinesis.

Zipping, the final tissue sealing in *Drosophila* dorsal closure, involves the formation of a single, lamellar membrane overlap surface by contacting cells. Overlap shortening pulls the sealing tissue fronts together. Evidence suggests that this involves membrane-anchored dynein pulling on microtubule plus ends at the new cell contact sites (yellow).

In vertebrates, dynein activity and microtubules in the cilia of nodal plate cells establish left/right asymmetry. The directionality of cilia motion (yellow arrow) generates a flow (red arrow) that moves determinants toward the future left.

Growth/Division-Mediated Forces

Regional differences in growth rates induce mechanical stress in tissues. If the tissue is constrained within stiff limits, growing cell monolayers can buckle and fold. In plant morphogenesis, two main forces act together: cell hydrostatic turgor pressure stretches the cell wall and increases its porosity, while newly synthesized and cross-linked cell wall constituents integrate into the matrix and push other components to orient in parallel to the cellulose microfibrils. In rapidly growing tissues such as the *Arabidopsis* shoot meristem and *Drosophila* wing imaginal discs, cells growing in the tissue center create compacting, isotropic pressure, while peripheral cell growth generates circumferential tension and tangential tissue expansion. To generate such inhomogeneity, polarity cues orient peripheral cell divisions (planar cell polarity pathway in *Drosophila*, and oriented, microtubule-mediated deposition of cell wall remodeling enzymes in shoot meristems). This triggers a positive feedback loop in which oriented tension maintains oriented divisions.

In mitosis, cells usually adopt a spherical shape, which increases their surface tension and osmotic pressure. During *Drosophila* tracheal placode invagination, mitotic cell rounding accelerates tissue folding.

Hydrostatic Forces

Secretion of inherently incompressible fluids into a luminal space generates substantial hydrostatic pressure that drives lumen formation of many tubular structures. Subsequent fluid flow contributes to lumen opening.

Fluid loss, triggered by the activation of the apoptotic pathway at the onset of *Drosophila* dorsal closure, causes volume reduction of amnioserosa cells, which contributes to subsequent, actin/myosin II-mediated tissue contraction.

Adhesion

In development, adhesion elements (yellow) bi-directionally transduce forces between cells and their environment. Key players are cadherins in the adherens junctions that interconnect cells and integrins that connect cells with extracellular matrix (exemplified as basal lamina in purple). Inside cells, these molecules connect to the cytoskeleton. Adhesion sites mediate input from active environments such as neighboring cells and tissues that move, contract, or expand, as well as (resistance) forces from the comparatively passive environment formed by extracellular matrix. Inversely, cells use the same adhesion sites in combination with actin/myosin II networks to exert force on their environment, thereby deforming it, moving over it, or probing its stiffness.

Mechanosensing in Development

Mechanosensing can be passive or active. Cells sense and react to forces imposed by neighbors based on changes in membrane curvature, shearing of the underlying actin cortex, or opening of mechanically gated ion channels. The latter may propagate pulsed cell contractions within the amnioserosa tissue during *Drosophila* dorsal closure. In this scenario, the contraction of one cell pulls open mechanically gated ion channels in the neighboring cells, which triggers them to contract in turn. Inversely, actively probing the stiffness of the environment contributes to cell fate commitment. A stiff extracellular matrix causes cell spreading by promoting integrin-mediated adhesion. As a result, cells flatten and their nuclei deform, which in turn affects lamina composition and gene expression.

Force Analysis Tools

Forces are generally measured indirectly via their effects. Molecular approaches include functionalized molecules or particles, which change behavior when experiencing forces. This includes quantum dots, mechanophores, and FRET sensors; for instance, a cadherin-based FRET sensor reacts to forces applied by neighboring cells by revealing changes in distance between cell adhesion sites and cortical actin.

Image-analysis-based tools qualitatively deduct forces from time-lapse image series. Simple proxies for forces in tissues are changes in cellular aspect ratios or in fluorescence intensities of tagged force producers (e.g., myosin II). More intricate approaches consider properties such as the curvature of cell boundaries. A recent approach involves deformation measurement of lipid droplets introduced into the tissue.

Substrate-based analysis characterizes cell to extracellular matrix interactions by measuring substrate deformation. Traction force microscopy follows the displacement of fluorophores embedded in the substrate to which cells adhere (mostly synthetic) to infer force fields with standard microscopy. The substrate can be designed by printing defined 3D shapes such as pillars or microposts, the deformation of which is then measured.

External interference tools exert force or disrupt the sample. A frequently used technique is to ablate cell connections, individual cells, or tissue domains with a laser beam. Forces are inferred from recoil velocities of surrounding landmarks or the dimension of the wound area.

External forces are applied in various ways. In atomic force microscopy, the cantilever is transiently pressed onto cells. The reflection angle change of a laser beam measures cantilever deformation, from which the acting forces are computed. Magnetic tweezers generate a magnetic field, which applies force to a magnetic bead inside, or attached to cells. The force acting on the bead can be inferred from its velocity and the known magnetic force. Optical tweezers work similarly, but forces come from the refractive mismatch of the dielectric bead material or certain cellular structures with differing refractive index (e.g., lipid droplets). Pushing microneedles against a biological sample and measuring needle deformation via bright field microscopy similarly allow deducing forces. Cantilever tips and bead or needle surfaces can be functionalized. More macroscale approaches apply forces on organs or organisms in various ways (e.g., compression between microscopic slides, poking with needles, and sample suction).

REFERENCES

Chanet, S., and Martin, A.C. (2014). Prog. Mol. Biol. Transl. Sci. *126*, 317–352.

Cosgrove, D.J. (2005). Nat. Rev. Mol. Cell Biol. *6*, 850–861.

Eltsov, M., Dubé, N., Yu, Z., Pasakarnis, L., Haselmann-Weiss, U., Brunner, D., and Frangakis, A.S. (2015). Nat. Cell Biol. *17*, 605–614.

Ivanovska, I.L., Shin, J.-W., Swift, J., and Discher, D.E. (2015). Trends Cell Biol. *25*, 523–532.

Kondo, T., and Hayashi, S. (2013). Nature *494*, 125–129.

Kotak, S., and Gönczy, P. (2013). Curr. Opin. Cell Biol. *25*, 741–748.

LeGoff, L., and Lecuit, T. (2015). Cold Spring Harb. Perspect. Biol. *8*, a019232.

Navis, A., and Bagnat, M. (2015). Curr. Opin. Genet. Dev. *32*, 24–30.

Saias, L., Swoger, J., D'Angelo, A., Hayes, P., Colombelli, J., Sharpe, J., Salbreux, G., and Solon, J. (2015). Dev. Cell *33*, 611–621.

Sirbuly, D.J., Friddle, R.W., Villanueva, J., and Huang, Q. (2015). Rep. Prog. Phys. *78*, 024101.

  DOI http://dx.doi.org/10.1016/j.cell.2016.04.060

nature cell biology

Quantitative analysis of cytoskeletal reorganization during epithelial tissue sealing by large-volume electron tomography

Mikhail Eltsov[1,2,3], Nadia Dubé[2,4,5], Zhou Yu[1], Laurynas Pasakarnis[4], Uta Haselmann-Weiss[3], Damian Brunner[2,4,6] and Achilleas S. Frangakis[1,6]

The closure of epidermal openings is an essential biological process that causes major developmental problems such as spina bifida in humans if it goes awry. At present, the mechanism of closure remains elusive. Therefore, we reconstructed a model closure event, dorsal closure in fly embryos, by large-volume correlative electron tomography. We present a comprehensive, quantitative analysis of the cytoskeletal reorganization, enabling separated epidermal cells to seal the epithelium. After establishing contact through actin-driven exploratory filopodia, cells use a single lamella to generate 'roof tile'-like overlaps. These shorten to produce the force, 'zipping' the tissue closed. The shortening overlaps lack detectable actin filament ensembles but are crowded with microtubules. Cortical accumulation of shrinking microtubule ends suggests a force generation mechanism in which cortical motors pull on microtubule ends as for mitotic spindle positioning. In addition, microtubules orient filopodia and lamellae before zipping. Our 4D electron microscopy picture describes an entire developmental process and provides fundamental insight into epidermal closure.

The closure of tissue gaps is an essential process in wound healing and the development of multicellular organisms. In humans, closure defects result in spina bifida and cleft lips or palates. Similarly, persisting tissue gaps and lethality result from inaccurate dorsal closure (DC) in the fruit fly *Drosophila melanogaster*. The process provides a powerful model system for studying molecular mechanisms and forces driving epithelial tissue closure and sealing[1]. During DC, a large opening in the embryonic dorsal epidermis closes. The amnioserosa (AS) cells that fill the opening drive the initial dorsalward convergence of the two laterally positioned epidermis fronts. Therefore, they generate pulsed contraction forces that pull the surrounding epidermis dorsally[2]. A gradual decrease of the apical cell surfaces coincides with the reduction of the overall tissue surface[3,4]. Simultaneously, the dorsalmost row of epidermis cells, which forms the leading edge (LE) framing the opening, produces a complementary force by placing a contractile actin/myosin II (MyoII) cable at their dorsal–apical front in response to Jun N-terminal kinase activation[5–7]. The sum of these cables produces a line of tension that surrounds the entire opening[8].

Whereas force generation by AS and LE cells has been intensively studied, the mechanisms of 'zipping', the final tissue sealing, remain elusive. This is largely due to insufficient imaging resolution, which prevented the exact description of the multiple cellular tasks occurring in a very small region during a short time period. Zipping starts at the anterior and posterior canthi of the eye-shaped opening. The two zipping fronts sweep towards each other, eventually meeting and completing closure[9]. During zipping, opposing LE cells with identical positional identity recognize each other and build up adhesion sites. They are believed to progress zipping by pulling on each other, which brings the next neighbours closer together and pushes the AS tissue down inside the embryo. For zipping, LE cells form dynamic, actin-based lamellipodia and filopodia at the dorsal–apical surface[9]. These scan the space above the AS tissue in search for the matching cell from the opposite side. Traditional electron microscopy imaging had suggested that during zipping these protrusions form a complex and strongly intertwined interaction surface. Actin-mediated protrusion shortening was hypothesized to generate the zipping force, reshaping this surface into normal epithelial cell–cell contacts[9–11]. LE cells also reorganize

[1]Goethe University Frankfurt, Buchmann Institute for Molecular Life Sciences and Institute for Biophysics, Max-von-Laue Str. 15, 60438 Frankfurt am Main, Germany. [2]Cell Biology and Biophysics Unit, European Molecular Biology Laboratory, Meyerhofstr. 1, 69117 Heidelberg, Germany. [3]Electron Microscopy Core Facility, European Molecular Biology Laboratory, Meyerhofstr. 1, 69117 Heidelberg, Germany. [4]University of Zurich, Institute of Molecular Life Sciences, Winterthurerstr. 190, 8057 Zurich, Switzerland. [5]Institut de recherches cliniques de Montréal (IRCM), 110 avenue des Pins Ouest, Montréal (Québec), H2W 1R7, Canada.
[6]Correspondence should be addressed to D.B. or A.S.F. (e-mail: damian.brunner@imls.uzh.ch or achilleas.frangakis@biophysik.org)

Received 12 March 2014; accepted 13 March 2015; published online 20 April 2015; DOI: 10.1038/ncb3159

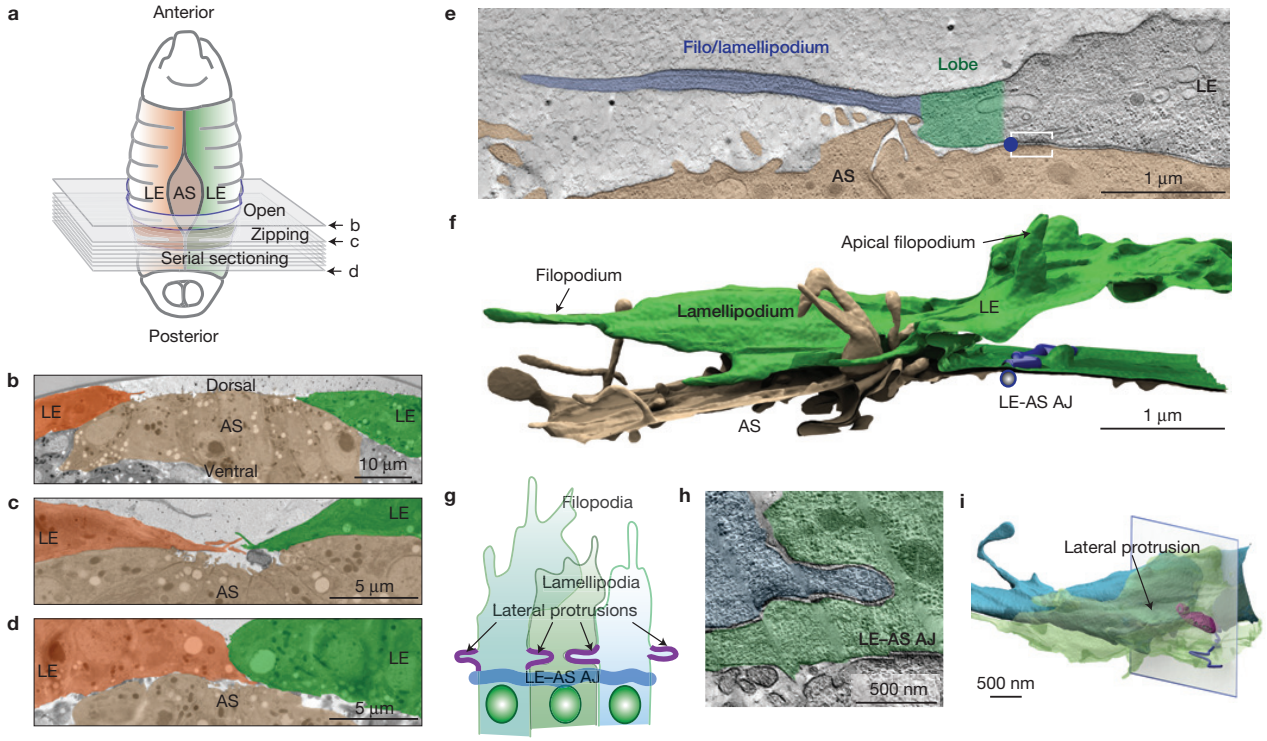

Figure 1 DC with electron microscopy resolution. (**a**) Schematic representation of an embryo showing the orientation of the sectioning plane. The eye-shaped gap in the epidermis (red/green) is filled with AS (brown) tissue. The sectioning starts from the open area, then a serial section stack was collected in one of the zipping areas, which occur on the opening canthi. (**b**–**d**) Low-magnification electron micrographs of sections as indicated in **a**. As the epidermal cells at the LE (red/green) converge, the AS tissue (brown) switches curvature from convex to concave. (**e**) High-magnification electron micrograph of the cross-section through the apical part of two AS cells (brown) and the dorsal–apical side of an LE cell (green) before zipping. The white box demarcates the AJs (LE–AS AJs) connecting the two tissues. The blue dot marks the beginning of the free-floating cell extension with the lobe part (green) and the filopodium–lamella part (blue). The filopodia generally extended off a lamellipodium. In cross-section, they were about 200 nm thick and contained mainly cytoskeletal elements. The lobes were considerably thicker and contained other organelles as well (for example vesicles and mitochondria). (**f**) 3D reconstruction showing the surfaces of the cells in **e**. The extension of the LE cell (green) consists of a wide lamellipodium with filopodium-like tips. Short apical filopodia are also present. The AS cells (brown) form multiple pleomorphic filopodia (see also Supplementary Fig. 1A). The blue cylinder denotes the LE–AS AJs. (**g**) Schematic representation showing top view of neighbouring LE cells and their lateral protrusions (purple) that lie above LE–AS AJs. (**h**) Tomographic slice through a lateral protrusion connecting neighbouring LE cells (as marked in **i**). (**i**) Isosurface representation of a lateral protrusion connecting two LE cells. Purple spheres mark predicted AJs. The blue cylinder indicates the LE–AS AJs.

their microtubules (MTs) into multiple, parallel bundles, each made of dynamic antiparallel MTs, at the apical cell surfaces[12]. The bundles are oriented such that the MT plus ends grow into the cell protrusions. In the absence of MTs, zipping arrests for unknown reasons[12].

To clarify the roles of actin and MTs during zipping, the exact morphology of interacting LE cells needs correlation with cytoskeleton architecture as the process proceeds. Recently, electron tomography enabled a comprehensive three-dimensional (3D) description of an entire eukaryotic cell at the required resolution[13]. Here, we present a similar 3D reconstruction of an entire developmental process. Our large-scale electron tomography of intact *Drosophila* embryos generates a comprehensive description of the zipping process at cellular and subcellular resolution. We analysed cell surface morphology, membrane interactions, cytoskeleton architecture and the presumptive adhesion sites of LE cells before and during zipping. Owing to the sequential nature of zipping, our data provide a time-resolved picture. We discovered that interacting LE cells generate a single 'roof tile'-like, lamellar overlap with dispersed adhesion sites, rather than intertwining multiple cellular protrusions as previously thought. The overlaps subsequently shorten and remodel into normal epidermal cell–cell interaction surfaces. The shortening overlap regions are filled with MTs, whereas detectable actin filament ensembles are absent, suggesting MT- rather than actin-mediated force generation. A timely switch in MT dynamics fits with a known MT-based force-generating mechanism.

Our data revealed evidence for another function of MTs in orienting LE-cell protrusions through direct interaction with actin bundles to promote the initial contacting of opposing LE cells before zipping. Finally, we observed changes in 3D curvature of the AS tissue before zipping, which may be functionally significant for tissue closure.

RESULTS

Cell surface topology before zipping

We established a protocol providing sufficient preservation of embryos to enable the following electron tomography study (Methods). We first traced the topology of AS- and LE-cell surfaces, from serial

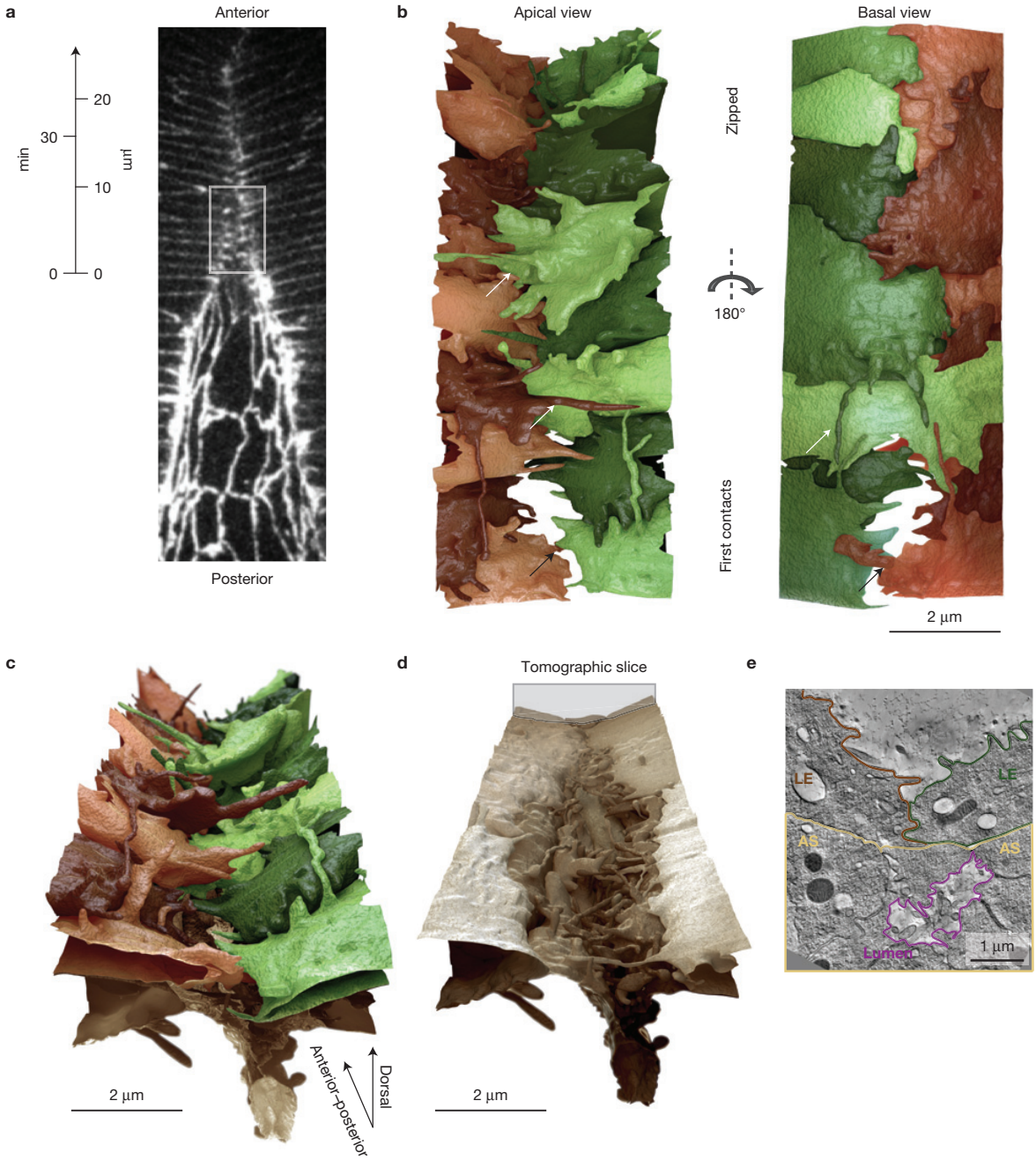

Figure 2 3D reconstruction of zipping. (**a**) Fluorescence confocal microscopy image of an early anterior zipping region of an embryo with fluorescently marked ARM–GFP. The scale bar depicts the length of the zipping area in relation to the approximate zipping duration. The white box depicts the area that is reconstructed in **b**–**d**, covering the dorsal–apical surface of 17 LE cells and the apical surface of eight AS cells. (**b**) Apical and basal views of the zipping LE-cell surfaces. Membranes are coloured in shades of brown and green to discriminate individual cells and their left/right origin respectively. At the front cells are in the early zipping phase, making first contacts; at the back they are in the late zipping phase. Black arrows point to the first contact. White arrows point to some filopodia and lamellipodia formed outside the zipping overlap. (**c**) Perspective view of the zipping area, coloured as in **b**. (**d**) The same view as in **c** with the LE cells computationally removed to reveal the AS cells. (**e**) Tomographic slice from the advanced zipping area at the position indicated by the section in **d**. AS cells (brown) located below LE cells (green and shades of red) form a tube, with the lumen (pink) filled with AS protrusions.

cross-sections of five embryos (Fig. 1a). We observed a distinct 3D morphology of the AS tissue, which comprised a convex curvature in central regions of the opening and a switch to concave towards the anterior and posterior zipping canthi (Fig. 1b–d). Outlining the apical membrane of each AS cell was a ring of filopodia. These were less than 200 nm in diameter and extended out into the perivitelline

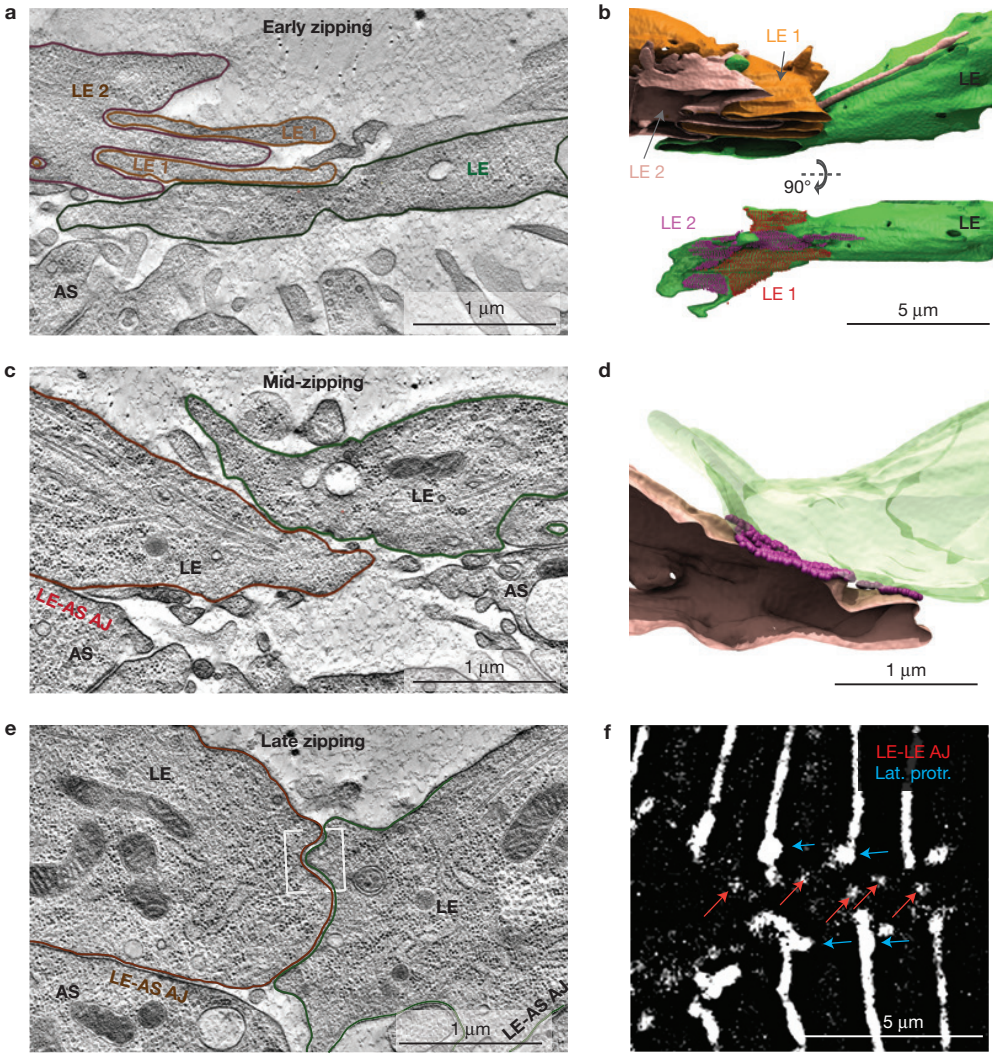

Figure 3 Opposing LE cells generate a single membrane overlap. (**a**) Tomographic slice showing the single membrane interaction interface of opposing LE cells (green and shades of red respectively) during early zipping. LE 1 and LE 2 are neighbouring cells. (**b**) Surface representation of the cellular interactions shown in **a**. The lower panel shows the interaction surface of the green LE cell with LE cells 1 and 2 after a 90° rotation. The red and purple spheres indicate the positions with 30 nm intercellular spacing predictive of AJs between the green LE and LEs 1 and 2 respectively. (**c**) Tomographic slice showing a single interface of interacting LE cells during mid-zipping. (**d**) Surface representation of the cellular interactions shown in **c**. Purple spheres depict the newly formed AJs. (**e**) Tomographic slice showing a single interface of interacting LE cells during late zipping. The boxed region highlights the AJs. (**f**) Fluorescence image of an embryo expressing GFP-tagged α-catenin, which strongly labels AJs of lateral protrusions (blue arrows) and weakly labels newly formed junctions connecting opposing LE cells (red arrows).

space (Supplementary Fig. 1a). LE cells were repelled by AS-cell protrusions that reached into their territory, forming cavities around them (Supplementary Fig. 1b).

Moreover, LE cells had lamellipodia and filopodia of variable length and shape at their dorsalmost apical sides, reflecting a snapshot of their dynamicity (Fig. 1e,f)[9]. LE-cell protrusions were demarcated from the cell body by the adherens junctions that connect LE and AS cells (LE–AS AJs; Supplementary Fig. 1c)[14]. From there they protruded above the filopodia of the AS cells, largely directed towards the opposing epidermis front. LE-cell protrusions could be dissected into three parts: the finger-like filopodia, the flat lamellipodia and the lobes forming the base of all protrusions (Fig. 1e,f). Lamellipodia and lobes of neighbouring LE cells frequently formed lateral overlaps (Supplementary Fig. 1d). Neighbouring LE cells were apicolaterally interlocked, jigsaw-like, by finger-like protrusions, invading neighbouring cells (Fig. 1g–i).

Zipping LE cells generate a simple surface overlap

Next, we generated a detailed reconstruction of the zipping process by joining 34 serial tomograms reconstructed from a 2 × 2-montaged tilt series. We analysed a volume of about 500 µm^3 extending about 10 µm along the anterior–posterior axis. This covered the dorsalmost apical cell surfaces of eight and nine neighbouring LE cells from either side and the apical cell surfaces of the interjacent AS cells (Fig. 2a–d

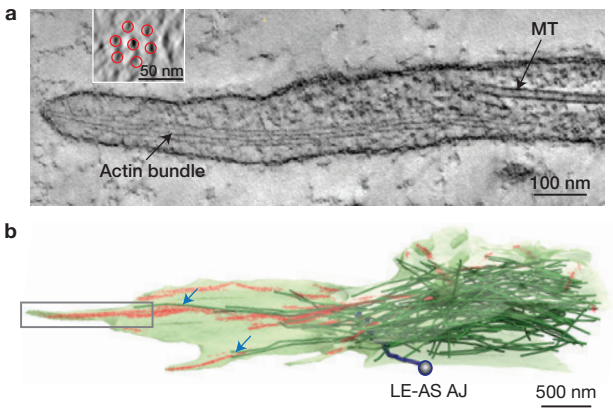

Figure 4 Cytoskeleton organization within LE cell before zipping. (**a**) Longitudinal tomographic slice through a filopodium tip showing an MT and an actin bundle. A tomographic slice of the actin bundle (inset) reveals the hexagonal order of the actin cable packing. (**b**) MTs (green, indicated by arrows) co-localize and co-orient with actin bundles (red) in LE-cell extensions. Also in the cell body, MTs preferentially orient towards the opposing LE cell. The blue cylinder indicates LE–AS AJs. The rectangle outlines the location of the structures visualized in **a**.

and Supplementary Video 1). Below zipping LE cells the AS tissue increased convexity. Eventually, the lateralmost AS cells sealed with each other, forming a tube below the AS–LE contacts (Fig. 2d,e).

On the basis of LE-cell interaction morphology, we subdivided zipping into three regions: early, mid- and late. In early zipping, LE cells from opposite sides made filopodial contacts, which developed into significant membrane overlaps (Fig. 2c). Such contacts were detected in approximately 50% of opposing LE cells (25 cells from three embryos) after cell fronts had reached a distance of about 10 μm between opposing LE–AS AJs. Most of them probably correspond to the frequent, transient interactions seen with fluorescence microscopy[9]. Clearly representing stable contacts were the larger membrane surface overlaps with prospective adhesion sites we observed. As in previous analysis, we detected substantial membrane intertwining in early zipping[9]. However, we found that this exclusively connected LE cells from the same side of the opening (Fig. 3a,b and Supplementary Video 2). Zipping LE cells instead expanded a lamellipodium to generate a single, 'roof tile'-like interaction surface, without any obvious handedness (Fig. 3a,b and Supplementary Video 2). In this lamellar overlap we used a distance-tracing algorithm to identify areas with an intermembrane spacing of about 30 nm, which is typical for adhesion sites (Fig. 3b; Methods)[15]. Isolated electron densities in these intermembrane regions indicated the presence of a film of adhesion molecules (Supplementary Fig. 2a).

In mid-zipping the lamellar overlap areas of opposing cells shortened and cell adhesions matured. Lamellar overlap shortening coincided with gradual, proximal–distal thickening of the lamellae (Fig. 3c). Consequently, the initially horizontal connection turned into a vertical orientation, parallel to the proximal–distal embryo axis (Fig. 3a,c,e). Simultaneously, distinct AJs, about 10,000 nm^2 in size, appeared in between the lamellar overlaps (Fig. 3d). Their position correlated well with α-catenin spots, detected with live fluorescence imaging[16] (Fig. 3f and Supplementary Video 3). In mid-zipping, the intertwined membranes of neighbouring LE cells also resolved.

In late zipping, the interface of opposing LE cells adopted the orientation of normal epidermis cell interfaces (Fig. 3e). At this stage, the lobes continued thickening and adhesion sites further expanded and became associated with a pronounced intracellular plaque. They were not yet showing the typical linear arrangement of epidermal AJs[17]. This linearization extended over a further two to five cell pairs. Its completion marked the end of zipping (Supplementary Fig. 2b).

Correlating electron tomography data with live imaging observations suggested the transition from initial protrusion contacts to a seamless epithelial layer lasts up to an hour. This way, approximately 15 neighbouring cells are simultaneously zipping at different stages. LE cells continued producing filopodia and lamellipodia above the lamellar overlap region throughout zipping. However, these did not produce further cell–cell contacts (Fig. 2b and Supplementary Video 1).

MTs invade actin-based protrusions before zipping

Our tomograms enabled us to visualize both MTs and actin filament ensembles (Fig. 4a). On the basis of their texture and immunogold labelling, we could determine whether or not the latter harboured MyoII (Supplementary Figs 3 and 4). Before zipping, we detected actin bundles in all LE-cell protrusions (Fig. 4a,b). They were 0.5–3 μm in length and consisted of parallel actin filaments with 15–20 nm spacing. The computationally generated cross-sections showed that within bundles actin filaments formed a hexagonal lattice (Fig. 4a). In each LE cell we also detected a prominent MyoII-containing actin bundle, positioned apicolaterally with anterior–posterior orientation (Supplementary Figs 3 and 4b,c). On the basis of appearance and position, together these form the actin–MyoII purse string surrounding the opening[7]. The ends of actin–MyoII bundles invaded lateral protrusions harbouring multiple AJs (Supplementary Fig. 3b). These cell surface extensions probably propagate the contractile actin–MyoII cable forces.

Confirming previously published work, we detected a high density of MTs in the apical part of the LE cells[12] (Fig. 4b). A few MTs continued to grow into the lamellipodia and filopodia, where they frequently reached the protrusion tip. MTs were close to, and precisely aligned with, the actin bundles, indicating a cooperative role in protrusion formation. We also detected MTs closely following the actin–MyoII purse string all the way into the lateral protrusions (Supplementary Fig. 3b).

Zipping involves considerable cytoskeleton reorganization

Lamellar overlap shortening during mid-zipping remains the obvious zipping force-generating step. To investigate the role of the cytoskeleton, we reconstructed all visible cytoskeleton elements in the lamellar overlaps. Throughout zipping, we detected actin bundles in all non-interacting lamellipodia and filopodia of LE cells. In early zipping, actin bundles were present in the forming lamellar overlap regions. In contrast, the shortening lamellar overlaps mid-zipping were devoid of any detectable actin filament ensembles. Instead, they were crowded with MTs throughout the shortening period (Fig. 5a,b). To further verify the role of actin we carried out latrunculin B (LatB) injections to interfere with actin polymerization. Immediately following injection the known actin-based force-generating systems,

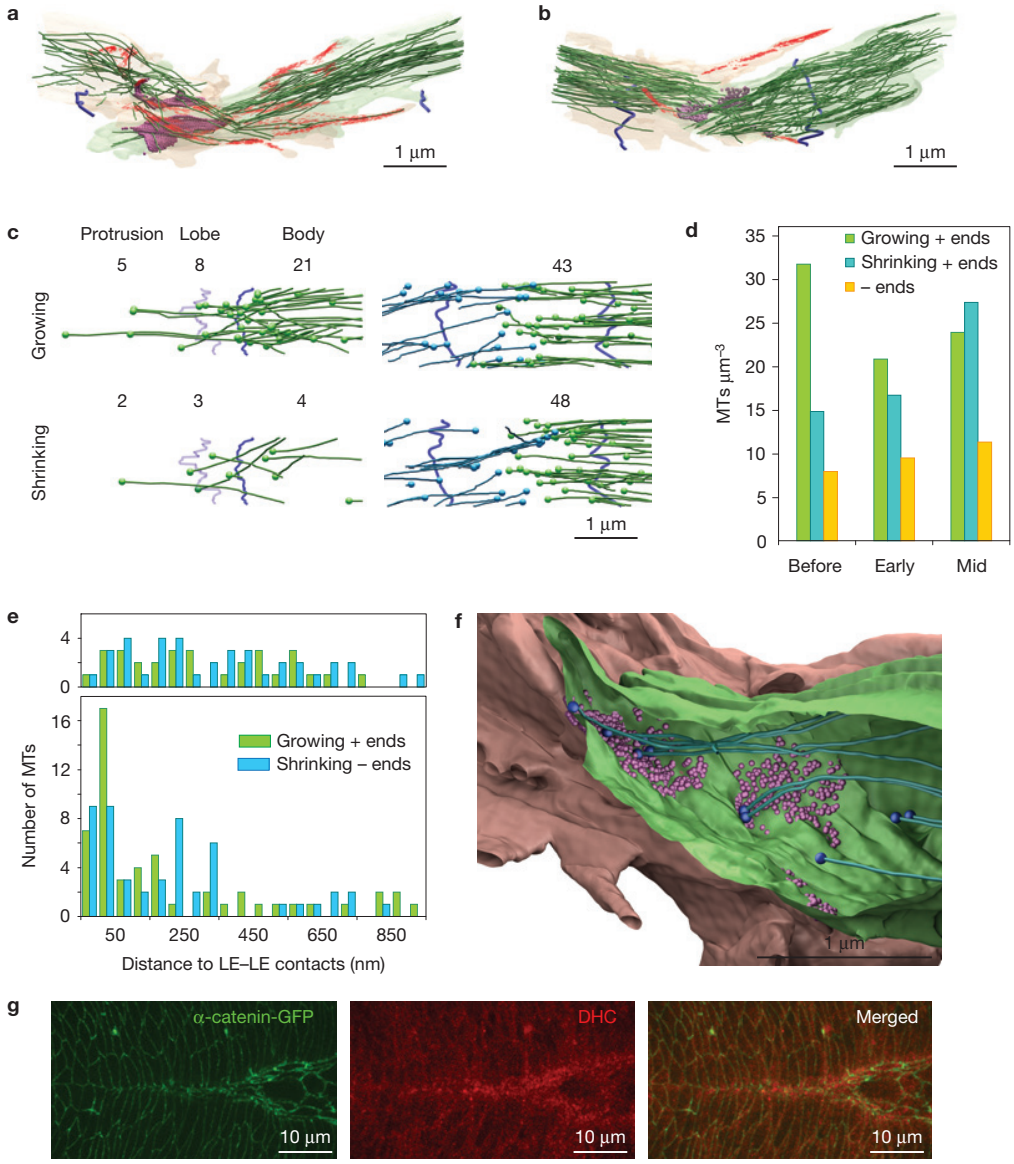

Figure 5 MTs as zipping force generators. (**a**) Lateral view of actin bundles (red) and MTs (green) in the extensions of two interacting LE cells from opposing epidermal fronts in early zipping. Purple spheres depict LE–LE contacts. The blue cylinders indicate LE–AS AJs. (**b**) The mid-zipping organization of the MTs and actin bundles. The colouring is described in **a**. (**c**) Representation of MT polarity and growth states in different parts of LE-cell protrusions before zipping (left) and mid-zipping (right). (**d**) Quantification of MT growth states and MT polarity in LE-cell extensions before zipping (three cells covering 2.38 μm^3) and during early zipping (six cells covering 6.36 μm^3) and mid-zipping (five cells covering 5.07 μm^3). (**e**) Histogram showing the distance of growing and shrinking MT ends to the cell–cell contacts of zipping LE cells during early (68 MT ends from six cells; top panel) and mid-zipping (102 MT ends from six cells; bottom panel). (**f**) Isosurface representation of the extensions of two opposing LE cells (brown and green colour) that interact mid-zipping. Purple spheres depict AJs connecting the cells. Blue spheres depict the ends of shrinking MTs (green cylinders). (**g**) Immunofluorescence labelling with antibodies recognizing the dynein heavy chain (DHC; in red). Cell borders are visualized using α-catenin–GFP (in green). In the merged image it can be seen that dynein accumulates in the dorsal ends of all LE cells and disappears after the completion of zipping.

the actin–MyoII purse string and the AS tissue, lost tension (Supplementary Fig. 5 and Methods). The consequence was an almost immediate disintegration of the entire DC area, including rapid expansion of the AS tissue, ventralward retraction of the LE and massive local rupturing of the epidermis front. In contrast, the zipping region only started disintegrating with a clear delay, showing that the zipping force is less sensitive to actin filament destruction. Together these observations suggest that zipping force generation is an MT- rather than actin-based process.

To investigate how MTs could generate the zipping force, we first analysed MT polarity by following the green fluorescent protein (GFP)-tagged MT end-tracking protein EB1 (GFP–EB1; refs 18,19). Previous GFP–EB1 tracking revealed an antiparallel, dorsal–ventral MT arrangement with stable MT minus ends and dynamic plus

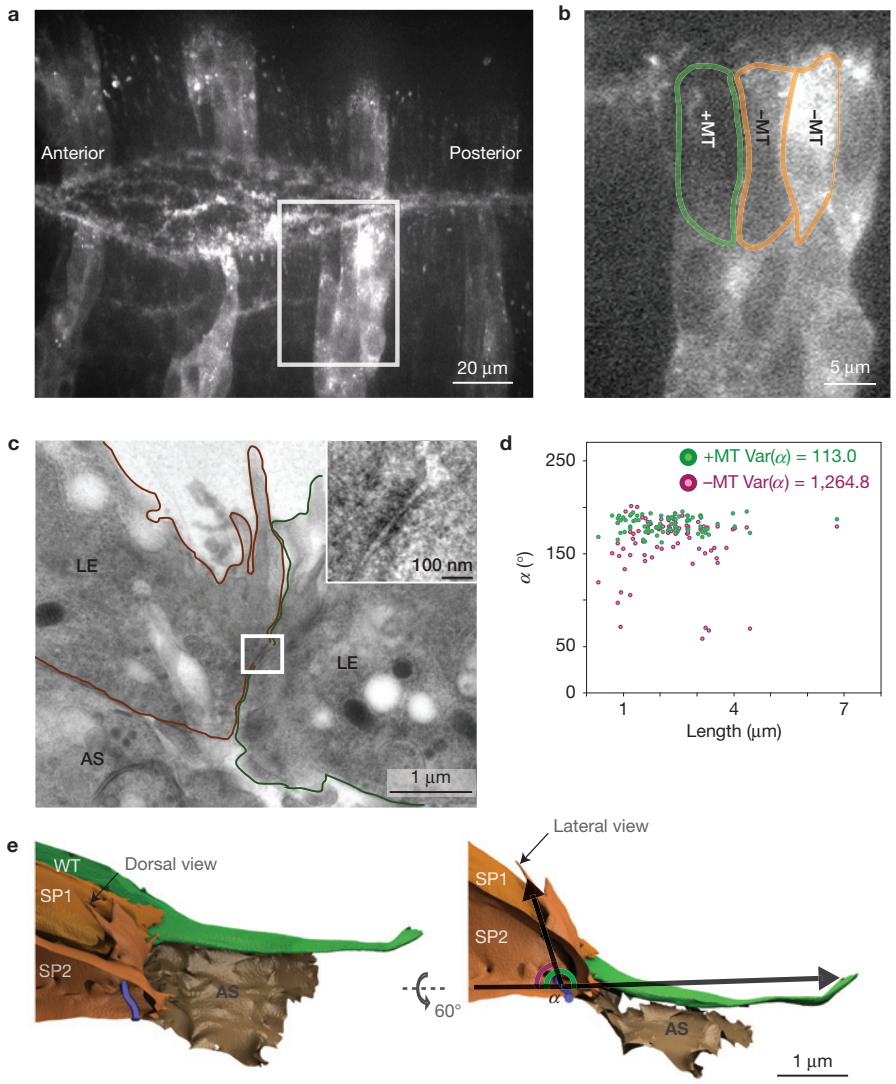

Figure 6 MTs orient cellular extensions. (**a**) Fluorescent image of the dorsal opening showing stripes of epidermal cells expressing Spastin–eGFP (enhanced green fluorescent protein) under the control of the engrailed promoter and ubiquitously expressed Moesin–GFP to outline the cell borders. (**b**) Magnified cells from the highlighted box in **a** showing the variability in Spastin–eGFP expression levels. (**c**) Tomographic slice showing a single membrane interaction interface with an AJ of opposing LE cells (green and shades of brown) expressing Spastin–eGFP. The inset shows the magnified view of the AJ outlined in the rectangle. (**d**) Plot showing the orientation of LE-cell protrusions as a function of the angle over the length of the protrusion (90 sections from 13 Spastin-expressing cells; 81 sections from 16 wild-type (WT) cells; see Methods for details). (**e**) 3D reconstruction of the surfaces of the magnified LE cells in **b**. The weakly Spastin-expressing LE cell (green) still contains MTs (Supplementary Fig. 6a) whereas the other two cells (shades of brown) express sufficient Spastin–eGFP to eliminate the MTs and thus affect cell extension orientation. In the lateral view, the vectors depict the angles of the two protrusions.

ends in LE-cell bodies[12]. However, in zipping LE-cell protrusions we detected almost exclusively GFP–EB1 moving dorsally into the protrusions, suggesting that they mainly contain MTs with plus ends facing the protrusion tips (Supplementary Video 4). We further analysed polarity and dynamic state of these MTs by analysing MT end morphologies in our tomographic images[20] (Supplementary Fig. 6a,c). We detected capped and thus stable MT minus ends in the cell body and lobe regions but not in LE filopodia and lamellipodia. Because measurement of MT growth speeds had previously excluded the presence of uncapped, dynamic MT minus ends, this suggests that LE-cell protrusions harbour mainly MT plus ends[11]. Most of these could be classified as being in a dynamic, growing or shrinking state.

In dynamic equilibrium more growing than shrinking MT plus ends are expected, because MT depolymerization is significantly faster than polymerization[21]. Consistently, we observed more growing MTs in LE-cell protrusions before and during early zipping (Fig. 5c,d and Supplementary Fig. 6b). Depolymerizing and polymerizing MT ends were distributed throughout the protrusion, supporting the picture of MTs dynamically switching between growing and shrinking states.

In mid-zipping, however, MTs in the shortening lamellar overlap regions of opposing cells changed their dynamicity, as we detected more shrinking than growing MTs. Moreover, a majority of the shrinking MT ends were situated end on, at the putative cell–cell adhesion sites, suggesting that MTs are not freely depolymerizing but are tethered, at least temporarily, to the adhesion sites (Fig. 5e,f). Tethering of MT ends by cortical dynein motors was shown to generate forces positioning spindles and nuclei[22–24]. Interestingly, immunofluorescence staining revealed dynein enrichment at the dorsal end of LE cells, indicating a similar mechanism acting to generate zipping forces (Fig. 5g). Together, these results provide further support for MT-mediated zipping force generation.

MTs control cell protrusion orientation before zipping

A role for the MTs in force generation could explain their essential function in zipping progression. Alternatively, the initial cell–cell contacting could be inhibited, as the absence of MTs was shown to alter protrusion size and number also[12]. To investigate this further, we made electron tomograms of embryos ectopically expressing the MT-severing protein Spastin in epidermal cell stripes (Fig. 6a,b). This enabled a side-by-side analysis of cells with and without MTs (ref. 12). As expected, Spastin-expressing cells virtually lacked MTs (Supplementary Fig. 7a). At the arrested zipping fronts, Spastin-expressing LE cells still made contacts and formed proper AJs (Fig. 6c). This shows that MT function is not essential for junction formation or cell–cell recognition.

Before zipping, LE cells lacking MTs showed shorter lobe regions than the wild type (~0.75 μm versus ~1.7 μm on average), but the overall length of lamellipodia and filopodia was unaffected (Fig. 6d and Supplementary Fig. 7b). Furthermore, wild-type cell protrusions consistently extended straight towards opposing LE cells, whereas filopodia and lamellipodia lacking MTs showed a tenfold higher variability in the directionality of their protrusion and often extended upwards into the perivitelline space or laterally over the bodies of neighbouring cells (Fig. 6e and Methods). We conclude that, before zipping, MTs affect the orientation of cell protrusions, possibly to accelerate the initial contacting of opposing LE cells.

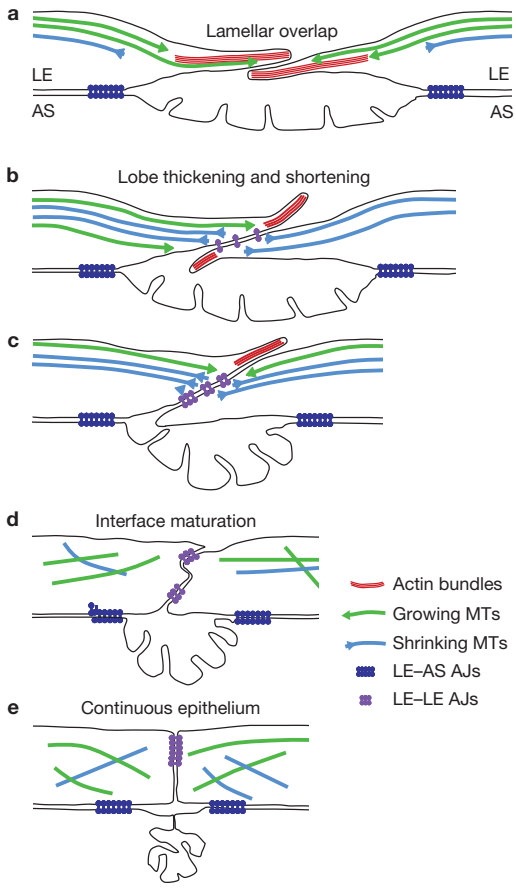

Figure 7 Proposed model of zipping. (**a**–**e**) Schematic representation of cell membrane organization and cytoskeletal remodelling of the LE cells during early (**a**), mid- (**b**,**c**) and late zipping (**d**), and after zipping is completed (**e**). Growing and shrinking MTs are represented as green and light blue arrows respectively. Actin bundles are illustrated as red lines. AS–LE AJs are depicted as dark blue dots and LE–LE AJs as purple dots.

DISCUSSION

Here, we reconstruct the zipping process, which represents a general model for developmental tissue sealing and wound healing[25]. Previous work had suggested that zipping starts when dynamic lamellipodia and filopodia of opposing cells intertwine in a random manner. It was speculated that actin-mediated shortening of these complex membrane overlap regions generates the zipping force[1]. Our data reveal different scenarios for these processes. We find that the complex membrane intertwining describes the interaction surface of neighbouring LE cells, whereas zipping LE cells generate a single, flat, lamellar overlap region (Fig. 7a). This 'roof tile'-like overlap subsequently resolves, whereby the horizontal membrane interaction surface rotates into a vertical orientation (Fig. 7b–e). Our observations suggest that this is achieved by shortening and concomitant thickening of the overlapping protrusions. Because at this point zipping cells have established mature junctions, simultaneous protrusion shortening will automatically pull the two cell bodies together. This brings the laterally attached neighbours into closer proximity, which facilitates their interaction and thus zipping progression.

Our observations indicate that zipping cells autonomously pull the distal end of the lamellar protrusion towards their cell body. The hypothesis of actin-mediated force generation was based on the abundance of actin cables in the dynamic cell protrusions before zipping, which we confirm with our electron microscopy tomograms[1]. However, we cannot find evidence for actin filament ensembles in the shortening overlap regions of zipping cells. Instead we find them crowded with MTs, making these the prime candidates for being force generators. The finding that zipping forces are more resistant to latrunculin than other, actin-based DC forces supports this view. Notably, we cannot completely rule out a role for actin, because individual actin filaments could have escaped detection. Yet, we detect a switch in MT dynamics in the shortening overlap region that suggests a possible mechanism: before zipping, LE cells contain more polymerizing than depolymerizing MT ends, which is in agreement with a dynamic instability equilibrium of MT growth and shrinkage[21]. In the shortening overlap region of zipping cells MTs are more often shrinking than growing and they cluster at prospective AJs, towards

which they seem to be pushed or pulled. The absence of major MT bending favours the latter, pointing towards a well-known mechanism: in human cells and *Caenorhabditis elegans* zygotes cortically tethered dynein motors position mitotic spindles by pulling on astral MTs, and in fission yeast they generate oscillatory movements of the meiotic nucleus[22–24]. Common to all, dynein captures the plus ends of incoming MTs and pulls on them by walking towards their minus ends, even while they are depolymerizing. Consistently, we detected significant dynein enrichment in the dorsal region of LE cells. It is intriguing to speculate that this mechanism, known to position subcellular structures, is used to shape cells and tissues. Unfortunately, straightforward genetic analysis of dynein was not possible, as the maternal contribution enables survival of dynein mutants beyond DC (ref. 26). Further analysis thus requires development of tools for selective dynein elimination in LE cells. Altogether, these findings may reveal a conserved mechanism driving tissue fusion in all embryogenesis and even in wound healing.

In addition to the role in zipping, we found that before zipping MTs help in orienting cell protrusions. In their absence, the dynamic lamellipodia and filopodia of LE cells frequently grew sidewards or upwards or even backwards, rather than straight forward, towards the opposing LE cells. The immediate proximity of MTs and actin bundles suggests that this involves direct contacts between these cytoskeletal elements. LE cells with misoriented protrusions will clearly take longer to find their interaction partners. Importantly, this would merely slow down zipping, whereas the reported zipping arrest caused by MT absence must involve another MT function[12]. Distorting MT-mediated cell–cell recognition or adhesion is unlikely to be causative, because at the arrested zipping canthi opposing LE cells still recognize each other and form AJs. Therefore, the essential role of MTs in zipping is most probably linked to the subsequent force generation step. Intimate interaction of MTs and actin bundles may also be relevant to control directionality of other cellular protrusions. For instance, turning of neuronal growth cones, actin-based structures, was shown to require MT function[27].

Finally, we observe a 3D rearrangement of AS tissue that switches from a convex to a concave curvature near the zipping fronts. So far, the AS tissue has been treated as a two-dimensional (2D) system, and cell surface dynamics was measured accordingly. Tissue curvature is likely to affect the outcome of such analysis and the interpretation of forces. Notably, switching tissue curvature is the hallmark of tissue invagination during gastrulation[28]. It is possible that near zipping fronts the AS tissue behaves similarly to gastrulating ectoderm. Pulsed cell surface contractions and continuous cell surface constriction are common to both[2,4,29]. The AS tissue eventually even closes into a tube, indicating further mechanistic similarities to neurulation in vertebrate development[30].

Our work emphasizes the fundamental importance of detailed, high-resolution characterization of cellular architecture for the understanding of developmental processes and their underlying mechanisms, as well as for the interpretation of mutant phenotypes. We only addresses a small fraction of the overwhelming information on subcellular architecture and changes thereof contained within our tomograms. To enable further exploitation by the scientific community we make them available as a resource at EMDB (reference number 11915). □

METHODS

Methods and any associated references are available in the online version of the paper.

Note: Supplementary Information is available in the online version of the paper

ACKNOWLEDGEMENTS

We are particularly grateful to the EMBL electron microscopy facility and S. Pruggnaller, A. Habermann, V. Rybin, Y. Belyaev and R. Gibeaux for help with embryo processing, image acquisition and image analysis. We are grateful to J. Ellenberg, M. Vabulas and C. Pohl for critical reading and discussion of the manuscript. We thank I. Simeonova, A. Schmidkunz, N. Wollf, S. Wali and V. Eltsova for tracing. M.E. was supported by an EIPOD fellowship; N.D. was supported in part by a Fellowship from the Canadian Cancer Society Research Institute (Terry Fox Foundation, award no. 018608). Core funding (EMBL, University of Zurich, CEF and CEFII) and an ERC starting grant to A.S.F. provided further support.

AUTHOR CONTRIBUTIONS

M.E. designed and carried out experiments, analysed data and wrote the manuscript. N.D., Z.Y., L.P. and U.H-W. carried out experiments and analysed data. D.B. and A.S.F. designed experiments, analysed data and wrote the manuscript. All authors have proofread the manuscript.

COMPETING FINANCIAL INTERESTS

The authors declare no competing financial interests.

Published online at www.nature.com/doifinder/10.1038/ncb3159
Reprints and permissions information is available online at www.nature.com/reprints

1. Jacinto, A., Martinez-Arias, A. & Martin, P. Mechanisms of epithelial fusion and repair. *Nat. Cell Biol.* **3,** 117–123 (2001).
2. Solon, J., Kaya-Copur, A., Colombelli, J. & Brunner, D. Pulsed forces timed by a ratchet-like mechanism drive directed tissue movement during dorsal closure. *Cell* **137,** 1331–1342 (2009).
3. Kiehart, D. P., Galbraith, C. G., Edwards, K. A., Rickoll, W. L. & Montague, R. A. Multiple forces contribute to cell sheet morphogenesis for dorsal closure in *Drosophila*. *J. Cell Biol.* **149,** 471–490 (2000).
4. Gorfinkiel, N., Blanchard, G. B., Adams, R. J. & MartinezArias, A. Mechanical control of global cell behaviour during dorsal closure in *Drosophila*. *Development* **136,** 1889–1898 (2009).
5. Riesgo-Escovar, J. R., Jenni, M., Fritz, A. & Hafen, E. The *Drosophila* Jun-N-terminal kinase is required for cell morphogenesis but not for DJun-dependent cell fate specification in the eye. *Genes Dev.* **10,** 2759–2768 (1996).
6. Morel, V. & Arias, A. M. Armadillo/β-catenin-dependent Wnt signalling is required for the polarisation of epidermal cells during dorsal closure in *Drosophila*. *Development* **131,** 3273–3283 (2004).
7. Young, P. E., Richman, A. M., Ketchum, A. S. & Kiehart, D. P. Morphogenesis in *Drosophila* requires nonmuscle myosin heavy chain function. *Genes Dev.* **7,** 29–41 (1993).
8. Hutson, M. S. *et al.* Forces for morphogenesis investigated with laser microsurgery and quantitative modeling. *Science* **300,** 145–149 (2003).
9. Jacinto, A. *et al.* Dynamic actin-based epithelial adhesion and cell matching during *Drosophila* dorsal closure. *Curr. Biol.* **10,** 1420–1426 (2000).
10. Jacinto, A. & Martin, P. Morphogenesis: unravelling the cell biology of hole closure. *Curr. Biol.* **11,** R705–R707 (2001).
11. Jacinto, A. *et al.* Dynamic analysis of actin cable function during *Drosophila* dorsal closure. *Curr. Biol.* **12,** 1245–1250 (2002).
12. Jankovics, F. & Brunner, D. Transiently reorganized microtubules are essential for zippering during dorsal closure in *Drosophila* melanogaster. *Dev. Cell* **11,** 375–385 (2006).
13. Hoog, J. L. & Antony, C. Whole-cell investigation of microtubule cytoskeleton architecture by electron tomography. *Methods Cell Biol.* **79,** 145–167 (2007).
14. Wada, A., Kato, K., Uwo, M. F., Yonemura, S. & Hayashi, S. Specialized extraembryonic cells connect embryonic and extraembryonic epidermis in response to Dpp during dorsal closure in *Drosophila*. *Dev. Biol.* **301,** 340–349 (2007).
15. Boggon, T. J. *et al.* C-cadherin ectodomain structure and implications for cell adhesion mechanisms. *Science* **296,** 1308–1313 (2002).
16. Oda, H. & Tsukita, S. Nonchordate classic cadherins have a structurally and functionally unique domain that is absent from chordate classic cadherins. *Dev. Biol.* **216,** 406–422 (1999).
17. Tepass, U. & Hartenstein, V. The development of cellular junctions in the *Drosophila* embryo. *Dev. Biol.* **161,** 563–596 (1994).
18. Akhmanova, A. & Hoogenraad, C. C. Microtubule plus-end-tracking proteins: mechanisms and functions. *Curr. Opin. Cell Biol.* **17,** 47–54 (2005).
19. Rogers, S. L., Rogers, G. C., Sharp, D. J. & Vale, R. D. *Drosophila* EB1 is important for proper assembly, dynamics, and positioning of the mitotic spindle. *J. Cell Biol.* **158,** 873–884 (2002).

20. Mandelkow, E. M., Mandelkow, E. & Milligan, R. A. Microtubule dynamics and microtubule caps: a time-resolved cryo-electron microscopy study. *J. Cell Biol.* **114,** 977–991 (1991).
21. Mitchison, T. & Kirschner, M. Dynamic instability of microtubule growth. *Nature* **312,** 237–242 (1984).
22. Gonczy, P., Pichler, S., Kirkham, M. & Hyman, A. A. Cytoplasmic dynein is required for distinct aspects of MTOC positioning, including centrosome separation, in the one cell stage Caenorhabditis elegans embryo. *J. Cell Biol.* **147,** 135–150 (1999).
23. Kotak, S., Busso, C. & Gonczy, P. Cortical dynein is critical for proper spindle positioning in human cells. *J. Cell Biol.* **199,** 97–110 (2012).
24. Vogel, S. K., Pavin, N., Maghelli, N., Julicher, F. & Tolic-Norrelykke, I. M. Self-organization of dynein motors generates meiotic nuclear oscillations. *PLoS Biol.* **7,** e1000087 (2009).
25. Wood, W. *et al.* Wound healing recapitulates morphogenesis in *Drosophila* embryos. *Nat. Cell Biol.* **4,** 907–912 (2002).
26. Gepner, J. *et al.* Cytoplasmic dynein function is essential in *Drosophila* melanogaster. *Genetics* **142,** 865–878 (1996).
27. Suter, D. M., Schaefer, A. W. & Forscher, P. Microtubule dynamics are necessary for SRC family kinase-dependent growth cone steering. *Curr. Biol.* **14,** 1194–1199 (2004).
28. Leptin, M. Gastrulation in *Drosophila*: the logic and the cellular mechanisms. *EMBO J.* **18,** 3187–3192 (1999).
29. Martin, A. C., Kaschube, M. & Wieschaus, E. F. Pulsed contractions of an actin-myosin network drive apical constriction. *Nature* **457,** 495–499 (2009).
30. Suzuki, M., Morita, H. & Ueno, N. Molecular mechanisms of cell shape changes that contribute to vertebrate neural tube closure. *Dev. Growth Differ.* **54,** 266–276 (2012).